Bartosz Daniel Turkowyd

DISSERTATION

STUDIES OF SINGLE-MOLECULE DYNAMICS IN MICROORGANISMS

Max Planck Institute for Terrestrial Microbiology

Department of Systems and Synthetic Microbiology

Marburg, Germany

01.02.2015 - 30.04.2019

written by Bartosz Daniel Turkowyd

born 18.03.1988 in Wrocław (Poland)

Die Untersuchungen zur vorliegenden Arbeit wurden von Februar 2015 bis April 2019 in der Abteilung System- und Synthetische Mikrobiologie des Max-Planck-Institutes für terrestrische Mikrobiologie in Marburg in der Arbeitsgruppe von Dr. Ulrike Endesfelder durchgeführt.

Vom Fachbereich Biologie der Philipps-Universität Marburg als Dissertation angenommen am:

Gutachter dieser Arbeit waren:

Erstgutachter: Dr. Ulrike Endesfelder

Zweitgutachter: Prof. Dr. Martin Thanbichler

Erklärung

Ich versichere, dass ich meine Dissertation mit dem Titel "Studies of Single-Molecule Dynamics in Microorganisms" selbstständig, ohne unerlaubte Hilfe angefertigt und mich dabei keiner anderen als der von mir ausdrücklich bezeichneten Quellen und Hilfsmittel bedient habe.

Diese Dissertation wurde in der jetzigen oder einer ähnlichen Form noch bei keiner anderen Hochschule eingereicht und hat noch keinen sonstigen Prüfungszwecken gedient.

Bartosz Turkowyd

Marburg, den 30.04.2019

Contents

List of Acronyms

AFM Atomic Force Microscopy

Cas CRISPR-Associated Proteins

Cascade CRISPR-Associated Complex for Antiviral Defense

CRISPR Clustered Regularly Interspaced Short Palindromic Repeats

crRNA CRISPR RNA

DIC Differential Interference Contrast

DNA Deoxyribonucleic Acid

dsDNA Double-Stranded DNA

(d)STORM (direct) Stochastic Optical Reconstruction Microscopy

EGFP Enhanced Green Fluorescent Protein

EOP Efficiency of Plaquing

EosFP Eos Fluorescent Protein

GSDIM Ground-State Depletion followed by Individual Molecule Return

MGEs Mobile Genetic Elements

mKikGR Monomeric Kik Green-to-Red Fluorescent Protein

mRNA Messenger RNA

PAC Primed Acquisition Complex

paFPs Photoactivatable Fluorescent Proteins

paGFP Photoactivatable Green Fluorescent Protein

PAINT Point Accumulation for Imaging in Nanoscale Topography

PALM Photoactivated Localization Microscopy

PAM Protospacer Adjacent Motif

PC Primed Conversion

pcDronpa Photoconvertible Dronpa Fluorescent Protein

pcFPs Photoconvertible Fluorescent Proteins

pre-crRNA Precursor crRNA

PS-CFP2 Photoswitchable Cyan Fluorescent Protein 2

PSF Point Spread Function

PSmOrange Photoswitchable Monomeric Orange Fluorescent Protein

RNA Ribonucleic Acid

RNP Ribonucleoprotein

rRNA Ribosomal RNA

SE Standard Error

smFRET Single-Molecule Förster Resonance Energy Transfer

SMLM Single-Molecule Localization Microscopy

SPT Single-Particle Tracking

sptPALM Single-Particle Tracking PALM

tracrRNA Trans-Activating crRNA

Summary

Fluorescence microscopy is one of the most extensively used techniques in the life sciences. Considering the non-invasive sample preparation, enabling live-cell compliant imaging, and the specific fluorescence labeling, allowing for a specific visualization of virtually any cellular compound, it is possible to localize even a single molecule in living cells. This makes modern fluorescence microscopy a powerful toolbox.

In the recent decades, the development of new, "super-resolution" fluorescence microscopy techniques, which surpass the diffraction limit, revolutionized the field. Single-Molecule Localization Microscopy (SMLM) is a class of super-resolution microscopy methods and it enables resolution of down to tens of nanometers. SMLM methods like Photoactivated Localization Microscopy (PALM), (direct) Stochastic Optical Reconstruction Microscopy ((d)STORM), Ground-State Depletion followed by Individual Molecule Return (GSDIM) and Point Accumulation for Imaging in Nanoscale Topography (PAINT) have allowed to investigate both, the intracellular spatial organization of proteins and to observe their real-time dynamics at the single-molecule level in live cells.

The focus of this thesis was the development of novel tools and strategies for live-cell Single-Particle Tracking PALM (sptPALM) imaging and implementing them for biological research. In the first part of this thesis, I describe the development of new Photoconvertible Fluorescent Proteins (pcFPs) which are optimized for sptPALM lowering the phototoxic damage caused by the imaging procedure. Furthermore, we show that we can utilize them together with Photoactivatable Fluorescent Proteins (paFPs) to enable multi-target labeling and read-out in a single color channel, which significantly simplifies the sample preparation and imaging routines as well as data analysis of multi-color PALM imaging of live cells.

In parallel to developing new fluorescent proteins, I developed a high throughput data analysis pipeline. I have implemented this pipeline in my second project, described in the second part of this thesis, where I have investigated the protein organization and dynamics of the CRISPR-Cas antiviral defense mechanism of bacteria *in vivo* at a high spatiotemporal level with the sptPALM approach. I was successful to show the differences in the target search dynamics of the CRISPR effector complexes as well as of single Cas proteins for different target complementarities. I have also first data describing longer-lasting bound-times between effector complex and their potential targets *in vivo*, for which only *in vitro* data has been available till today.

In summary, this thesis is a significant contribution for both, the advances of current sptPALM

imaging methods, as well as for the understanding of the native behavior of CRISPR-Cas systems *in vivo*.

Zusammenfassung

Fluoreszenzmikroskopie ist eine der am häufigsten genutzten Techniken in den Lebenswissenschaften. Betrachtet man die nichtinvasive Probenvorbereitung, welche Lebendzell-verträgliche Bildgebung ermöglicht, und die spezifische Fluoreszenzmarkierung, welche die spezifische Visualisierung von nahezu jedem Zellbestandteil zulässt, ist sogar die Lokalisierung eines einzelnen Moleküls in lebenden Zellen möglich. Dies macht moderene Fluoreszenzmikroskopie zu einem leistungsstarken Werkzeugkasten.

In den vergangen Jahrzehnten hat die Entwicklung neuer, hochauflösender Fluoreszenzmikroskopietechniken das Forschungsfeld revolutioniert. SMLM ist eine Klasse dieser hochauflösenden Mikroskopiemethoden und ermöglicht die Auflösung bis auf zehn Nanometer. SMLM Methoden wie PALM, (d)STORM, GSDIM und PAINT haben es erlaubt sowohl die intrazelluläre, räumliche Organisation von Proteinen als auch ihre Echtzeitdynamiken auf der Einzelmolekülebene in lebenden Zellen zu untersuchen.

Der Fokus dieser Doktorarbeit war die Entwicklung neuer Werkzeuge und Strategien für die Lebendzell-sptPALM Bildgebung und deren Anwendung für die biologische Forschung. Im ersten Teil meiner Arbeit beschreibe ich die Entwicklung von neuen pcFPs, welche für sptPALM optimiert sind und den durch die Bildgebung verursachten phototoxischen Schaden verringern. Des Weiteren zeigen wir die Verwendung zusammen mit paFPs, was uns die Markierung mehrerer Ziele und das Auslesen in einem einfarbigen Kanal ermöglicht und sowohl die Probenvorbereitung, die Routine der Bildaufnahme als auch die Datenauswertung der Vielfarbenbildgebung lebender Zellen erheblich vereinfacht.

Parallel zur Entwicklung neuer fluoreszierender Proteine habe ich eine Hochdurchsatz-Datenauswertungs-Pipeline entwickelt. Angewendet habe ich diese Pipeline in meinem zweiten Projekt, das im zweiten Teil meiner Arbeit beschrieben ist, in welchen ich die Proteinorganisation und -dynamik des CRISPR-Cas antiviralen Abwehrmechanismus von Bakterien *in vivo* auf hoher räumlich-zeitlicher Ebene mit dem sptPALM Ansatz untersucht habe. Ich konnte erfolgreich den Unterschied in den Zielsuchdynamiken der CRISPR Effektor-Komplexe sowie einzelner Cas Proteine für unterschiedliche Zielsequenz-Komplementaritäten zeigen. Außerdem präsentiere ich erste Daten, die langanhaltende Bindungszeiten zwischen Effektor-Komplex und ihren potentiellen Zielen *in vivo* beschreiben, für die bislang nur *in vitro* Daten verfügbar waren.

Zusammenfassend ist diese Doktorarbeit ein signifikanter Beitrag sowohl für den Fortschritt der derzeitigen sptPALM Bildgebungsmethoden, als auch für das bessere Verständnis des natürlichen

Verhaltens des CRISPR-Cas Systems *in vivo*.

1 | Introduction

In this introduction to the methods, I first make use of our recent review article [1], which, next to a general introduction to super-resolution methods, gives a detailed introduction into SMLM techniques. As sptPALM imaging is not described in detail in this review, I furthermore append the Section 1.2 to provide more details about this specific technique.

1.1 Introduction to Single-Molecule Localization Microscopy Techniques

From single molecules to life: microscopy at the nanoscale

Bartosz Turkowyd, David Virant, Ulrike Endesfelder

This part of the thesis is written in the manuscript style and was published in Analytical and Bioanalytical Chemistry in 2016. I contributed in this work by doing a literature research, preparing figures and tables and writing parts of the text. [1]

Anal Bioanal Chem (2016) 408:6885–6911
DOI 10.1007/s00216-016-9781-8

REVIEW

From single molecules to life: microscopy at the nanoscale

Bartosz Turkowyd[1] · **David Virant**[1] · **Ulrike Endesfelder**[1]

Received: 31 March 2016 / Revised: 30 June 2016 / Accepted: 7 July 2016 / Published online: 9 September 2016

Abstract Super-resolution microscopy is the term commonly given to fluorescence microscopy techniques with resolutions that are not limited by the diffraction of light. Since their conception a little over a decade ago, these techniques have quickly become the method of choice for many biologists studying structures and processes of single cells at the nanoscale. In this review, we present the three main approaches used to tackle the diffraction barrier of ~200 nm: stimulated-emission depletion (STED) microscopy, structured illumination microscopy (SIM), and single-molecule localization microscopy (SMLM). We first present a theoretical overview of the techniques and underlying physics, followed by a practical guide to all of the facets involved in designing a super-resolution experiment, including an approachable explanation of the photochemistry involved, labeling methods available, and sample preparation procedures. Finally, we highlight some of the most exciting recent applications of and developments in these techniques, and discuss the outlook for this field.

Keywords Super-resolution microscopy · Photophysics and photochemistry of fluorophores · Live cell imaging · Quantitative cell biology

Bartosz Turkowyd and David Virant contributed equally to this work.

✉ Ulrike Endesfelder
ulrike.endesfelder@synmikro.mpi-marburg.mpg.de

[1] Department of Systems and Synthetic Microbiology, Max Planck Institute for Terrestrial Microbiology and LOEWE Center for Synthetic Microbiology (SYNMIKRO), Karl-von-Frisch-Str. 16, 35043 Marburg, Germany

Spatial and temporal scales in the life sciences and microscopy

The timescales and spatial scales of the processes and molecules associated with life span extremely broad ranges, covering many orders of magnitude (Fig. 1). For instance, intracellular regulation (e.g., conformational changes or biochemical reactions within molecules) takes place at submillisecond timescales, nanosized molecules such as ATP (which serves the energy demands of cells) diffuse in milliseconds through cell volumes ranging from several micrometers up to millimeters, while (clustered) membrane receptors move at speeds that are about a magnitude slower. Large multicomponent machineries realize and control complex multilayered cellular functions that occur in seconds to hours. The ribosome, a large macromolecule which consists of two functional subunits of several dozen proteins on nucleic acid chain scaffolds, takes a matter of seconds to synthesize new peptide chains comprising hundreds of amino acids, which then quickly fold up into functional proteins. On the other hand, the replication of a full genome requires at least about 40 min for the 4.6 million nucleic acid base pairs of the bacterium *Escherichia coli*, and the cellular division cycle ranges from tens of minutes for *E. coli* to several hours for mammalian cells.

Observing and understanding all of these components of life requires us to be, at best, passive witnesses of undisturbed processes, but also to demand hard observational data that can allow us to quantitatively measure and trace all of the players involved—ranging from small molecules up to the interactions of whole cells in cellular communities—with the highest specificity and precision.

To achieve this, instrumentation is needed that permits a wide three-dimensional view but also allows details to be

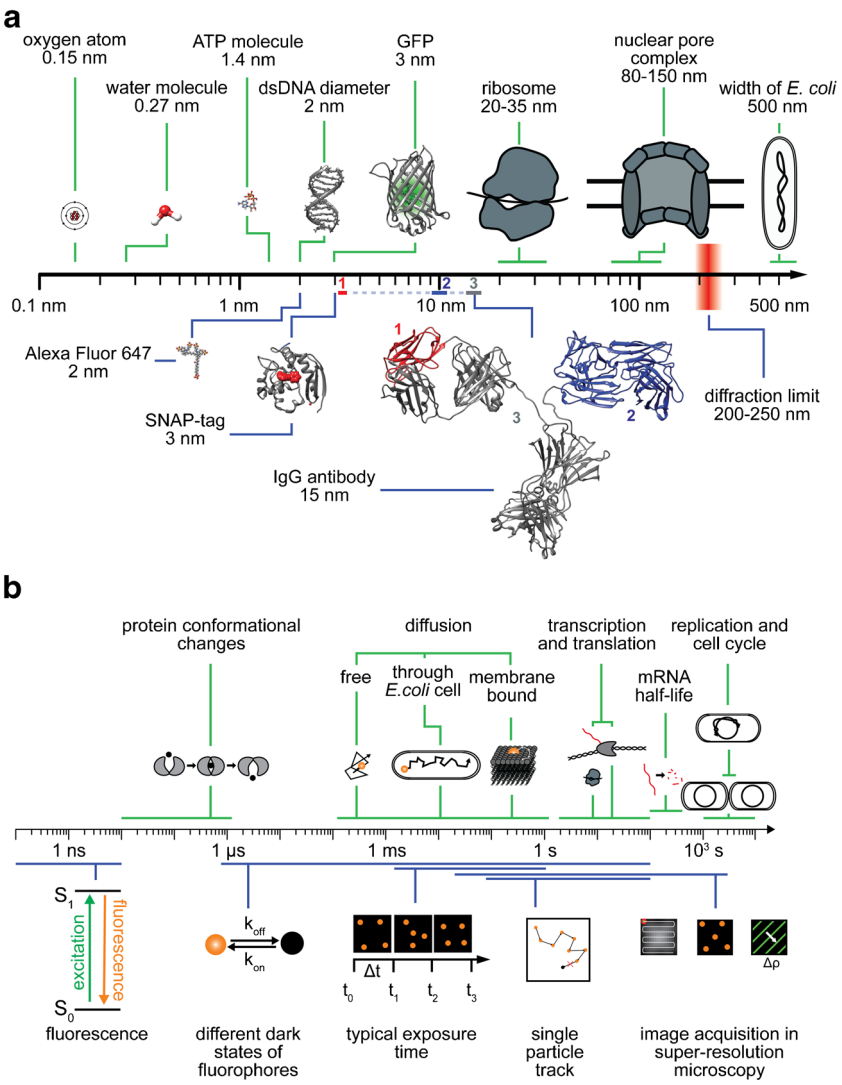

Fig. 1a–b Spatial and temporal scales in the life sciences and microscopy. **a** Selected characteristic submicrometer objects are separated on the basis of biological (*above the axis*, *green*) and technical (*below the axis*, *blue*) significance. The IgG antibody structure (15 nm) contains two other notable structures: the antigen-binding region, called the Fab fragment (10 nm, *blue*) and the single-variable domain (3 nm, *red*), from which so-called nanobodies from cameloids are derived. Structures are taken from the PDB [GFP 1KYS, IgG 1IGT, SNAP 3KZZ, DNA 4LEY] and PubChem [ATP CID 5957, Alexa Fluor 647 CID 102227060]. **b** Timescales of various important biological processes (*above the axis*, *green*) and physical events, as well as typical timescales associated with microscopy procedures (*below the axis*, *blue*)

explored in high resolution, is noninvasive but can tell different cellular components apart, and offers detection that is rapid enough to be able to probe the processes of interest.

Today, the use of modern super-resolution fluorescence microscopes allows us to zoom into the intracellular structures of live cells [1, 2]. It is not only possible to resolve specimens in greater detail than naturally possible using the discriminating power of the human eye through the application of conventional light microscopes, but we are also able to circumvent the diffraction limit of light and study structures at near-molecular scale. This significant gain in resolution (which has revealed the heterogeneous nature of the lives of single cells), the inherent specific contrast of single fluorescent labels, and the ability to live-cell image single cells and large multicellular organisms have made fluorescence super-resolution microscopy one of the most powerful tools applied in the life sciences.

Nevertheless, there are limitations: the maximal photon flux of a fluorophore—which is mainly determined by its fluorescence lifetime—yields a lower bound for the detection range when observing molecular dynamics, and its maximum photon budget (above which it is irreversibly destroyed, i.e., photobleached) marks the upper bound for studying individual molecules. Technology-wise, minimal exposure times in the millisecond range limit the maximum observation rate of a planar live image array [3], and (for example) the sizes of labeling molecules such as dyes, protein tags, and antibodies yield steric resolution limits [4, 5]. Typical sizes of labeling molecules and the range of timescales of various life processes and imaging procedures are visualized in the lower panels of Fig. 1a and b.

It is important to point out that none of the advanced super-resolution microscopy techniques are routine methods as yet. They work close to current technological limits, and thus improve with each new implementation. Behind their stunning results and attractive images hide highly complex and tailored experimental designs. It is thus advisable to define the particular biological question

to be answered as precisely as possible, and to plan biological experiments such that they suit the techniques well. Therefore, here, we will briefly review the basic principles of the three most widely used super-resolution microscopy techniques: stimulated-emission depletion (STED) microscopy [6], structured illumination microscopy (SIM) [7], and single-molecule localization microscopy (SMLM) [8–10], as depicted in Fig. 2 and summarized in Table 1. We explain, in detail, the essential characteristics of currently used reporter fluorophores, from their individual photophysics to general labeling strategies. Finally, we highlight the recent advances of the last few years, which have not only allowed the molecular compositions and structures of individual cellular components to be elucidated, but have also enabled us to place them into their native environmental context of large-scale spatial organization and to follow their dynamics. At the end of the paper, we emphasize the main challenges we currently face in order to achieve further improvements in these techniques and we introduce promising correlative schemes and sophisticated algorithmic and analytic tools which facilitate large-data and computational systems biology approaches.

Principles of super-resolution microscopy

The resolution of light microscopy is often introduced via the Rayleigh criterion. Light from point-like sources is convolved by the so-called point-spread function (PSF) of an optical system when transmitted through a diffraction-limited microscope (Fig. 2a). In 1896, Lord Rayleigh defined the maximum resolution of an optical system as the minimum distance between two point-like objects which can be separated as individual sources. He regarded two point sources of equal strength as just discernible when the main diffraction maximum of one image coincides with the first minimum of the other. For an epifluorescence microscope with a circular aperture where the light is collected with the same objective, this yields

$$d = \frac{0.61\lambda}{\mathrm{NA}},$$

where λ is the wavelength of light and NA is the numerical aperture [16].

Nevertheless, as already demonstrated by Zsigmondy using his ultramicroscope in 1902 [17], particles with dimensions below the resolution limit of visible light can be resolved. Also, confocal or multiphoton fluorescence approaches possess higher resolution than epifluorescence microscopes, as these techniques repress out-of-focus fluorescence, permitting straightforward three-dimensional imaging [18]. The resolution of near-field scanning microscopy (NSOM) is not limited by diffraction, as the diffraction limit applies only to light that has propagated a distance that is sufficiently larger than its wavelength. NSOM is therefore only limited by the aperture of the nanometer-sized excitation and detection tip placed near the sample [19].

Since the development of STED, the first far-field super-resolution fluorescence microscopy technique, many new methods that spatially or temporally confine fluorescence (which allows them to circumvent the diffraction barrier) have evolved. They can be categorized into two types of super-resolved far-field methods, with the first group concentrating on particular incident excitation light patterns and the second focusing on the modulation of the detected emission light over time. To be more specific, the first group, including techniques such as STED and SIM, make use of structured illumination schemes which spatially modulate the fluorescence of molecules such that not all of them simultaneously emit light. The second group, namely SMLM, rely on single-molecule imaging, and uses stochastic photomodulation of individual fluorophores. The number of photoswitchable fluorophores in their active fluorescent state can be controlled by irradiating the fluorophores with specific wavelengths of light. Thus, the stochastic activation of fluorescence at low rates allows the fluorescence emissions of single fluorophores to be spatially and temporally separated.

Stimulated-emission depletion microscopy

In STED microscopy [6], the sample is scanned by a subdiffraction excitation spot. This spot is realized by superimposing two lasers: an excitation laser with a focused beam waist limited by diffraction and a STED depletion laser in a donut-shaped mode (achieved by phase modulation) with a wavelength at the far end of the fluorescence spectrum of the fluorophore used (Fig. 2bi). As a consequence, all of the fluorophores in the focal spot of the excitation laser are excited, whereas those located within the area of the donut-shaped STED laser are again quickly depleted from the excited state and forced back to their ground state by stimulated emission, resulting in the release of a photon identical to the incident STED depletion photon. This process only leaves fluorophores at the subdiffraction-sized central spot in the excited state, and their spontaneous fluorescence emission is measured. By precisely scanning the entire sample and measuring the respective fluorescence intensity of each subdiffraction area (Fig. 2bi, bottom), then, without the need for any further post-processing steps (Fig. 2bii), an image is reconstructed (Fig. 2biii).

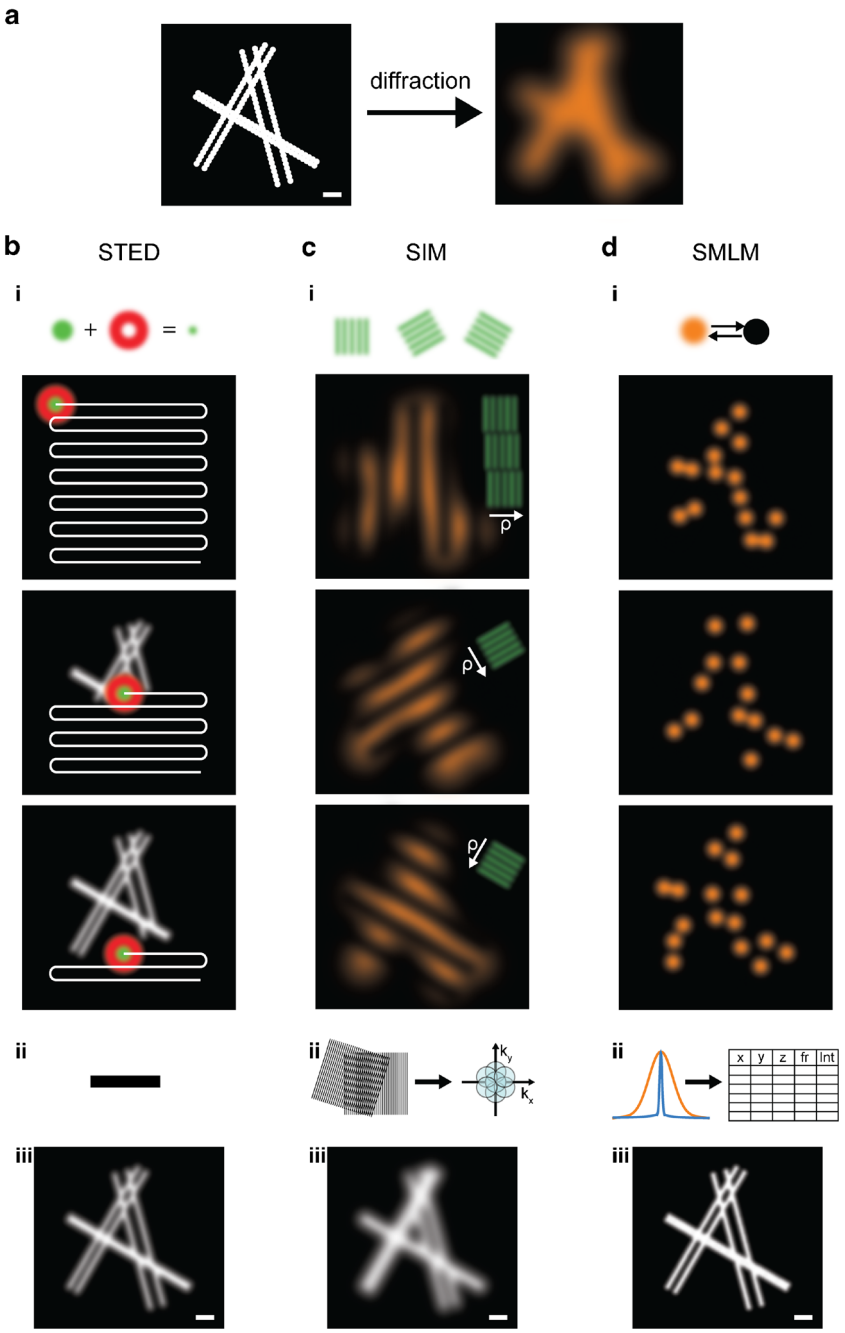

Fig. 2a–d Principles of super-resolution microscopy techniques. **a** *Left*: Scheme of six filaments decorated with fluorophores (represented by large icons for visibility) and grouped into three pairs at simulated distances of 50, 100, and 150 nm; *scale* 200 nm. *Right*: A typical image of this structure obtained by conventional fluorescence microscopy is limited by the diffraction of light. **b** *i*, *top*: For STED, the structure is scanned by a subdiffraction excitation spot obtained by combining an excitation laser (*green*) with a, by phase-modulation shaped, depletion laser (*red*). After scanning the entire structure (*i*, *bottom*), and without performing any further post-processing steps (*ii*), an image is reconstructed (*iii*). **c** In SIM, fluorophores are excited by a series of regularly spaced illumination patterns of known frequency, orientation, and phase which modulate the fluorophore emissions. This results in visible low-frequency Moiré patterns that are dependent on the structure imaged (*i*). By analyzing the images for their spatial frequencies, an enlarged frequency space is obtained (*ii*), and a subdiffraction image is reconstructed (*iii*). **d** In SMLM, the fluorescence is modulated by photoswitching between "off" and "on" states. Most of the fluorophores are forced to reside in a dark off state; only a small subset of spatially separated fluorophores in the on state is allowed to emit fluorescence at a given time. After sequentially imaging thousands of subsets of fluorophores (*i*), the nanometer-precise fluorophore positions can be extracted from the diffraction-limited individual emissions (*ii*), and an image is reconstructed (*iii*). The three super-resolved images labeled (*iii*) visualize typical resolutions obtained by the methods: on the order of 50 nm (STED), 100 nm (SIM), and 20 nm (SMLM); *scale* 200 nm

Table 1 Overview of the characteristics of various super-resolution microscopy techniques

	STED	Linear SIM	Nonlinear SIM	SMLM
Microscope type	Laser scanning	Widefield	Widefield	Widefield
xy resolution (nm)	20–70	80–100	~45	10–40
z resolution (nm)	30–100	~300	~170	10–50
Temporal resolution	ms to s	ms to s	ms to s	s to min
Laser intensities [W/cm^2]	~10^4–10^9	~ 10–10^2	~ 10^2–10^6	~ 10^3–10^4
Suitable fluorophores	Photostable fluorophores	All common fluorophores	Photostable or photoswitchable fluorophores	Photoswitchable fluorophores
Number of colors	3	3	1	4
Photobleaching	Moderate to high	Low to moderate	Moderate to high	Low to moderate (reversible switching) High (irreversible switching)

Values are taken from [10–15]

The size of this effective subdiffraction scanning beam can be varied depending on the intensity of the STED depletion beam. The resulting resolution of STED microscopy can be described by

$$d_{\mathrm{STED}} = \frac{d}{\sqrt{1 + I/I_{\mathrm{s}}}},$$

where d is the conventional resolution limit as defined by the Rayleigh criterion, I is the intensity of the STED depletion laser, and I_{s} is the effective saturation intensity, which can be defined as the intensity at which the probability of fluorescence emission is reduced by half [20].

By choosing the wavelength of the STED depletion laser to be at the far end of the fluorophore's spectrum, reabsorption from the ground state as well as further absorption processes from the excited state can be neglected. Further, the resulting stimulated photons identical to the STED depletion wavelength possess a longer wavelength than the majority of photons obtained by spontaneous fluorescence emission. They can therefore be easily spectrally filtered, and—as stimulated emission also occurs on faster timescales—filtered temporally too. As it is a confocal technique, STED microscopy naturally permits optical sectioning, but three-dimensional imaging schemes have been further improved by, for example, creating an isotropic focal scanning spot using two opposing objectives [21].

The sample is scanned in steps as small as the effective subdiffraction-sized excitation spot, but is irradiated by the much larger, diffraction-limited, foci of the excitation and STED depletion lasers. Thus, the fluorophores are subjected to multiple excitation and de-excitation steps under high STED laser intensities, which requires them to be extraordinarily photostable. STED microscopy was initially realized in a pulsed laser scheme [6]; continuous-wave illumination STED microscopy was implemented later [22]. However, rather high intensities are required in both imaging schemes, leading to increased photobleaching and phototoxicity in the sample. This negative effect can be reduced by employing sophisticated imaging modes which lower or shorten the applied laser intensities, e.g., by time gating [23], by selective, feedbacked use of the depletion beam to reduce the number of state transition cycles [24], or by replacing (a concept also termed RESOLFT: reversible saturable optical (fluorescence) transition) [25] or assisting [26] the stimulated depletion mechanism with an on–off photoswitch. STED utilizing moderate laser power schemes can be applied to the imaging of live cells as well as living tissue and living organisms (for a detailed review, see [27]).

For multicolor STED microscopy, either a pair of lasers is required for each fluorophore [28], or, for spectrally close fluorescence spectra, only one depletion laser is needed [29]. This further automatically coaligns the effective scanning spots of both colors. Very specific fluorophore pairs, chosen to be suitable for spectral demixing approaches or to demonstrate reverse photochromic behavior, can be operated by just one pair of lasers [30, 31].

Structured illumination microscopy

SIM uses regularly spaced patterns of known spatial frequency, orientation, and phase to illuminate the sample by a

structured excitation light series ([7]; detailed review [32]). This leads to modulated fluorescence emissions which form defined interference Moiré fringes of high and low frequencies, as the light emitted from a specific point in the sample is the product of the local structure of the sample (more precisely the spatial distribution of the fluorophores) and the local excitation intensity. As the corresponding fluorescence image seen through the microscope is diffraction limited and thus convolved with the PSF of the optical system, only the low-frequency Moiré patterns can be measured. These structure-specific patterns are registered for different sequential phases and orientations of the illumination pattern to sample the maximum isotropic frequency space (Fig. 2ci). By measuring the apparent Moiré fringes and knowing the properties of the chosen illumination patterns, it is possible to retrieve information at higher spatial frequencies than normally possible in a widefield microscope (Fig. 2cii): the diffraction limit can be described as a circular boundary in the transmitted frequency space with a maximal frequency of $k_{\max}$, equaling $1/d$. Thus, only the spatial frequencies with $k \ll k_{\max}$ pass through the optical system. Using structured illumination, which allows the detection of low-frequency Moiré interference patterns, spatial information about the sample from higher frequency bands is shifted into detectable lower frequency bands. All of the acquired images can be analyzed for their spatial frequencies and then be unmixed by their multiple overlapping components in frequency space. This allows the high frequencies obtained using the Moiré information to be shifted back to their original frequencies. The resulting enlarged frequency space encompasses about $2k_{\max}$, as the low-frequency Moiré patterns must remain visible above the diffraction limit. Using an inverse Fourier transform back into image space, a super-resolved SIM image showing a linear twofold increase in resolution can then be reconstructed (Fig. 2ciii).

Ignoring for a brief moment the rather complex post-processing of the raw data acquired by sophisticated SIM software (recently published open-source options are [33, 34]), SIM is the most straightforward approach in the field of super-resolution microscopy: the technique is based on standard widefield fluorescence microscopes, only requires (in the simplest version of SIM) a movable grating placed in a Fourier plane of the illumination path, and works for all common (albeit best for bright) fluorophores. SIM can be used to image live cells [11, 35] and has been extended to three-dimensional SIM [12], is capable of imaging live organisms [36], and allows for multicolor imaging [37]. Nevertheless, common artifacts (arising from imperfect imaging or algorithms) should be carefully considered, avoided, or corrected for: stripes in a reconstituted SIM image emerge from photobleaching, sample drift, or setup vibrations, a low fluorescence modulation contrast results in noise in the high-frequency range, and spherical aberration as well as refractive index mismatching creates halos or the doubling of features [38].

A higher resolution than that obtained by linear SIM is achieved by nonlinear SIM, which is realized by either saturating the fluorescence through the application of strong illumination intensities [39] or by using photoswitchable fluorophores [13, 40] (similar to RESOLFT [25]) to create illumination patterns that include higher harmonic frequencies. However, the increased resolution of this technique comes at the expense of a limited choice of fluorophores, which need to be either highly photostable (in order to withstand the strong illumination intensities) or photoswitchable. The resolution obtained using SIM approaches can be determined via

$$d_{SIM} \approx \frac{d}{2+h},$$

where d is the conventional resolution limit and h is the number of higher harmonics achieved when applying nonlinear SIM schemes [13, 39, 40]. For linear SIM, h equals zero, so the resolution enhancement is about twofold.

Single-molecule localization microscopy

Single-molecule localization-based techniques such as photoactivated localization microscopy (PALM) ([8], (*direct*) stochastic optical reconstruction microscopy ((*d*)STORM) [9, 10], ground-state depletion followed by individual molecule return (GSDIM) [41], and many other related techniques [42] are commonly grouped together under the term "single-molecule localization microscopy" (SMLM). They all require tight control over the photoswitching of individual fluorophores, as discussed in detail in this review, and they rely on the use of post-processing algorithms to generate the super-resolved data (see the review by Small and Stahlheber [43] and comparative studies of localization algorithms [44] and single-particle tracking algorithms [45]; most of the relevant algorithms are openly available).

In SMLM, the main principle is stochastic photoswitching and the detection of single spatially separated fluorophores. To achieve this, all fluorophores are modulated by photoswitching them between "off" and "on" states. Most of the fluorophores are forced to reside in a long-lasting dark off-state; only a small subset of fluorophores in the on state are allowed to emit fluorescence at a given time. By sequentially imaging typically several thousand subsets of spatially distinguishable fluorophores, all of the emitters are detected over time (Fig. 2di). The photons emitted from the fluorophores are distributed in diffraction-limited spots and registered in a stack of time-resolved images until all of the fluorophores have been read out. The spots can be identified by image-processing algorithms, allowing the positions of the

fluorophores and other properties (fluorescence intensity, duration of fluorescence, precision of the positioning fit, etc.) to be precisely determined and then stored in a large table (Fig. 2dii). Using the fluorophore centroids, a super-resolved image is reconstructed (Fig. 2diii).

The resolution limit of SMLM is mainly determined by the precision with which individual fluorophores are localized, which can be simplified to

$$d_{\mathrm{SMLM}} \approx \frac{d}{\sqrt{\mathrm{N}}},$$

where d is the conventional resolution limit and N is the number of photons detected in a single fluorescence spot [46].

SMLM approaches are more sensitive to background signals than both of the previously described methods, as SMLM determines the positions of individual molecules to a high precision based on their individual fluorescence levels. To assign as many photons as possible to a single fluorophore, it is highly desirable to achieve the best possible signal-to-noise ratio. For thin (mainly two-dimensional) samples, effective background noise reduction can be achieved using total internal reflection fluorescence microscopy (TIRF), where the incident laser light is totally internally reflected at the glass–water boundary between the coverslip and sample [47]. In this illumination scheme, only the fluorophores in a very thin layer within the exponentially decaying evanescent field above the coverslip can fluoresce. Thus, a large fraction of the usual background signal caused by autofluorescence or by the scattering of the laser light and originating from the whole sample volume is suppressed. Another approach is to illuminate the sample in a highly inclined and laminated optical sheet (HILO) [48]. In this mode, the excitation laser light leaves the objective at a very narrow angle, which results in an inclined beam passing through the sample. This illumination in the form of an optical light sheet is then almost perpendicular to the detection path of the microscope.

To allow for three-dimensional SMLM imaging, several optical methods have been utilized to encode the third dimension: astigmatic PSF shaping by a cylindrical lens, biplane alignment, a dual-objective scheme allowing for the interference of the signal, and several further phase modulations have been developed that (for example) create a double-helically arranged PSF or a self-bending PSF which spans a large field of view at isotropic resolution [1]. These three-dimensional SMLM read-out schemes can be combined with spatially confined activation approaches based on temporal focusing [49], selective plane illumination microscopy [50], or lattice light sheet illumination [51].

SMLM allows for multicolor imaging if the photoswitching mechanisms of the fluorophores used fit together well; i.e., when they tolerate the same imaging environment such as the same specialized switching buffers [52–54] or a mounting medium combined with high laser intensities [55], by employing complementary photoactivation schemes [56, 57], or by using dye activator–reporter pairs [58]. Most multicolor approaches are assisted by sophisticated read-out schemes [59–63]. We discuss how to choose appropriate fluorophores to use in a particular study and the parameters that should be taken into account in the next section of this review, where we introduce the basic photophysics and explain how to switch or stabilize fluorophores.

Structural live-cell SMLM imaging of only slowly changing structures can be performed as the imaging speed is fast compared to the phenomenon being imaged. For these structures, it is possible to capture a sufficient number of subsets of fluorophores to fill a subdiffraction sampling space before the structure has changed significantly. Nevertheless, a gain in temporal resolution will always result in a loss of structural spatial resolution caused by lower sampling, and vice versa [55, 64–66]. Uniquely, SMLM can be combined with single-particle tracking (SPT); unlike diffraction-limited SPT methods, where only a strictly limited number of fluorophores can be followed per cell to keep them separable, sptPALM [67] is readily capable of measuring a large batch of statistics on single-molecule tracks for the same type of molecule inside a single cell by sequential photoactivation. It is thus possible to obtain spatially and temporally highly resolved diffusion maps that combine a multitude of tracks and accordingly unravel possible dynamic heterogeneities and subpopulations. sptPALM has been applied to a wide range of biological systems (some examples are given in [68–70]), and can be combined with structural SMLM imaging [71]. It is nevertheless important to note that the minimum time needed to precisely localize a single fluorophore is influenced by imaging parameters such as the camera sensitivity, the minimum applicable acquisition times (in the range of a few milliseconds), as well as the contrast of the fluorophore (determined by its quantum yield in the specific sample, the laser intensities, and the background noise). This means that sptPALM is only well suited to studying slow diffusion processes, where the fluorophores move slowly compared to the image acquisition time; it is not applicable to processes with faster dynamics such as that visualized in Fig. 1b.

Designing the optimal experiment

Choosing a suitable fluorophore

Normally, fluorophores reside in their most relaxed molecular state, the electronic ground state (S_0). When a fluorophore absorbs a photon, it is excited within femtoseconds to a higher energy state (S_1, S_2, …, S_n). Depending on the exact energy of

the absorbed photon, the fluorophore can be excited to various energy levels that correspond to its electronic, vibrational, and rotational molecular configurations. As depicted in Fig. 3a (in which, for simplicity, only the S_0, S_1, and T_1 electronic states and the vibrational states for S_1 are shown), the fluorophore then relaxes within picoseconds to the lowest level of the excited electronic state S_1, transferring its vibrational energy to its surroundings.

The time a fluorophore spends in the lowest level of the excited state, often called the fluorescence lifetime, is normally in the nanosecond range, though it depends on the specific molecule and its environment. When returning to the electronic ground state, nonfluorescing molecules release their energy through nonradiative processes such as internal conversion. Fluorophores, on the other hand, exhibit a high probability of a radiative transition; they release energy through the emission of a single fluorescence photon. As a portion of the energy is also lost before this transition through vibrational state relaxation, the fluorescence photon actually has a longer wavelength than the wavelength of the photon originally absorbed. This phenomenon is known as the Stokes shift.

Besides relaxing directly to the ground state through either photon emission or nonradiative internal conversion, an excited fluorophore can release its excess energy by undergoing several other intramolecular and intermolecular processes. Such events decrease the photon yield and are collectively termed quenching. Through the intramolecular transition process known as intersystem crossing, fluorophores can reach an intermediate energy state called the triplet state (T_1). This process involves flipping the spin of the excited electron, and has a miniscule probability (i.e., it is quantum-mechanically forbidden) of occurring during each excitation–relaxation cycle. The triplet state has a much longer lifetime, typically several microseconds, during which the excited molecule remains prone to electron transfer reactions. The result of such a reaction can be a nonfluorescent radical state ($F^{\bullet-}$) in which the fluorophore can remain for several seconds or even minutes. Occasionally it can result in irreversible destruction of the fluorophore through photobleaching processes, leading to a permanent loss of fluorescence. Other dark, nonfluorescent states can be caused by conformational changes in the chromophore, the formation of complexes with other molecules, or a collision with a molecule that is capable of receiving the fluorophore's surplus energy (e.g., oxygen, halogens, and amines). Collisional quenching requires direct proximity of the quencher molecule to the chromophore, and its rate is drastically decreased in fluorescent proteins where the chromophore is protected by its beta-sheet barrel (Fig. 3bi). Finally, the energy of an excited fluorophore can also be transferred to another molecule by photoinduced electron transfer (PET) or Förster resonance energy transfer (FRET), both of which are often exploited in advanced imaging schemes that measure interaction dynamics within or between proteins of interest [82].

The most common types of fluorophores are fluorescent proteins such as GFP (Fig. 3bi) and organic dyes such as rhodamines, carbocyanines, and oxazines (Fig. 3bii). At the heart of every fluorophore is the chromophore, a conjugated π-electron system that gives a molecule its light-absorbing properties. A chromophore can consist of aromatic rings as well as C=C, C=O, or N=N bonds. Its spectral properties are determined by the length of the conjugated electronic system, the number of electrons, and different substituents [83]. Usually, elongation of the conjugated system will shift the absorption maximum and thus also the emission maximum to longer wavelengths. This can easily be seen in cyanines, a class of fluorescent dyes with different polymethine chain lengths. Stretching the chain from Cy3 to Cy7 shifts the emission spectrum from green to dark red (Fig. 3bii). Every fluorophore thus possesses a unique excitation and emission spectrum. These spectra need to be compatible with the available microscopic system (i.e., in terms of illumination wavelengths, spectral filter combinations, or the sensitivity of the given detector). The excitation and emission wavelengths should be separated by a sufficiently large Stokes shift, and, in multicolor experiments, the chosen set of fluorophores should exhibit sharp and defined spectra with ideally no overlap, thus minimizing crosstalk between the different colors. Alternatively, overlapping spectra can be separated by spectral demixing approaches, which also nicely avoid chromatic aberrations and can allow the use of a single excitation source [60–63]. Sample specifications must also be taken into account; live cells are usually more sensitive to irradiation with shorter-wavelength light; imaging for extended periods of time with light in the ultraviolet (UV) range can lead to a range of defects in cells, from DNA damage to death [84]. Certain biological samples exhibit pronounced autofluorescence in some spectral ranges, usually in shorter wavelengths. The majority of this background fluorescence is caused by aromatic amino acids (mainly tryptophan), the phosphate chain of DNA, intracellular nicotinamide adenine dinucleotide (NADH), and coenzymes [85]. Longer wavelengths of light can penetrate deeper into a tissue, making red and near-infrared fluorophores the most suitable for imaging thicker samples [18].

The chosen fluorophore should be as bright as possible to ensure that sufficient signal is detected to allow it to be distinguished from the background. This is especially crucial for single-molecule imaging when the fluorescence of individual fluorophores is captured. The fluorophore's brightness is determined by its dipole orientation in relation to the excitation light, its extinction coefficient (which quantifies how well a

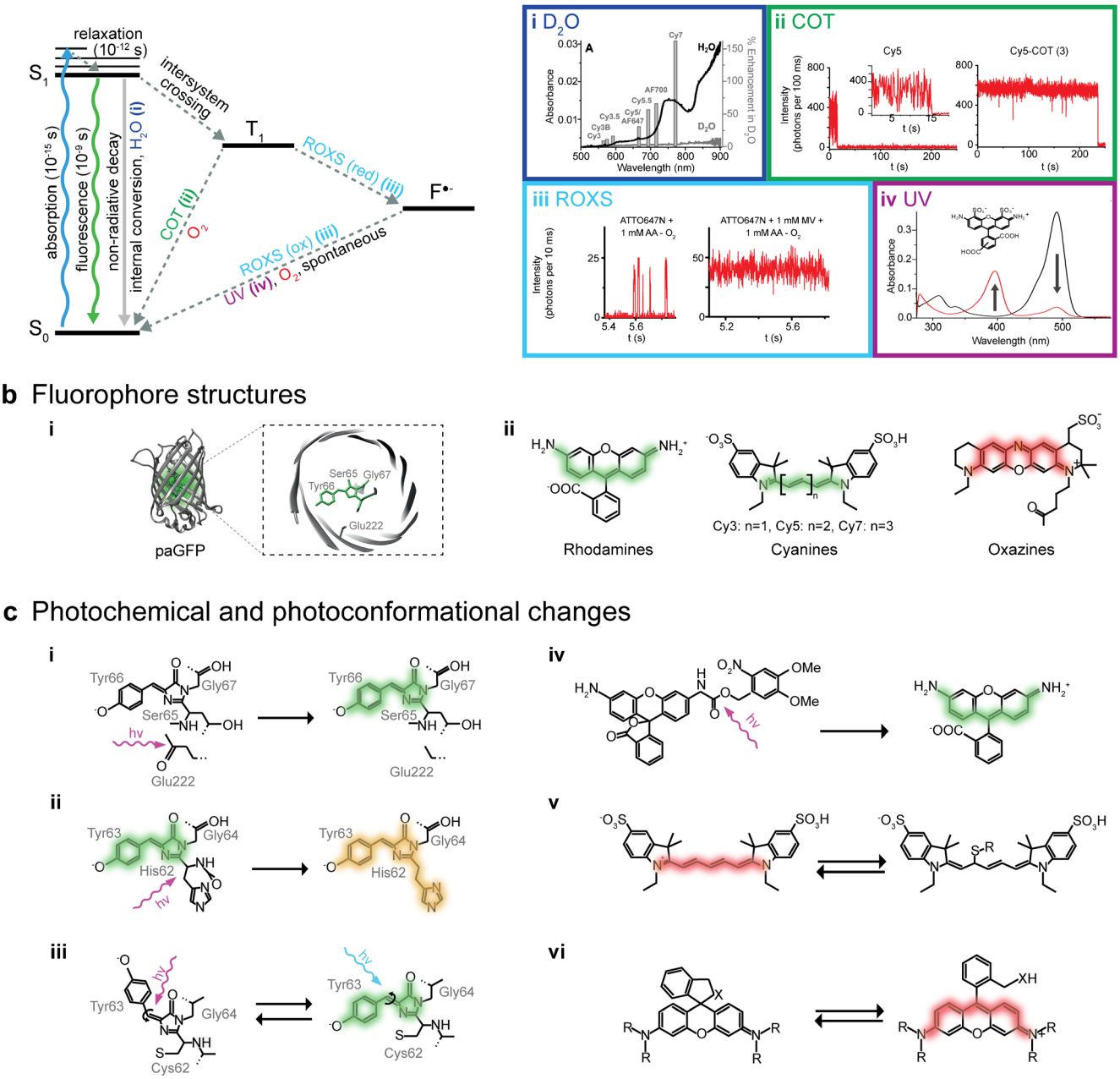

Fig. 3a–b Photophysics and photochemistry of fluorophores. **a** *Left*: Jabłoński energy diagram representing energy states and transitions of a fluorophore. S_0 ground singlet state, S_1 excited singlet state, T_1 triplet state, $F^{\bullet-}$ radical state. Different compounds can affect brightness and photostability or shift the fluorophore into a radical state. (*i*) absorption spectra of H_2O and D_2O, and correlated enhancements of the fluorescence emissions of different fluorophores in D_2O versus H_2O for the visible range of light. Adapted from [72] with permission. (*ii*) Cyclooctatetraene (COT) quenches the triplet state by quickly transferring fluorophores back into the ground state and thus stabilizes the fluorescence. Adapted with permission from [73]. (*iii*) A reducing and oxidizing system (ROXS) accelerates the transition of a fluorophore from its triplet state back to the electronic ground state by performing fast sequential reducing and oxidizing steps. Adapted with permission from [74]. (*iv*) The radical states of some dyes (e.g., the Alexa Fluor 488 fluorophore, as shown in *black* here; *red* indicates the radical) possess an absorption peak in the UV range. By exciting the radicals with UV light to higher intermediate states, they can be quickly brought back down to their electronic ground state. Adapted with permission from [75]. **b** Different fluorophore structures: (*i*) Barrel structure of the photoactivatable green fluorescent protein (paGFP) and a close-up of its chromophore. (*ii*) Overview of organic dye classes. **c** Different photochemical and conformational changes that affect fluorescence: (*i*) photoactivation of paGFP [76], (*ii*) green-to-red photoconversion of mEos2 [77], (*iii*) reversible *cis*/*trans*-photoswitching of Dronpa [78], (*iv*) cleavage of a photocage from a rhodamine [79], (*v*) reversible fluorescence quenching of Cy5 by covalent binding of a thiol [80], and (*vi*) reversible cyclization of rhodamine HMSiR [81]

fluorophore absorbs a certain wavelength), and its quantum yield (the ratio of absorbed to emitted photons). Ideally, the excited fluorophore would emit a single photon in every excitation–emission cycle, thus exhibiting a quantum yield of 1. However, due to the alternative process of excited-state relaxation described earlier, this is not the case in practice. A fluorophore featuring a relatively low quantum yield can nevertheless produce a sufficient fluorescent signal, provided that its extinction coefficient is high enough and its rate of entry into the excited state is maximized by applying high excitation light intensities, leading to more rapid cycling through the excitation–emission cycle (Fig. 3a).

A constant flux of emitted photons (i.e., the fluorophore's photostability) is another important factor. Fluctuations in fluorescence can be attributed to reversible or irreversible losses of fluorescence, and depend on the chemical properties of the fluorophore, its environment, and the light intensities that it is exposed to. Oxygen and reactive oxygen species play a large role in irreversible bleaching, which is caused by a permanent change in the molecular structure of the fluorophore [86]. Absorption of a second photon while already in the excited state is believed to be another major cause of photobleaching. Low irreversible bleaching rates allow for longer measurements or at higher excitation light intensities. Reversible losses of fluorescence are caused by transitions to several intermediate nonfluorescent electronic or conformational states, as sketched in Fig. 3a. Minimizing the time a fluorophore spends in these states improves the fluorescence signal stability and increases the time that a fluorophore spends performing its excitation–emission cycle, yielding a more constant photon flux.

The solubility and cell permeability of fluorophores must also be considered. Relatively few fluorophores can be transported through a live cell membrane (these are highlighted in Table 2) due to either size or charge constraints. Fluorescent proteins are highly live-cell compatible but can be a steric hindrance in some cases, and can impact cell viability when fused to certain proteins. They have also been shown to form artificial aggregates, depending on the abundance and spatial organization of the target molecule [122].

Importantly, each super-resolution technique has special demands. The most common fluorophores employed, their properties, and (in the case of SMLM) the most popular multi-color combinations are given in Table 2. In STED, the molecules are constantly forced from the excited state into the electronic ground state via stimulated emission. Fluorophores with high extinction coefficients, high quantum yields, and high stimulated emission cross-sections are favorable, as they allow for the best possible contrast in the detection of the fluorescing fluorophores left in the center of the excitation pattern. The rate of stimulated depletion of the excited state scales with the depletion energy applied, so fluorophores chosen for STED have to be exceptionally photostable. Further, the depletion wavelength should be carefully chosen to ensure that it does not re-excite any of the fluorophores that are depleted to the ground state. For SIM, the most crucial parameters are the photostability and overall brightness of the fluorophore, as the technique works by measuring the fluorescence response of a defined patterned excitation. This modulation of fluorescence should be clearly detectable based on a strong and inherently stable fluorescence signal. Since illumination-independent fluctuations in fluorescence result in artifacts, the use of an effective antifading agent is common practice. Almost all modern fluorophores can be used for SIM (which is why we do not provide a selection of SIM fluorophores in Table 2). Finally, for SMLM techniques, rigid control of photoswitching is crucial. The nonfluorescing dark times of the fluorophores must be long enough to guarantee the separation of single-molecule signals in the sample at any time during the experiment. Even when applying algorithms that can handle high numbers of fluorescent molecules at a time, the techniques are easily impaired when the density of molecules is too high [123].

The dye Alexa Fluor 647 is the fluorophore of choice in a great majority of fixed cell SMLM studies, due to its robust photoswitching and good photon yields. Since it is not membrane permeable, ATTO 655, tetramethylrhodamine, SiR, and Oregon Green are utilized in most live cell studies. When multicolor imaging is desired, Alexa Fluor 568 and 532 are often used with Alexa Fluor 647. Fluorescent proteins are more suitable for quantitative approaches or noninvasive live cell studies. A collection of popular fluorophores as well as multicolor schemes is provided in Table 2. In this context, different photoswitching strategies (as evaluated in detail below) require individual optimizations such as customized specific photoactivation and photoconversion efficiencies for convertible fluorophores that allow for sequential activation [57] and tailored imaging buffers for selected organic dyes.

Even more complex imaging experiments involve additional considerations, such as the need to carefully choose the spectral overlap between donor emission and acceptor excitation for optimal FRET, the selection of appropriate strategies for optimal multiphoton absorbance or when utilizing fluorophores as biosensors [82].

Labeling strategies

Choosing a strategy to label the biomolecule of interest is a crucial part of the experiment. Luckily, strategies suitable for many biological applications are commercially available and, for the best results, experiments should be planned with the labeling strategy in mind from the very beginning. It is important to emphasize that it is always the label attached to the molecule of interest that is visualized, not the molecule itself—the signal we see on the microscope is a label's length away. Using large labels in combination with high resolutions

Table 2 List of recommended and promising new fluorophores for super-resolution microscopy

STED

	Name	Appl.	Exc (nm)	Em (nm)	STED (nm)	Structure	ε ($M^{-1} * cm^{-1}$)	φ
Fluorescent proteins	Citrine	[23]	516	529	595	m	77 000	0.76
	eYFP	[30]	514	527	598	m	84 000	0.61
	Dronpa	[31]	503	517	488 (405)	m	95 000	0.85
	eGFP	[30]	488	510	575	m	55 000	0.6
Organic dyes	SiR (§)	[87]	652	674	775	r	100 000	0.32
	ATTO 647N	[22]	646	664	750	r	150 000	0.65
	AberriorStar635P	[29]	635	651	750-780		125 000	0.92
	ATTO 594	[29]	603	626	775	r	120 000	0.85
	Alexa Fluor 594	[88]	590	617	690	r	92 000	0.66
	ATTO 565	[22]	564	590	640-660	r	120 000	0.9
	Aberrior Star 488	[89]	503	524	585-605		64 500	0.89
	Alexa Fluor 488 (§)	[23]	495	519	592	r	83 000	0.92
	Aberrior Star 440SXP	[89]	432	511	590-620		33 000	0.57

SMLM

	Name	Appl.	Exc (nm)	Em (nm)	Act/con (nm)	UV abs radical state*	Structure	ε ($M^{-1} * cm^{-1}$)	φ	Dual color combinations	Triple color combinations
Fluorescent proteins	mEos2 (G)	[77]	506	519			m	56 000	0.84	AF 647 [90-92], ATTO 655 [53], Caged SiRhQ [57], Dronpa [56], psCFP2 [56]	
	mEos2 (R)		573	584	405			46 000	0.66		
	PAmCherry1	[59]	564	595	405		m	18 000	0.46	paGFP [59]	eYFP + NileRed [93], PAmKate + Dendra2 [60]
	Dendra2 (G)	[94]	490	507			m	45 000	0.5		PAmKate + PAmCherry1 [60]
	Dendra2 (R)		553	573	405, 488			35 000	0.55		
	paGFP	[95]	504	517	405		m	17 400	0.79	PAmCherry [59]	PAmKate + PAmCherry1 [60], PAtagRFP + ATTO 655 [95]
Organic dyes	Alexa Fluor 750	[96]	749	775		++	c	290 000	0.12	AF 647 [97]	
	CF 680	[63]	681	698		-	c	210 000		AF 647 (#) [62, 98, 99]	CF 660C + DyLight 650 + Dy 634 (#) [62], CF 647 + CF 568 (#) [63]
	ATTO 655 (§)	[100]	663	680		+	o	125 000	0.3	ATTO 520 [52], mEos2 [53]	PAtagRFP + paGFP [95]
	SiR (§)	[101]	652	674		-	r	100 000	0.08 - 0.32	mEos2 [57]	TMR + paGFP [102]
	Alexa Fluor 647	[10]	650	665		++	c	270 000	0.33	ATTO 520 [103], AF 532 [104, 105], ATTO 532 [54], AF 546 [54], AF 568 [54], TMR [106], mEos2 [90-92], AF 488 [91], psCFP2 [56], mMaple [99], ATTO 488 [107], CF 680 (#) [62,98, 99], AF 700 (#) [61], AF 750 (#) [97], Dy678 (#) [108], Dronpa [109]	AF 568 + ATTO 488 [107]
	CF 647	[110]	650	665			c	270 000			CF 680 (#) + CF 568 [63]
	Cy5	[10]	646	670		++	c	250 000	0.28		
	Alexa Fluor 568	[75]	578	603		+	r	91 300	0.69	AF 647 [54]	AF 647 + ATTO 488 [107]
	CF 568	[63]	562	583		-		88 000			CF 680 + CF 647 [63]
	TMR (§)	[106]	557	576		-	r			AF 647 [106], Citrine [55]	SiR + paGFP [102]
	Alexa Fluor 532	[75]	532	554		+	r	81 000	0.61	AF 647 [104, 105]	
	ATTO 520	[111]	517	538		+	o	110 000	0.9	AF 647 [103], ATTO 655 [52]	
	Alexa Fluor 488 (§)	[111]	490	519		+	r	73 000	0.92	AF 647 [91]	AF 647 + AF 568 [107], Cy3 + ATTO 532 [55], Rhodamine 3C + AF 514 [55]
	Cy5/AF 647 readout dye pairs	[9]		670						Reporter: AF 750 [112] Activator: Cy3 + AF 405 [112]	Reporters: Cy7 + Cy5.5 [58] Activators: Cy3 + Cy2 + AF 405 [58]

New promising fluorophores

	Name	Ref.	Exc (nm)	Em (nm)	Act/con (nm)	Structure	ε ($M^{-1} * cm^{-1}$)	φ	Comments
	mEos3.1 (G)	[113]	505	513		m	8 840	0.83	Lower tendency for oligomerization than mEos2.
	mEos3.1 (R)		570	580	405		33 500	0.62	
	mEos3.2 (G)	[113]	507	516		m	63 400	0.84	Lower tendency for oligomerization than mEos2.
	mEos3.2 (R)		572	580	405		32 200	0.55	
	mEos4 (G)	[114]	505	516		m	~ 80 000	0.85	Fluorescence comparable to precursor, but lower tendency for oligomerization.
	mEos4 (R)		570	580	405		~ 58 000	0.71	
	mMaple3 (G)	[115]	489	505		m			Improved version of mMaple.
	mMaple3 (R)		566	583	405				
	NijiFP (G)	[116]	469	507		m	41 100	0.64	Reversibly photoswitchable in both colors.
	NijiFP (R)		526	569	405		42 000	0.65	
	Skylan-S	[117]	499	513	405	m	152 400	0.64	High brightness and photostability.
	HMSiR (§)	[81]	650	670		r	100 000	0.39	Cell-permeable, laser intensity-independent blinking.

Numbers are taken from the manufacturers and from [59, 77, 81, 94, 101, 113–120]

Appl Example of the use of the fluorophore for super-resolution microscopy, *Exc* excitation peak, *Em* emission peak, *Act/con* activation or conversion wavelength, *ε* molar extinction, *φ* quantum yield, *m* monomeric, *c* cyanine, *o* oxazine, *r* rhodamine, (§) cell-permeable dyes

* [75, 121]; (#) spectral demixing

Table 3 Summary of labeling strategies commonly used in super-resolution microscopy

	Label	Appl.	Size	Description	Possible uses	Considerations
Affinity binding	**Antibody IgG or Fab fragment**	[125]	Up to 20 nm	IgG: antigen-specific immunoglobulin G antibodies consisting of two identical heavy chains and two identical light chains arranged in a Y-shape. Fab: antigen-specific monovalent fragments from IgG and IgM, consisting of the variable regions of both heavy and light chains linked by a disulfide bond.	Classic immunofluorescence by primary and secondary antibody combination.	Requires no genetic modification of the target. Modular, as secondary antibodies are available for a wide range of fluorophores. Large tags which limit the image resolution. Not cell-permeable, thus limiting live-cell staining as specialized delivery method is needed. Prone to background from nonspecific labeling.
	Nanobody	[4, 126]	~ 3 nm	Antigen-specific single variable domain (VHH) of single-chain antibody with nanomolar affinity.	Live-cell stain by recombinant expression of antigen-specific nanobody and fluorescent protein in living cells. Classic immunofluorescence stain without the need for a secondary antibody.	Anti-GFP nanobody is a popular stain. Live-cell stain results in nonspecific background due to lack of washing. Prone to background in SMLM.
Click chemistry	**Unnatural amino acids**	[127]	< 1 nm	Not naturally occurring and chemically reactive cell component analogues, mostly with alkyne or azide groups for Huisgen cycloaddition.	Nonspecific labeling of newly synthesized proteins, membranes, nucleic acids. Pulse labeling for a short time period. Site-specific labeling of proteins by codon reassigment methods.	Require no genetic modification of the target for nonspecific incorporation. Modular, as a large selection of fluorophores with reactive groups are available. Incorporation of analogues may impact cell physiology. Live-cell staining only possible for cell-permeable fluorophores or a specialized delivery method.
	Unnatural lipids	[128]				
	Unnatural nucleotides	[129]				
FISH	**Fluorescent oligonucleotides**	[130]	< 1 nm	Fluorescently labeled oligonucleotides	Sequence-specific 16S rRNA stain. Specific gene/genetic region DNA stain. RNA stain.	Highly modular: various oligonucleotides can be designed and coupled to a large selection of fluorophores. Limited compatibility with live-cell studies due to harsh hybridization conditions.
Target specific drugs	**MitoTracker**	[35]	< 1 nm	Various small molecules that bind to specific targets.	Staining of fixed cells. Live-cell staining for cell-permeable drugs.	Large selection of drugs coupled to various fluorophores. Live-cell staining only possible for cell-permeable fluorophores or specialized delivery method.
	LysoTracker	[131]				
	Phalloidin	[87]				
	SiR-Tubulin	[132]				
	SiR-Actin	[132]				
	SiR-DNA	[133]				
	DAPI	[37]				
	mCling	[134]				
	LifeAct	[13]				
Genetic fusions	**SNAP**	[135]	~ 3 nm	Genetic fusion of ligand binding enzyme to protein of interest.	Stable cell line under endogenous promoter. Transient plasmid with known/inducible expression. Staining with ligand coupled to fluorophore of choice.	Large selection of ligands coupled to various fluorophores. Require an additional staining step which is highly specific and covalent. Genetic fusion may interfere with protein localization and function. Live-cell staining only possible for cell-permeable fluorophores or specialized delivery methods.
	CLIP	[136]				
	HALO	[137]				
	eDHFR	[138]				
	Fluorescent proteins	[118]	~ 3 nm	Genetic fusion of fluorophore to protein of interest.	Stable cell line under endogenous promoter. Transient plasmid with known/inducible expression.	Live-cell imaging. No need for staining step adding external fluorophores during the sample preparation. Highly specific tag. Genetic fusion may interfere with protein localization and function. Factors like maturation time or misfolding must be taken into account. Some fluorescent proteins tend to artificially aggregate for concentrations above a certain threshold.

can thus lead to artificial inflation of the structure [4, 5]. The size and dipole orientation of the fluorophore and the achievable labeling density directly impact the resolution attained. High density—which requires at least an average nearest-neighbor label distance of less than twice the sampling rate according to the Shannon–Nyquist criterion—is necessary

[124], or important sample information can be missed. Here, we evaluate the common strategies used (see also Table 3).

Affinity-based labeling is probably the approach most widely used across all fluorescence microscopy applications [104, 105, 125, 139]. Antibodies can target virtually any cellular component as an antigen, making the technique extremely flexible. Using combinations of primary and secondary antibodies also makes the approach very modular. Nevertheless, the technique suffers from several drawbacks. First, background due to nonspecific staining is quite common [140], and antibodies may detach from their targets when irradiated with high laser intensities [141]. Second, a typical primary and secondary antibody combination is ~20 nm in size, which is sufficient to cause imaging artifacts at resolutions realized in super-resolution microscopy. Nanobodies [4], ~3 nm single-variable domains of single-chain antibodies isolated from cameloids, virtually eliminate this size problem. They can also be fused to fluorescent proteins and recombinantly expressed in live cells [126]. Aptamers—small RNA structures that function much like antibodies and are suitable for live-cell staining [142]—are worth mentioning, though their use is currently limited by poor availability. Much promise is shown by the GFP mimic family of aptamers, which form a GFP-like chromophore when bound to a nonfluorescent substrate [143].

Click chemistry is the term used to describe a set of reactions that occur at high yields in aqueous environments under mild conditions. It thus allows for effective labeling of biomolecules based on the incorporation of unnatural analogues of amino acids [127], nucleotides [129], or lipids [128] carrying a reactive chemical group such as an alkyne, azide, or cyclooctene into cellular structures. Fluorophores carrying the complementary group can then be covalently bound via (for example) cycloaddition [129]. Live-cell imaging is possible with some modifications [144]. This method is suitable for imaging DNA, RNA, proteins, and membranes, and produces very low background fluorescence but usually does not target specific biomolecules. Genetically programmable site-specific unnatural amino acid incorporation can be realized by codon reassignment [145, 146].

Fluorescence in situ hybridization (FISH) [130] allows nucleic acids to be labeled by complementary oligonucleotide probes coupled to fluorophores. The technique is often employed with 16S rRNA complementary probes to study microbe communities [147]. In super-resolution applications, it is a powerful tool for studying chromatin structure and organization, gene location [148, 149], RNA localization and quantification [148], telomere structure [150], etc. As the hybridization protocols involve harsh chemical and temperature treatments, this technique has limited live-cell compatibility.

Engineered ligand-binding enzymes which are genetically fused to the protein of interest are the basis of protein tags such as SNAP [135], CLIP [136], HALO [137], and eDHFR [138]. Such an enzyme label can then be stained by covalently binding its fluorophore-bound specific ligand (benzylguanine, benzylcytosine, chloroalkanes, and trimethoprim, respectively). Such ligands can be fused to virtually any fluorophore, which makes these tags very popular in multicolor applications [66, 95, 106].

Specific labeling options are available for several targets. Fluorescently labeled phalloidin is a toxin commonly used as a filamentous actin stain [87]. SiR-actin, SiR-tubulin [132], and LifeAct [13] are live-cell cytoskeleton stains. Some fluorescently labeled lipid analogues [151] and the recently developed mCling peptide [134] have been used as direct membrane stains. Other target-specific drugs include organelle specific probes such as the mitochondrion stain MitoTracker [35], the lysosome stain LysoTracker, or the ER stain ER-Tracker [131].

All these methods require the introduction of an extrinsic fluorophore into the cell. In fixed cells, this is usually not an issue, and this process can be greatly facilitated by introducing a permeabilization step in which the cell membrane or wall is perforated. Live-cell applications necessitate the use of membrane-permeable fluorophores such as the rhodamine dyes SiR [101], TMR-STAR [106], and Oregon Green [66] and, to a lesser degree, some oxazine dyes such as ATTO 655 [95]. Membrane permeability can be improved by performing certain modifications such as fusion to a permeable peptide [152]. Many alternative strategies for fluorophore delivery, such as electroporation, bead loading, membrane transfer, and micro- or nanoinjection techniques have been developed over the years [153–157].

The discovery and subsequent cloning of green fluorescent protein (GFP) [158] introduced the possibility of small, endogenous, and inherently fluorescent labels. Fluorescent protein fusions, which require no further staining, have become a widespread labeling strategy and are available in a variety of colors [118]. They are highly suited to live-cell studies as long as the cells are carefully checked for physiology after the genetic modification. Unfortunately, they exhibit relatively poor photostability and at best a fifth of the brightness of organic dyes [159]. Since the resolution achievable in SMLM increases with the square root of the amount of photons emitted by a single fluorophore, this can directly impact the resolution of SMLM [46]. Factors such as protein folding as well as the efficiency and velocity of chromophore maturation are important and can differ depending on the environment, e.g., the presence of molecular oxygen is usually needed for final chromophore maturation [160, 161]. Their properties can be readily modified by changing the amino acid sequence, and several versions have been designed to have improved brightness and photostability [162] and switching properties for SMLM imaging. These include photoactivatable proteins such as paGFP [119] and PAmCherry1 [59], reversibly switchable FPs such as Dronpa [120] and Dreiklang [163], and photoconvertible FPs such as Kaede [164], mEos2 [77], or Dendra2 [94]. An often overlooked factor is codon usage

bias, and all endogenous tags, including self-labeling enzymes, should be codon-optimized for the organism used [165].

Controlling the fluorescence of the sample

Robust control of the molecular states is crucial in most super-resolution microscopy applications. Certain steps can be taken to improve the stability, longevity, and intensity of fluorescence, as well as to achieve the on and off switching required for SMLM.

Considering that most microscope cameras record with millisecond-range exposure times, triplet-state transitions and collisional quenching events—which occur several orders of magnitude faster than these exposure times—are not registered as individual events but rather as a loss of signal intensity. Collisional quenching is mostly avoided by imaging in defined, impurity-free buffer solutions, though water shows absorbance in the visible range of light due to its molecular vibrations, as shown in Fig. 3ai. When these molecular vibrations are in resonance with the emission wavelength of a fluorophore, the fluorophore can transfer its excited-state energy to a water molecule during a collision. Heavy-water (D_2O) molecules vibrate at significantly lower frequencies due to the presence of deuterium. Substituting water in the imaging solution with D_2O thus increases the overall photon yield. The magnitude of fluorescence enhancement in D_2O versus H_2O for a specific fluorophore thus correlates with the spectral overlap of the light absorption of H_2O with the emission of the fluorophore, as seen for different fluorophores in Fig. 3ai [72].

Molecular oxygen plays an important role in many of the fluorophore's electronic state transitions. Since the ground state of molecular oxygen is also a triplet, it easily reacts with a triplet-state fluorophore in an electron transfer reaction. This can return the fluorophore to its ground state, but it also produces singlet oxygen and reactive oxygen species (ROS), which can then cause irreversible photobleaching [86]. To avoid the bleaching caused by a buildup of ROS, oxygen can be removed from the imaging solution by adding enzymatic systems such as a combination of glucose oxidase, glucose, and catalase (GLOX) [166], a mix of protocatechuate dioxygenase and protocatechuic acid (PCA/PCD) [167], or a system containing pyranose oxidase, glucose, and catalase [168], as summarized in Table 4. It is worth mentioning that it has recently been reported that most commercial glucose oxidase preparations used in the popular GLOX system suffer from nuclease contamination. Such contamination can cause fluorescent background and introduce artifacts into nucleic acid studies. Furthermore, the GLOX reaction lowers the pH of the solution over time, while other systems do not [177]. Fast, efficient chemical oxygen removal has also been reported to be achieved with methylene blue (MB) and mercaptoethylamine (MEA) [170].

However, since oxygen is such an efficient triplet-state quencher, its depletion can result in a high fraction of fluorophores populating the triplet state, significantly impairing the photon yield. There are several strategies that enable us to circumvent this problem while still removing the risk of bleaching by ROS. The first is to add the chemical cyclooctatetraene (COT), which, much like oxygen, directly returns triplet-state fluorophores to their ground states. As this process significantly shortens the residence time of the fluorophore in the triplet state, the overall fluorescence is stabilized and intensity fluctuations are reduced, as shown in Fig. 3aii [73, 176].

The second approach is to quench the triplet state by colliding the fluorophore with certain reducing agents, thus converting it into the dark, nonfluorescent, anionic radical form $F^{\bullet-}$, as shown in Fig. 3aiii. To do this, chemicals such as mercaptoethylamine (MEA) [176, 178], β-mercaptoethanol (BME) [166], dithiothreitol (DTT) [111], glutathione (GSH) [111], 6-hydroxy-2,5,7,8-tetramethylchroman-2-carboxylic acid (Trolox) [174, 179], ascorbic acid (AA) [74], and potassium iodide (KI) [180] can be added to the imaging buffer. However, to return to the ground state, the $F^{\bullet-}$ fluorophore must be oxidized, a task in which oxygen again plays a crucial role. Removing oxygen can thus lead to very long $F^{\bullet-}$ dark states, a property exploited in SMLM. Using high excitation light intensities ensures that the fluorophores are quickly cycled into the triplet state, from where they are promptly reduced to the dark radical state. Cyanine fluorophores such as Alexa Fluor 647 require a primary thiol (e.g., BME, MEA, GSH, or DTT) in the switching buffer, and undergo a thiol group addition reaction at one of the C atoms in the π-system (Fig. 3cv) [80]. A similar effect can be observed with a phosphine group upon the addition of tris(2-carboxyethyl)phosphine (TCEP) [172]. Since complete oxygen removal is impossible, the few residual oxygen molecules can stochastically oxidize individual fluorophores into the ground state, causing the on and off fluorescence "blinking" desired in SMLM. Many fluorophores develop a distinct absorption peak at shorter wavelengths in their radical state, likely due to disruption of the π-system. Indeed, in cyanine dyes, this system is thought to be practically split in two [80]. Irradiation by UV light thus expedites the return of $F^{\bullet-}$ fluorophores to the ground state [75], as depicted in Fig. 3aiv. Embedding samples in resin greatly suppresses collisional interactions, meaning that reactivation by UV is the only means of returning to the ground state [64], making the method viable for correlative light electron microscopy [181].

Oxygen in the solution can also be replaced with an alternative oxidizer such as methylviologen (MV) [74] or Trolox, which can be converted into an oxidizing quinone form upon UV irradiation [174]. The blinking rate can be adjusted by

Table 4 Summary of labeling strategies commonly used in super-resolution microscopy

	Buffer class	Buffer base	Compounds	Organic dyes used in switching buffer / description	Ref.
Switching buffers	**Reducer - O_2**	PBS/TRIS pH 7.4 - 9 - O_2	10 - 100 mM MEA	AF 750 [96], CF 680 [63], CF 647 [63], AF 647 and Cy5 [10], CF 568 [63], AF 532 [106], ATTO 520 [103]	[10]
			0.5 - 1% BME	AF 750 [112], CF 680 [98], Cy5 readout pairs [9, 58], AF 647 [92]	[58]
			10 - 100 mM GSH	AF 647 [106], TMR [106]	[106]
	Reducer only	PBS/TRIS pH 7.4 - 9	10 - 100 mM MEA	AF 647 [54], ATTO 655 [100], AF 568 [54], ATTO 520 [111], AF 532 [105], AF 488 [111]	[52, 111]
			0.5 - 1% BME	ATTO 655 [100]	[100]
			50 µM AA	ATTO 655 [169]	[169]
			10 - 100 mM GSH	ATTO 655 [52], ATTO 520 [52]	[52, 111]
			50 mM TCEP + 2 mM COT	AF 750 [97], AF 647 [97]	[97]
	Oxygen removal (- O_2)	PBS/TRIS pH 7.4 - 9	GLOX*	AF 568 [121], ATTO 520 [121], AF 488 [121]	[121]
			PCD/PCA*		[167]
			POC*		[168]
			100 mM MEA + 1 µM MB	Cy5 [170]	[170]
	Switching ROXS reducer and oxidizer - O_2	PBS/TRIS pH 7.4 - 9 - O_2	500 µM AA + 25 µM MV	ATTO 655 [171]	[171]
			1 mM AA + 1 mM MV + 25 mM TCEP, pH 9	AF 750 [172], AF 647 [172], Cy5 [172]	[172]
	Switching mount	Vectashield	20% Vectashield + 80% (95% glycerol 50 mM TRIS)	AF 647 [110], CF 647 [110]	[110]
		Mowiol	0.5% Mowiol + 50 mM DTT	SiR [101]	[101]
		Resin	100% dehydration + EM resin embedding		[173]
		PVA	1% in PBS, spin coat	Oregon Green [41], AF 488 [41]	[41]
	Live-cell media	DMEM, modified to not contain phenol red	None	SiR [102], TMR [55, 102]	[55]
			100 mM GSH + GLOX	AF 647 [106], TMR [106]	[106]
			25 mM TCEP	AF 647 [172], Cy5 [172]	[172]
Stabilizing buffers	**Stabilizing ROXS** reducer and oxidizer - O_2	PBS/TRIS pH 7.4 - 9 -O_2	1 mM AA + 1 mM MV	Triplet-state quenching and fluorescence stabilizer.	[74]
			1 mM Trolox + Trolox-quinone	Triplet-state quenching and fluorescence stabilizer.	[174]
	Mounting	Vectashield	Sample mount	Sample mounting media that retard photobleaching, stabilize fluorescence, and can be used for longer-term sample preservation (Mowiol).	[175]
		Mowiol			
		SlowFade			
		Fluor-Stop			
Additives	**TSQ** triplet-state quenchers	Cyclooctatetraene	2 mM COT	Direct triplet-state quenching by energy transfer.	[73, 176]
		Nitrobenzyl alcohol	2 mM NBA	Fluorescence enhancer and stabilizer, redox triplet quencher.	[73]
	Antifading agents	n-Propyl gallate	10 - 100 µM NPG	Antioxidant fluorescence protectant.	[176]
		1,4-Diazabicyclo [2.2.2]octane	10 mM - 1 M	Antifading agent.	[167]

The switching buffers section of the table includes a list of working dye/buffer combinations. Example buffer compilation: decide on buffer class (e.g., "Reducer with $–O_2$"), and then decide on the buffer base, the pH, oxygen removal ($–O_2$), and the final compounds based on the fluorophore used (e.g., CF 680 with 10–100 mM MEA [63])

AF Alexa Fluor, $–O_2$ oxygen removal, for the abbreviations of the chemicals, see the text or the corresponding references

* For the exact formulations of GLOX, PCD/PCA, and PCO, see the corresponding references

fine-tuning the ratios of these compounds while keeping the reducer at a high concentration and the oxidizer at a low concentration [171]. The exact concentrations heavily depend on the redox potentials of the fluorophore–reducer/oxidizer pairs. Since the reduction potential of the $F^{\bullet-}$ state varies with the fluorophore considered, different fluorophores can exhibit different blinking behaviors in the same buffer. The pH influences the redox potentials of the compounds in the solution, so changing the pH provides yet another way of adjusting blinking rates [111]. For some fluorophores, the reducing environment inside living cells is sufficient to induce long dark states [106]. In some cases, oxygen removal can be omitted and the addition of a reducer is sufficient [169].

In the cases of STED and SIM, the same strategy can be used to stabilize the fluorescence. Provided the concentrations of both the reducer and the oxidizer are high enough (usually in the millimolar range), the triplet state is efficiently reduced to a radical state that is rapidly oxidized back to the ground state upon formation. The rapidity of this process of reduction and oxidation significantly shortens the overall time the fluorophore spends in nonfluorescing states. The stabilizing effects of a reducing and oxidizing system (ROXS) such as

that shown in Fig. 3aiii were reported before the development of SMLM [74].

Fluorophores can also be protected from bleaching by the addition of antioxidants such as *n*-propyl gallate (nPG) [176] or antifading reagents such as nitrobenzyl alcohol (NBA), paraphenylenediamine (PPD), 1,4-diazabicyclo[2.2.2]octane (DABCO), and commercial products such as Vectashield, Fluor-stop, Mowiol, or SlowFade [175, 182]. Vectashield has also been reported to be an effective and very simple SMLM switching medium for several dyes, acting through an unspecified mechanism [110]. COT, NBA, and Trolox have also been (covalently) linked to fluorophores, introducing the concept of "self-healing" dyes [183]. All of these components as well as some popular SMLM buffer formulations that facilitate photoswitching of common fluorophores are summarized in Table 4.

In addition to electronic state transitions, switching is also caused by conformational changes in the chromophore or its surrounding environment. Three main conformational blinking mechanisms exist in fluorescent proteins: photoactivation, photoconversion, and photoswitching [184]. In photoactivatable fluorescent proteins such as paGFP, interactions between the chromophore and a side chain in the beta-barrel stabilize the conjugated π-system in a neutral nonfluorescent state. Irradiation with UV decarboxylates the side chain, shifting the equilibrium of the chromophore towards its anionic state, thus making the protein fluorescent (Fig. 3ci) [76]. Similarly, photoconvertible fluorescent proteins such as mEos2 [77] undergo a fluorescence wavelength shift from green to orange when a peptide bond in the chromophore is cleaved by UV irradiation, causing an extension of the π-system, as seen in Fig. 3cii [185]. Finally, photoswitchable fluorescent proteins undergo reversible on and off switching as a result of UV-induced *cis*/*trans* isomerization like that shown for the fluorescent protein Dronpa in Fig. 3ciii. The isomerization causes protonation changes similar to those that occur in photoactivatable proteins, but which result in the reversible formation of a nonfluorescent form of the fluorophore [78]. Switching properties of fluorescent proteins can be adjusted by modifying the amino acid sequence. Two interesting examples of this are IrisFP and NijiFP [116], which can both be irreversibly photoconverted by UV light from their initial green fluorescing form into an orange fluorescing form, as well as reversibly photoswitched between their fluorescing and dark state (in both the green and the orange fluorescent forms).

Organic dyes can also be made nonfluorescent by inducing reversible changes to the molecule through either *cis*/*trans* isomerization [186] and the addition of certain chemical groups [187] or reduction by $NaBH_4$ [188] in a process called photocaging, as seen in Fig. 3civ for a rhodamine dye [189]. Irradiation with the correct wavelength returns the molecule to its fluorescent state [79, 189, 190]. Slow stochastic activation followed by prompt bleaching enables the use of such dyes in SMLM [79, 190].

The novel dye HMSiR represents a class all of its own. This silicon-rhodamine-derived dye naturally resides in a nonfluorescent cyclized form (Fig. 3cvi). It very rarely undergoes a spontaneous change in conformation and becomes fluorescent for a short time. Since this blinking does not require a specialized and probably live-cell-incompatible buffer and is independent of the excitation light intensity, it is very suitable for live-cell imaging [81].

The photochemical properties of individual fluorophores are especially important when designing multicolor experiments. Some fluorescent proteins need specific conditions for proper folding or switching. PAmCherry, for example, requires oxygen for activation, so it cannot be used in oxygen-free buffers [53, 161]. Further, the optimal imaging conditions of a fluorophore partially depend on its redox potential; a buffer that induces blinking in one fluorophore may stabilize another. Table 2 covers most of the working dual- and triple-fluorophore combinations used in SMLM to date.

Super-resolved cell biology

Direct observations of the molecular processes that take place in cells can help to advance our understanding of life and how the complex interdependencies of single molecules enable it. Using super-resolution microscopy, we can follow these molecules, measure diffusion and progress in assembly processes, and quantify the molecules in subcellular structures at unrivaled spatiotemporal resolution. Over the past decade, rapid developments in these techniques have created a wide spectrum of advanced experimental settings that have already unraveled several mysteries associated with cells, some of which are depicted in Fig. 4 and are briefly summarized below.

Molecular counting and spatial organization

SMLM data is built on individual single-molecule localizations, and thus allows the absolute stoichiometry of molecules in subcellular structures to be determined.

Here, several effects which compromise this straightforward strategy must be considered. First, undercounting of molecules occurs when some molecules are not counted during the experiment due to, for example, incomplete labeling by the fluorophore, immature or misfolded genetic fluorescent tags, limited photoactivation or switching efficiencies, or insufficient algorithmic registration. The latter problem can be resolved to some degree by using multiemitter fitting algorithms or fluorophore density estimators when there are high fluorescent spot densities,

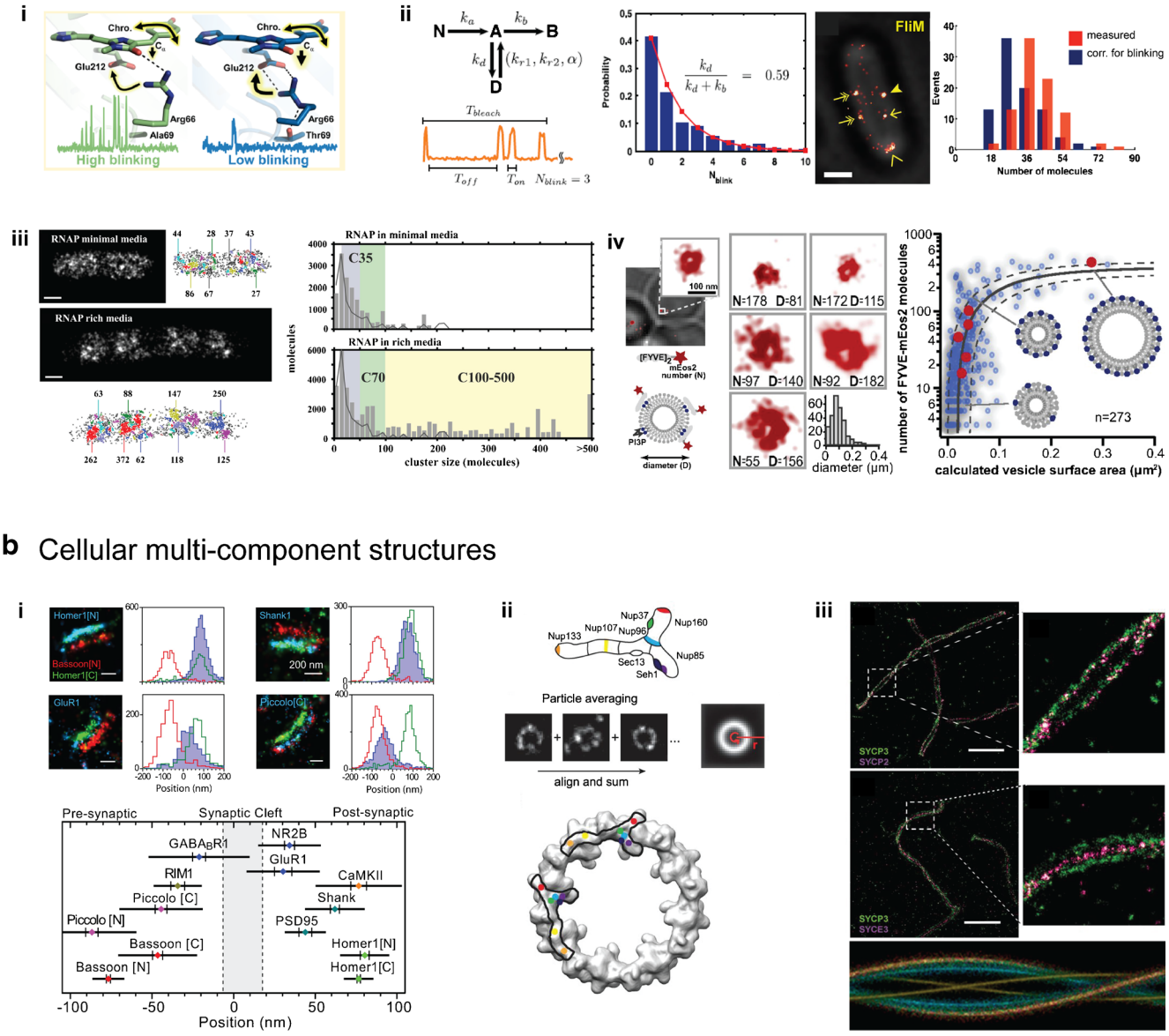

Fig. 4a–b Quantitative super-resolution microscopy. **a** SMLM allows the stoichiometry of a molecule to be determined, with several over- or undercounting effects taken into account. (*i*) The photochemical properties of fluorescent proteins lead to specific blinking and bleaching behaviors. The high-blinking and fast-bleaching behaviors shown by mEos2 (*left*) and Dendra2 (*right*), respectively, are largely determined by the orientation of the single residue arginine 66. Reprinted with permission from [191]. (*ii*) Fluorophore blinking behavior can be corrected for using kinetic fluorophore schemes. In this strategy, the number of FliM proteins per flagellar motor is counted in vivo. Reprinted from [192]. (*iii*) Spatial organization of *E. coli* RNA polymerases under minimal as well as rich growth conditions. Reprinted with permission from [193]. (*iv*) Maturation of endocytic vesicles into late endosomes. Reprinted from [194]. (*b*) Structural super-resolution microscopy reveals the molecular architecture of cellular multicomponent complexes. (*i*) Mutual organization of various pre- and postsynaptic proteins in relation to the proteins Bassoon and Homer1. Reprinted with permission from [139]. (*ii*) Combining data from identical particles yields a high-resolution average. Systematic SMLM imaging of the Y-shaped subunit of the nuclear pore complex allows it to be aligned onto the electron density of the nuclear pore (*bottom*). Reprinted with permission from [104]. (*iii*) Aligning different pairs of synaptonemal proteins onto a helical template yields the three-dimensional model of the synaptonemal complex with isotropic resolution. Reprinted from [105]. Scale bars: **a***ii* and **a***iii* 500 nm; **a***iv* 100 nm; **b***i* 200 nm; **b***iii* 2 μm

thus decreasing the number of missed localizations [43]. Second, overcounting effects can occur when localized local background fluctuations lead to falsely included positions, during multiple target counting by multiple antibodies or multiple fluorescent labels, or due to multiple localizations per fluorophore caused by blinking behavior. Uncorrected SMLM data can thus result in apparent self-clustering of localizations, which tends to be

misinterpreted as clustered organization of the target molecule. These effects can be reduced by, for example, using a fast-maturing one-to-one endogenous fluorescent protein fusion with (engineered) low-blinking behavior. Recently, a mechanistic study revealed that the side-chain conformation of arginine 66 seen in Fig. 4ai is sufficient to cause the popular fluorophores mEos2 (left) and Dendra2 (right) to either blink or bleach, respectively. Consequently, the engineered single mutants mEos2-A69T and Dendra2-T69A show completely swapped behaviors [191].

To further account for miscounting effects, SMLM localizations can be tracked for fluorescent emissions spanning several imaging frames, weighted by known fluorophore detection efficiencies, and statistically corrected for fluorophore blinking [192, 194–196]. For example, as seen in Fig. 4aii, Lee et al. introduced kinetic fluorophore models and accessed the blinking probability of the fluorescent protein tag in order to then count 33 molecules of FliM protein per bacterial flagellar motor in vivo [192]. Further, the varying spatial organization of DNA transcribing *E. coli* RNA polymerase for different metabolic conditions (Fig. 4aiii) as well as the maturation pathway of small endocytic vesicles which form at the membrane and then develop into late endosomes in yeast (Fig. 4aiv) have been revealed.

Cellular multicomponent structures

Using super-resolution methods, not only can individual molecules be precisely localized, but the large molecular architecture of multiprotein complexes and whole organelles as well as the organization of the genome or membrane can be targeted in the native cellular environment. This yields detailed quantitative molecular maps that capture these large assemblies and place hundreds of different molecules into assembled three-dimensional structures while maintaining the high spatiotemporal resolution of the method. These structures, such as the synapse depicted in Fig. 4bi, can allow us to advance our molecular understanding of their functions and reveal large-scale cellular organization. In the study shown in Fig. 4bi, various pre- and postsynaptic proteins were imaged in relation to the N-terminal localization of the protein Bassoon and the C-terminus of Homer1 by triple-color SMLM, which elucidated their mutual organization in proximity to the synaptic cleft. Indeed, the macromolecular assemblies studied so far using super-resolution techniques comprise an impressive list, including the nuclear pore complex, the ESCRT transport machinery, the neuronal architecture, focal adhesions, the centrosome and cellular division, the endocytosis pathway, as well as the organization of chromatin and membrane lipid domains (see the detailed review in [197]).

Averaging the data for super-resolved identical particles involves combining the individual copies of the same structure into a high-resolution average that complements the single images. This is useful because a single image may have some information missing due to absent affinity labels, imperfect photoswitching of the fluorophores, or nonisotropic resolution. Such a particle averaging strategy can help to elucidate the compositions and organization of macromolecular structures; for instance, the organization of the Y-shaped nuclear pore complex (NPC) subunit Nup107-160 was retrieved and matched with the electron density of the cytoplasmic ring of the nuclear pore via systematic two-dimensional SMLM imaging (Fig. 4bii) [104]. Aligning two-color and two-dimensional SMLM data from different pairs of synaptonemal proteins onto a helical template yielded a three-dimensional model of the synaptonemal complex with isotropic resolution (Fig. 4biii) [105]. The centrosomes of *Drosophila* [198], yeast [199], and humans [200] were studied by combining three-dimensional SIM images. Thus, super-resolution microscopy combined with particle averaging complements current structural biology studies, as it can target structures that are too large for cryoelectron microscopy or when preparation for X-ray crystallography fails. In this context, techniques like subtomogram averaging [201] adapted for three-dimensional super-resolution microscopy could allow us to resolve even more structures at higher in situ resolution, and correlative interaction networks combining super-resolved data with other (e.g., biochemical or genetic) analyzes could lead to large systems biology approaches, which could further refine current studies.

Live-cell imaging

Fluorescence microscopy plays a key role in revealing the structures and functions of living cells in a minimally invasive manner through the use of genetic tags, and thus profits greatly from efficient genome engineering, such as the developing CRISPR-Cas technique [202]. For example, by applying STED microscopy to the visual cortex of YFP-transgenic and anesthetized (but live) mice, it has been possible to observe fine details and measure the dynamics of the tiny dendritic spines in vivo (Fig. 5ai) [203]. In order to improve live-cell super-resolution microscopy strategies, new designs are mainly focusing on three goals: accelerating the imaging speed, lowering the phototoxicity, and expanding the field of view in the lateral as well as vertical directions, all without compromising the resolution. The most critical issues to address are the laser intensities and imaging times used, which, depending on the wavelength of the laser and the irradiation dose, can compromise the health of the cells being studied [141, 207, 208]. Possible solutions involve developing new fast switching fluorophores that can be applied at lower laser

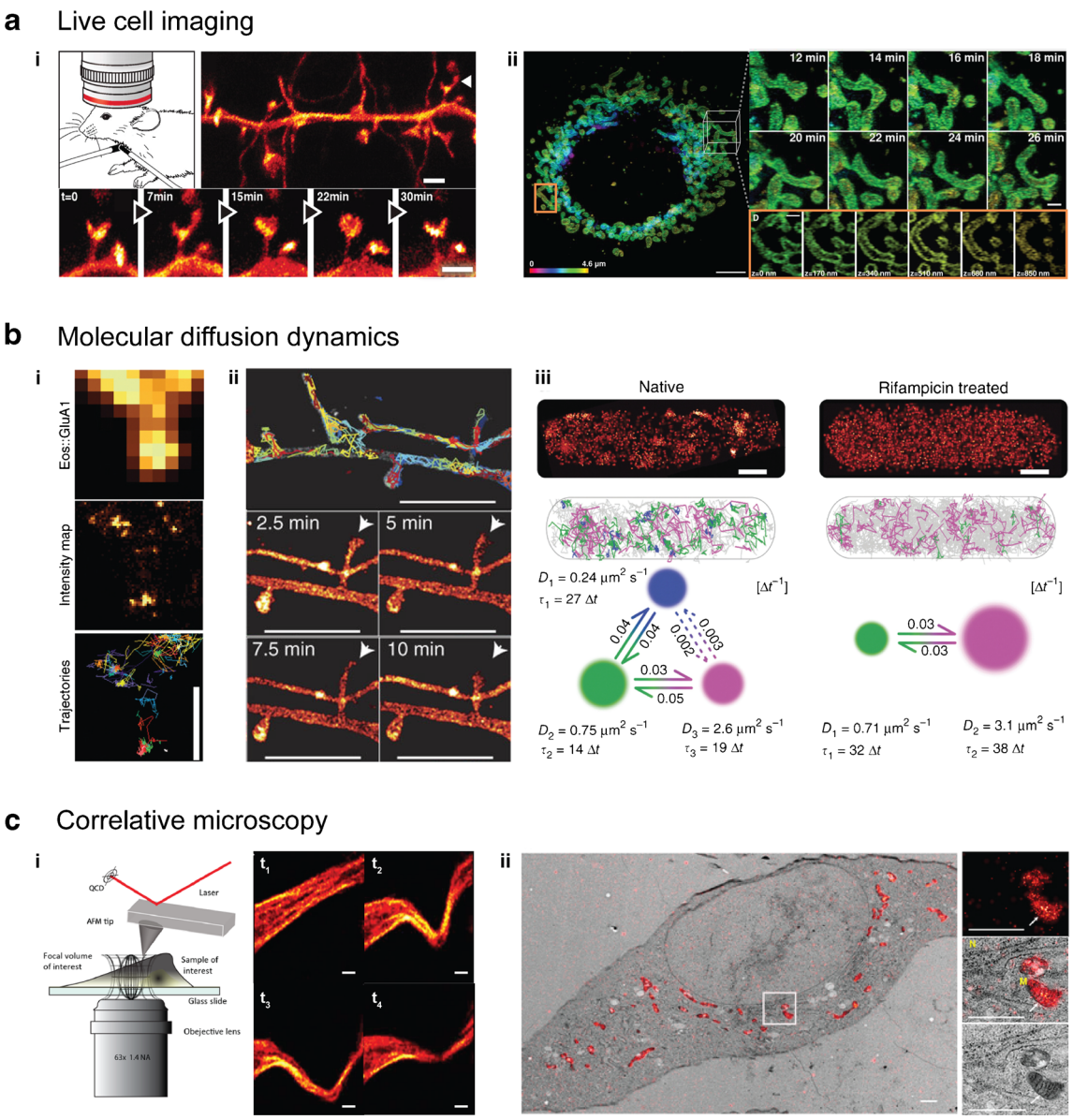

Fig. 5a–c Advanced dynamic and correlative super-resolution microscopy approaches. **a** Live imaging has been successfully performed on living cells and mammals. (*i*) STED microscopy of the dynamics of dendritic spines (*arrows*) in the visual cortex of living, YFP-transgenic, anesthetized mouse. Reprinted with permission from [203]. (*ii*) Mitochondrial fusion and fission dynamics imaged over a period of several tens of minutes by nonlinear SIM in lattice light sheet configuration. Reprinted with permission from [13]. **b** Single-particle tracking schemes elucidate molecular diffusional dynamics. (*i*) High-density tracking of AMPA receptors reveals confined nanodomains in the postsynaptic regions. Reprinted with permission from [204]. (*ii*) In contrast, membrane-bound GPI demonstrates a more homogeneous diffusion. Reprinted with permission from [4]. (*iii*) Bayesian hidden Markov model assessment of Hfq protein dynamics in *E. coli* cells. When mRNA synthesis is inhibited, the fraction of Hfq-binding mRNA (state of slowest diffusion) disappears. Reprinted with permission from [205]. **c** Correlative microscopy allows diverse features of a sample to be measured. (*i*) STED microscopy combined with atomic force microscopy (AFM) visualizes the response of the cytoskeleton upon nanomanipulation by the AFM tip. Reprinted with permission from [206]. (*ii*) Correlative PALM and electron microscopy of the mitochondrially targeted fluorescent protein mEos4 verifies its intact photoconversion and fluorescence under heavy osmium tetroxide fixation. Reprinted by permission from [114]. Scales: **a***i* 1 µm; **a***ii* 5 µm (*left*) and 1 µm (*right*); **b***i* 800 nm; **b***ii* 2 µm; **b***iii* 500 nm; **c***i* 2 µm, **c***ii* 1 µm

irradiations; fluorescent proteins that are usable in the longer (less toxic) near-infrared wavelength range, thus permitting deep-tissue imaging; as well as protected dyes that are shielded from the environment, similar to a fluorescent protein barrel. Such a protective structure could then also shield the cell from ROS and free radicals originating from photochemical reactions in the proximity of the chromophore during excitational or switching processes. New technical implementations which optimize the use of the limited photon budget per fluorophore as well as the imaging speed are

favored, such as methods which confine but also parallelize the imaging by multifocal or lattice-like excitation or allow for multifocal detection [209–212]. New rapid and large sCMOS detectors increase the observation volume and allow for faster SMLM switching [3].

During the last few years it has therefore become possible to image whole living cells and organisms over longer timescales. One recent implementation of various types of SIM designs is a three-dimensional nonlinear SIM developed by Li et al. that uses photoswitchable fluorophores combined with lattice-lightsheet microscopy to show endocytic and cytoskeletal dynamics as well as the fission and fusion of mitochondria of whole live cells by labeling their membranes. They resolved the intracellular dynamics at individual mitochondrial constrictions over a period of several tens of minutes at a resolution of about 45 nm laterally and 170 nm vertically (Fig. 5aii) [13].

Another technical advance that is currently being explored is the implementation of adaptive optics to correct for aberrations in large sample volumes, e.g., multicellular organisms [213]. All three-dimensional localization microscopy algorithms have been challenged to participate in a large assessment, in order to evaluate their performance and identify common limitations on them. The results should ultimately guide development work aimed at optimizing three-dimensional SMLM resolution when studying protein ultrastructure in vivo [214].

Following molecule diffusion dynamics

Single-particle tracking schemes directly monitor the kinetics of intracellular processes. In combination with photoactivatable fluorescent proteins in sptPALM, it is possible to follow the diffusion of individual proteins on cell membranes as well as in the cytoplasm of living cells, and to measure thousands of short single-molecule trajectories by sequential photoactivation. High-density tracking of the GluA1 subunits of AMPA receptors in the membranes of dendritic spines of live hippocampal neurons has revealed their discrete organization in 70–100 nm diameter nanodomains, and has shown that the receptors are mainly immobilized in the postsynapse (Fig. 5bi) [204], in contrast to the membrane-anchored glycosylphosphatidylinositol-GFP (Fig. 5bii). It is also possible to classify individual trajectories by their apparent diffusion constant into distinct states of diffusion, corresponding, for example, to different states of binding. This allows spatial and temporal heterogeneities in protein properties to be resolved. These are normally hidden in ensemble averages but are highly valuable when used in mathematical models for systems biology: by performing Bayesian assessments of hidden Markov models that combine the information from all short trajectories, it has recently been shown that the diffusion constants and state transition rates as well as the number of states in the model can be extracted [205]. This approach has been tested for the protein Hfq in *E. coli*, which mediates post-transcriptional gene regulation by facilitating interactions between mRNA and noncoding small RNA. The Hfq dynamics are highly altered when transcription is blocked using the drug rifampicin, as this decreases the mRNA level in the cell. The state with the slowest diffusion—most likely Hfq binding to the mRNA being transcribed—disappears, and the fraction occupying the intermediate state decreases substantially (Fig. 5biii).

Correlative microscopy

Correlative microscopy combines the advantages of and opportunities provided by different methods, and thus allows different features of the exact same sample to be measured. For instance, a correlative approach can combine dynamic tracking studies with structural imaging when mapping intracellular vesicle transport on the cytoskeleton [71]. Also possible is the real-time visualization of the fast responses of the cytoskeleton of HeLa cells upon physical nanomanipulation by an atomic force microscopy tip in correlative STED microscopy (Fig. 5ci) [206]. Another direction in correlative imaging is to combine the high ultrastructural resolution and cellular context information of electron microscopy with the specific localization of molecules in super-resolution microscopy (Fig. 5cii) [215]. Unfortunately, most current correlative schemes still suffer from complex and tedious fixation protocols as well as limited labeling and imaging strategies, i.e., the cryo- or resin-covered environments used for electron microscopy impair the photophysics of most standard fluorophores. However, technical implementations develop rapidly; for instance, a correlative fluorescent protein tag, mEos4, which fluoresces and photoconverts normally under heavy osmium tetroxide fixation has recently been developed (Fig. 5c, ii) [114], and the dye TMR has been shown to not only preserve its fluorescence during high-pressure freezing and freeze substitution preparations, but to be able to photooxidize diaminobenzidine (DAB) too, which then yields high electron-microscopic contrast [173, 216].

In an optimistic but still realistic future, super-resolution microscopy will push beyond its current limits of routinely achieving experimental resolutions of tens of nanometers to approach the distances of typical single-molecule FRET measurements (2–10 nm) as well as the structural resolution of cryoelectron microscopy and X-ray crystallography (about 2–3 Å), which will allow us to more directly combine the heterogeneity and dynamics of protein complexes measured in vivo with the precise structural information available from purified protein complexes.

Outlook

Over the last few decades, super-resolution microscopy has proven its value in the life sciences, and a myriad of biological applications of super-resolution microscopy have emerged. The super-resolution toolbox currently consists of many diverse methods and application strategies that complement traditional cell biology studies as well as techniques from molecular biology or biochemistry. Super-resolution microscopy is on its way to becoming a standard research tool, which is leading to a huge demand for computer-based data processing and openly available analysis software for (advanced) data evaluation, visualization, and comparison, as well as accessible, affordable, and simple-to-use hardware implementations. Also, super-resolution microscopy traditionally yields large volumes of microscopic data, which would ideally be stored and handled in open-access public platforms. Whether this vision comes to pass largely depends on the development of new algorithms as well as open-source software and strategies for efficient large-scale data handling.

Acknowledgments Open access funding provided by Max Planck Society.

Compliance with ethical standards

Conflicts of interest The authors declare that they have no conflict of interest.

References

1. Liu Z, Lavis LD, Betzig E. Imaging live-cell dynamics and structure at the single-molecule level. Mol Cell. 2015;58(4):644–59. doi:10.1016/j.molcel.2015.02.033.
2. Hell SW, Sahl SJ, Bates M, Zhuang XW, Heintzmann R, Booth MJ et al. The 2015 super-resolution microscopy roadmap. J Phys D Appl Phys. 2015;48(44). doi:10.1088/0022-3727/48/44/443001.
3. Winter PW, Shroff H. Faster fluorescence microscopy: advances in high speed biological imaging. Curr Opin Chem Biol. 2014;20:46–53. doi:10.1016/j.cbpa.2014.04.008.
4. Ries J, Kaplan C, Platonova E, Eghlidi H, Ewers H. A simple, versatile method for GFP-based super-resolution microscopy via nanobodies. Nat Methods. 2012;9(6):582–4. doi:10.1038/nmeth.1991.
5. Vreja IC, Nikic I, Gottfert F, Bates M, Krohnert K, Outeiro TF, et al. Super-resolution microscopy of clickable amino acids reveals the effects of fluorescent protein tagging on protein assemblies. ACS Nano. 2015;9(11):11034–41. doi:10.1021/acsnano.5b04434.
6. Klar TA, Hell SW. Subdiffraction resolution in far-field fluorescence microscopy. Opt Lett. 1999;24(14):954–6.
7. Gustafsson MG. Surpassing the lateral resolution limit by a factor of two using structured illumination microscopy. J Microsc. 2000;198(Pt 2):82–7.
8. Betzig E, Patterson GH, Sougrat R, Lindwasser OW, Olenych S, Bonifacino JS, et al. Imaging intracellular fluorescent proteins at nanometer resolution. Science. 2006;313(5793):1642–5. doi:10.1126/science.1127344.
9. Rust MJ, Bates M, Zhuang X. Sub-diffraction-limit imaging by stochastic optical reconstruction microscopy (STORM). Nat Methods. 2006;3(10):793–5. doi:10.1038/nmeth929.
10. Heilemann M, van de Linde S, Schuttpelz M, Kasper R, Seefeldt B, Mukherjee A, et al. Subdiffraction-resolution fluorescence imaging with conventional fluorescent probes. Angew Chem Int Ed. 2008;47(33):6172–6. doi:10.1002/anie.200802376.
11. Kner P, Chhun BB, Griffis ER, Winoto L, Gustafsson MGL. Super-resolution video microscopy of live cells by structured illumination. Nat Methods. 2009;6(5):339–42. doi:10.1038/nmeth.1324.
12. Gustafsson MG, Shao L, Carlton PM, Wang CJ, Golubovskaya IN, Cande WZ, et al. Three-dimensional resolution doubling in wide-field fluorescence microscopy by structured illumination. Biophys J. 2008;94(12):4957–70. doi:10.1529/biophysj.107.120345.
13. Li D, Shao L, Chen BC, Zhang X, Zhang M, Moses B, et al. Extended-resolution structured illumination imaging of endocytic and cytoskeletal dynamics. Science. 2015;349(6251), aab3500. doi:10.1126/science.aab3500.
14. Bückers J, Wildanger D, Vicidomini G, Kastrup L, Hell SW. Simultaneous multi-lifetime multi-color STED imaging for colocalization analyses. Opt Express. 2011;19(4):3130–43. doi:10.1364/OE.19.003130.
15. Xu K, Babcock HP, Zhuang X. Dual-objective STORM reveals three-dimensional filament organization in the actin cytoskeleton. Nat Methods. 2012;9(2):185–8.
16. Rayleigh XV. On the theory of optical images, with special reference to the microscope. Philos Mag. 1896;42(255):167–95. doi:10.1080/14786449608620902.
17. Siedentopf H, Zsigmondy R. Über Sichtbarmachung und Größenbestimmung ultramikoskopischer Teilchen, mit besonderer Anwendung auf Goldrubingläser. Ann Phys. 1902;315(1):1–39. doi:10.1002/andp.19023150102.
18. König K. Multiphoton microscopy in life sciences. J Microsc. 2000;200(2):83–104. doi:10.1046/j.1365-2818.2000.00738.x.
19. Betzig E, Lewis A, Harootunian A, Isaacson M, Kratschmer E. Near field scanning optical microscopy (NSOM): development and biophysical applications. Biophys J. 1986;49(1):269–79. doi:10.1016/S0006-3495(86)83640-2.
20. Harke B, Keller J, Ullal CK, Westphal V, Schonle A, Hell SW. Resolution scaling in STED microscopy. Opt Express. 2008;16(6):4154–62.
21. Schmidt R, Wurm CA, Jakobs S, Engelhardt J, Egner A, Hell SW. Spherical nanosized focal spot unravels the interior of cells. Nat Methods. 2008;5(6):539–44. doi:10.1038/nmeth.1214.
22. Willig KI, Harke B, Medda R, Hell SW. STED microscopy with continuous wave beams. Nat Methods. 2007;4(11):915–8. doi:10.1038/nmeth1108.
23. Vicidomini G, Moneron G, Han KY, Westphal V, Ta H, Reuss M, et al. Sharper low-power STED nanoscopy by time gating. Nat Methods. 2011;8(7):571–3. doi:10.1038/nmeth.1624.
24. Staudt T, Engler A, Rittweger E, Harke B, Engelhardt J, Hell SW. Far-field optical nanoscopy with reduced number of state transition cycles. Opt Express. 2011;19(6):5644–57. doi:10.1364/OE.19.005644.
25. Grotjohann T, Testa I, Leutenegger M, Bock H, Urban NT, Lavoie-Cardinal F, et al. Diffraction-unlimited all-optical imaging and writing with a photochromic GFP. Nature. 2011;478(7368):204–8. doi:10.1038/nature10497.
26. Danzl JG, Sidenstein SC, Gregor C, Urban NT, Ilgen P, Jakobs S, et al. Coordinate-targeted fluorescence nanoscopy

with multiple off states. Nat Photonics. 2016;10(2):122–8. doi:10.1038/nphoton.2015.266.
27. Eggeling C, Willig KI, Barrantes FJ. STED microscopy of living cells—new frontiers in membrane and neurobiology. J Neurochem. 2013;126(2):203–12. doi:10.1111/jnc.12243.
28. Donnert G, Keller J, Wurm CA, Rizzoli SO, Westphal V, Schönle A, et al. Two-color far-field fluorescence nanoscopy. Biophys J. 2007;92(8):L67–9. doi:10.1529/biophysj.107.104497.
29. Gottfert F, Wurm CA, Mueller V, Berning S, Cordes VC, Honigmann A, et al. Coaligned dual-channel STED nanoscopy and molecular diffusion analysis at 20 nm resolution. Biophys J. 2013;105(1):L01–3. doi:10.1016/j.bpj.2013.05.029.
30. Tonnesen J, Nadrigny F, Willig KI, Wedlich-Soldner R, Nagerl UV. Two-color STED microscopy of living synapses using a single laser-beam pair. Biophys J. 2011;101(10):2545–52. doi:10.1016/j.bpj.2011.10.011.
31. Willig KI, Stiel AC, Brakemann T, Jakobs S, Hell SW. Dual-label STED nanoscopy of living cells using photochromism. Nano Lett. 2011;11(9):3970–3. doi:10.1021/nl202290w.
32. Jost A, Heintzmann R. Superresolution multidimensional imaging with structured illumination microscopy. Annu Rev Mater Res. 2013;43(1):261–82. doi:10.1146/annurev-matsci-071312-121648.
33. Ball G, Demmerle J, Kaufmann R, Davis I, Dobbie IM, Schermelleh L. SIMcheck: a toolbox for successful super-resolution structured illumination microscopy. Sci Rep. 2015;5:15915. doi:10.1038/srep15915.
34. Muller M, Monkemoller V, Hennig S, Hubner W, Huser T. Open-source image reconstruction of super-resolution structured illumination microscopy data in ImageJ. Nat Commun. 2016;7:10980. doi:10.1038/ncomms10980.
35. Hirvonen LM, Wicker K, Mandula O, Heintzmann R. Structured illumination microscopy of a living cell. Eur Biophys J. 2009;38(6):807–12. doi:10.1007/s00249-009-0501-6.
36. York AG, Parekh SH, Dalle Nogare D, Fischer RS, Temprine K, Mione M, et al. Resolution doubling in live, multicellular organisms via multifocal structured illumination microscopy. Nat Methods. 2012;9(7):749–54. doi:10.1038/nmeth.2025.
37. Schermelleh L, Carlton PM, Haase S, Shao L, Winoto L, Kner P, et al. Subdiffraction multicolor imaging of the nuclear periphery with 3D structured illumination microscopy. Science. 2008;320(5881):1332–6. doi:10.1126/science.1156947.
38. Schaefer LH, Schuster D, Schaffer J. Structured illumination microscopy: artefact analysis and reduction utilizing a parameter optimization approach. J Microsc. 2004;216(2):165–74. doi:10.1111/j.0022-2720.2004.01411.x.
39. Gustafsson MG. Nonlinear structured-illumination microscopy: wide-field fluorescence imaging with theoretically unlimited resolution. Proc Natl Acad Sci USA. 2005;102(37):13081–6. doi:10.1073/pnas.0406877102.
40. Rego EH, Shao L, Macklin JJ, Winoto L, Johansson GA, Kamps-Hughes N, et al. Nonlinear structured-illumination microscopy with a photoswitchable protein reveals cellular structures at 50-nm resolution. Proc Natl Acad Sci USA. 2012;109(3):E135–43. doi:10.1073/pnas.1107547108.
41. Fölling J, Bossi M, Bock H, Medda R, Wurm CA, Hein B, et al. Fluorescence nanoscopy by ground-state depletion and single-molecule return. Nat Methods. 2008;5(11):943–5.
42. Moerner WE. Microscopy beyond the diffraction limit using actively controlled single molecules. J Microsc. 2012;246(3):213–20. doi:10.1111/j.1365-2818.2012.03600.x.
43. Small A, Stahlheber S. Fluorophore localization algorithms for super-resolution microscopy. Nat Methods. 2014;11(3):267–79. doi:10.1038/nmeth.2844.
44. Sage D, Kirshner H, Pengo T, Stuurman N, Min J, Manley S, et al. Quantitative evaluation of software packages for single-molecule localization microscopy. Nat Methods. 2015;12(8):717–24. doi:10.1038/nmeth.3442.
45. Chenouard N, Smal I, de Chaumont F, Maska M, Sbalzarini IF, Gong Y, et al. Objective comparison of particle tracking methods. Nat Methods. 2014;11(3):281–9. doi:10.1038/nmeth.2808.
46. Thompson RE, Larson DR, Webb WW. Precise nanometer localization analysis for individual fluorescent probes. Biophys J. 2002;82(5):2775–83.
47. Axelrod D. Total internal reflection fluorescence microscopy in cell biology. Methods Enzymol. 2003;361:1–33.
48. Tokunaga M, Imamoto N, Sakata-Sogawa K. Highly inclined thin illumination enables clear single-molecule imaging in cells. Nat Methods. 2008;5(2):159–61. doi:10.1038/nmeth1171.
49. York AG, Ghitani A, Vaziri A, Davidson MW, Shroff H. Confined activation and subdiffractive localization enables whole-cell PALM with genetically expressed probes. Nat Methods. 2011;8(4):327–33.
50. Cella Zanacchi F, Lavagnino Z, Perrone Donnorso M, Del Bue A, Furia L, Faretta M, et al. Live-cell 3D super-resolution imaging in thick biological samples. Nat Methods. 2011;8(12):1047–9.
51. Chen BC, Legant WR, Wang K, Shao L, Milkie DE, Davidson MW, et al. Lattice light-sheet microscopy: imaging molecules to embryos at high spatiotemporal resolution. Science. 2014;346(6208):1257998. doi:10.1126/science.1257998.
52. van de Linde S, Endesfelder U, Mukherjee A, Schuttpelz M, Wiebusch G, Wolter S, et al. Multicolor photoswitching microscopy for subdiffraction-resolution fluorescence imaging. Photochem Photobiol Sci. 2009;8(4):465–9. doi:10.1039/B822533H.
53. Endesfelder U, Malkusch S, Flottmann B, Mondry J, Liguzinski P, Verveer PJ, et al. Chemically induced photoswitching of fluorescent probes—a general concept for super-resolution microscopy. Molecules. 2011;16(4):3106.
54. Laine RF, Albecka A, van de Linde S, Rees EJ, Crump CM, Kaminski CF. Structural analysis of herpes simplex virus by optical super-resolution imaging. Nat Commun. 2015;6. doi:10.1038/ncomms6980.
55. Testa I, Wurm CA, Medda R, Rothermel E, von Middendorf C, Fölling J, et al. Multicolor fluorescence nanoscopy in fixed and living cells by exciting conventional fluorophores with a single wavelength. Biophys J. 2010;99(8):2686–94. doi:10.1016/j.bpj.2010.08.012.
56. Shroff H, Galbraith CG, Galbraith JA, White H, Gillette J, Olenych S, et al. Dual-color superresolution imaging of genetically expressed probes within individual adhesion complexes. Proc Natl Acad Sci USA. 2007;104(51):20308–13. doi:10.1073/pnas.0710517105.
57. Grimm JB, Klein T, Kopek BG, Shtengel G, Hess HF, Sauer M, et al. Synthesis of a far-red photoactivatable silicon-containing rhodamine for super-resolution microscopy. Angew Chem Int Ed. 2016;55(5):1723–7. doi:10.1002/anie.201509649.
58. Bates M, Huang B, Dempsey GT, Zhuang X. Multicolor super-resolution imaging with photo-switchable fluorescent probes. Science. 2007;317(5845):1749–53. doi:10.1126/science.1146598.
59. Subach FV, Patterson GH, Manley S, Gillette JM, Lippincott-Schwartz J, Verkhusha VV. Photoactivatable mCherry for high-resolution two-color fluorescence microscopy. Nat Methods. 2009;6(2):153–9.
60. Gunewardene Mudalige S, Subach Fedor V, Gould Travis J, Penoncello Gregory P, Gudheti Manasa V, Verkhusha Vladislav V, et al. Superresolution imaging of multiple fluorescent proteins with highly overlapping emission spectra in living cells. Biophys J. 2011;101(6):1522–8. doi:10.1016/j.bpj.2011.07.049.
61. Lampe A, Haucke V, Sigrist SJ, Heilemann M, Schmoranzer J. Multi-colour direct STORM with red emitting carbocyanines. Biol Cell. 2012;104(4):229–37. doi:10.1111/boc.201100011.
62. Zhang Z, Kenny SJ, Hauser M, Li W, Xu K. Ultrahigh-throughput single-molecule spectroscopy and spectrally resolved super-

resolution microscopy. Nat Methods. 2015;12(10):935–8. doi:10.1038/nmeth.3528.
63. Lehmann M, Lichtner G, Klenz H, Schmoranzer J. Novel organic dyes for multicolor localization-based super-resolution microscopy. J Biophotonics. 2016;9(1–2):161–70. doi:10.1002/jbio.201500119.
64. Biteen JS, Thompson MA, Tselentis NK, Bowman GR, Shapiro L, Moerner WE. Super-resolution imaging in live *Caulobacter crescentus* cells using photoswitchable EYFP. Nat Methods. 2008;5(11):947–9.
65. Wombacher R, Heidbreder M, van de Linde S, Sheetz MP, Heilemann M, Cornish VW, et al. Live-cell super-resolution imaging with trimethoprim conjugates. Nat Methods. 2010;7(9):717–9.
66. Jones SA, Shim S-H, He J, Zhuang X. Fast, three-dimensional super-resolution imaging of live cells. Nat Methods. 2011;8(6):499–505.
67. Manley S, Gillette JM, Patterson GH, Shroff H, Hess HF, Betzig E, et al. High-density mapping of single-molecule trajectories with photoactivated localization microscopy. Nat Methods. 2008;5(2):155–7.
68. Frost NA, Shroff H, Kong H, Betzig E, Blanpied TA. Single-molecule discrimination of discrete perisynaptic and distributed sites of actin filament assembly within dendritic spines. Neuron. 2010;67(1):86–99. doi:10.1016/j.neuron.2010.05.026.
69. Rossier O, Octeau V, Sibarita J-B, Leduc C, Tessier B, Nair D, et al. Integrins β1 and β3 exhibit distinct dynamic nanoscale organizations inside focal adhesions. Nat Cell Biol. 2012;14(10):1057–67.
70. Sanamrad A, Persson F, Lundius EG, Fange D, Gynnå AH, Elf J. Single-particle tracking reveals that free ribosomal subunits are not excluded from the *Escherichia coli* nucleoid. Proc Natl Acad Sci USA. 2014;111(31):11413–8. doi:10.1073/pnas.1411558111.
71. Bálint Š, Verdeny Vilanova I, Sandoval Álvarez Á, Lakadamyali M. Correlative live-cell and superresolution microscopy reveals cargo transport dynamics at microtubule intersections. Proc Natl Acad Sci USA. 2013;110(9):3375–80. doi:10.1073/pnas.1219206110.
72. Klehs K, Spahn C, Endesfelder U, Lee SF, Furstenberg A, Heilemann M. Increasing the brightness of cyanine fluorophores for single-molecule and superresolution imaging. ChemPhysChem. 2014;15(4):637–41. doi:10.1002/cphc.201300874.
73. Zheng Q, Jockusch S, Zhou Z, Altman RB, Warren JD, Turro NJ, et al. On the mechanisms of cyanine fluorophore photostabilization. J Phys Chem Lett. 2012;3(16):2200–3. doi:10.1021/jz300670p.
74. Vogelsang J, Kasper R, Steinhauer C, Person B, Heilemann M, Sauer M, et al. A reducing and oxidizing system minimizes photobleaching and blinking of fluorescent dyes. Angew Chem Int Ed. 2008;47(29):5465–9. doi:10.1002/anie.200801518.
75. van de Linde S, Krstic I, Prisner T, Doose S, Heilemann M, Sauer M. Photoinduced formation of reversible dye radicals and their impact on super-resolution imaging. Photochem Photobiol Sci. 2011;10(4):499–506. doi:10.1039/c0pp00317d.
76. Henderson JN, Gepshtein R, Heenan JR, Kallio K, Huppert D, Remington SJ. Structure and mechanism of the photoactivatable green fluorescent protein. J Am Chem Soc. 2009;131(12):4176–7.
77. McKinney SA, Murphy CS, Hazelwood KL, Davidson MW, Looger LL. A bright and photostable photoconvertible fluorescent protein. Nat Methods. 2009;6(2):131–3. doi:10.1038/nmeth.1296.
78. Habuchi S, Dedecker P, Hotta J-i, Flors C, Ando R, Mizuno H, et al. Photo-induced protonation/deprotonation in the GFP-like fluorescent protein Dronpa: mechanism responsible for the reversible photoswitching. Photochem Photobiol Sci. 2006;5(6):567–76.
79. Banala S, Maurel D, Manley S, Johnsson K. A caged, localizable rhodamine derivative for superresolution microscopy. ACS Chem Biol. 2011;7(2):289–93.
80. Dempsey GT, Bates M, Kowtoniuk WE, Liu DR, Tsien RY, Zhuang X. Photoswitching mechanism of cyanine dyes. J Am Chem Soc. 2009;131(51):18192–3. doi:10.1021/ja904588g.
81. Uno SN, Kamiya M, Yoshihara T, Sugawara K, Okabe K, Tarhan MC, et al. A spontaneously blinking fluorophore based on intramolecular spirocyclization for live-cell super-resolution imaging. Nat Chem. 2014;6(8):681–9. doi:10.1038/nchem.2002.
82. Lakowicz JR. Principles of fluorescence spectroscopy. New York: Springer; 2013.
83. Klessinger M. Konstitution und Lichtabsorption organischer Farbstoffe. Chem Unserer Zeit. 1978;12(1):1–11. doi:10.1002/ciuz.19780120102.
84. Sinha RP, Häder D-P. UV-induced DNA damage and repair: a review. Photochem Photobiol Sci. 2002;1(4):225–36.
85. Aubin JE. Autofluorescence of viable cultured mammalian cells. J Histochem Cytochem. 1979;27(1):36–43. doi:10.1177/27.1.220325.
86. DeRosa MC, Crutchley RJ. Photosensitized singlet oxygen and its applications. Coord Chem Rev. 2002;233:351–71.
87. D'Este E, Kamin D, Göttfert F, El-Hady A, Hell Stefan W. STED nanoscopy reveals the ubiquity of subcortical cytoskeleton periodicity in living neurons. Cell Rep. 2015;10(8):1246–51. doi:10.1016/j.celrep.2015.02.007.
88. Wildanger D, Medda R, Kastrup L, Hell SW. A compact STED microscope providing 3D nanoscale resolution. J Microsc. 2009;236(1):35–43. doi:10.1111/j.1365-2818.2009.03188.x.
89. Schachtrup C, Ryu JK, Mammadzada K, Khan AS, Carlton PM, Perez A, et al. Nuclear pore complex remodeling by p75(NTR) cleavage controls TGF-beta signaling and astrocyte functions. Nat Neurosci. 2015;18(8):1077–80. doi:10.1038/nn.4054.
90. Malkusch S, Endesfelder U, Mondry J, Gelleri M, Verveer PJ, Heilemann M. Coordinate-based colocalization analysis of single-molecule localization microscopy data. Histochem Cell Biol. 2012;137(1):1–10. doi:10.1007/s00418-011-0880-5.
91. Zessin PJ, Krüger CL, Malkusch S, Endesfelder U, Heilemann M. A hydrophilic gel matrix for single-molecule super-resolution microscopy. Opt Nanoscopy. 2013;2(1):1–8.
92. French JB, Jones SA, Deng H, Pedley AM, Kim D, Chan CY, et al. Spatial colocalization and functional link of purinosomes with mitochondria. Science. 2016;351(6274):733–7. doi:10.1126/science.aac6054.
93. Gahlmann A, Ptacin JL, Grover G, Quirin S, von Diezmann AR, Lee MK, et al. Quantitative multicolor subdiffraction imaging of bacterial protein ultrastructures in three dimensions. Nano Lett. 2013;13(3):987–93. doi:10.1021/nl304071h.
94. Gurskaya NG, Verkhusha VV, Shcheglov AS, Staroverov DB, Chepurnykh TV, Fradkov AF, et al. Engineering of a monomeric green-to-red photoactivatable fluorescent protein induced by blue light. Nat Biotechnol. 2006;24(4):461–5. doi:10.1038/nbt1191.
95. Wilmes S, Staufenbiel M, Lisse D, Richter CP, Beutel O, Busch KB, et al. Triple-color super-resolution imaging of live cells: resolving submicroscopic receptor organization in the plasma membrane. Angew Chem Int Ed. 2012;51(20):4868–71. doi:10.1002/anie.201200853.
96. Baddeley D, Crossman D, Rossberger S, Cheyne JE, Montgomery JM, Jayasinghe ID, et al. 4D super-resolution microscopy with conventional fluorophores and single wavelength excitation in optically thick cells and tissues. PLoS One. 2011;6(5), e20645. doi:10.1371/journal.pone.0020645.
97. Zhao T, Wang Y, Zhai Y, Qu X, Cheng A, Du S, et al. A user-friendly two-color super-resolution localization microscope. Opt Express. 2015;23(2):1879–87. doi:10.1364/OE.23.001879.
98. Platonova E, Winterflood CM, Ewers H. A simple method for GFP- and RFP-based dual color single-molecule localization microscopy. ACS Chem Biol. 2015;10(6):1411–6. doi:10.1021/acschembio.5b00046.

99. Salvador-Gallego R, Mund M, Cosentino K, Schneider J, Unsay J, Schraermeyer U, et al. Bax assembly into rings and arcs in apoptotic mitochondria is linked to membrane pores. EMBO J. 2016;35(4):389–401. doi:10.15252/embj.201593384.
100. van de Linde S, Kasper R, Heilemann M, Sauer M. Photoswitching microscopy with standard fluorophores. Appl Phys B. 2008;93(4):725–31.
101. Lukinavicius G, Umezawa K, Olivier N, Honigmann A, Yang G, Plass T, et al. A near-infrared fluorophore for live-cell super-resolution microscopy of cellular proteins. Nat Chem. 2013;5(2):132–9. doi:10.1038/nchem.1546.
102. Beinlich FR, Drees C, Piehler J, Busch KB. Shuttling of PINK1 between mitochondrial microcompartments resolved by triple-color superresolution microscopy. ACS Chem Biol. 2015;10(9):1970–6. doi:10.1021/acschembio.5b00295.
103. Loschberger A, van de Linde S, Dabauvalle MC, Rieger B, Heilemann M, Krohne G, et al. Super-resolution imaging visualizes the eightfold symmetry of gp210 proteins around the nuclear pore complex and resolves the central channel with nanometer resolution. J Cell Sci. 2012;125(Pt 3):570–5. doi:10.1242/jcs.098822.
104. Szymborska A, de Marco A, Daigle N, Cordes VC, Briggs JAG, Ellenberg J. Nuclear pore scaffold structure analyzed by super-resolution microscopy and particle averaging. Science. 2013;341(6146):655–8. doi:10.1126/science.1240672.
105. Schücker K, Holm T, Franke C, Sauer M, Benavente R. Elucidation of synaptonemal complex organization by super-resolution imaging with isotropic resolution. Proc Natl Acad Sci USA. 2015;112(7):2029–33. doi:10.1073/pnas.1414814112.
106. Klein T, van de Linde S, Sauer M. Live-cell super-resolution imaging goes multicolor. Chembiochem. 2012;13(13):1861–3. doi:10.1002/cbic.201200347.
107. Allen JR, Ross ST, Davidson MW. Sample preparation for single molecule localization microscopy. Phys Chem Chem Phys. 2013;15(43):18771–83. doi:10.1039/c3cp53719f.
108. Lampe A, Tadeus G, Schmoranzer J. Spectral demixing avoids registration errors and reduces noise in multicolor localization-based super-resolution microscopy. Methods Appl Fluoresc. 2015;3(3):034006.
109. Ribeiro SA, Vagnarelli P, Dong Y, Hori T, McEwen BF, Fukagawa T, et al. A super-resolution map of the vertebrate kinetochore. Proc Natl Acad Sci USA. 2010;107(23):10484–9. doi:10.1073/pnas.1002325107.
110. Olivier N, Keller D, Rajan VS, Gönczy P, Manley S. Simple buffers for 3D STORM microscopy. Biomedical optics express. 2013;4(6):885–99.
111. Heilemann M, van de Linde S, Mukherjee A, Sauer M. Super-resolution imaging with small organic fluorophores. Angew Chem Int Ed. 2009;48(37):6903–8. doi:10.1002/anie.200902073.
112. Bates M, Dempsey GT, Chen KH, Zhuang X. Multicolor super-resolution fluorescence imaging via multi-parameter fluorophore detection. ChemPhysChem. 2012;13(1):99–107. doi:10.1002/cphc.201100735.
113. Zhang M, Chang H, Zhang Y, Yu J, Wu L, Ji W, et al. Rational design of true monomeric and bright photoactivatable fluorescent proteins. Nat Methods. 2012;9(7):727–9.
114. Paez-Segala MG, Sun MG, Shtengel G, Viswanathan S, Baird MA, Macklin JJ, et al. Fixation-resistant photoactivatable fluorescent proteins for CLEM. Nat Methods. 2015;12(3):215–8.
115. Wang S, Moffitt JR, Dempsey GT, Xie XS, Zhuang X. Characterization and development of photoactivatable fluorescent proteins for single-molecule-based superresolution imaging. Proc Natl Acad Sci USA. 2014;111(23):8452–7.
116. Adam V, Moeyaert B, David CC, Mizuno H, Lelimousin M, Dedecker P, et al. Rational design of photoconvertible and biphotochromic fluorescent proteins for advanced microscopy applications. Chem Biol. 2011;18(10):1241–51. doi:10.1016/j.chembiol.2011.08.007.
117. Zhang X, Chen X, Zeng Z, Zhang M, Sun Y, Xi P, et al. Development of a reversibly switchable fluorescent protein for super-resolution optical fluctuation imaging (SOFI). ACS Nano. 2015;9(3):2659–67.
118. Chudakov DM, Matz MV, Lukyanov S, Lukyanov KA. Fluorescent proteins and their applications in imaging living cells and tissues. Physiol Rev. 2010;90(3):1103–63. doi:10.1152/physrev.00038.2009.
119. Patterson GH, Lippincott-Schwartz J. A photoactivatable GFP for selective photolabeling of proteins and cells. Science. 2002;297(5588):1873–7. doi:10.1126/science.1074952.
120. Andresen M, Stiel AC, Trowitzsch S, Weber G, Eggeling C, Wahl MC, et al. Structural basis for reversible photoswitching in Dronpa. Proc Natl Acad Sci USA. 2007;104(32):13005–9. doi:10.1073/pnas.0700629104.
121. Dempsey GT, Vaughan JC, Chen KH, Bates M, Zhuang X. Evaluation of fluorophores for optimal performance in localization-based super-resolution imaging. Nat Methods. 2011;8(12):1027–36. doi:10.1038/nmeth.1768.
122. Landgraf D, Okumus B, Chien P, Baker TA, Paulsson J. Segregation of molecules at cell division reveals native protein localization. Nat Methods. 2012;9(5):480–2.
123. Wolter S, Endesfelder U, van de Linde S, Heilemann M, Sauer M. Measuring localization performance of super-resolution algorithms on very active samples. Opt Express. 2011;19(8):7020–33.
124. Shannon CE. Communication in the presence of noise. P IEEE. 1949;37(1):10–21.
125. Coons AH, Creech HJ, Jones RN. Immunological properties of an antibody containing a fluorescent group. Exp Biol Med. 1941;47(2):200–2. doi:10.3181/00379727-47-13084p.
126. Rothbauer U, Zolghadr K, Tillib S, Nowak D, Schermelleh L, Gahl A, et al. Targeting and tracing antigens in live cells with fluorescent nanobodies. Nat Methods. 2006;3(11):887–9.
127. Beatty KE, Liu JC, Xie F, Dieterich DC, Schuman EM, Wang Q, et al. Fluorescence visualization of newly synthesized proteins in mammalian cells. Angew Chem Int Ed. 2006;45(44):7364–7. doi:10.1002/anie.200602114.
128. Neef AB, Schultz C. Selective fluorescence labeling of lipids in living cells. Angew Chem Int Ed. 2009;48(8):1498–500. doi:10.1002/anie.200805507.
129. Salic A, Mitchison TJ. A chemical method for fast and sensitive detection of DNA synthesis in vivo. Proc Natl Acad Sci USA. 2008;105(7):2415–20. doi:10.1073/pnas.0712168105.
130. Rudkin GT, Stollar BD. High resolution detection of DNA-RNA hybrids in situ by indirect immunofluorescence. Nature. 1977;265(5593):472–3.
131. Shim SH, Xia C, Zhong G, Babcock HP, Vaughan JC, Huang B, et al. Super-resolution fluorescence imaging of organelles in live cells with photoswitchable membrane probes. Proc Natl Acad Sci USA. 2012;109(35):13978–83. doi:10.1073/pnas.1201882109.
132. Lukinavicius G, Reymond L, D'Este E, Masharina A, Gottfert F, Ta H, et al. Fluorogenic probes for live-cell imaging of the cytoskeleton. Nat Methods. 2014;11(7):731–3. doi:10.1038/nmeth.2972.
133. Lukinavicius G, Blaukopf C, Pershagen E, Schena A, Reymond L, Derivery E, et al. SiR-Hoechst is a far-red DNA stain for live-cell nanoscopy. Nat Commun. 2015;6:8497. doi:10.1038/ncomms9497.
134. Revelo NH, Kamin D, Truckenbrodt S, Wong AB, Reuter-Jessen K, Reisinger E, et al. A new probe for super-resolution imaging of membranes elucidates trafficking pathways. J Cell Biol. 2014;205(4):591–606. doi:10.1083/jcb.201402066.

135. Sun X, Zhang A, Baker B, Sun L, Howard A, Buswell J, et al. Development of SNAP-tag fluorogenic probes for wash-free fluorescence imaging. ChemBioChem. 2011;12(14):2217–26. doi:10.1002/cbic.201100173.
136. Gautier A, Juillerat A, Heinis C, Corrêa Jr IR, Kindermann M, Beaufils F, et al. An engineered protein tag for multiprotein labeling in living cells. Chem Biol. 2008;15(2):128–36. doi:10.1016/j.chembiol.2008.01.007.
137. Los GV, Encell LP, McDougall MG, Hartzell DD, Karassina N, Zimprich C, et al. HaloTag: a novel protein labeling technology for cell imaging and protein analysis. ACS Chem Biol. 2008;3(6):373–82. doi:10.1021/cb800025k.
138. Chen Z, Jing C, Gallagher SS, Sheetz MP, Cornish VW. Second-generation covalent TMP-tag for live cell imaging. J Am Chem Soc. 2012;134(33):13692–9. doi:10.1021/ja303374p.
139. Dani A, Huang B, Bergan J, Dulac C, Zhuang X. Superresolution imaging of chemical synapses in the brain. Neuron. 2010;68(5):843–56.
140. Fritschy J-M. Is my antibody-staining specific? How to deal with pitfalls of immunohistochemistry. Eur J Neurosci. 2008;28(12):2365–70. doi:10.1111/j.1460-9568.2008.06552.x.
141. Hinterdorfer P, Van Oijen A. Handbook of single-molecule biophysics. New York: Springer; 2009.
142. Opazo F, Levy M, Byrom M, Schafer C, Geisler C, Groemer TW, et al. Aptamers as potential tools for super-resolution microscopy. Nat Methods. 2012;9(10):938–9.
143. Paige JS, Wu KY, Jaffrey SR. RNA mimics of green fluorescent protein. Science. 2011;333(6042):642–6. doi:10.1126/science.1207339.
144. Nikić I, Kang JH, Girona GE, Aramburu IV, Lemke EA. Labeling proteins on live mammalian cells using click chemistry. Nat Protoc. 2015;10(5):780–91. doi:10.1038/nprot.2015.045.
145. Lajoie MJ, Rovner AJ, Goodman DB, Aerni H-R, Haimovich AD, Kuznetsov G, et al. Genomically recoded organisms expand biological functions. Science. 2013;342(6156):357–60. doi:10.1126/science.1241459.
146. Uttamapinant C, Howe JD, Lang K, Beránek V, Davis L, Mahesh M, et al. Genetic code expansion enables live-cell and super-resolution imaging of site-specifically labeled cellular proteins. J Am Chem Soc. 2015;137(14):4602–5. doi:10.1021/ja512838z.
147. Amann R, Fuchs BM. Single-cell identification in microbial communities by improved fluorescence in situ hybridization techniques. Nat Rev Microbiol. 2008;6(5):339–48.
148. Patel NS, Rhinn M, Semprich CI, Halley PA, Dollé P, Bickmore WA, et al. FGF signalling regulates chromatin organisation during neural differentiation via mechanisms that can be uncoupled from transcription. PLoS Genet. 2013;9(7), e1003614. doi:10.1371/journal.pgen.1003614.
149. Nora EP, Lajoie BR, Schulz EG, Giorgetti L, Okamoto I, Servant N, et al. Spatial partitioning of the regulatory landscape of the X-inactivation center. Nature. 2012;485(7398):381–5. doi:10.1038/nature11049.
150. Doksani Y, Wu JY, de Lange T, Zhuang X. Super-resolution fluorescence imaging of telomeres reveals TRF2-dependent T-loop formation. Cell. 2013;155(2):345–56. doi:10.1016/j.cell.2013.09.048.
151. Vicidomini G, Ta H, Honigmann A, Mueller V, Clausen MP, Waithe D, et al. STED-FLCS: an advanced tool to reveal spatiotemporal heterogeneity of molecular membrane dynamics. Nano Lett. 2015;15(9):5912–8. doi:10.1021/acs.nanolett.5b02001.
152. Pan D, Hu Z, Qiu F, Huang ZL, Ma Y, Wang Y, et al. A general strategy for developing cell-permeable photo-modulatable organic fluorescent probes for live-cell super-resolution imaging. Nat Commun. 2014;5:5573. doi:10.1038/ncomms6573.
153. Taylor DL, Wang Y-L. Molecular cytochemistry: incorporation of fluorescently labeled actin into living cells. Proc Natl Acad Sci USA. 1978;75(2):857–61.
154. Neumann E, Schaefer-Ridder M, Wang Y, Hofschneider P. Gene transfer into mouse lyoma cells by electroporation in high electric fields. EMBO J. 1982;1(7):841.
155. McNeil PL, Warder E. Glass beads load macromolecules into living cells. J Cell Sci. 1987;88(5):669–78.
156. Barber K, Mala RR, Lambert MP, Qiu R, MacDonald RC, Klein WL. Delivery of membrane-impermeant fluorescent probes into living neural cell populations by lipotransfer. Neurosci Lett. 1996;207(1):17–20.
157. Bruckbauer A, James P, Zhou D, Yoon JW, Excell D, Korchev Y, et al. Nanopipette delivery of individual molecules to cellular compartments for single-molecule fluorescence tracking. Biophys J. 2007;93(9):3120–31.
158. Prasher DC, Eckenrode VK, Ward WW, Prendergast FG, Cormier MJ. Primary structure of the *Aequorea victoria* green-fluorescent protein. Gene. 1992;111(2):229–33.
159. Xu K, Shim S-H, Zhuang X. Super-resolution imaging through stochastic switching and localization of single molecules: an overview. In: Tinnefeld P, Eggeling C, Hell SW, editors. Far-field optical nanoscopy. Berlin: Springer; 2013. p. 27–64.
160. Heim R, Prasher DC, Tsien RY. Wavelength mutations and post-translational autoxidation of green fluorescent protein. Proc Natl Acad Sci USA. 1994;91(26):12501–4.
161. Subach FV, Malashkevich VN, Zencheck WD, Xiao H, Filonov GS, Almo SC, et al. Photoactivation mechanism of PAmCherry based on crystal structures of the protein in the dark and fluorescent states. Proc Natl Acad Sci USA. 2009;106(50):21097–102.
162. Cormack BP, Valdivia RH, Falkow S. FACS-optimized mutants of the green fluorescent protein (GFP). Gene. 1996;173(1 Spec No):33–8.
163. Brakemann T, Stiel AC, Weber G, Andresen M, Testa I, Grotjohann T, et al. A reversibly photoswitchable GFP-like protein with fluorescence excitation decoupled from switching. Nat Biotechnol. 2011;29(10):942–7. doi:10.1038/nbt.1952.
164. Schafer SP, Dittrich PS, Petrov EP, Schwille P. Single molecule fluorescence imaging of the photoinduced conversion and bleaching behavior of the fluorescent protein Kaede. Microsc Res Tech. 2006;69(3):210–9. doi:10.1002/jemt.20283.
165. Shin YC, Bischof GF, Lauer WA, Desrosiers RC. Importance of codon usage for the temporal regulation of viral gene expression. Proc Natl Acad Sci USA. 2015;112(45):14030–5. doi:10.1073/pnas.1515387112.
166. Kishino A, Yanagida T. Force measurements by micromanipulation of a single actin filament by glass needles. Nature. 1988;334(6177):74–6.
167. Aitken CE, Marshall RA, Puglisi JD. An oxygen scavenging system for improvement of dye stability in single-molecule fluorescence experiments. Biophys J. 2008;94(5):1826–35. doi:10.1529/biophysj.107.117689.
168. Swoboda M, Henig J, Cheng HM, Brugger D, Haltrich D, Plumere N, et al. Enzymatic oxygen scavenging for photostability without pH drop in single-molecule experiments. ACS Nano. 2012;6(7):6364–9. doi:10.1021/nn301895c.
169. Cordes T, Strackharn M, Stahl SW, Summerer W, Steinhauer C, Forthmann C, et al. Resolving single-molecule assembled patterns with superresolution blink-microscopy. Nano Lett. 2010;10(2):645–51. doi:10.1021/nl903730r.
170. Schäfer P, van de Linde S, Lehmann J, Sauer M, Doose S. Methylene blue- and thiol-based oxygen depletion for super-resolution imaging. Anal Chem. 2013;85(6):3393–400. doi:10.1021/ac400035k.
171. Vogelsang J, Cordes T, Forthmann C, Steinhauer C, Tinnefeld P. Controlling the fluorescence of ordinary oxazine dyes for single-molecule switching and superresolution microscopy. Proc Natl Acad Sci USA. 2009;106(20):8107–12. doi:10.1073/pnas.0811875106.

172. Vaughan JC, Dempsey GT, Sun E, Zhuang X. Phosphine quenching of cyanine dyes as a versatile tool for fluorescence microscopy. J Am Chem Soc. 2013;135(4):1197–200. doi:10.1021/ja3105279.
173. Perkovic M, Kunz M, Endesfelder U, Bunse S, Wigge C, Yu Z, et al. Correlative light-and electron microscopy with chemical tags. J Struct Biol. 2014;186(2):205–13.
174. Cordes T, Vogelsang J, Tinnefeld P. On the mechanism of Trolox as antiblinking and antibleaching reagent. J Am Chem Soc. 2009;131(14):5018–9. doi:10.1021/ja809117z.
175. Longin A, Souchier C, Ffrench M, Bryon P. Comparison of anti-fading agents used in fluorescence microscopy: image analysis and laser confocal microscopy study. J Histochem Cytochem. 1993;41(12):1833–40.
176. Widengren J, Chmyrov A, Eggeling C, Lofdahl PA, Seidel CA. Strategies to improve photostabilities in ultrasensitive fluorescence spectroscopy. J Phys Chem A. 2007;111(3):429–40. doi:10.1021/jp0646325.
177. Senavirathne G, Liu J, Lopez Jr MA, Hanne J, Martin-Lopez J, Lee JB, et al. Widespread nuclease contamination in commonly used oxygen-scavenging systems. Nat Methods. 2015;12(10):901–2. doi:10.1038/nmeth.3588.
178. Song L, Varma CA, Verhoeven JW, Tanke HJ. Influence of the triplet excited state on the photobleaching kinetics of fluorescein in microscopy. Biophys J. 1996;70(6):2959–68. doi:10.1016/S0006-3495(96)79866-1.
179. Rasnik I, McKinney SA, Ha T. Nonblinking and long-lasting single-molecule fluorescence imaging. Nat Methods. 2006;3(11):891–3. doi:10.1038/nmeth934.
180. Chmyrov A, Sanden T, Widengren J. Iodide as a fluorescence quencher and promoter—mechanisms and possible implications. J Phys Chem B. 2010;114(34):11282–91. doi:10.1021/jp103837f.
181. Johnson E, Seiradake E, Jones EY, Davis I, Grunewald K, Kaufmann R. Correlative in-resin super-resolution and electron microscopy using standard fluorescent proteins. Sci Rep. 2016;6:22681. doi:10.1038/srep22681.
182. Valnes KR, Brandtzaeg P. Retardation of immunofluorescence fading during microscopy. J Histochem Cytochem. 1985;33(8):755–61.
183. Tinnefeld P, Cordes T. 'Self-healing' dyes: intramolecular stabilization of organic fluorophores. Nat Methods. 2012;9(5):426–7. doi:10.1038/nmeth.1977.
184. Lukyanov KA, Chudakov DM, Lukyanov S, Verkhusha VV. Innovation: photoactivatable fluorescent proteins. Nat Rev Mol Cell Biol. 2005;6(11):885–91. doi:10.1038/nrm1741.
185. Wiedenmann J, Ivanchenko S, Oswald F, Schmitt F, Rocker C, Salih A, et al. EosFP, a fluorescent marker protein with UV-inducible green-to-red fluorescence conversion. Proc Natl Acad Sci USA. 2004;101(45):15905–10. doi:10.1073/pnas.0403668101.
186. Levitus M, Ranjit S. Cyanine dyes in biophysical research: the photophysics of polymethine fluorescent dyes in biomolecular environments. Q Rev Biophys. 2011;44(1):123–51. doi:10.1017/S0033583510000247.
187. Marriott G, Ottl J. Synthesis and applications of heterobifunctional photocleavable cross-linking reagents. Methods Enzymol. 1998;291:155–75.
188. Vaughan JC, Jia S, Zhuang X. Ultrabright photoactivatable fluorophores created by reductive caging. Nat Methods. 2012;9(12):1181–4. doi:10.1038/nmeth.2214.
189. Mitchison TJ, Sawin KE, Theriot JA, Gee K, Mallavarapu A. Caged fluorescent probes. Methods Enzymol. 1998;291:63–78.
190. Wysocki LM, Grimm JB, Tkachuk AN, Brown TA, Betzig E, Lavis LD. Facile and general synthesis of photoactivatable xanthene dyes. Angew Chem Int Ed. 2011;50(47):11206–9. doi:10.1002/anie.201104571.
191. Berardozzi R, Adam V, Martins A, Bourgeois D. Arginine 66 controls dark-state formation in green-to-red photoconvertible fluorescent proteins. J Am Chem Soc. 2016;138(2):558–565.
192. Lee S-H, Shin JY, Lee A, Bustamante C. Counting single photoactivatable fluorescent molecules by photoactivated localization microscopy (PALM). Proc Natl Acad Sci USA. 2012;109(43):17436–41.
193. Endesfelder U, Finan K, Holden SJ, Cook PR, Kapanidis AN, Heilemann M. Multiscale spatial organization of RNA polymerase in *Escherichia coli*. Biophys J. 2013;105(1):172–81. doi:10.1016/j.bpj.2013.05.048.
194. Puchner EM, Walter JM, Kasper R, Huang B, Lim WA. Counting molecules in single organelles with superresolution microscopy allows tracking of the endosome maturation trajectory. Proc Natl Acad Sci USA. 2013;110(40):16015–20.
195. Lando D, Endesfelder U, Berger H, Subramanian L, Dunne PD, McColl J, et al. Quantitative single-molecule microscopy reveals that CENP-A(Cnp1) deposition occurs during G2 in fission yeast. Open Biol. 2012;2(7):120078. doi:10.1098/rsob.120078.
196. Durisic N, Laparra-Cuervo L, Sandoval-Álvarez Á, Borbely JS, Lakadamyali M. Single-molecule evaluation of fluorescent protein photoactivation efficiency using an in vivo nanotemplate. Nat Methods. 2014;11(2):156–62.
197. Sydor AM, Czymmek KJ, Puchner EM, Mennella V. Super-resolution microscopy: from single molecules to supramolecular assemblies. Trends Cell Biol. 2015;25(12):730–48.
198. Mennella V, Keszthelyi B, McDonald KL, Chhun B, Kan F, Rogers GC, et al. Subdiffraction-resolution fluorescence microscopy reveals a domain of the centrosome critical for pericentriolar material organization. Nat Cell Biol. 2012;14(11):1159–68. doi:10.1038/ncb2597.
199. Burns S, Avena JS, Unruh JR, Yu Z, Smith SE, Slaughter BD, et al. Structured illumination with particle averaging reveals novel roles for yeast centrosome components during duplication. Elife. 2015;4, e08586.
200. Sonnen KF, Schermelleh L, Leonhardt H, Nigg EA. 3D-structured illumination microscopy provides novel insight into architecture of human centrosomes. Biol Open. 2012;1(10):965–76. doi:10.1242/bio.20122337.
201. Briggs JA. Structural biology in situ—the potential of subtomogram averaging. Curr Opin Struct Biol. 2013;23(2):261–7. doi:10.1016/j.sbi.2013.02.003.
202. Ran FA, Hsu PD, Wright J, Agarwala V, Scott DA, Zhang F. Genome engineering using the CRISPR-Cas9 system. Nat Protoc. 2013;8(11):2281–308.
203. Berning S, Willig KI, Steffens H, Dibaj P, Hell SW. Nanoscopy in a living mouse brain. Science. 2012;335(6068):551. doi:10.1126/science.1215369.
204. Maglione M, Sigrist SJ. Seeing the forest tree by tree: super-resolution light microscopy meets the neurosciences. Nat Neurosci. 2013;16(7):790–7.
205. Persson F, Lindén M, Unoson C, Elf J. Extracting intracellular diffusive states and transition rates from single-molecule tracking data. Nat Methods. 2013;10(3):265–9.
206. Chacko JV, Harke B, Canale C, Diaspro A. Cellular level nanomanipulation using atomic force microscope aided with superresolution imaging. J Biomed Opt. 2014;19(10):105003. doi:10.1117/1.JBO.19.10.105003.
207. Wagner M, Weber P, Bruns T, Strauss WS, Wittig R, Schneckenburger H. Light dose is a limiting factor to maintain cell viability in fluorescence microscopy and single molecule detection. Int J Mol Sci. 2010;11(3):956–66.
208. Wäldchen S, Lehmann J, Klein T, van de Linde S, Sauer M. Light-induced cell damage in live-cell super-resolution microscopy. Sci Rep. 2015;5:15348.

209. Keller PJ, Schmidt AD, Santella A, Khairy K, Bao Z, Wittbrodt J, et al. Fast, high-contrast imaging of animal development with scanned light sheet-based structured-illumination microscopy. Nat Methods. 2010;7(8):637–42.
210. Gao L, Shao L, Higgins CD, Poulton JS, Peifer M, Davidson MW, et al. Noninvasive imaging beyond the diffraction limit of 3D dynamics in thickly fluorescent specimens. Cell. 2012;151(6):1370–85.
211. Ingaramo M, York AG, Wawrzusin P, Milberg O, Hong A, Weigert R, et al. Two-photon excitation improves multifocal structured illumination microscopy in thick scattering tissue. Proc Natl Acad Sci USA. 2014;111(14):5254–9.
212. Hajj B, Wisniewski J, El Beheiry M, Chen J, Revyakin A, Wu C, et al. Whole-cell, multicolor superresolution imaging using volumetric multifocus microscopy. Proc Natl Acad Sci USA. 2014;111(49):17480–5.
213. Ji N, Milkie DE, Betzig E. Adaptive optics via pupil segmentation for high-resolution imaging in biological tissues. Nat Methods. 2010;7(2):141–7.
214. Holden S, Sage D. Imaging: super-resolution fight club. Nat Photonics. 2016;10(3):152–3.
215. Endesfelder U. Advances in correlative single-molecule localization microscopy and electron microscopy. NanoBioImaging. 2014;1(1).
216. Liss V, Barlag B, Nietschke M, Hensel M. Self-labelling enzymes as universal tags for fluorescence microscopy, super-resolution microscopy and electron microscopy. Sci Rep. 2015;5:17740.

1.2 sptPALM

1.2.1 Single-Particle Tracking Prior to SMLM

Over thirty years ago, first Single-Particle Tracking (SPT) methods were developed using 40 nm gold particles that were attached to the molecule of interest and subsequently visualized via bright-field microscopy (nanovid microscopy) [2, 3]. Due to the large Rayleigh scattering of the gold nanoparticles, localizing the particles with a nanometer precision could be achieved. Utilizing this method, the process of endocytosis and protein motility on the cell membrane could be investigated for the very first time [4]. Later studies using SPT in combination with gold nanoparticles investigated membrane compounds extensively [5, 6, 7, 8, 9]. In 1988, the method was improved by applying Differential Interference Contrast (DIC) microscopy to measure kinesin-driven movements [10]. These early implementations of SPT, despite their advantages, such as a high spatial and temporal resolution up to tens of microseconds [11] and long trajectories due to the lack of photobleaching, also have some limitations. One limitation is the increased size of the nanoparticle compared to the investigated biomolecule that can reach from tens of nanometers for gold beads to hundreds of nanometers for polymer beads, which therefore results in a highly biased dynamics and localization read-out. To reduce this bias, the bead sizes could be decreased, however, this would lead to a reduction of the Rayleigh scattering which is depending on the sixth power of the particle diameter [12] and therefore, nanometer precise detection of nanoparticles is virtually impossible. In 1990s, nanoparticles were exchanged with fluorescent molecules to label a molecule of interest and follow their movement with SPT [13, 14].

1.2.2 sptPALM

In sptPALM, the single-particle tracking method mentioned above is combined with PALM (see Section 1.1), which is based on the detection of the fluorescent signal of photoactivatable or -convertible fluorescent proteins that can be genetically fused to a protein of interest. Therefore, sptPALM enables high-density mapping of single-particle trajectories of individual proteins in a living cell. Establishing sptPALM, Manley and co-workers (2008) [15], investigated Gag and VSVG membrane proteins in mammalian COS-7 cells fused to the green-to-red photoconvertible Eos Fluorescent Protein (EosFP) [16]. They were able to obtain a few orders of magnitude more trajectories within a single cell than with conventional SPT methods as well as to create high-density super-resolved trajectory maps. Since then, this technique was used to study e.g. transcription, translation, replication and Deoxyribonucleic Acid (DNA) repair machineries in *Escherichia coli* [17, 18, 19, 20, 21] or DNA polymerase dynamics in *Bacillus subtilis* [22].

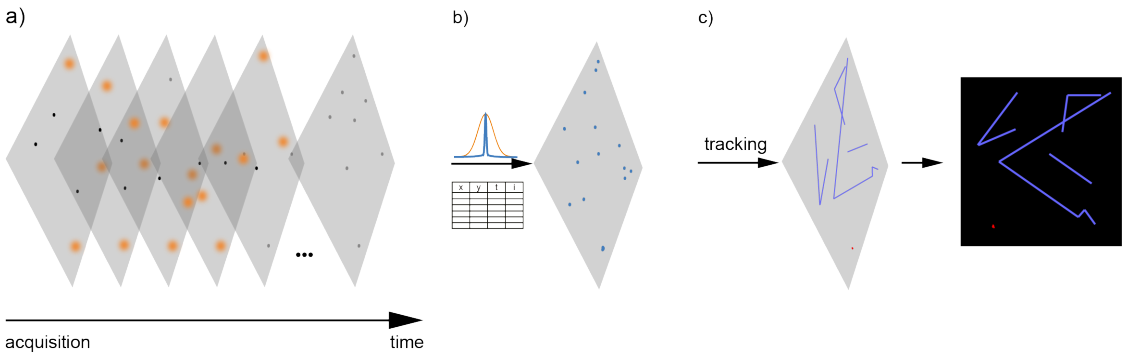

Figure 1.1: Principle of sptPALM. (a) Image acquisition. Fluorescence signals of individual molecules are collected in an acquisition sequence over time. Fluorophores are photoswitched sequentially to spatially separate the individual signals. (b) Localization routine. Each fluorescent spot in form of a Point Spread Function (PSF) is fitted by a localization algorithm to extract its centroid which determines the fluorophores localization with nanometer precision. (c) Tracking routine. Localizations are classified into single-molecule trajectories by a tracking algorithm. The dynamics of the single proteins can be inferred from the obtained trajectories. Adapted with permission from [23].

The imaging workflow is similar to conventional PALM, which was described in our review in Section 1.1, though a few additional factors have to be considered during data acquisition procedure presented in Figure 1.1. As the idea of a sptPALM experiment, as for all SPT methods, is visualizing and tracking dynamic molecules by connecting localizations in adjacent frames which stem from the same emitter, the camera integration time has to be adjusted to collect a sharp fluorescent signal originating from diffusing particles and usually this integration time is shorter than in the case of structural PALM. If the camera integration time is too long, PSFs detected on the camera chip will be blurred, and thus it is difficult to estimate the precise localization of the emitter from the blurred PSF. Additionally, to reduce the blurring effect, it is recommended to use a stroboscopic illumination pattern, where the excitation laser is present only for a fraction of the imaging interval [24, 25, 26]. In addition to that, the data acquisition frequency has to be adjusted to the dynamics of the studied proteins. In case of a highly dynamic protein of interest (e.g. a freely diffusing protein) it might be required to increase the camera frame rate to hundreds of Hz (less than a 10 ms frame rate), while less dynamic proteins can be sampled in the range of tens of Hz [27, 28, 22, 19]. Another is the need of distributing the total photon budget of a fluorophore before it photobleaches on several camera frames to visualize particle diffusion. In contrast to non-fluorescent SPT techniques, trajectory length in fluorescence microscopy is limited by photobleaching of the fluorophore, which poses a problem especially for fluorescent proteins, whose photon budget is low compared to organic dyes (see Section 1.1)

Taken all these facts into consideration, a sptPALM experiment has to be precisely planned and appropriate data acquisition parameters have to be determined. On the one hand using a high frame rate, a high read-out laser intensity and a stroboscopic illumination pattern will enable to follow a highly dynamic protein, but on the other hand trajectories will contain only few localizations as the fluorescent marker protein will bleach after typically 10-20 frames.

Another difference between sptPALM and structural PALM imaging poses the data analysis for

which a detailed description can be found in Section 3.1.

1.3 CRISPR-Cas systems

1.3.1 General Overview on CRISPR-Cas Systems

CRISPR-Cas - Clustered Regularly Interspaced Short Palindromic Repeats (CRISPR)-CRISPR-Associated Proteins (Cas) systems are adaptive, sequence-specific immunity mechanisms against foreign nucleic acids from Mobile Genetic Elements (MGEs) from viruses or plasmids [29, 30, 31, 32]. In 1987, Ishino and coworkers first found an unusual pattern of interrupted, direct-repeat sequences with a dyad symmetry in the *E. coli* genome, which was a first indication of the CRISPR-Cas system. However, the function of these repeats was unclear at that time [33]. Thereafter, similar patterns were discovered in the genome of *Mycobacterium tuberculosis* in 1993 [34, 35]. At the turn of the millennium, Mojica and others performed extensive research in published genomes and they found similar repeat clusters in genomes of 20 prokaryotic species [36], however, the role of these sequences was still elusive. Two years later, Jansen and colleagues discovered few homologous genes located in proximity to previously described repeat arrays. These genes were identified as encoding proteins with nuclease and helicase motifs, which hinted that they might be involved in the structuring of the CRISPR array [37]. In 2005, three research groups independently proposed that CRISPR-Cas might serve as an adaptive immune system in prokaryotes as they identified that sequences separating repeats (spacers) in clusters are derived from phage DNA and non-genomic DNA [38, 39, 40]. This hypothesis was finally confirmed experimentally two years later by Barrangou et al. [29]. Currently, we know that CRISPR-Cas systems are very common in prokaryotes. It is present in nearly a half of bacterial and almost in all archaeal genomes [41, 42, 43]. Even though the identified CRISPR-Cas systems are very diverse, they share some common features (see Section 1.3.3 and [44, 45]).

1.3.2 Mechanism of Action

The CRISPR-Cas mechanism can be summarized by three major steps as it is shown in Figure 1.2:

1. Spacer acquisition (primed adaptation);
2. Assembly of the effector complex (biogenesis);
3. Interference with the foreign nucleic acid.

The spacer acquisition step is similar for most known CRISPR-Cas systems and consists of a stable complex of two proteins, the endonuclease Cas1 and the structural subunit Cas2, which recognizes foreign nucleic acid fragments (called protospacers) preceded by a short motif called Protospacer Adjacent Motif (PAM). PAMs are highly diverse between different CRISPR-Cas types (two to five nucleotides in length) but at the same time are strongly conserved within types [46, 47]. After successful identification of the PAM, the protospacer is integrated into the CRISPR array [48, 49]. Utilization of the PAM is essential in preventing CRISPR-Cas systems from targeting genetic host material, which could be lethal [50].

During the biogenesis step, the full Ribonucleoprotein (RNP) surveillance complex is being

assembled. It consists of one or multiple proteins, depending on the system type, the CRISPR RNA (crRNA), and, in some cases, Trans-Activating crRNA (tracrRNA). Initially, crRNAs are transcribed from the CRISPR array sequences into a Precursor crRNA (pre-crRNA) and further maturated by the type-specific Cas endonuclease, which cuts pre-crRNA in repeat sequences, into individual crRNA molecules which contain a single spacer sequence flanked by the repeat fragments [51, 52]. Thereafter, other Cas proteins are assembled into the surveillance complex. As the Cas protein assembly is different for each CRISPR-Cas type and merely the type I-Fv effector complex was investigated in this thesis, the detailed assembly of the type I-Fv effector complex is described in Section 1.3.4 exclusively.

The last step of CRISPR-Cas functionality is an interference with the potential target. This step is varying most among all CRISPR-Cas types. Thereby, it will not be described in detail here, but two crucial processes during the interference will be marked: (i) PAM recognition by Cas proteins, where the PAM sequence is identified by the Cas proteins and the surveillance complex starts to unwind the target nucleic acid and (ii) recognition of the potential target. Here crRNA has an essential role, as the spacer sequence carried by the surveillance complex is being matched with the potential target by forming a DNA-Ribonucleic Acid (RNA) heteroduplex called R-loop.

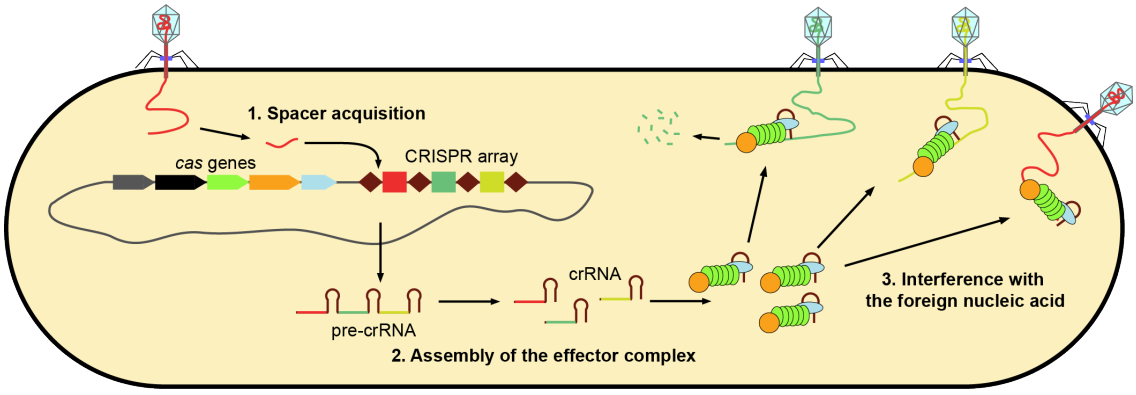

Figure 1.2: Mechanism of action of the CRISPR-Cas system. 1. Foreign DNA is identified, degraded and a short piece is integrated into the CRISPR array for memory (primed adaptation). 2. Assembly of the effector complex. CRISPR array is transcribed into pre-crRNA which is matured to crRNA. Cas proteins are recruited and form the effector complex together with the crRNA. 3. Interference. DNA is scanned by the effector complex. When the crRNA matches the target sequence, it forms a stable interference complex to degrade it.

1.3.3 Classification of CRISPR-Cas Systems

CRISPR-Cas systems classification is a challenging task. There is no straightforward approach to classify similar systems into individual clusters. Nevertheless, researchers managed to develop a semi-formal, combined classification approach, which takes certain factors into account:

1. Number of Cas proteins building the surveillance complex,
2. Signature *cas* genes, which are specific for each type,
3. Amino acid sequence similarities between multiple Cas proteins,
4. Phylogeny of Cas1 protein, which is the most conserved protein among CRISPR-Cas systems,
5. *cas* genes organization within the CRISPR-Cas loci.

In consequence, CRISPR-Cas systems are classified into two major classes based on the number of Cas proteins in the surveillance complex, which are divided into six types and based on the signature *cas* gene and Cas1 phylogeny, branching into several subtypes each (Figure 1.3 and Figure 1.4). Detalied description of the CRISPR-Cas classification can be found in [44, 45].

Class 2

Class 2 consists of all systems where the surveillance complex is a single, multidomain Cas protein, which can cope with the whole interference process. Within this class, there are three types: II, V and VI. In type II the *cas9* is the signature gene, encoding a Cas9 interference protein, which gained huge popularity due to use in genome editing approaches [53] and brought large attention to the CRISPR research field [54, 55, 56]. In contrast to type II, type V is characterized by the *cas12* gene. Despite functional similarities between types II and V, structural differences between Cas9 and Cas12 proteins indicate that these functionalities evolved separately, thus classifying those two types individually [57, 58]. Finally, the *cas13* gene characterizes type VI, which is targeting the RNA exclusively [59].

Class 1

Systems with multiprotein surveillance complexes, called effector complexes, were assigned to class 1, which is divided into the types I, III and IV. In all effector complexes of these types, a Cas7 backbone protein is present in multiple copies and they cover the crRNA spacer sequence. Type I is characterized by the *cas3* signature gene, which encodes a helicase (Cas3) with the ability to unwind Double-Stranded DNA (dsDNA) and DNA-RNA duplexes [60, 61, 62, 63]. The effector complexes in type I are commonly called CRISPR-Associated Complex for Antiviral Defense (Cascade). Type I is the most wide spread in prokaryotes, however, also most diverse type. Recently, type I CRISPR-Cas systems were divided into eight subtypes (I-A to I-F, I-Fv and I-U) [44, 45]. The system which is in the scope of this thesis, is type I-Fv from *Shewanella putrefaciens* CN-32 which is cognate to type I-E from *E. coli* and type I-F (*Pectobacterium atrosepticum*).

Type I-E was found in *E. coli* [64] and it is the best studied among type I systems. The effector complex consists of a 61 nt crRNA, generated from pre-crRNA in a maturation step by a Cas6e protein, and five different Cas proteins with the following stoichiometry: $(Cas7)_6$-$(Cse2)_2$-$(Cse1)_1$-$(Cas5)_1$-$(Cas6e)_1$ [65]. As mentioned before, few, in this case six, copies of Cas7 form

the structural scaffold of the complex holding the crRNA sequence, while Cas5 and Cas6e cover the 5' and 3' ends of the crRNA, respectively. Cse1 (Cas8e), also called a large subunit protein, is involved in PAM recognition and later in Cas3 nuclease recruitment. A small subunit potein (Cse2, Cas11) stabilizes R-loop structure by binding to a non-target DNA strand [66].

Type I-F, present in species like *Pectobacterium atrosepticum*, *Pseudomomnas aureginosa* or *Yersinia pseudotuberculosis*, is similar to type I-E (Figure 1.5a). Cas6f (Csy4) maturates a 60 nt long crRNA [67], stays at its 3' end and initiates Cascade assembly [65, 68]. As for type I-E, six Cas7 (Csy3) proteins shield the crRNA whose 5' end is capped by Cas5 (Csy2). Similarly to Cse1 in I-E, Csy1 performs the target recognition and initiates the interference process [69]. There are, however, some remarkable differences between types I-E and I-F which prevents assigning them to the same type. First, I-F lacks a homologue of the small subunit present in I-E, thus, the Cascade stoichiometry is: $(Cas7)_6$-$(Csy1)_1$-$(Cas5)_1$-$(Cas6f)_1$ [69]. Second, for type I-F Cas3 protein, involved in target degradation, a Cas2-like domain at the N-terminus has been found. This hints at a double role of the Cas3 protein: target degradation and spacer acquisition [69].

Type III consists of systems which contain a *cas10* signature gene and are mainly found in archaea, where they are usually found to be co-existing with type I CRISPR-Cas systems. Similar to type VI, type III systems target RNA [70, 71, 72] although they are also capable to target DNA by utilizing a different Cas protein in their effector complex [73]. Lastly, type IV, with the signature gene *csf1*, also known as *cas8*-like, likewise co-exist together with type I CRISPR systems as they lack the adaptation system [44, 45].

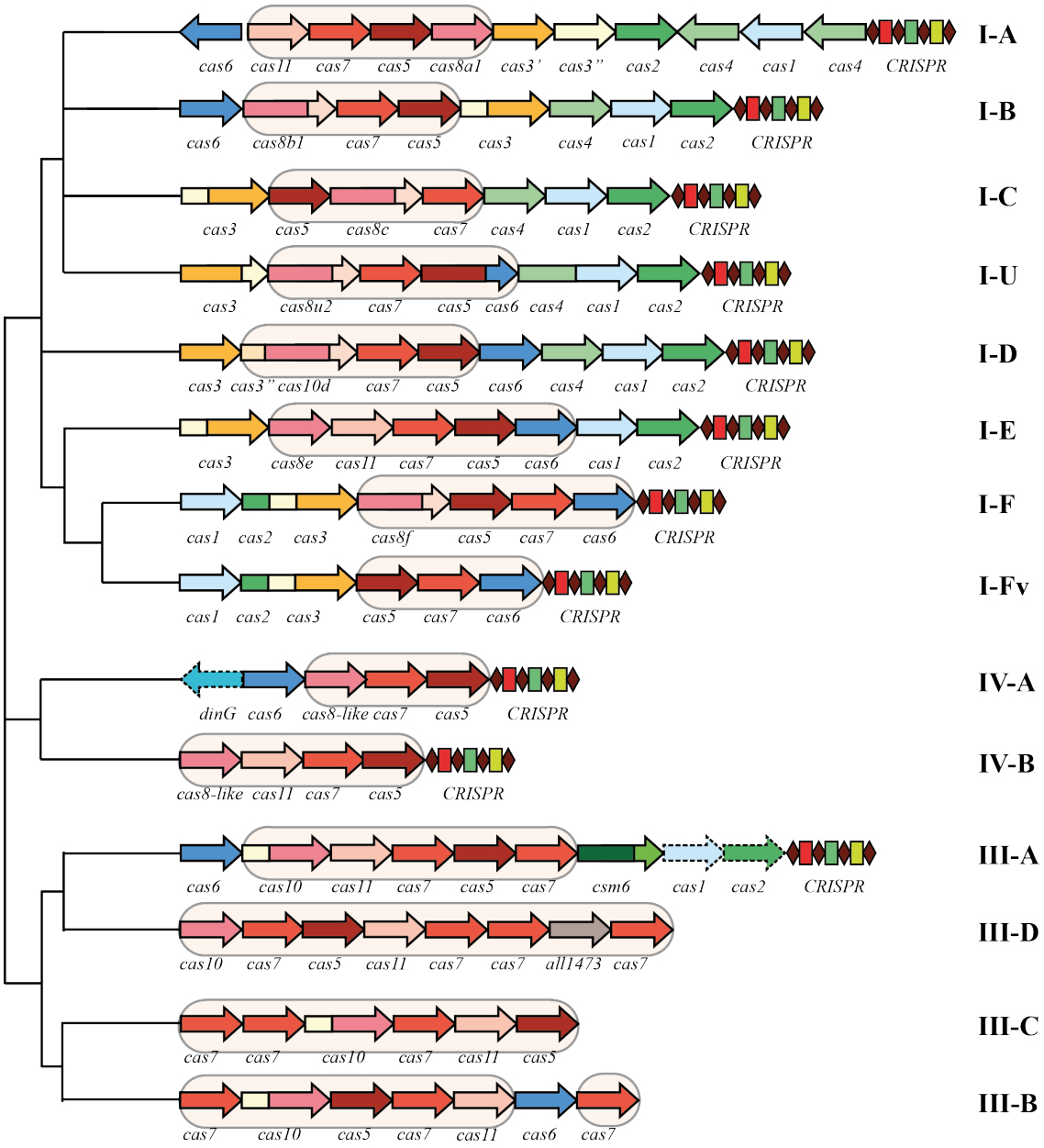

Figure 1.3: Class 1 CRISPR-Cas systems.

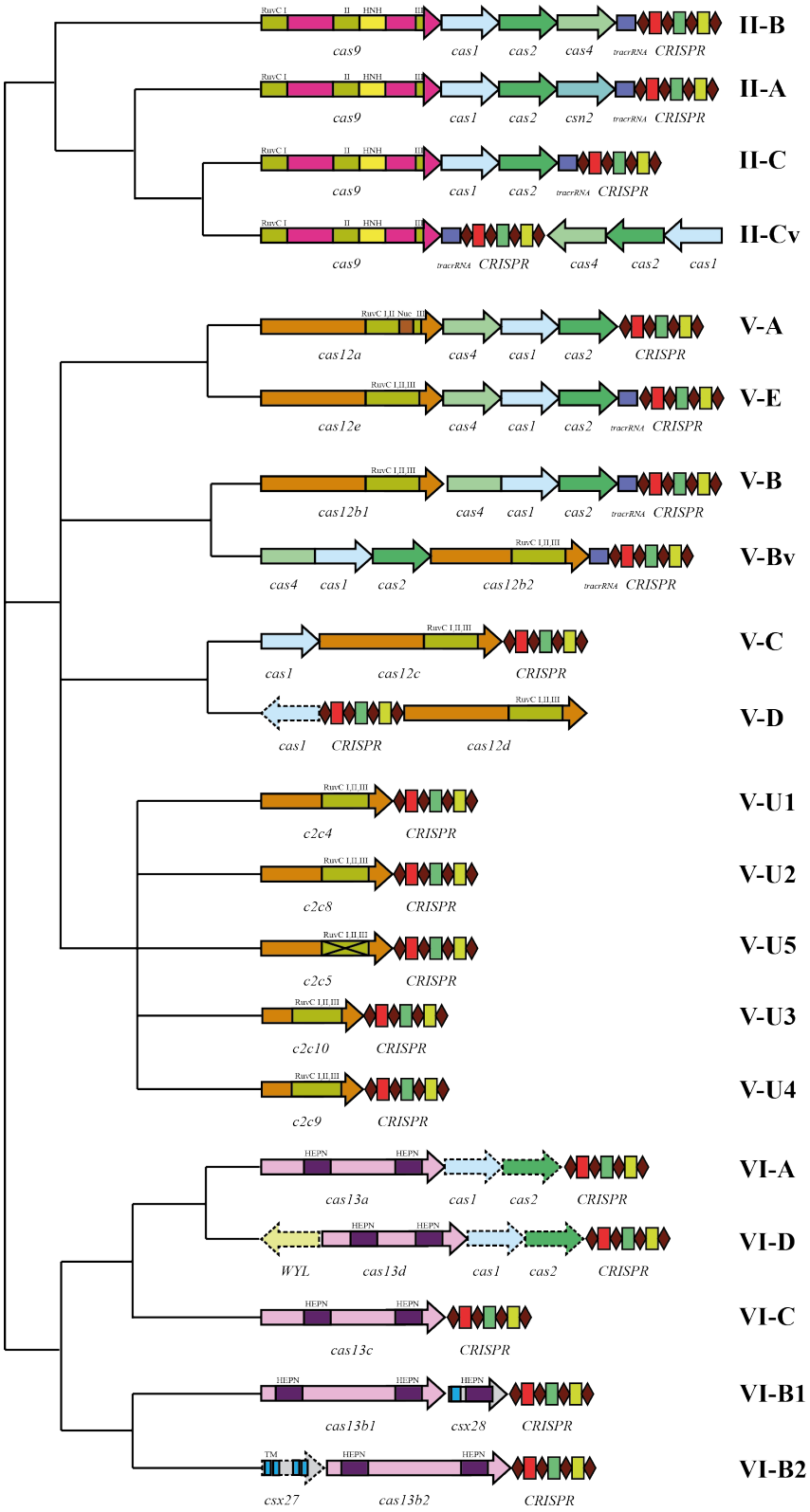

Figure 1.4: Class 2 CRISPR-Cas systems.

1.3.4 CRISPR-Cas Type I-Fv

Initially, the type I-Fv CRISPR-Cas system was found in few beta and gamma-proteobacteria and was characterized in *S. putrefaciens* strain CN-32 [68]. This type possesses a 60 nt crRNA with a 8 nucleotide long 5' repeat, 20 nucleotide long 3' repeat forming a stable loop structure and 32 nucleotide long spacer sequence. It lacks both the small and large subunits (Cas11 and Cas8) (Figure 1.5a) and the amino acid sequences of two proteins show no similarities to other known Cas proteins [68]. Further investigation and characterization of these proteins for their functionality allowed to name them Cas5fv and Cas7fv (Figure 1.5a) [68, 74]. Eventually, X-ray crystallography studies of the type I-Fv revealed that Cas7fv and Cas5fv possess extra domains (compared to Cas7f and Cas5f) which functionally replace Cas11 and Cas8 proteins, respectively. While Cas5fv is involved in PAM recognition, it is remarkable that this recognition process is performed from the DNA major groove side by an alpha-helical (AH) domain, unlike in other systems [75]. Fully functional I-Fv Cascade consists of merely three proteins, with the following stoichiometry $(Cas7fv)_6$-$(Cas5fv)_1$-$(Cas6f)_1$. Type I-Fv contains only five *cas* genes, which makes the I-Fv a minimal type I-F system (Figure 1.5). The process of effector complex assembly is shown in Figure 1.6. Briefly, Cas genes and CRISPR array are expressed from the CRISPR operon, while Cas6f protein maturates the pre-crRNA and stays bound to the 3' end of the crRNA. Later, Cas5fv binds to 5' end of the crRNA and six units of Cas7fv form the backbone structure of the Cascade complex (Figure 1.6).

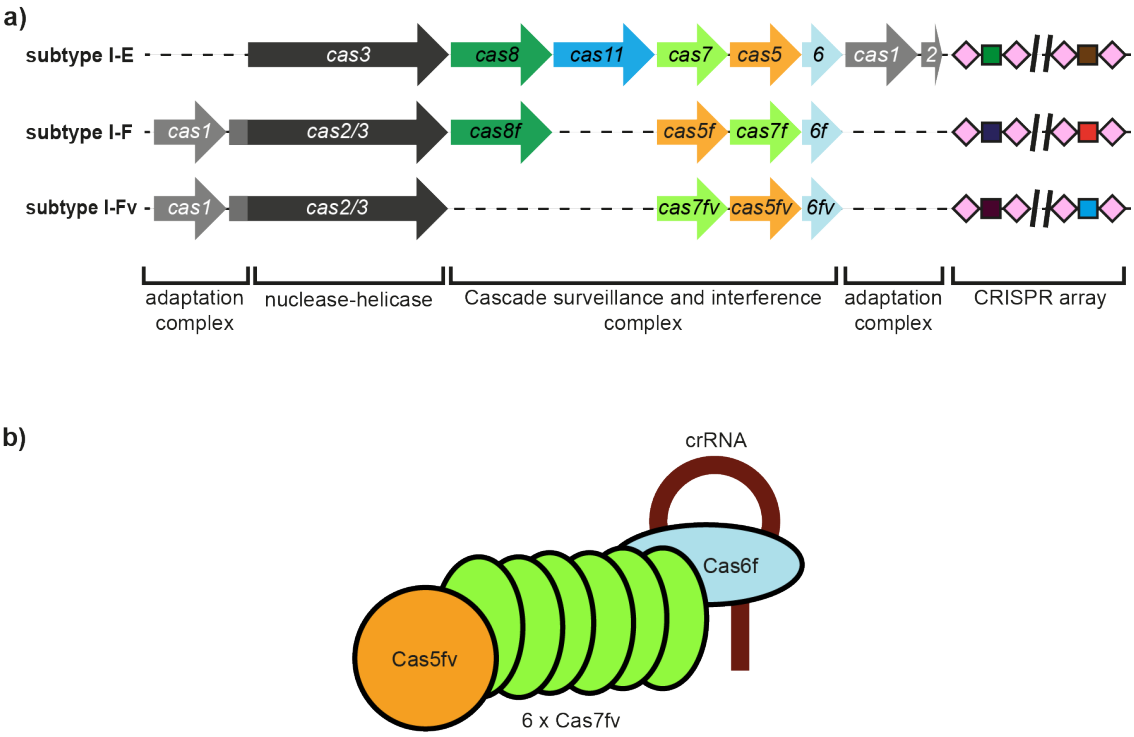

Figure 1.5: (a) Structure and organization of the CRISPR-Cas operons in types I-E, I-F, I-Fv; (b) Cartoon representation of the type I-Fv effector complex.

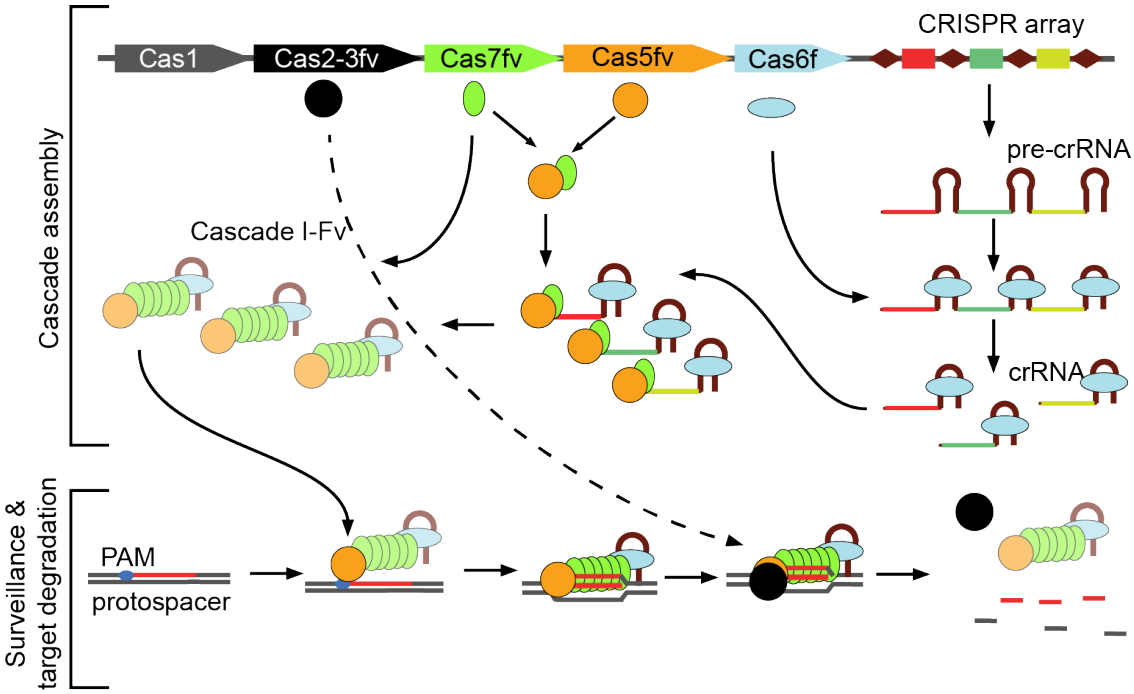

Figure 1.6: Schematic representation of the Cascade I-Fv assembly process (top) and surveillance and interference process (bottom)

1.3.5 *In vitro* Single-Molecule Studies of CRISPR-Cas Systems

Because of the importance of CRISPR-Cas systems to the host organism and their use as precise gene editing tools, CRISPR-Cas systems have nowadays become the target of rigorous study. Next to classic biochemical studies, CRISPR-Cas is also investigated with single-molecule approaches *in vitro*.

Target Search Process

Sternberg and co-workers visualized the real-time DNA interrogation process of a single Cas9 protein by using DNA curtains and showed that the target search process occurs via random 3D diffusion [76]. Similar studies were performed also for the type I-E surveillance complexes from *E. coli* [77] and type V-A Cas12a protein [78]. Redding et al. reported three-dimensional diffusion of Cascades while scanning the DNA, similarly to Cas9, although the authors also speculated lateral diffusion along the DNA upon PAM recognition, which was later confirmed for Cas9 using Single-Molecule Förster Resonance Energy Transfer (smFRET) studies [79] showing that, upon finding a PAM sequence, Cas9 searches neighboring sequences via 1D diffusion [80]. However, Dillard and colleagues recently reported an almost exclusive one-dimensional diffusion of the Cascade I-E from *Thermobifida fusca* even if the surveilled DNA is not an appropriate target [81].

Target Binding, Dynamics and R-loop Formation Processes

Next to the target search process, single-molecule methods, thanks to their sensitivity, allowed to characterize binding events, which occur between CRISPR RNPs and surveilled DNA. Two studies, one using DNA curtains and another using smFRET measurements, revealed that

Cascade can locate targets in a PAM-dependent and PAM-independent manner [77, 82], however PAM presence increases the affinity [77]. When the target is flanked by the PAM sequence, Cas3 is recruited to a Cascade-bound target strand to perform degradation. Nevertheless, if no PAM sequence is present, Cas3 is also recruited to the target in presence of the Cascade, though only if the Cas1-Cas2 complex, required for the primed adaptation, is present and the Cas3 nuclease activity is impaired [77]. Formation of the Primed Acquisition Complex (PAC) consisting of Cas1-Cas2, Cas3 and Cascade was also confirmed by Dillard et al. [81]. Furthermore, in this report it was shown that PAC is capable of displacing different protein roadblocks while Cascade-Cas3 complexes can stall on these roadblocks and lead to double-strand DNA breaks [81].

Redding et al. as well as Blosser et al. [77, 82], showed that the Cascade-DNA complex stability is depending on the spacer-protospacer match ratio (Figure 1.7). Redding and colleagues also demonstrated that upon finding a PAM-flanked target and fully matching the crRNA spacer sequence, the Cascade-protospacer complex is very stable (>57 min, reaching the method limitation), while for targets with a non-full match to crRNA spacer, the interaction time is approximately 25 s. Finally, when the Cascade is probing the DNA, their interaction lasts in the second range [77]. Similarly to that, Blosser et al. [82] showed that long-lived interactions remained irreversible in the timescale of the experiment (approx. 1000 s) and short-lived interactions with 24.8 ± 7.3 s were assigned to R-loop formation which did not progress into a locked state (non-full complementarity spacer vs. protospacer). Additionally, they found 1.6 ± 0.4 s for transient interactions between Cascade and protospacer prior to R-loop formation [82]. Additionally, the Cas9 interrogation process was also studied via smFRET demonstrating that the Cas9-target complex is very stable (> 1 hour) if the target contains less than 12 bp PAM-distal mismatches and stability drops to 0.1-15 s when the number of mismatches is higher. On the other hand, complex stability is strongly disturbed by two PAM-proximal mismatches [83, 84].

Moreover, Szczelkun et al. [85] and Rutkauskas et al. [86] were capable of measuring the R-loop formation rate, its dissolution and also R-loop stability of *Streptococcus thermophilus* Cas9 and Cascade, respectively, using magnetic tweezers [87]. They reported that the PAM presence affects the R-loop formation, but has no influence on the R-loop dissolution. Contrary to that, PAM-distal mismatches have no effect on the R-loop formation, but increase the rate of its dissolution. These results strongly indicate a directional formation of the DNA-RNA duplex between crRNA and protospacer and that the R-loop stability depends on the spacer-protospacer complementarity. Similar conclusions concerning the R-loop stability have been drawn by Lim et al. in their smFRET study [88] and in [89], where they employed Atomic Force Microscopy (AFM) to investigate single Cas9-DNA complexes carrying different crRNA sequences.

In summary, single-molecule studies conducted *in vitro* provided already many insights into the mechanisms of CRISPR-Cas systems, which enabled the direct observation and quantification of different proposed processes: target search and recognition, R-loop formation and stability, formation of the interference and PAC. These findings are essential to understand the concrete working process of the CRISPR molecular machinery, and they also serve as a road sign to perform *in vivo* single-molecule studies. First single-molecule experiments were already conducted *in vivo* for Cas9 in mammalian [90] and *E. coli* cells [91, 92]. Additionally to that, recently similar studies

were published as a preprint for Cascade type I-E [93]. However, up to now, our knowledge about CRISPR-Cas *in vivo* kinetics in class I systems is poorly understood, which indicates this to be a challenging task. One of the tasks of my Ph.D. work was the investigation of the type I-Fv CRISPR-Cas system *in vivo*, using sptPALM methods.

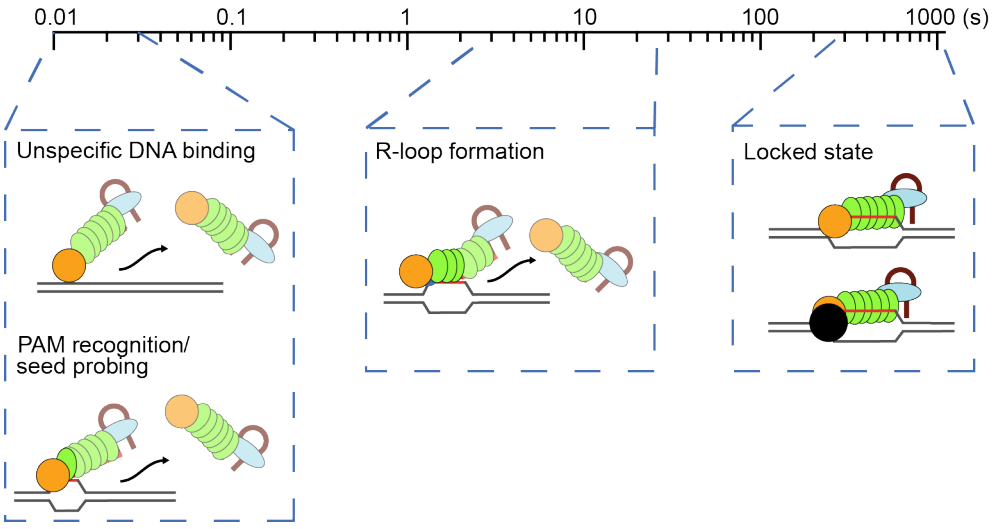

Figure 1.7: Cascade-DNA interactions range from milliseconds to minutes range, when measured *in vitro* [77, 82]. Unspecific DNA binding and PAM recognition last milliseconds. R-loop structure is stable for seconds and then either Cascade unbinds and searches for another target, or, if crRNA-DNA pairing is perfect, Cascade enters a so-called "locked state" and recruits Cas2-3 nuclease.

2 | Developing New Imaging Strategies for (spt)PALM

In this chapter, I will report the development of new imaging strategies. In the first part, I will introduce a new class of pcFPs which we developed for a less phototoxic live-cell imaging, by using a novel photoconversion mechanism (Primed Conversion (PC)). In the second part, I will present a new multi-color, aberration-free imaging strategy, by combining the use of pcFPs and paFPs.

2.1 Live-cell Single-Molecule Imaging With Reduced Phototoxicity

A General Mechanism of Photoconversion of Green-to-Red Fluorescent Proteins Based on Blue and Infrared Light Reduces Phototoxicity in Live-Cell Single-Molecule Imaging

Bartosz Turkowyd, Alexander Balinovic, David Virant, Haruko G. Gölz Carnero, Fabienne Caldana, Marc Endesfelder, Dominique Bourgeois, Ulrike Endesfelder

This part of the thesis is written in the manuscript style and was published in Angewandte Chemie in 2017. I contributed in this work by desiging and performing experiments, analyzing data and by preparing the manuscript text and figures. [94]

Supplementary information to this part are included in Supplementary Materials

Single-Molecule Microscopy

International Edition: DOI: 10.1002/anie.201702870
German Edition: DOI: 10.1002/ange.201702870

A General Mechanism of Photoconversion of Green-to-Red Fluorescent Proteins Based on Blue and Infrared Light Reduces Phototoxicity in Live-Cell Single-Molecule Imaging

*Bartosz Turkowyd[+], Alexander Balinovic[+], David Virant, Haruko G. Gölz Carnero, Fabienne Caldana, Marc Endesfelder, Dominique Bourgeois, and Ulrike Endesfelder**

Abstract: *Photoconversion of fluorescent proteins by blue and complementary near-infrared light, termed primed conversion (PC), is a mechanism recently discovered for Dendra2. We demonstrate that controlling the conformation of arginine at residue 66 by threonine at residue 69 of fluorescent proteins from Anthozoan families (Dendra2, mMaple, Eos, mKikGR, pcDronpa protein families) represents a general route to facilitate PC. Mutations of alanine 159 or serine 173, which are known to influence chromophore flexibility and allow for reversible photoswitching, prevent PC. In addition, we report enhanced photoconversion for pcDronpa variants with asparagine 116. We demonstrate live-cell single-molecule imaging with reduced phototoxicity using PC and record trajectories of RNA polymerase in Escherichia coli cells.*

Photoconvertible fluorescent proteins (pcFPs) irreversibly change their optical properties when illuminated by specific wavelengths. They are key for single-molecule super-resolution imaging,[1] single-molecule tracking[2] and dynamic imaging.[3] Fast maturing and monomeric variants are a common choice in quantitative fluorescence microscopy applications.[4] Among the various fluorescent proteins available, green-to-red pcFPs, that change their fluorescence spectra from GFP- to RFP-type fluorescence upon near-UV illumination, have been particularly popular, owing to their high brightness, photostability, photoconversion contrast and the option for imaging the initial green as well as the converted red form.[1a,b]

Green-to-red pcFPs primarily originate from stony corals of suborder Faviina and in a few cases from closely related soft corals and one corallimorph coral.[5] Improved versions were derived from either naturally green-to-red converting, non-monomeric proteins like Kaede,[6] the Eos family[7] and Dendra2,[8] or from only green fluorescing but monomeric proteins, which were modified into pcFPs like mKikGR[9] and the mMaple[10] and Dronpa families.[11] All green-to-red pcFPs are monophyletically related and exhibit a very similar chromophore structure and neighboring amino acid residues.

Green-to-red pcFPs initially fold into their green form. The chromophores settle in a pH-dependent equilibrium between their neutral (N) and anionic (A) state. Only the anionic chromophore fluoresces upon 488 nm illumination and exhibits a fluorescence maximum in the 500–520 nm range (Figure 1 a, left). 405 nm irradiation mediated photoconversion into the red form occurs from the neutral (non-fluorescent) chromophore state (Figure 1 a, left). While the exact mechanism is still under debate, it was shown to involve the cleavage of the histidine 62 N^{α}–C^{α} bond (numbering according to *Aequorea victoria* GFP) and the formation of a C^{α}–C^{β} double bond in the histidine 62 side chain, which extends the delocalized π-electron system of the His-Tyr-Gly tripeptide chromophore (Figure 1 a (ii)).[12] The anionic state of the red form fluoresces with a maximum in the 570–590 nm range upon 561 nm illumination (Figure 1 a, right). Dendra2 has shown to also photoconvert from its anionic green chromophore when irradiated by 488 nm light, but at a reduced efficiency.[8]

However, a novel switching mechanism, termed primed conversion (PC), using combined illumination at 488 nm and near-infrared light at 700–800 nm has recently shown to be very efficient for Dendra2 although it was poor for mEos2.[13] This mechanism is of particularly high interest for live-cell microscopy, as it avoids phototoxic illumination by 405 nm light.[13–14] The exact mechanism is not yet understood, but pH dependence and 488 nm irradiation hint at an excitation of the anionic green chromophore from which it is "primed" into a millisecond long intermediate state, followed by a conversion into the red chromophore induced by irradiation with near-infrared light[13–14] (Figure 1 a (i)).

As the Anthozoan pcFPs only differ slightly among each other, we were able to identify several amino acid residues which we expected to be critical for PC by systematically comparing their structural characteristics and photophysical behavior as reported in the literature (see Figure S1 a in the Supporting Information).

Of particular interest was residue 69, as it was shown that Dendra2 and mEos2 interchange their photophysical proper-

[*] B. Turkowyd,[+] A. Balinovic,[+] D. Virant, H. G. G. Carnero, F. Caldana, Dr. U. Endesfelder
Department of Systems and Synthetic Microbiology, Max Planck Institute for Terrestrial Microbiology &
LOEWE Center for Synthetic Microbiology (SYNMIKRO)
Karl-von-Frisch-Str. 16, 35043 Marburg (Germany)
E-mail: ulrike.endesfelder@synmikro.mpi-marburg.mpg.de
M. Endesfelder
Institut für Assyriologie und
Ludwig-Maximilians-Universität München
Geschwister-Scholl-Platz 1, 80539 München (Germany)
Dr. D. Bourgeois
Institut de Biologie Structurale, CNRS
Université Grenoble Alpes, CEA, IBS, 38044 Grenoble (France)
[+] These authors contributed equally to this work.
Supporting information and the ORCID identification number(s) for the author(s) of this article can be found under: https://doi.org/10.1002/anie.201702870.

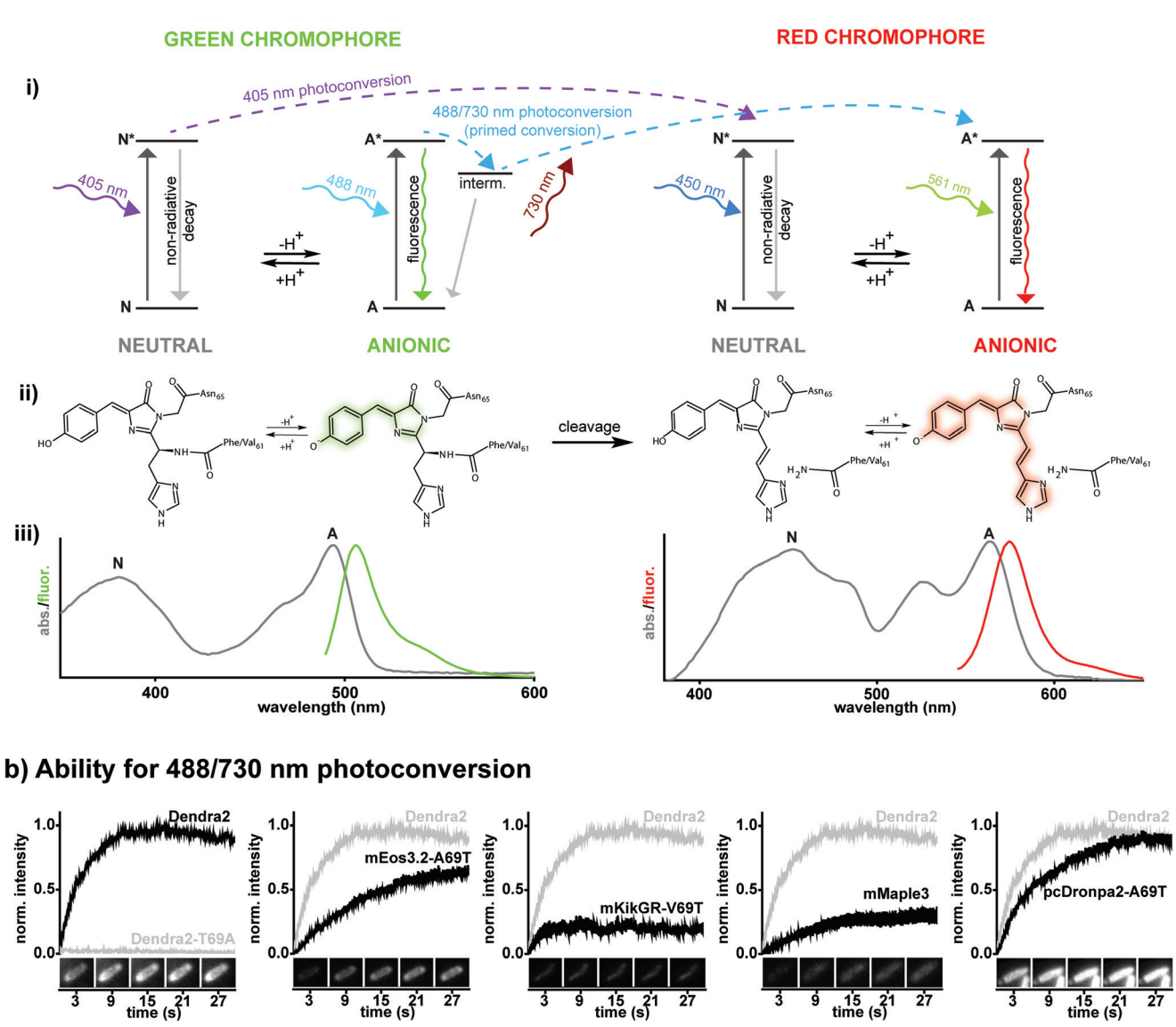

Figure 1. a) Photoconversion of green-to-red pcFPs. The green chromophore of pcFPs absorbs in the near-UV range in its neutral (N) and in the blue range in its anionic (A) form (left, i–iii)). Fluorescence occurs from the excited anionic state (A*) with a maximum at about 500–520 nm (left, colored in green). A light-induced cleavage of the fluorophore backbone extends the chromophore which then absorbs in the blue range in its neutral and in the green/orange range in its anionic form. The latter emits orange/red fluorescence in the range of 570–590 nm (right, colored in red). UV-light mediated photoconversion (violet dashed arrow) starts from the neutral state, whereas PC (blue dashed arrows) originates from the anionic form which can be "primed" into a millisecond long intermediate state. By additional irradiation with near-infrared 730 nm light, the chromophore is converted into its red form. b) 488/730 nm photoconversion ability of pcFPs from different protein families. Protein variants of different families were irradiated by 488/730 nm to characterize their ability to undergo PC by measuring the increase in red fluorescence. Insets show the fluorescence increase of transiently overexpressed free pcFPs upon 488/730 illumination in single *Escherichia coli* cells.

ties (i.e. their brightness, photoblinking and -bleaching behavior) when transposing residue 69 in the variants mEos2-A69T and Dendra2-T69A.[15] Crystal structures reveal that this can be explained by the altered conformation of arginine 66 which interacts with the chromophore and glutamate 212.[15] The latter is responsible for redox-induced photobleaching by decarboxylation.[15] We thus tested mEos2-A69T for PC which indeed efficiently photoconverts under 488/730 nm light, while Dendra2-T69A does not (Figure S1 b (i)).

We then generated threonine 69 variants for several pcFPs (Table S1) and found them capable of PC while their originals (with alanine or valine 69) were not (Figure 1 b, Figure S1 b). The mMaple family, which already contains threonine 69, naturally shows PC (Figure 1 b).

When investigating the properties of the threonine 69 pcFPs variants, we found them to exhibit a lower extinction coefficient and a hypsochromic shift of absorption and emission maxima of about 10 nm, compared to the alanine or valine 69 variants (Table 1, Table S2). Their pK_a values are

Table 1: Properties of green-to-red pcFPs capable of PC.[a]

Name	Genetic background	λ_{exc} [nm]	λ_{em} [nm]	oligomeric state	ε [$M^{-1}cm^{-1}$]	Φ	pK_a	$k_{488/730nm}$ [$10^{-2}s^{-1}$]	rel. photon counts	$t_{0.5\%int}$ [s]	opt. pH_{405}	opt. $pH_{488/730}$	Ref.
Dendra2	Dendra A224V	490[a]/ 553[a]	507[a]/ 573[a]	m	33300[a]/ 17300[a]	0.53[a]/ 0.74[a]	7.5[a]/ 7.9[a]	21.3	1	1/1	8	8.5–10	[a],[15] this work
mMaple	mClavGR2 220-224 HSGLP to RNSTD and A145V G171S G225S	489[b]/ 566[b]	505[b]/ 583[b]	m	15000[b]/ 30000[b]	0.74[b]/ 0.56[b]	8.2[b]/ 7.3[b]	11.6	ND	4.0/ 1.2	7–8	8.5–9	[b],[10a] this work
mMaple3	mMaple I111N Y198A E82R D83K D197K	489[b]/ 566[b]	505[b]/ 583[b]	m	74000/ ND	ND	7.9/ 7.2	5.5	1.5	3.3/ 1.4	7–8	8–10	[b],[10b] this work
mMaple3-V157I	mMaple3 V157I	490/ 570	505/ 582	m	28000/ ND	ND	8.2/ 7.8	3.3	ND	2.4/ 2.0	6–8	8.5–10	this work
mEos2-A69T	EosFP N11K E70K A69T H74N H121Y	495[a]/ 565[a]	509[a]/ 580[a]	m	24300[a]/ 11500[a]	0.87[a]/ 0.66[a]	8.2[a]/ 7.4[a]	9.4	ND	3.4/ 1.1	6–8	8.5–10	[a],[15] this work
mEos3.2-A69T	mEos2 A69T I102N H158E Y189A	494/ 562	507/ 573	m	44000/ ND	ND	6.7/ 6.7	7.7	1.2	3.8/ 1.5	6–8	7.5–10	this work
mEos4b-V69T	mEos4b V69T	494/ 562	505/ 581	m	50000/ ND	ND	7.7/ 7.1	6.2	1.1	3.0/ 0.5	6–8	8–10	this work
pcDronpa-A69T	Dronpa V60A C62H A69T N94S N102I E218G	494[c]	507[c]	t	34000[c]	0.82[c]	8.0[c]	7.9	ND	1.0/ 3.1	6–7	8–10	[c],[11b] this work
pcDronpa2-A69T	pcDronpa Y116N A69T	494/ 564	506/ 575	t	51000/ ND	ND	8.6/ 7.9	16.2	1.2	1.9/ 0.9	6–8	8–10	this work
mKikGR-V69T	mKikGR V69T	492/ 570	506/ 580	m	ND	ND	8.2/ 7.2	19.5	ND	4.8/ 0.3	7–7.5	8.5–10	this work

[a] Table summarizing the properties of green-to-red pcFPs which can by photoconverted by 488/730 nm illumination. Listed are their key photophysical properties with λ_{exc}—excitation wavelength; λ_{em}—emission wavelength; ε—molar extinction coefficient at pH 7.5; Φ—fluorescence quantum yield; $k_{488/730nm}$—photoconversion rate for ensemble measurements at pH 8 (Figure S3); relative photon counts of fluorescence spots in single molecule experiments in relation to Dendra2 (Figure S8) and $t_{0.5\%int}$—time of 50% intensity loss when irradiated by 488 nm or 561 nm light, respectively at pH 7.5 in relation to Dendra2 (Figure S3e). Furthermore, their genetic background, oligomeric state (m—monomeric; t—tetrameric), the pKa values of the chromophores (Figure S2) as well as the optimal pH for 405 nm and 488/730 nm light-mediated photoconversion are given (Figure S3). Values are either from the literature as labeled or were measured in this study. ND—not determined.

higher as the imidazolinone moiety of the chromophore is no longer stabilized by the repositioned arginine 66 residue (Figure S1c(i), Figure S2). These findings are consistent with reported data.[11b,15]

The PC rate, as measured for Dendra2, increases with the applied laser intensities, but the PC efficiency drops at higher 488 nm intensities, probably due to photobleaching (Figure S3a,b). 405 nm-mediated photoconversion generally dominates the lower and PC the higher pH range (Figure S3c). This can be related to the ratio of near-UV light absorbing neutral chromophores and blue light absorbing anionic ones dependent on the pK_a value of the hydroxyphenyl group of the chromophore. We do not, however, find a one-to-one correlation. In agreement with previous studies, the rate of conversion instead seems to be determined by the local pK_a values of several residues close to the chromophore which form an internal charge network and are directly involved in the photoconversion mechanism.[11b,16]

To investigate the intermediate state possibly induced by 488 nm irradiation and suspected to be the entry point for 730 nm mediated photoconversion in Dendra2,[13] we probed its expected half-life in threonine 69 pcFPs by delaying the conversion laser by 0–30 ms in relation to the 488 nm laser pulse. In all FPs, the attained fluorescence intensity of the converted fluorophores decreased exponentially when prolonging the delay and was consistent with a 4–5 ms half-life of the intermediate state (Figure S4).

An advantage of all threonine 69 variants is an increased photostability, as we found their loss of fluorescence to be significantly slower for both their green and red form, enabling longer imaging times (Table 1 and Figure S3d). Furthermore, they also convert to some extent when using 640 nm instead of 730 nm light and under 488 nm light only (Figure S3e). For 640 nm illumination, this reduces efficiency by 55–75% but it makes them, like Dendra2,[17] accessible to fluorescence microscopes equipped with a red laser source.

We then investigated whether mutations that introduce chromophore flexibility and allow for *cis–trans* isomerization may interfere with the PC mechanism, as reversible off-switching from the fluorescent *cis*- to the non-planar, dark *trans*-isoform is facilitated by 488 nm illumination.[16a,18] For reversible photoswitching NijiFP (=Dendra2-F173S) and Dendra2-M159A we did not observe any 488/730 nm mediated photoconversion (Figure S1b(ii), c(ii)).

We hypothesized that the inability of mKikGR-V69T, mMaple and mMaple3 to undergo efficient PC (Figure 1b, Figure S3c(iii,iv)) is related to valine 157 and a possibly twisted or *trans*-chromophore dark state.[19] As mMaple3 is a monomeric, bright fluorophore and thus a good choice for super-resolution studies (Figure S8), we constructed

mMaple3-V157I. Unfortunately, mMaple3-V157I lost fluorescence brightness. However, the comparatively high ratio between the maximal red fluorescence intensities attained by 488/730 nm and 405 nm conversion, respectively suggests a higher PC efficiency for the mutant (Figure S3 c (iii)).

As all photoswitching GFP-type FPs[11b,19a,c,20] and also the green forms of mEos2 and Dendra2[15–16] are reported to enter temporary, UV-reversible dark states upon 488 nm illumination, we measured the liability of all pcFPs to do so and compared the results to their ability to undergo PC. We found the green fluorescence of all pcFPs to decrease significantly under extended moderate 488 nm illumination (Figure S5). Subsequent UV illumination restored 60–100 % of the lost intensity, demonstrating that a large fraction of pcFPs had entered reversible dark states (Figure S5 b). Remarkably, the fluorescence of all pcFPs not capable of PC rapidly dropped to the background level, whereas all FP variants that can undergo PC decayed more slowly and retained significant fluorescence after 60 s of 488 nm illumination (Figure S5). As the recovery was equal or larger for non-PC-converting pcFPs, this difference cannot be explained by increased photobleaching or -conversion of the latter (Figure S5). Instead, the experiment suggests an increased tendency for non-PC-converting pcFPs to enter seconds to minutes long, by 405 nm-light reversible dark states which also relates to the observed difference in photostability (Figure S3 d).

We then focused on the residues close to the chromophore which are described to be involved in UV-light mediated photoconversion.[12] pcDronpa-A69T possesses tyrosine 116, a position identified as critical for enhanced photoconversion,[11b,12d,21] and has been reported as non-converting under 405 nm illumination.[11b] We wondered whether pcDronpa-A69T may photoconvert under 488/730 nm light and indeed found moderately effective PC (Figure S1 b (iii), c (iii), Figure S3 c (v)). We then mutated tyrosine 116 to asparagine, a common amino acid for efficiently converting pcFPs, which significantly improved PC and restored 405 nm photoconversion (Figure 1 b).

For Dendra2, the only pcFP exhibiting PC with glutamine 116 (Figure S1 a,c (iii)), we generated Q116N and Q116Y mutants. We hypothesized that changes to the charge network surrounding the Dendra2 chromophore (S105/Q116), which differs from all other pcFPs (N105/N116), would affect the photoconversion capability. Indeed, the mutants neither showed UV- nor PC photoconversion but displayed photoswitching dynamics comparable to only UV-converting pcFPs (Figure S5). A further mutation to Dendra2-S105N-Q116N mimics the N105/N116 network and restored photoconversion, but at a significantly lower level than for Dendra2 (Figure S1 b (iii)). This might hint at a reduced chromophore stability of the mutant.

In conclusion, the ability of pcFPs to undergo PC critically depends on threonine 69 which controls the conformation of arginine 66. A short, milliseconds long intermediate state appears to be the entry point into the PC mechanism. PC appears to be in direct competition with the FP′s tendency to photoswitch into a long-lasting dark state reversible by 405 nm light (Figure S6). This explains the immediate dependency of PC on the conformation of arginine 66[15] as well as the (partial) suppression of PC in NijiFP, Dendra2-M159A or the Eos proteins with alanine 69 as well as mKikGR-V69T and the mMaple family. Changes to the amino acid network known to be involved in the UV-light mediated photoconversion process seem to affect PC and UV conversion efficiency equally, suggesting similar charge transfer processes inducing the backbone cleavage. However, as in the case of pcDronpa-A69T, (moderately efficient) PC might be possible when UV conversion is not.

Finally, we tested whether the new pcFPs can be applied advantageously in single-particle tracking photoactivated localization microscopy (sptPALM).[22] sptPALM imaging typically involves irradiation of the probe by 405 nm light for FP photoconversion and 561 nm light for fluorescence read-out. We investigated whether PC, involving 488/730 nm instead of 405 nm irradiation, might reduce photoinduced damages to the probe which primarily depend on the applied laser intensity and wavelength.[23] We recorded single-molecule trajectories (i.e. individual molecules traced through several images) of RNA polymerases tagged with Dendra2 in living *Escherichia coli* cells under common sptPALM conditions and monitored their growth before and after sptPALM imaging by recording brightlight movies for several hours (Figure 2 a and Videos S1–6). Cells, for which the single-molecule dynamics were recorded over 6 minutes using PC-photoconversion, resembled control cells which were only irradiated by the 561 nm read-out laser for the same period. Both exhibited a high percentage of cells which continue to grow normally. Cells whose single-molecule dynamics were imaged by 405 nm photoconversion showed an already significantly reduced cell survival after only 4 minutes of sptPALM imaging and a significant fraction of cells which paused their growth for 2–3 hours (Figure 2 b and Videos S1–6). For PC experiments, the continuous 561 nm read-out turned out to be the most limiting factor for cell viability. The impact of its accumulating illumination dose becomes severe after 8 minutes of sptPALM imaging at critical doses similar to doses observed before.[23]

We then assessed the quality of the sptPALM data. PC yielded more trajectories at slightly lower conversion intensity whereas the obtained trajectory lengths and spot intensities for both modes were comparable (Figure S7). Even though 405 nm irradiation caused growth delay and death in many cells, the observed RNA polymerase dynamics did not deviate from cells measured using PC and were similar to previously reported statistics:[24] on average, 70 % of RNA polymerases appeared to be actively transcribing, 27 % to be mostly DNA-bound and about 3 % diffused freely (Figure S7).

We then measured the apparent single-molecule brightness for all PC-converting FPs by preparing single-molecule surfaces (Figure S8). The threonine 69 variants showed slightly decreased photon counts, for example, Dendra2-T69A was about 20 % brighter than Dendra2. mMaple3 displayed the highest photon count being 30 % brighter than Dendra2 but its PC efficiency on the single-molecule level was, like in ensemble measurements, low (data not shown) which largely disqualifies it from quantitative imaging purposes using PC.

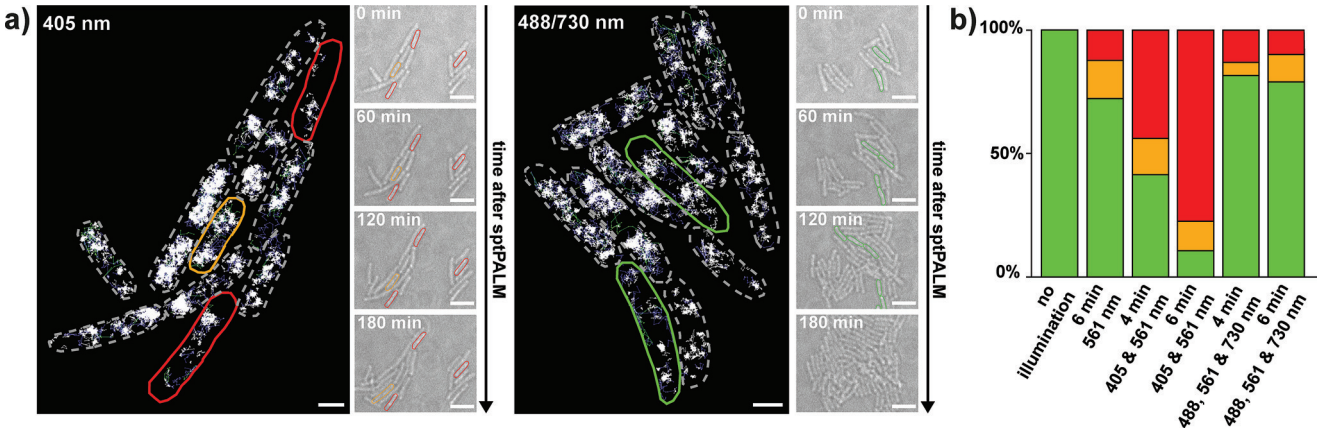

Figure 2. Phototoxicity of 488/730 and 405 nm photoconversion in sptPALM experiments in living *Escherichia coli* cells when imaging Dendra2-tagged RNA polymerase dynamics. a) Trajectories of single RNA polymerase molecules obtained over 6 minutes of sptPALM imaging. Trajectories are color coded by their apparent diffusion coefficient D: 0.0–0.15 $\mu m^2 s^{-1}$ (white), 0.15–0.8 $\mu m^2 s^{-1}$ (blue), larger than 0.8 $\mu m^2 s^{-1}$ (green). Cell shapes are marked by dashed outlines, solid outlines (red dead, orange paused, green undisturbed) highlight exemplary cells which are also marked in the brightlight images depicting cell growth after sptPALM over several hours (right, and Videos S1–6). Scale bars 1 µm (sptPALM), 5 µm (brightlight). b) Cell viability after sptPALM experiments. Controls were not illuminated by any laser or for 6 minutes by 561 nm laser light only. sptPALM experiments of 4 and 6 minutes were conducted using either 405 nm or 488/730 nm irradiation (Materials and Methods). Cellular growth of the imaged areas was monitored by brightlight imaging and evaluated for cell viability. Green bars mark the fraction of cells growing without any visible effects, orange bars represent cells which paused their growth for 2–3 hours and red bars mark cells with no detectable growth until the end of the experiment after 8 hours. $n = 368$ cells.

In summary, PC can be enabled for all green-to-red pcFP families by generating threonine 69 variants. Dendra2, pcDronpa2-A69T and the Eos family exhibit efficient PC, whereas mKikGR and mMaple variants only show reduced efficiency. As pcDronpa2-A69T is efficiently photoconverted by both modes and offers the highest quantum yield of all considered pcFPs, it is an interesting FP for future studies. However, its tetrameric behavior considerably limits its usefulness in practice.[10b] We therefore recommend the use of mEos3.2-A69T or Dendra2, which also show good performance. We predict that threonine 69 variants of other pcFPs like Kaede or calcium sensors based on Eos (CamPARI[25]) and mMaple (GR-GECOs[26]) will also exhibit PC. Even though our efforts to improve PC efficiencies and fluorescence brightness by modifying residues 105/116 of Dendra2 and 157 of mMaple3 proved unsuccessful, we believe that different strategies, for example, suppressing the transition into the dark states, might yield more favorable results. For example, a promising route could be to systematically modify other important amino acids like serine 142 or histidine 194. Furthermore, to advance live-cell compatibility, proteins converting and emitting at longer wavelengths would be especially desirable, which immediately raises the question if PC-like mechanisms can be transferred to FPs absorbing these wavelengths, for example, psmOrange[27] or new pcFPs found/designed in future studies.

Acknowledgements

We thank V. Adam, IBS Grenoble, France, S. Wang and X. Zhuang, Harvard University, US and P. Dedecker, Leuven University, Belgium for kindly sharing their fluorescent protein plasmids. This work was funded by the Max Planck Society, SYNMIKRO and the Fonds der Chemischen Industrie.

Conflict of interest

The authors declare no conflict of interest.

Keywords: fluorescent proteins · live-cell microscopy · phototoxicity · primed conversion · single-molecule microscopy

How to cite: *Angew. Chem. Int. Ed.* **2017**, *56*, 11634–11639
Angew. Chem. **2017**, *129*, 11792–11798

[1] a) K. Nienhaus, G. U. Nienhaus, *Chem. Soc. Rev.* **2014**, *43*, 1088–1106; b) E. A. Rodriguez, R. E. Campbell, J. Y. Lin, M. Z. Lin, A. Miyawaki, A. E. Palmer, X. Shu, J. Zhang, R. Y. Tsien, *Trends Biochem. Sci.* **2017**, *42*, 111–129; c) B. Turkowyd, D. Virant, U. Endesfelder, *Anal. Bioanal. Chem.* **2016**, *408*, 6885–6911.
[2] a) L. Cognet, C. Leduc, B. Lounis, *Curr. Opin. Chem. Biol.* **2014**, *20*, 78–85; b) A. Gahlmann, W. E. Moerner, *Nat. Rev. Microbiol.* **2014**, *12*, 9–22.
[3] I. Nemet, P. Ropelewski, Y. Imanishi, *Photochem. Photobiol. Sci.* **2015**, *14*, 1787–1806.
[4] a) S. H. Lee, J. Y. Shin, A. Lee, C. Bustamante, *Proc. Natl. Acad. Sci. USA* **2012**, *109*, 17436–17441; b) D. Lando, U. Endesfelder, H. Berger, L. Subramanian, P. D. Dunne, J. McColl, D. Klenerman, A. M. Carr, M. Sauer, R. C. Allshire, M. Heilemann, E. D. Laue, *Open Biol.* **2012**, *2*, 120078; c) E. M. Puchner, J. M. Walter, R. Kasper, B. Huang, W. A. Lim, *Proc. Natl. Acad. Sci. USA* **2013**, *110*, 16015–16020.
[5] N. O. Alieva, K. A. Konzen, S. F. Field, E. A. Meleshkevitch, M. E. Hunt, V. Beltran-Ramirez, D. J. Miller, J. Wiedenmann, A. Salih, M. V. Matz, *PLoS One* **2008**, *3*, e2680.

[6] R. Ando, H. Hama, M. Yamamoto-Hino, H. Mizuno, A. Miyawaki, *Proc. Natl. Acad. Sci. USA* **2002**, *99*, 12651 – 12656.
[7] a) S. A. McKinney, C. S. Murphy, K. L. Hazelwood, M. W. Davidson, L. L. Looger, *Nat. Methods* **2009**, *6*, 131 – 133; b) M. Zhang, H. Chang, Y. Zhang, J. Yu, L. Wu, W. Ji, J. Chen, B. Liu, J. Lu, Y. Liu, J. Zhang, P. Xu, T. Xu, *Nat. Methods* **2012**, *9*, 727 – 729; c) M. G. Paez-Segala, M. G. Sun, G. Shtengel, S. Viswanathan, M. A. Baird, J. J. Macklin, R. Patel, J. R. Allen, E. S. Howe, G. Piszczek, H. F. Hess, M. W. Davidson, Y. Wang, L. L. Looger, *Nat. Methods* **2015**, *12*, 215 – 218.
[8] D. M. Chudakov, S. Lukyanov, K. A. Lukyanov, *Biotechniques* **2007**, *42*, 553.
[9] S. Habuchi, H. Tsutsui, A. B. Kochaniak, A. Miyawaki, A. M. van Oijen, *Plos One* **2008**, *3*, e3944.
[10] a) A. L. McEvoy, H. Hoi, M. Bates, E. Platonova, P. J. Cranfill, M. A. Baird, M. W. Davidson, H. Ewers, J. Liphardt, R. E. Campbell, *PLoS One* **2012**, *7*, e51314; b) S. Wang, J. R. Moffitt, G. T. Dempsey, X. S. Xie, X. Zhuang, *Proc. Natl. Acad. Sci. USA* **2014**, *111*, 8452 – 8457.
[11] a) R. Ando, H. Mizuno, A. Miyawaki, *Science* **2004**, *306*, 1370 – 1373; b) B. Moeyaert, N. Nguyen Bich, E. De Zitter, S. Rocha, K. Clays, H. Mizuno, L. van Meervelt, J. Hofkens, P. Dedecker, *ACS Nano* **2014**, *8*, 1664 – 1673.
[12] a) K. Nienhaus, G. U. Nienhaus, J. Wiedenmann, H. Nar, *Proc. Natl. Acad. Sci. USA* **2005**, *102*, 9156 – 9159; b) I. Hayashi, H. Mizuno, K. I. Tong, T. Furuta, F. Tanaka, M. Yoshimura, A. Miyawaki, M. Ikura, *J. Mol. Biol.* **2007**, *372*, 918 – 926; c) H. Tsutsui, H. Shimizu, H. Mizuno, N. Nukina, T. Furuta, A. Miyawaki, *Chem. Biol.* **2009**, *16*, 1140 – 1147; d) H. Kim, T. Zou, C. Modi, K. Dorner, T. J. Grunkemeyer, L. Chen, R. Fromme, M. V. Matz, S. B. Ozkan, R. M. Wachter, *Structure* **2015**, *23*, 34 – 43.
[13] W. P. Dempsey, L. Georgieva, P. M. Helbling, A. Y. Sonay, T. V. Truong, M. Haffner, P. Pantazis, *Nat. Methods* **2015**, *12*, 645 – 648.
[14] M. A. Mohr, P. Argast, P. Pantazis, *Nat. Protoc.* **2016**, *11*, 2419 – 2431.
[15] R. Berardozzi, V. Adam, A. Martins, D. Bourgeois, *J. Am. Chem. Soc.* **2016**, *138*, 558 – 565.
[16] a) V. Adam, B. Moeyaert, C. C. David, H. Mizuno, M. Lelimousin, P. Dedecker, R. Ando, A. Miyawaki, J. Michiels, Y. Engelborghs, J. Hofkens, *Chem. Biol.* **2011**, *18*, 1241 – 1251; b) H. Kim, T. J. Grunkemeyer, C. Modi, L. Chen, R. Fromme, M. V. Matz, R. M. Wachter, *Biochemistry* **2013**, *52*, 8048 – 8059.
[17] N. V. Klementieva, K. A. Lukyanov, N. M. Markina, S. A. Lukyanov, E. V. Zagaynova, A. S. Mishin, *Chem. Commun.* **2016**, *52*, 13144 – 13146.
[18] V. Adam, M. Lelimousin, S. Boehme, G. Desfonds, K. Nienhaus, M. J. Field, J. Wiedenmann, S. McSweeney, G. U. Nienhaus, D. Bourgeois, *Proc. Natl. Acad. Sci. USA* **2008**, *105*, 18343 – 18348.
[19] a) A. C. Stiel, S. Trowitzsch, G. Weber, M. Andresen, C. Eggeling, S. W. Hell, S. Jakobs, M. C. Wahl, *Biochem. J.* **2007**, *402*, 35 – 42; b) M. Andresen, A. C. Stiel, J. Folling, D. Wenzel, A. Schonle, A. Egner, C. Eggeling, S. W. Hell, S. Jakobs, *Nat. Biotechnol.* **2008**, *26*, 1035 – 1040; c) R. Ando, C. Flors, H. Mizuno, J. Hofkens, A. Miyawaki, *Biophys. J.* **2007**, *92*, L97 – L99.
[20] H. Chang, M. Zhang, W. Ji, J. Chen, Y. Zhang, B. Liu, J. Lu, J. Zhang, P. Xu, T. Xu, *Proc. Natl. Acad. Sci. USA* **2012**, *109*, 4455 – 4460.
[21] S. F. Field, M. V. Matz, *Mol. Biol. Evol.* **2010**, *27*, 225 – 233.
[22] S. Manley, J. M. Gillette, J. Lippincott-Schwartz, *Methods Enzymol.* **2010**, *475*, 109 – 120.
[23] S. Wäldchen, J. Lehmann, T. Klein, S. van de Linde, M. Sauer, *Sci. Rep.* **2015**, *5*, 15348.
[24] a) U. Endesfelder, K. Finan, S. J. Holden, P. R. Cook, A. N. Kapanidis, M. Heilemann, *Biophys. J.* **2013**, *105*, 172 – 181; b) M. Stracy, C. Lesterlin, F. Garza de Leon, S. Uphoff, P. Zawadzki, A. N. Kapanidis, *Proc. Natl. Acad. Sci. USA* **2015**, *112*, E4390 – E4399.
[25] B. F. Fosque, Y. Sun, H. Dana, C. T. Yang, T. Ohyama, M. R. Tadross, R. Patel, M. Zlatic, D. S. Kim, M. B. Ahrens, V. Jayaraman, L. L. Looger, E. R. Schreiter, *Science* **2015**, *347*, 755 – 760.
[26] H. Hoi, T. Matsuda, T. Nagai, R. E. Campbell, *J. Am. Chem. Soc.* **2013**, *135*, 46 – 49.
[27] O. M. Subach, G. H. Patterson, L. M. Ting, Y. Wang, J. S. Condeelis, V. V. Verkhusha, *Nat. Methods* **2011**, *8*, 771 – 777.

Manuscript received: March 20, 2017
Revised manuscript received: April 27, 2017
Accepted manuscript online: June 2, 2017
Version of record online: July 17, 2017

2.2 Aberration-Free, Live-Cell Compliant Multi-Color Single-Molecule Localization Microscopy Imaging

Combining Primed Photoconversion and UV-Photoactivation for Aberration-Free, Live-Cell Compliant Multi-Color Single-Molecule Localization Microscopy Imaging

David Virant, Bartosz Turkowyd, Alexander Balinovic, Ulrike Endesfelder

This part of the thesis is written in the manuscript style and was published in International Journal of Molecular Sciences in 2017. I contributed in this work by desiging and performing experiments, analyzing data and by preparing the manuscript text and figures. [95]

Supplementary information to this part are included in Supplementary Materials

International Journal of
Molecular Sciences

MDPI

Article

Combining Primed Photoconversion and UV-Photoactivation for Aberration-Free, Live-Cell Compliant Multi-Color Single-Molecule Localization Microscopy Imaging

David Virant, Bartosz Turkowyd, Alexander Balinovic and Ulrike Endesfelder *

Department of Systems and Synthetic Microbiology, Max Planck Institute for Terrestrial Microbiology & LOEWE Center for Synthetic Microbiology (SYNMIKRO), Karl-von-Frisch-Str. 16, 35043 Marburg, Germany; david.virant@synmikro.mpi-marburg.mpg.de (D.V.); bartosz.turkowyd@synmikro.mpi-marburg.mpg.de (B.T.); alexander.balinovic@synmikro.mpi-marburg.mpg.de (A.B.)

* Correspondence: ulrike.endesfelder@synmikro.mpi-marburg.mpg.de; Tel.: +49-6421-28-21619

Received: 11 June 2017; Accepted: 5 July 2017; Published: 14 July 2017

Abstract: Super-resolution fluorescence microscopy plays a major role in revealing the organization and dynamics of living cells. Nevertheless, single-molecule localization microscopy imaging of multiple targets is still limited by the availability of suitable fluorophore combinations. Here, we introduce a novel imaging strategy which combines primed photoconversion (PC) and UV-photoactivation for imaging different molecular species tagged by suitable fluorescent protein combinations. In this approach, the fluorescent proteins can be specifically photoactivated/-converted by different light wavelengths using PC and UV-activation modes but emit fluorescence in the same spectral emission channel. We demonstrate that this aberration-free, live-cell compatible imaging method can be applied to various targets in bacteria, yeast and mammalian cells and can be advantageously combined with correlative imaging schemes.

Keywords: multi-color imaging; primed conversion; live cell imaging; single-molecule localization microscopy

1. Introduction

Over the past decade, rapid advances in single-molecule localization microscopy (SMLM) techniques have created a large, quantitative imaging toolbox which allows for the direct observations of molecular processes of life at the nanometer scale [1–3]. Part of its tremendous impact is owed to the fact that, just like in conventional fluorescence microscopy, individual species of molecules can be visualized and placed into context to each other by specific fluorescence tags in situ as well as in vivo.

Nowadays, multi-color SMLM imaging is frequently performed. However, while several approaches for multi-color SMLM imaging in fixed cells have been optimized for ideal combinations of bright fluorophores with complementary staining (e.g., antibody, nanobody or protein-tag stainings), similar photoswitching requirements and distinct read-out, the choice of fluorophore combinations for multi-color imaging of difficult-to-access or densely packed samples or under physiological conditions and in living cells remains challenging [3–5]. Especially in live-cell applications the choice of suitable fluorophore pairs is limited: apart from a small number of membrane-permeable, fluorescent dyes, which photoswitch in cellular environments without the need of further imaging buffers (e.g., tetramethylrhodamine (TMR) or Atto655 [3] or the recently developed paJF549 [6]), the most popular fluorophores are genetically encoded, photoactivatable or photoconvertible fluorescent proteins (pa- and pcFPs) like the widespread Anthozoan green-to-red pcFPs (e.g., the Eos, Dendra, Maple and Dronpa families) and DsRed derived dark-to-red paFPs (e.g., PAmCherry, PAmKate and

PAtagRFPs) [1,4,5,7]. Despite being popular in quantitative imaging and single-particle tracking approaches [2,5,8], the simultaneous use of multiple pcFPs and paFPs is largely precluded by their overlapping absorption and emission spectra: they are photoactivated/-converted by illumination in the near UV light range and a vast majority of common FPs with desirable properties (being bright and monomeric, exhibiting robust photophysics in varying redox-environment and a quantitative read-out [1,4,5]) emit fluorescence in a narrow, orange-red emission channel with only a few alternative FPs in other color channels, e.g., the green fluorescing paGFP [9], psCFP2 and Dronpa [10], or the red fluorescing psmOrange [11], which have been used for dual-color SMLM.

By utilizing the recently developed photoconversion technique of primed conversion (PC) for green-to-red pcFPs, we here introduce a new dual-color strategy. PC, which was first identified and characterized for Dendra2 [12,13] and has recently been shown to be very efficient for green-to-red pcFPs with threonine at residue 69, makes use of a combined illumination of 488 nm and near-infrared light in the range 700–800 nm instead of the common UV-photoconversion to convert common pcFPs from their green to their red form [12,14]. paFPs, on the other hand, only absorb light in the ultraviolet range prior to activation. As such, the 488 nm light used for PC should have no effect on the paFP. We propose that this fact could be advantageously exploited in a dual-phase, dual-color imaging scheme with a single fluorescence read-out channel. First, a PC-suitable pcFP, e.g., Dendra2 [12–15] or mEos3.2-A69T [14], is imaged using a combination of 488 and 730 nm light for photoconversion. After all pcFPs have been read out, the still-intact paFP, e.g., the commonly used PAmCherry [16], can be imaged in the second phase by UV-light mediated photoactivation. The benefits of such an approach are substantial. Since both targets are imaged in the same channel, chromatic aberration is eliminated. Both FP-tags can be endogenous, requiring no additional staining, and the above chosen FPs are bright and show no oligomerization tendencies [17]. In addition, as they fluoresce with a maximum in the 570–590 nm range upon 561 nm illumination, possible auto-fluorescence of biological samples and phototoxicity are reduced when compared to techniques using shorter wavelength channels [14,18]. This makes this labeling choice favorable compared to other, e.g., non-red, less bright and photostable or potentially self-oligomerizing pcFPs and paFPs such as paGFP [9,19], psCFP2 and Dronpa [10] or PAtagRFP [20] and PAmKate [7]. Finally, our strategy works hand in hand with existing, multi-channel approaches and can be easily used to expand them.

2. Results and Discussion

To evaluate the viability of the proposed imaging scheme, two main concerns had to be addressed. First, does PC illumination have any effect on the paFP? Second, is it possible to sufficiently eliminate the pcFP imaged by PC to not cause any cross-talk during the second imaging phase as any residual, non-converted pcFP molecule would also be read-out by UV light. To test this, we performed experiments on fixed *Escherichia coli* cells, where the native RNA polymerase (RNAP) protein was endogenously tagged with either Dendra2 or PAmCherry (Supplementary Material and Methods). RNAP molecules appear in large nucleoid-like patterns as they decorate the bacterial chromosome. Their numbers per unit of cell size are relatively stable when expressed under the native promoter, making RNAP a satisfactory target for quantitative controls [21].

First, we determined the minimum dose of 488 nm light required to permanently bleach all Dendra2-RNAP molecules in the *E. coli* cells (Figure S1a). A bleaching approach like this would be necessary in a worst-case scenario, where full readout of the PC-suitable pcFP is not feasible, e.g., in cases where the POI is highly abundant. We then evaluated the effect of this high 488 nm dose on the PAmCherry molecules (Figure S1a). While the vast majority of the Dendra2-RNAP read-out in the red channel was gone after 30 s of illumination with 1 kW/cm^2 of 488 nm light, we used 120 s for subsequent imaging since that is where the bleaching curve stabilized. Using the same settings, we found that 488 nm illumination slightly increased the fluorescence intensity in cells with PAmCherry-tagged RNAP, suggesting some minor activation (Figure S1a). With this information we were able to design a worst-case scenario control imaging scheme (Figure S1b,

left). To quantify the loss of PAmCherry during the first, PC-photoconversion stage of imaging and potential bleed-through of Dendra2 into the second UV-photoactivation phase, we performed localization counting on *E. coli* cells expressing RNAP-Dendra2 and RNAP-PAmCherry under several different illumination schemes (Figure S1b, right). RNAP-Dendra2 produced a mean of 1092 ± 175 (standard deviation) localization counts/μm^2 converted by primed conversion (I) and a mean of 999 ± 131 localization counts/μm^2 (II) by UV photoconversion which is in agreement with previous results on RNAP numbers [21,22] and reconfirms data of a recent study which did not show any differences in quality and quantitative numbers obtained in sptPALM tracking studies comparing UV and PC photoconversion of Dendra2 [14]. After 120 s of bleaching with 1 kW/cm^2 488 nm light, Dendra2 was activated by UV conversion and produced 54 ± 18 localization counts/μm^2 (III), which is at the level of false positive localization counts in wild type *E. coli* (data not shown), confirming that little to no Dendra2 survives the bleaching step. Next, we evaluated the UV readout of RNAP-PAmCherry, resulting in 1054 ± 217 counts/μm^2 (IV), which is comparable to the Dendra2 PC readout. To test the effects of high intensity 488 nm light on PAmCherry, RNAP-PAmCherry expressing cells were illuminated with the same high intensity of 1 kW/cm^2 488 nm light for 120 s, and then read out with UV activation, producing 916 ± 182 counts/μm^2 (V), further suggesting that 488 nm light activates PAmCherry with low efficiency. This, however, proved not to be an issue during the conversion imaging phase, where the overall dosage of 488 nm light is much lower (less than 0.1% of the bleaching dose of 1 kW/cm^2 used in this experiment). PAmCherry read out by PC activation, produced 45 ± 19 counts/μm^2 (VI), again at the level of background in wild type *E. coli*. To eliminate cross-talk, we thus implemented a brief, ~10 s pre-bleaching step with the 561 nm light readout laser before reading out the PAmCherry, bleaching away any pre-activated FP. These findings suggest that if the FP in the first phase of imaging is read out in full and a high intensity 488 nm post-bleaching step is not required, loss of PAmCherry is completely negligible. In such a case, both phases allow for a full quantitative SMLM readout.

Encouraged by the promising results of the controls, we decided to evaluate how well our approach performs in dual-color imaging of different biomolecules in *E. coli* and in a second step, how well it integrates with additional correlative imaging schemes such as membrane point accumulation for imaging of nanoscale topography (PAINT) and DNA stains [23]. To test this, we utilized the imaging scheme on an *E. coli* strain where RNAP was endogenously tagged with the PC-suitable mEos3.2-A69T mutant and transformed with the pJB063 plasmid bearing the sequence for FtsZ-PAmCherry. The green-to-red pcFP mEos3.2-A69T mutant has proven, like Dendra2, to be an excellent candidate for tagging native proteins in our previous work but with a 15–20% higher photoncount for single-molecule-spots than Dendra2—thus allowing for more precise sptPALM data [14]. RNAP-mEos3.2-A69T was imaged first and read out in full (Figure 1a), followed by a full readout of FtsZ-PAmCherry (Figure 1b). Nile-red was then added to the imaging solution to image the membrane by PAINT [24] (Figure 1c) and was finally replaced with a Sytox orange containing solution, to stain the DNA (Figure 1d), for a total of four effective colors all in the orange-red channel (Figure 1e).

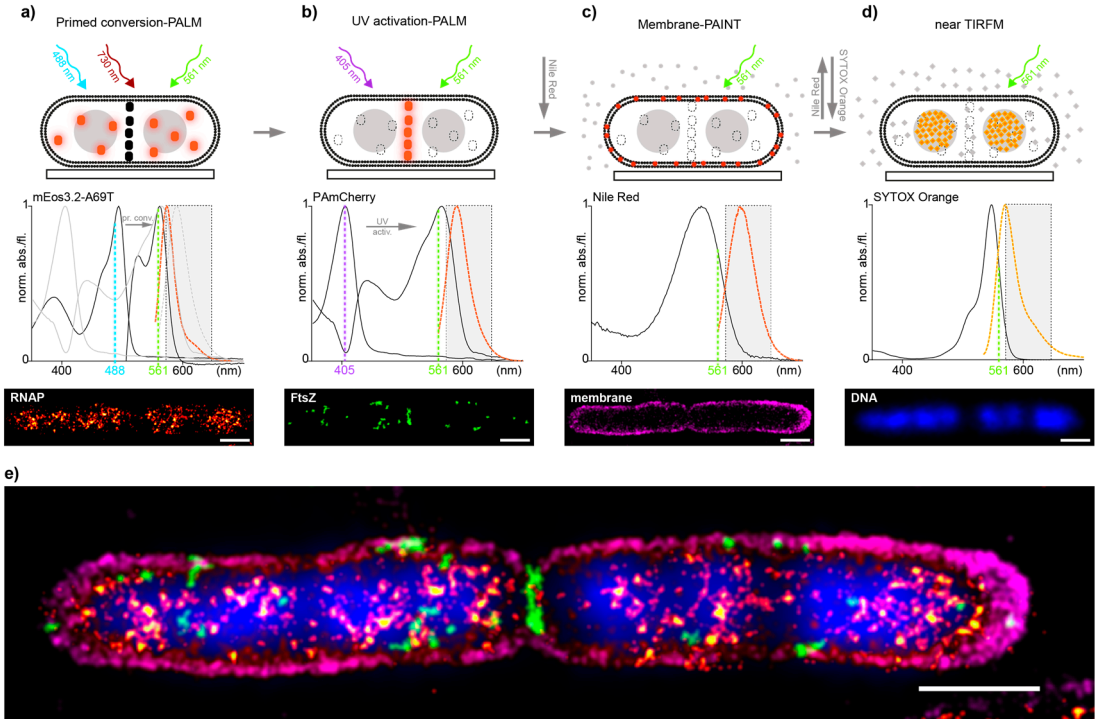

Figure 1. (**a**–**d**) Multi-color imaging workflow in *E. coli* cells. Top: scheme representing the acquisition sequence by first imaging RNAP-mEos3.2-A69T (orange dots) by primed conversion-PALM, not activated FtsZ-PAmCherry molecules are depicted as black dots (**a**); FtsZ-PAmCherry (orange dots) by UV activation-PALM, permanently bleached RNAP-mEos3.2-A69T are presented as dashed-lined white dots (**b**); The outer membrane by PAINT using NileRed- red dots depict fluorescent fraction of NileRed molecules in the membrane, whereas gray dots represent non-fluorescent NileRed in buffer/medium (**c**) and last the DNA stained by SYTOX Orange (orange diamonds) and read-out by near TIRF microscopy (**d**). Middle: Measured absorption and emission spectra of all four fluorophores used (Supplementary Material and Methods). Dashed line rectangle represents the optical bandpass-filter used to visualize the fluorescence channel of all four acquisitions. Bottom: SMLM image reconstructions (**a**–**c**) and nearTIRF-snapshot (**d**) recorded; (**e**) Overlay of all individual images to show the mutual organization of imaged compounds, aligned by fiducial markers (Supplementary Material and Methods). Localization precision of the channels after drift correction (whole ROI, NeNA values): mEos3.2-A69T (RNAP) 12.1 nm, PamCherry (FtsZ) 12.3 nm, NileRed (membrane) 11.8 nm, scale bars: 1 µm.

Next, we assessed how well the technique performs on larger samples in other organisms by imaging HeLa cells transiently transfected with a combination of an actin-PAmCherry plasmid together with either a keratin-Dendra2 plasmid (Figure 2a) or an H2B-Dendra2 plasmid (Figure 2b), details can be found in Supplementary Material and Methods. As before, the pcFP, Dendra2, was read out first. Due to the large size of the cell and large number of (overexpressed) molecules a full read-out was rather time consuming, thus we decided to bleach the residual Dendra2 molecules after obtaining a sufficient number of localizations for image reconstruction. The intensity of 488 nm bleaching step had to be increased to 4 kW/cm^2 in order to fully bleach the residual Dendra2 molecules above and below the imaging plane. No visible cross talk was present on any of the images, as showcased by the dark background around the H2B (Figure 2b(v)).

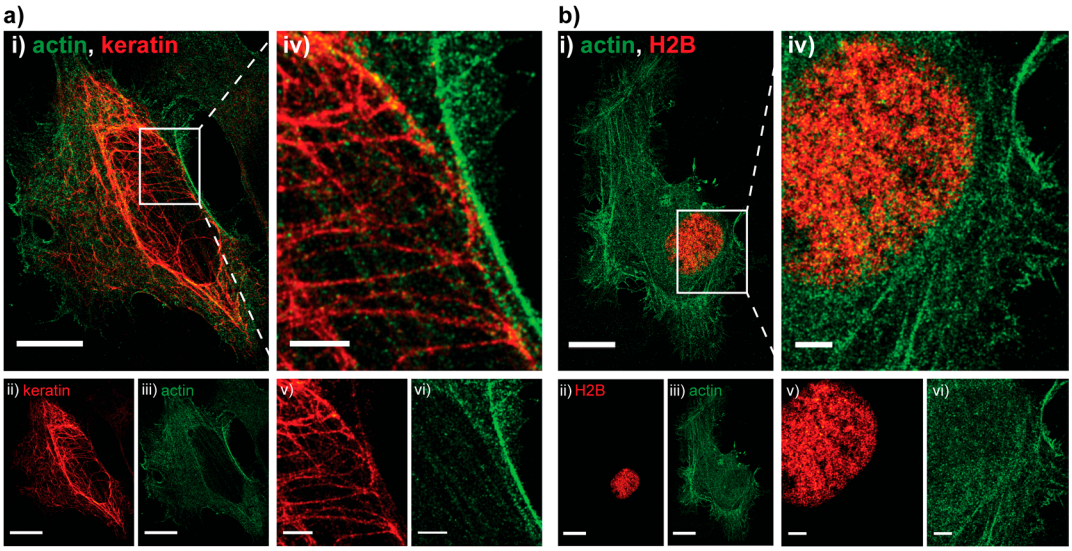

Figure 2. Two examples of Hela cells imaged with sequential PC activation. (**a**): (**i**) Dual-color PALM image of actin tagged with PamCherry (green) and keratin tagged with Dendra2 (red); (**ii**,**iii**) split channel PALM images of the same cell. Localization precision of the channels after drift correction (whole ROI, NeNA values): Dendra2 (red, keratin) 17.2 nm, PamCherry (green, actin) 17.4 nm, scale bars 5 µm; (**iv**–**vi**) zoom in on an area with details only visible in the super resolved image, scale bars 2 µm; (**b**): (**i**) Dual-color PALM image of actin tagged with PAmCherry (green) and H2B tagged with Dendra2 (red) and split channel images of the same cell (**ii**,**iii**). Localization precision of the channels after drift correction (whole ROI, NeNA values): Dendra2 (red, H2B) 16.1 nm, PamCherry (green, actin) 18.9 nm, scale bars 5 µm; (**iv**–**vi**) zoom in on the nucleus, showcasing the absence of bleed through (dark background on (**vi**)), scale bars 2 µm.

A major advantage of the approach is its potential for use in living cells, especially for targets which are difficult-to-reach by extrinsic fluorescent markers or have precluded SMLM read-out channels due to low signal-to-noise/high background, e.g., arising from intracellular autofluorescence. Like all (sequential) SMLM techniques, our approach is limited by the temporal resolution needed for structural studies of abundant proteins but offers the read-out of two different proteins by intrinsic FP labels with excellent SMLM properties to measure their molecule dynamics within the same compartment or cell [25].

We thus first tested our *E. coli* strain under live conditions (Figure S2a), measuring diffusion dynamics for RNAP and FtsZ (Figure S2b,c) as reported before [14,26] and could confirm the cell survival after sptPALM imaging [14] (Figure S2d).

We then challenged our approach by creating a strain of the fission yeast *Schizosaccharomyces pombe*, where the DNA binding protein cbp1 and the centromeric histone variant protein cnp1 were endogenously tagged with Dendra2 and PAmCherry, respectively (Supplementary Material and Methods). Introducing fluorophores for live cell SMLM imaging into *S. pombe* is difficult. In our hands, only few extrinsic labels can be delivered to protein-tag-fusions but are prone to unspecific background staining due to the cell wall and dense intracellular environment and do not blink in the intracellular living yeast environment (unpublished data). Additionally, dual-color SMLM imaging including a green FP does not provide satisfactory single molecule signal above the intracellular background (unpublished data). Thus, even most recent SMLM studies of living *S. pombe* have remained exclusively single-color using mEos2/mEos3 [27,28] which is in contrast to mammalian cell studies, where multi-color SMLM introducing dye molecules that blink in the intracellular environment has been applied in various studies [1,3].

As in *E. coli*, control measurements characterizing the viability of our living cells revealed no negative effect of our imaging approach on the cellular growth (Figure S3a–d). As before, Dendra2

was read out first, with lower 561 nm readout laser intensities and shorter exposure times, to capture the movement of single molecules (Figure 3a,b(i)). PAmCherry-cnp1 was successfully read out in the second phase, with no apparent crosstalk (Figure 3a,b(ii)). The cells were then fixed and stained with DAPI (Figure 3a,b(iii)), since Sytox Orange penetrated the thick yeast cell wall poorly in our hands (data not shown). As expected, reconstructed PALM images showed cbp1 is present throughout the nucleus and co-localizes with DNA, while cnp1 appears as a single centromeric spot at the edge of the DNA (Figure 3a,b(iv)). We then applied a custom single particle tracking algorithm on the same data and visualized the results (details in materials and methods), which showed that the cbp1 diffuses around the nucleus, while the cnp1 is largely immobile (Figure 3a(v)). Finally, we calculated diffusion coefficients for tracks longer than four consecutive frames, revealing a mobile (fast) and an immobile (slow) fraction of cbp1 (Figure 3b(iv)) and exemplary mean squared displacement (MSD)-curves in Figure S4a). Imaging fixed cbp1 molecules as a control under otherwise same conditions reveals that the slow fraction is indeed not moving within the precision of the sptPALM measurements and represents immobile, DNA-bound cbp1 molecules whereas the fraction of mobile cbp1 with a more heterogeneous distribution of diffusion coefficients represents DNA-associated, but mobile cbp1 molecules (Figure S4b(i,ii)) [29,30].

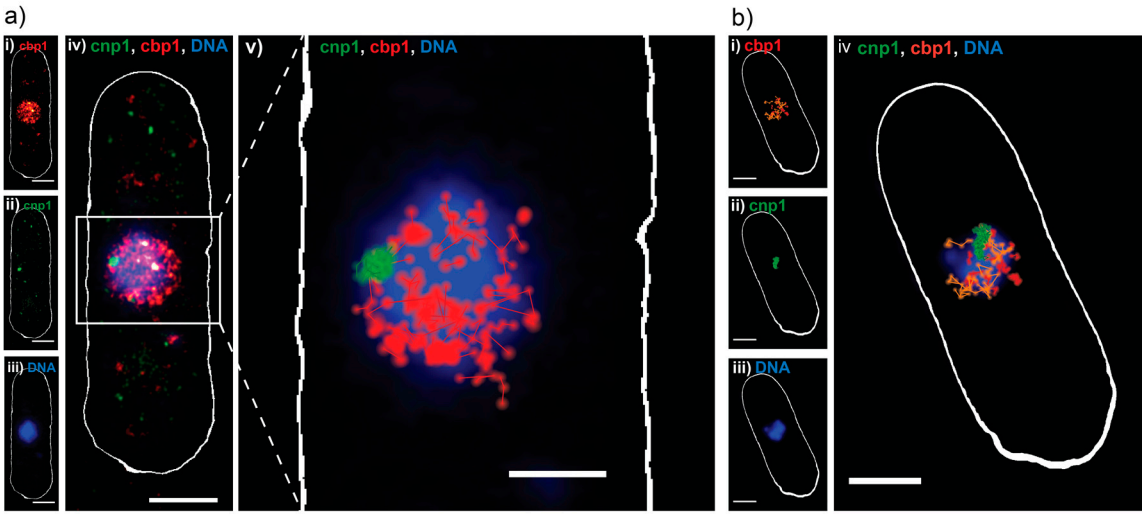

Figure 3. Sequential dual-color PALM on *S. pombe*. (**a**) Dual-color PALM image of a representative *S. pombe* cell, expressing the DNA binding protein cbp1 tagged with Dendra2 (red) and the centromeric protein cnp1 tagged with PAmCherry (green) and a widefield fluorescence image of DAPI stained DNA (blue): (**i**–**iii**) Split channels of the same cell and (**iv**) combined; (**v**) single particle track analysis performed on the same data, with tracks $\geq$3 consecutive frames represented in red (cbp1) and green (cnp1), on top of DNA (blue). Scale bars 2 µm; (**b**) single particle tracking analysis done on a different *S. pombe* cell: (**i**) single particle tracks of cbp1 $\geq$4 consecutive frames, color coded for their apparent diffusion coefficient D as calculated from a MSD analysis of the individual tracks, orange for fast moving particles ($D > 0.26\ \mu m^2/s$) and red for slow or immobile ($D < 0.26\ \mu m^2/s$); (**ii**) single particle tracks of cnp1 $\geq$ 4 consecutive frames; (**iii**) widefield fluorescence image of DNA in the same cell, after fixation; (**iv**) overlay of all three channels. Scale bars 2 µm.

3. Materials and Methods

Strain constructions for *E. coli* and *S. pombe* cell lines, transient transformations for mammalian samples, protein purification, live and fixed cell sample preparations for *E. coli*, *S. pombe* and mammalian cells as well as the microscopic and spectroscopic equipment are described in detail in the Supplementary Information (Supplementary Material and Methods).

3.1. Imaging Procedures

3.1.1. Influence of High Intensity of 488 nm Light on PAmCherry and Dendra2

To determine, whether high intensity of 488 nm light leads to irreversible bleaching of Dendra2 molecules while leaving PAmCherry intact, we imaged fixed MG1655 rpoC_Dendra2 and MG1655 rpoC_PAmCherry cells. First, cells were illuminated with 1 kW/cm^2 of 488 nm for 0 to 180 s (Figure S1a) and then illuminated for 15 s with 2.5 W/cm^2 of 405 nm light to perform photoactivation or photoconversion of non-bleached fluorescent proteins. In last step, three 60 ms frame snapshots with 800 W/cm^2 of the 561 nm laser were taken.

3.1.2. Quantitative Controls-RNAP Molecule Counting

To evaluate possible false positives of residual Dendra2 and the amount of pre-activated PAmCherry of the second phase of imaging (Dendra2 converted via UV light or PAmCherry preactivated via 488 nm light), a set of control experiments was performed (Figure S1b). In experiment (I) fixed MG1655 RNAP-Dendra2 cells were illuminated with three lasers: 488 nm pulsed every 20th frame and continuous 561 and 730 nm. Laser intensities were: 100–2500 mW/cm^2 of 488 nm (intensity was gradually increased during movie acquisition to keep the number of detected spots roughly on the same level), 800 W/cm^2 of 561 nm and 450 W/cm^2 of 730 nm. Movies were recorded at 16.67 Hz image acquisition (60 ms per frame) until no new fluorescent spots appeared to ensure for a full read-out of the FP. In experiment (II), MG1655 RNAP-Dendra2 was illuminated by conventional UV-conversion PALM: The 405 nm laser was pulsed every 20th frame, gradually increasing the intensity from 250–6500 mW/cm^2 and continuous 561 nm laser at a constant intensity of 800 W/cm^2. The field of view (FOV) was imaged until no new fluorescent spots appeared anymore. As a negative control (III), MG1655 RNAP-Dendra2 was first illuminated for two minutes with 1 kW/cm^2 of 488 nm laser to irreversibly bleach the Dendra2 molecules. Next, the same FOV was imaged with standard UV-conversion PALM. Laser intensities were the same as for (II). The FOV was imaged for 5 min with 60 ms exposure time per frame. Experiments (IV)–(VI) were performed on the MG1655 RNAP-PAmCherry strain. Experiment (IV) was a positive control where cells were imaged with UV-conversion PALM: 405 and 561 nm laser settings were the same as for experiment (II) and the FOV was imaged until no new spots appeared. In experiment (V) MG1655 RNAP-PAmCherry cells were imaged in a similar way as cells in experiment (III) with an extended imaging time until no new spots appeared, achieving full read-out. In experiment (VI) which serves as negative control, cells were imaged as the MG1655 RNAP-Dendra2 cells in experiment (I), to evaluate the activation of PAmCherry via primed conversion. FOV was imaged for 5 min. For each control experiment two FOVs were imaged.

3.1.3. *E. coli* Multi-Color Imaging

Detection of RNA polymerase (RNAP) fused with mEos3.2-A69T, FtsZ fused with PAmCherry, bacterial membrane and chromosomal DNA in fixed MG1655 rpoC_mEos3.2-A69T+pJB063 cells was performed sequentially (Figure 1). First, RNAP-mEos3.2-A69T molecules were imaged by primed conversion [14] (Figure 1a). Briefly, the sample was illuminated with three lasers: 488 nm pulsed every 20th frame and continuous 561 and 730 nm light. Laser intensities were: 100–2500 mW/cm^2 of 488 nm (intensity was gradually increased during movie acquisition), 800 W/cm^2 of 561 nm and 450 W/cm^2 of 730 nm. Movies were recorded at 16.67 Hz image acquisition (60 ms per frame) until no new spots appeared. After primed conversion PALM, the sample was illuminated for one minute with 1 kW/cm^2 of 488 nm laser to irreversibly bleach residual green form mEos3.2-A69T. In the second phase (Figure 1b) FtsZ-PAmCherry molecules were detected with UV-activation PALM: 405 nm laser pulsed every 20th frame (intensity gradually increasing from 250–6500 mW/cm^2) and continuous 800 W/cm^2 561 nm laser at 60 ms until all PAmCherry was read out. After finishing imaging both, RNAP-mEos3.2-A69T and FtsZ-PAmCherry, Nile Red (Sigma-Aldrich, Darmstadt, Germany) was

added (final concentration in imaging buffer: 7 nM) to visualize the bacterial membrane in the same cells by PAINT microscopy [24] (Figure 1c). Movies were recorded for 7 min with 60 ms exposure time per frame and the sample was illuminated with constant 1.2 kW/cm^2 of 561 nm laser. In the last, fourth step (Figure 1d), chromosomal DNA was visualized by addition of SYTOX Orange (Thermo Fischer, Darmstadt, Germany) to a final concentration 20 nM. One-frame 60 ms snapshots were taken with low intensity 561 nm laser (10 W/cm^2). For all fixed bacteria images, the Nearest Neighbor Analysis (NeNA) values [31] were in the range of 10–15 nm, exact values of the exemplary images are given in the respective captions.

Single-particle tracking PALM (sptPALM) imaging (Figure S2) of rpoC_mEos3.2-A69T+pJB063 cells was performed on a heating stage and heated objective at 32 °C. As for the fixed samples, RNAP-mEos3.2-A69T was imaged first and FtsZ-PAmCherry was imaged afterwards. Applied laser intensities were: 2 W/cm^2 of 405 nm, 600 mW/cm^2 of 488 nm, 450 W/cm^2 of 730 nm and 800 W/cm^2 of 561 nm laser light. 405 and 488 nm lasers were pulsed every 20th frame. Movies were recorded at 77 Hz image acquisition rate for two minutes to follow the diffusing RNA polymerase and at 33 Hz image acquisition rate for five minutes to follow the FtsZ protein. For the FtsZ imaging we used slower acquisition mode to exclude cytosolic FtsZ molecules—as they diffuse much faster than FtsZ built into the ring structures, their point-spread functions are blurred, thus most of the cytosolic FtsZ molecules are not included in further analysis steps. This approach was first used by Etheridge et al. in their work [32]. mEos3.2-A69T molecules were converted by primed conversion, while PAmCherry was photoactivated using UV. Right after recording the RNAP-mEos3.2-A69T molecules, a two minute bleaching step to bleach the remaining unconverted mEos3.2-A69T molecules was performed using 1 kW/cm^2 488 nm laser light illumination to avoid false positives during the FtsZ-PAmCherry readout. After sptPALM imaging, the cells of the imaged FOVs were tested for their cell viability. For this, all FOVs were imaged under bright light for three hours with two minutes interval to quantify their cellular growth after the sptPALM experiment.

3.1.4. HeLa Dual-Color Imaging

Keratin-Dendra2 or H2B-Dendra2 were imaged first, activated with 450 W/cm^2 of the 730 nm laser and 100–2500 mW/cm^2 of the 488 nm laser (pulsed every 20th frame) with the intensity gradually increased to keep the number of localizations per frame constant and read out with the 561 (800 W/cm^2) laser for 20 thousand frames at an exposure of 60 ms per frame. The sample was then illuminated with 4 kW/cm^2 of the 488 nm laser for 2 min, to bleach any residual Dendra2. Actin-PAmCherry was imaged second, activated with the 405 nm laser, pulsed on every 12th frame, with the intensity gradually adjusted from 250–6500 mW/cm^2 and read out with constant 561 illumination at 800 W/cm^2 for 10 to 20 thousand frames at an exposure time of 60 ms per frame. Lasers were angled to achieve near-TIRF illumination. For all mammalian images, the NeNA values were in the range of 15–20 nm, exact values of the exemplary images are given in the respective captions.

3.1.5. *S. pombe* Multi-Color Imaging

Cbp1-Dendra2 was imaged first, activated with 450 W/cm^2 of the 730 nm laser and 100–2500 mW/cm^2 of the 488 nm laser (pulsed every 20th frame) with the intensity gradually increased to keep the number of localizations per frame constant and read out with the 561 (500 W/cm^2) laser for 20 thousand frames at an exposure of 20 ms per frame. The sample was then illuminated with 2 kW/cm^2 of the 488 nm laser for 1 min, to bleach any residual Dendra2. Cnp1-PAmCherry was imaged second, activated with the 405 laser, pulsed on every 12th frame, with the intensity gradually adjusted from 250–6500 mW/cm^2 and read out with constant 561 illumination at 500 W/cm^2 for 10 thousand frames at an exposure time of 20 ms per frame. Finally, cells were fixed with 1% paraformaldehyde (Sigma-Aldrich, F8775) without moving the sample and stained for DNA with 1 µg/mL DAPI, read out by the 405 nm laser (10 W/cm^2).

3.1.6. Viability Controls

S. pombe cbp1-Dendra2 cnp1-PAmCherry cells were grown in YES medium at 25 °C overnight, then inoculated into fresh YES to a starting OD_{600} of 0.1 and grown for ~6 h before imaging. 1 mL of culture was spun down at 500× *g* for 5 min and resuspended in 10 µL fresh YES medium. Cells were immobilized on a 1% low-gelling temperature agarose pad (Sigma-Aldrich, A9414) in YES medium and covered with a coverslip previously cleaned with Hellmanex. Cells were imaged on a custom-built heating stage at 30 °C. To compare growth, 8 FOVs at least 1000 µm apart were chosen and bright field images were taken at time t_0. The first two FOVs were imaged with PC activation 450 W/cm^2 of the 730 nm laser and 100–2500 mW/cm^2 of the 488 nm laser (pulsed every 20th frame) with the intensity gradually increased to keep the number of localizations per frame constant and read out with the 561 (500 W/cm^2) laser for 20 thousand frames at an exposure of 15 ms per frame. The next two FOVs were imaged with the same conditions but also post-bleached with 2 kW/cm^2 of the 488 nm laser for 2 min. Two further FOVs were then imaged and post-bleached as described above, then also imaged with UV activation, 405 laser pulsed on every 12th frame, with the intensity gradually adjusted from 250–6500 mW/cm^2 and read out with constant 561 illumination at 500 W/cm^2 for 5 thousand frames at an exposure time of 30 ms per frame. A bright field of each position was taken every 10 min for 12 h after imaging with an automated µManager script, though FOVs were lost after ~4 h due to drift. Exemplary cells are depicted in Figure S3.

3.2. Data Analysis

3.2.1. Analysis of the Influence of High Intensity 488 nm Images

Acquired three-frame snapshots were analyzed with a custom written script in *Fiji software (ImageJ 1.51f)* [33]. Cell FOVs were extracted by identifying individual bacterial shapes from fluorescence averages excluding overlapping or out-of-focus cells. Averaged fluorescence intensity for each cell was used as a parameter of bleaching degree (Figure S1b).

3.2.2. Super-Resolution Image Reconstruction of Bacterial and Mammalian Multi-Color Images

Localizations of the fitted single fluorescent spots were obtained by the open source software *rapidSTORM* (version 3.3) [34]. Fitting parameters were determined individually for each kind of fluorophore (Dendra2, mEos3.2-A69T, PAmCherry and Nile Red). In the next step, localization precision for all FOVs was estimated using NeNA [31] as implemented in the open-source software *LAMA* (version 16.10) [35] on a section of the image that contained no fiducial markers. For all FOVs localization precision was determined between 10 and 15 nm for bacteria and 15 and 20 nm for mammalian cells. Localization data were filtered to connect neighboring localizations in adjacent frames, to avoid several-fold counting of molecules with fluorescence lifetimes exceeding the framerate of the movie. In the last post-processing step, all localization files were drift corrected with custom written *Python* algorithms that extract and correct for fluorescent bead trajectories. Additionally, for FtsZ-PAmCherry localizations, density based clustering analysis was performed with the density-based spatial clustering of applications with noise (DBSCAN) algorithm [36], as single cytosolic FtsZ-PAmCherry proteins were abundantly present in cell. Only clustered molecules (DBSCAN parameters: ε = 35 nm; MinPts = 10) were used for image reconstruction of FtsZ-PAmCherry. Super-resolution image reconstructions and DNA-Sytox Orange image were stacked and superimposed in *Fiji* software. For HeLa cells, images were reconstructed with a pixel size of 20 nm.

3.2.3. Single Particle Tracking in *E. coli* and *S. pombe*

Single molecule localizations were extracted from the movies with the open-source software *rapidSTORM*. Final images were reconstructed with a pixel size of 10 nm. Single particles were tracked with the help of customized tracking software written in C++ and visualized by customized software written in C++, to filter and group single molecule localizations or trajectories by their apparent

diffusion coefficient (as calculated by MSD analysis). For MSD analysis, only trajectories with 4 and more steps were used for calculating the MSD values. Independent of the total length of each trajectory, only the first steps of each trajectory were used for the MSD calculation (for the first 3 Δt values) to account for heterogeneous diffusion behavior over time as well as the confinement of the yeast nucleus/*E. coli* cell. To account for the localization precision σ of the data, the constant offset of $4*\sigma^2$ was included into the fit-function. For diffusion coefficient statistics, only MSD fits with an R^2 value of 0.85 or higher were used.

4. Summary and Conclusions

In summary, our new technique produced high quality PALM images on all tested samples. The controls showed there is little to no crosstalk between the two proteins and loss of PAmCherry is minimal. This can be further reduced by avoiding the post-bleaching step with high intensity of 488 nm light, by reading out the entire signal in the first phase of imaging and, for fixed cells, by increasing the pH to 8–8.5 where PC is most efficient [14]—making both phases of imaging fully quantitative. We have also shown that the approach is easily combined with other sequential imaging techniques, such as membrane PAINT. This correlative approach could be extended further, by e.g., substituting the Sytox Orange DNA stain for the transiently binding Hoechst-JF646 probe for DNA-PAINT [37].

Perhaps most importantly, the combination of a PC-suitable pcFP and an only UV-activatable paFP allows for dual-color SMLM imaging in living specimens, without the need for any additional staining steps, as shown in *E. coli* and *S. pombe*. Previously, this could only be done through the use of proteins with different emission spectra, such as paGFP or psCFP2. This requires imaging in different readout channels, introducing chromatic aberration, which makes overlaying the channels more difficult. Additionally, many biological samples, e.g., including *S. pombe*, can exhibit high degrees of autofluorescence in the GFP channel. Combined with the lower brightness of paGFP and psCFP2 compared to red paFPs, this results in a limited achievable resolution. Also, the superior brightness of FPs such as Dendra2, mEos3.2-A69T and PAmCherry allows for single particle tracking experiments, where brightness is essential due to shorter exposure times and lower excitation light intensities. That being said, our approach could potentially be combined with other FPs that emit in different channels, further expanding the palette of available colors for live-cell imaging or be used in tandem with enzyme tags such as Halo-tag [38] and SNAP-tag [39] together with membrane-permeable dyes (and e.g., as well using sequential orange stainings like TMR and paJF549).

In conclusion, our measurements demonstrate that this new method can be applied to various targets in different organisms and can be advantageously combined with existing imaging schemes. As it is an aberration-free, live-cell compatible method, which is simple to implement on conventional SMLM systems (even when using a red instead of an infrared laser source, PC can be efficient enough for SMLM imaging [13,14]), we believe it is a valuable addition to the current SMLM toolbox.

Supplementary Materials: Supplementary materials can be found at www.mdpi.com/1422-0067/18/7/1524/s1.

Acknowledgments: We thank Matthias Plessner, Institute of Pharmacology, Marburg, for the transient transfections of the Hela cells and Ilijana Vojnovic, MPI Marburg for her help with the cell culture during the revision of the manuscript. We further thank Jie Xiao, John Hopkins, Baltimore, USA, for kindly sharing their FtsZ-PAmCherry-plasmid pJB063. This work was funded by the Max Planck Society, SYNMIKRO and the Fonds der Chemischen Industrie.

Author Contributions: Ulrike Endesfelder and David Virant conceived the idea; Ulrike Endesfelder, David Virant, Alexander Balinovic and Bartosz Turkowyd designed the experiments; David Virant, Alexander Balinovic and Bartosz Turkowyd performed the experiments and analyzed the data; Ulrike Endesfelder and David Virant wrote the paper with the help of all authors.

Conflicts of Interest: The authors declare no conflict of interest.

Abbreviations

FP	Fluorescent protein
paFP	Photoactivatable fluorescent protein
PAINT	Points accumulation for imaging in nanoscale topography
PALM	Photoactivated localization microscopy
PC	Primed conversion
pcFP	Photoconvertible fluorescent protein
SMLM	Single molecule localization microscopy

References

1. Turkowyd, B.; Virant, D.; Endesfelder, U. From single molecules to life: Microscopy at the nanoscale. *Anal. Bioanal. Chem.* **2016**, *408*, 6885–6911. [CrossRef] [PubMed]
2. Nicovich, P.R.; Owen, D.M.; Gaus, K. Turning single-molecule localization microscopy into a quantitative bioanalytical tool. *Nat. Protoc.* **2017**, *12*, 453–460. [CrossRef] [PubMed]
3. Sauer, M.; Heilemann, M. Single-molecule localization microscopy in eukaryotes. *Chem. Rev.* **2017**, *117*, 7478–7509. [CrossRef] [PubMed]
4. Nienhaus, K.; Nienhaus, G.U. Fluorescent proteins for live-cell imaging with super-resolution. *Chem. Soc. Rev.* **2014**, *43*, 1088–1106. [CrossRef] [PubMed]
5. Shcherbakova, D.M.; Sengupta, P.; Lippincott-Schwartz, J.; Verkhusha, V.V. Photocontrollable fluorescent proteins for superresolution imaging. *Annu. Rev. Biophys.* **2014**, *43*, 303–329. [CrossRef] [PubMed]
6. Grimm, J.B.; English, B.P.; Choi, H.; Muthusamy, A.K.; Mehl, B.P.; Dong, P.; Brown, T.A.; Lippincott-Schwartz, J.; Liu, Z.; Lionnet, T.; et al. Bright photoactivatable fluorophores for single-molecule imaging. *Nat. Methods* **2016**, *13*, 985–988. [CrossRef] [PubMed]
7. Gunewardene, M.S.; Subach, F.V.; Gould, T.J.; Penoncello, G.P.; Gudheti, M.V.; Verkhusha, V.V.; Hess, S.T. Superresolution imaging of multiple fluorescent proteins with highly overlapping emission spectra in living cells. *Biophys. J.* **2011**, *101*, 1522–1528. [CrossRef] [PubMed]
8. Gahlmann, A.; Moerner, W.E. Exploring bacterial cell biology with single-molecule tracking and super-resolution imaging. *Nat. Rev. Microbiol.* **2014**, *12*, 9–22. [CrossRef] [PubMed]
9. Wilmes, S.; Staufenbiel, M.; Lisse, D.; Richter, C.P.; Beutel, O.; Busch, K.B.; Hess, S.T.; Piehler, J. Triple-color super-resolution imaging of live cells: Resolving submicroscopic receptor organization in the plasma membrane. *Angew. Chem.* **2012**, *51*, 4868–4871. [CrossRef] [PubMed]
10. Shroff, H.; Galbraith, C.G.; Galbraith, J.A.; White, H.; Gillette, J.; Olenych, S.; Davidson, M.W.; Betzig, E. Dual-color superresolution imaging of genetically expressed probes within individual adhesion complexes. *Proc. Natl. Acad. Sci. USA* **2007**, *104*, 20308–20313. [CrossRef] [PubMed]
11. Nahmani, M.; Lanahan, C.; DeRosier, D.; Turrigiano, G.G. High-numerical-aperture cryogenic light microscopy for increased precision of superresolution reconstructions. *Proc. Natl. Acad. Sci. USA.* **2017**, *114*, 3832–3836. [CrossRef] [PubMed]
12. Dempsey, W.P.; Georgieva, L.; Helbling, P.M.; Sonay, A.Y.; Truong, T.V.; Haffner, M.; Pantazis, P. In vivo single-cell labeling by confined primed conversion. *Nat. Methods* **2015**, *12*, 645–648. [CrossRef] [PubMed]
13. Klementieva, N.V.; Lukyanov, K.A.; Markina, N.M.; Lukyanov, S.A.; Zagaynova, E.V.; Mishin, A.S. Green-to-red primed conversion of dendra2 using blue and red lasers. *Chem. Commun.* **2016**, *52*, 13144–13146. [CrossRef] [PubMed]
14. Turkowyd, B.; Balinovic, A.; Virant, D.; Golz Carnero, H.G.; Caldana, F.; Endesfelder, M.; Bourgeois, D.; Endesfelder, U. A general mechanism of photoconversion of green-to-red fluorescent proteins based on blue and infrared light reduces phototoxicity in live-cell single-molecule imaging. *Angew. Chem.* **2017**. [CrossRef]
15. Mohr, M.A.; Argast, P.; Pantazis, P. Labeling cellular structures in vivo using confined primed conversion of photoconvertible fluorescent proteins. *Nat. Protoc.* **2016**, *11*, 2419–2431. [CrossRef] [PubMed]
16. Subach, F.V.; Patterson, G.H.; Manley, S.; Gillette, J.M.; Lippincott-Schwartz, J.; Verkhusha, V.V. Photoactivatable mcherry for high-resolution two-color fluorescence microscopy. *Nat. Methods* **2009**, *6*, 153–159. [CrossRef] [PubMed]

17. Wang, S.; Moffitt, J.R.; Dempsey, G.T.; Xie, X.S.; Zhuang, X. Characterization and development of photoactivatable fluorescent proteins for single-molecule–based superresolution imaging. *Proc. Natl. Acad. Sci. USA* **2014**, *111*, 8452–8457. [CrossRef] [PubMed]
18. Wäldchen, S.; Lehmann, J.; Klein, T.; van de Linde, S.; Sauer, M. Light-induced cell damage in live-cell super-resolution microscopy. *Sci. Rep.* **2015**, *5*, 15348. [CrossRef] [PubMed]
19. Patterson, G.H.; Lippincott-Schwartz, J. A photoactivatable gfp for selective photolabeling of proteins and cells. *Science* **2002**, *297*, 1873–1877. [CrossRef] [PubMed]
20. Subach, F.V.; Patterson, G.H.; Renz, M.; Lippincott-Schwartz, J.; Verkhusha, V.V. Bright monomeric photoactivatable red fluorescent protein for two-color super-resolution sptpalm of live cells. *J. Am. Chem. Soc.* **2010**, *132*, 6481–6491. [CrossRef] [PubMed]
21. Endesfelder, U.; Finan, K.; Holden, S.J.; Cook, P.R.; Kapanidis, A.N.; Heilemann, M. Multiscale spatial organization of rna polymerase in escherichia coli. *Biophys. J.* **2013**, *105*, 172–181. [CrossRef] [PubMed]
22. Stracy, M.; Lesterlin, C.; Garza de Leon, F.; Uphoff, S.; Zawadzki, P.; Kapanidis, A.N. Live-cell superresolution microscopy reveals the organization of rna polymerase in the bacterial nucleoid. *Proc. Natl. Acad. Sci. USA* **2015**, *112*, E4390–E4399. [CrossRef] [PubMed]
23. Spahn, C.; Cella-Zannacchi, F.; Endesfelder, U.; Heilemann, M. Correlative super-resolution imaging of rna polymerase distribution and dynamics, bacterial membrane and chromosomal structure inescherichia coli. *Methods Appl. Fluoresc.* **2015**, *3*, 014005. [CrossRef]
24. Sharonov, A.; Hochstrasser, R.M. Wide-field subdiffraction imaging by accumulated binding of diffusing probes. *Proc. Natl. Acad. Sci. USA* **2006**, *103*, 18911–18916. [CrossRef] [PubMed]
25. Jung, S.R.; Fujimoto, B.S.; Chiu, D.T. Quantitative microscopy based on single-molecule fluorescence. *Curr. Opin. Chem. Biol.* **2017**, *39*, 64–73. [CrossRef] [PubMed]
26. Niu, L.; Yu, J. Investigating intracellular dynamics of ftsz cytoskeleton with photoactivation single-molecule tracking. *Biophys. J.* **2008**, *95*, 2009–2016. [CrossRef] [PubMed]
27. Laplante, C.; Huang, F.; Tebbs, I.R.; Bewersdorf, J.; Pollard, T.D. Molecular organization of cytokinesis nodes and contractile rings by super-resolution fluorescence microscopy of live fission yeast. *Proc. Natl. Acad. Sci. USA* **2016**, *113*, E5876–E5885. [CrossRef] [PubMed]
28. Daigaku, Y.; Etheridge, T.J.; Nakazawa, Y.; Nakayama, M.; Watson, A.T.; Miyabe, I.; Ogi, T.; Osborne, M.A.; Carr, A.M. Pcna ubiquitylation ensures timely completion of unperturbed DNA replication in fission yeast. *PLoS Genet.* **2017**, *13*, e1006789. [CrossRef] [PubMed]
29. Zaratiegui, M.; Vaughn, M.W.; Irvine, D.V.; Goto, D.; Watt, S.; Bahler, J.; Arcangioli, B.; Martienssen, R.A. Cenp-b preserves genome integrity at replication forks paused by retrotransposon ltr. *Nature* **2011**, *469*, 112–115. [CrossRef] [PubMed]
30. Mizuguchi, T.; Barrowman, J.; Grewal, S.I. Chromosome domain architecture and dynamic organization of the fission yeast genome. *FEBS Lett.* **2015**, *589*, 2975–2986. [CrossRef] [PubMed]
31. Endesfelder, U.; Malkusch, S.; Fricke, F.; Heilemann, M. A simple method to estimate the average localization precision of a single-molecule localization microscopy experiment. *Histochem. Cell Biol.* **2014**, *141*, 629–638. [CrossRef] [PubMed]
32. Etheridge, T.J.; Boulineau, R.L.; Herbert, A.; Watson, A.T.; Daigaku, Y.; Tucker, J.; George, S.; Jonsson, P.; Palayret, M.; Lando, D.; et al. Quantification of DNA-associated proteins inside eukaryotic cells using single-molecule localization microscopy. *Nucleic Acids Res.* **2014**, *42*, e146. [CrossRef] [PubMed]
33. Schindelin, J.; Arganda-Carreras, I.; Frise, E.; Kaynig, V.; Longair, M.; Pietzsch, T.; Preibisch, S.; Rueden, C.; Saalfeld, S.; Schmid, B.; et al. Fiji: An open-source platform for biological-image analysis. *Nat. Methods* **2012**, *9*, 676–682. [CrossRef] [PubMed]
34. Wolter, S.; Loschberger, A.; Holm, T.; Aufmkolk, S.; Dabauvalle, M.C.; van de Linde, S.; Sauer, M. Rapidstorm: Accurate, fast open-source software for localization microscopy. *Nat. Methods* **2012**, *9*, 1040–1041. [CrossRef] [PubMed]
35. Malkusch, S.; Heilemann, M. Extracting quantitative information from single-molecule super-resolution imaging data with lama—Localization microscopy analyzer. *Sci. Rep.* **2016**, *6*, 34486. [CrossRef] [PubMed]
36. Ester, M.; Kriegel, H.P.; Sander, J.; Xu, X. *A Density-Based Algorithm for Discovering Clusters in Large Spatial Databases with Noise*; Kdd: Portland, OH, USA, 1996; pp. 226–231.

37. Legant, W.R.; Shao, L.; Grimm, J.B.; Brown, T.A.; Milkie, D.E.; Avants, B.B.; Lavis, L.D.; Betzig, E. High-density three-dimensional localization microscopy across large volumes. *Nat. Methods* **2016**, *13*, 359–365. [CrossRef] [PubMed]
38. Los, G.V.; Encell, L.P.; McDougall, M.G.; Hartzell, D.D.; Karassina, N.; Zimprich, C.; Wood, M.G.; Learish, R.; Ohana, R.F.; Urh, M.; et al. Halotag: A novel protein labeling technology for cell imaging and protein analysis. *ACS Chem. Biol.* **2008**, *3*, 373–382. [CrossRef] [PubMed]
39. Sun, X.; Zhang, A.; Baker, B.; Sun, L.; Howard, A.; Buswell, J.; Maurel, D.; Masharina, A.; Johnsson, K.; Noren, C.J.; et al. Development of snap-tag fluorogenic probes for wash-free fluorescence imaging. *Chembiochem* **2011**, *12*, 2217–2226. [CrossRef] [PubMed]

3 | Studying CRISPR-Cas Surveillance Complex Dynamics *In vivo* Using sptPALM

In this chapter, I will present my work on the investigation of the CRISPR-Cas type I-Fv system dynamics. In the first section, I will summarize the experimental design and data analysis pipeline. In the second part, I will report our current results of the type I-Fv system dynamics studies.

3.1 Live-cell sptPALM Imaging of Cascade Surveillance Complex

Live-cell single-particle tracking photoactivated localization microscopy of Cascade-mediated DNA surveillance

Bartosz Turkowyd, Hanna Müller-Esparza, Vanessa Climenti, Niklas Steube, Ulrike Endesfelder, Lennart Randau

This part of the thesis is written in the book chapter style and was published in Methods in Enzymology in 2019. I contributed in this work by doing a literature research and review, preparing figures and writing parts of the text. [23]

CHAPTER SEVEN

Live-cell single-particle tracking photoactivated localization microscopy of Cascade-mediated DNA surveillance

Bartosz Turkowyd[a,b,†], Hanna Müller-Esparza[c,†], Vanessa Climenti[a,b], Niklas Steube[c], Ulrike Endesfelder[a,b,*,†], Lennart Randau[b,c,*,†]

[a]Department of Systems and Synthetic Microbiology, Max Planck Institute for Terrestrial Microbiology, Marburg, Germany
[b]LOEWE Center for Synthetic Microbiology (SYNMIKRO), Marburg, Germany
[c]Prokaryotic Small RNA Biology Group, Max Planck Institute for Terrestrial Microbiology, Marburg, Germany
*Corresponding authors: e-mail address: ulrike.endesfelder@synmikro.mpi-marburg.mpg.de; lennart.randau@mpi-marburg.mpg.de

Contents

† Authors contributed equally.

Methods in Enzymology, Volume 616
ISSN 0076-6879
https://doi.org/10.1016/bs.mie.2018.11.001

Abstract

Type I CRISPR–Cas systems utilize small CRISPR RNA (crRNA) molecules to scan DNA strands for target regions. Different crRNAs are bound by several CRISPR-associated (Cas) protein subunits that form the stable ribonucleoprotein complex Cascade. The Cascade-mediated DNA surveillance process requires a sufficient degree of base-complementarity between crRNA and target sequences and relies on the recognition of small DNA motifs, termed protospacer adjacent motifs. Recently, super-resolution microscopy and single-particle tracking methods have been developed to follow individual protein complexes in live cells. Here, we described how this technology can be adapted to visualize the DNA scanning process of Cascade assemblies in *Escherichia coli* cells. The activity of recombinant Type I-Fv Cascade complexes of *Shewanella putrefaciens* CN-32 serves as a model system that facilitates comparative studies for many of the diverse CRISPR–Cas systems.

1. Introduction

Prokaryotes have evolved several mechanisms to evade phage infections, including restriction–modification systems (R/M) that are able to inactivate target DNA by cleavage (Pingoud, Fuxreiter, Pingoud, & Wende, 2005), toxin–antitoxin modules that result in abortive phage infection and CRISPR–Cas systems (Unterholzner, Poppenberger, & Rozhon, 2013). The acronym CRISPR–Cas is generated from the abbreviations for clustered regularly interspaced short palindromic repeats and CRISPR-associated proteins (Jansen, van Embden, Gaastra, & Schouls, 2002). CRISPR arrays were first discovered as unusual structures in the *Escherichia coli* K12 genome (Ishino, Shinagawa, Makino, Amemura, & Nakata, 1987), years before the detection of associated *cas* genes (Jansen et al., 2002). CRISPR–Cas was suggested to function as an adaptive immune system in prokaryotes in 2005 (Mojica, Díez-Villaseñor, García-Martínez, & Soria, 2005; Pourcel, Salvignol, & Vergnaud, 2005), which was experimentally confirmed two years later (Barrangou et al., 2007).

CRISPR–Cas RNA-guided immune systems are widespread in prokaryotes and play a major role in microbial evolution (Jore et al., 2011; Makarova et al., 2011). These systems can be found in about 50% and 90% of all sequenced bacteria and archaea, respectively (Grissa, Vergnaud, & Pourcel, 2007b). CRISPR–Cas systems offer prokaryotes a sequence-specific defense mechanism against invasion of foreign nucleic acids from viruses, plasmids, or other mobile genetic elements (MGEs) (Barrangou et al., 2007; Edgar & Qimron, 2010; Garneau et al., 2010; Marraffini & Sontheimer, 2008).

In this process, these immune systems do not rely on antigen–antibody interactions, but work directly at the nucleic acid level. Small prokaryotic CRISPR RNA molecules (crRNA) are able to guide a single Cas protein effector or a multisubunit Cas protein effector complex toward invading DNA or RNA stretches that exhibit base-complementarity to the crRNA. Subsequently, Cas nucleases destroy these foreign nucleic acids, disarming viral threats (Barrangou et al., 2007; Brouns et al., 2008; Mohanraju et al., 2016).

CRISPR–Cas immunity is established in three defined steps: (1) spacer acquisition or adaptation, (2) crRNA expression or biogenesis, and (3) interference. The CRISPR–*cas* locus usually describes a cluster of *cas* genes found next to one or several CRISPR arrays. These arrays contain several repetitions of identical sequences (repeats) and variable sequences (spacers). Spacer regions constitute sequences from viruses or MGEs that were integrated via CRISPR–Cas activity. Since integration is directional, the first spacers in a CRISPR array often correspond to the most recent interactions (Barrangou et al., 2007; Jansen et al., 2002; Pourcel et al., 2005).

The spacer acquisition step (adaptation) is similar for most CRISPR–Cas systems (Koonin, Makarova, & Zhang, 2017). An adaptation module consists of two Cas proteins: the endonuclease Cas1 and the structural subunit Cas2 (Amitai & Sorek, 2016). These two proteins form a stable complex (Nunez et al., 2014; Wang et al., 2015) that is responsible for the recognition of foreign DNA or RNA as targets, following integration of a 20–40 bp sequence into the CRISPR array. In this process, the first repeat sequence is duplicated. To identify foreign nucleic acids as a target, a specific sequence motif is recognized (Sun et al., 2013). This so-called protospacer adjacent motif (PAM) consists of two to five nucleotides and is located directly adjacent to the sequence that gets inserted into the CRISPR array, the protospacer (Brouns et al., 2008).

In the subsequent biogenesis step, the CRISPR array is transcribed into a long precursor crRNA (pre-crRNA) that is processed into individual, mature crRNA pieces by type-dependent Cas proteins. Each of these mature crRNAs consists of a single-spacer sequence and fragments of the flanking repeat regions. In addition, the *cas* genes are transcribed, translated, and assembled into protein complexes with single crRNAs (Carte, Wang, Li, Terns, & Terns, 2008; Haurwitz, Jinek, Wiedenheft, Zhou, & Doudna, 2010).

The final step, interference, exhibits most variation in regard to the involved Cas proteins and mechanisms (Koonin et al., 2017; Makarova et al., 2011, 2015). Different crRNA-guided effector complexes enable

recognition and destruction of foreign genetic material. Hallmark features of this process are (i) crRNAs that utilize base-complementarity between their spacer sequence and nucleic acids to identify targets and (ii) Cas protein complexes that identify PAM sequences near the potential target to prevent harmful self-targeting (Marraffini & Sontheimer, 2010). The PAM sequences differ strongly between subtypes of CRISPR–Cas systems, but are highly conserved within subtypes (Chylinski, Makarova, Charpentier, & Koonin, 2014; Makarova et al., 2011). The diversification of Cas protein interference complexes required an elaborate classification approach for the different CRISPR–Cas systems.

In the current classification, the largest distinction was made in regard to the number of Cas proteins that are present in the effector complex that binds the crRNA. Class II encompasses Type II, V, and VI systems that rely on a single large Cas protein for interference. In Type II systems, this effector is called Cas9, a widely used tool for genome editing approaches (Cong et al., 2013; Komor, Badran, & Liu, 2017). Type V systems are characterized by Cas12 effector proteins that target DNA molecules, while Type VI systems have Cas13 effector proteins that specifically target RNA molecules (Koonin et al., 2017).

Class I CRISPR–Cas systems are differentiated from class II systems by the use of multisubunit effector complexes. Among them, Type I systems are the most common and diverse in nature. Type III systems are mostly found in archaea and act together with Type I systems. Similarly, Type IV systems appear to rely on the presence of Type I CRISPR–Cas systems as they usually lack adaptation modules. All of these systems form multiprotein complexes with a backbone of several Cas7 subunits proteins that contain a signature RNA recognition motif. Cas7 covers the spacer sequence of the associated crRNA. RNA interactions are also mediated via Cas5 and Cas6 proteins that cap the 5′ and 3′ termini of the crRNA, respectively. Additional proteins, called large and small subunits, are mostly responsible for DNA interactions in the CRISPR–ribonucleoprotein complexes (crRNPs) (Hochstrasser et al., 2014; Jackson et al., 2014; Staals et al., 2014; van der Oost, Westra, Jackson, & Wiedenheft, 2014; Zhao et al., 2014).

In Type I CRISPR–Cas systems, these crRNPs are termed CRISPR-associated complex for antiviral defense (Cascade). Cascade assemblies of different subtypes differ in the number of involved Cas proteins as well as in size and shape of the crRNP (Makarova et al., 2015; Pausch et al., 2017). The seahorse-shaped Cascade architecture of subtype I-E systems is generated by Cas5, Cas6, Cas7, Cas8, and Cas11 in a stoichiometry of 1:1:6:1:2

(Hayes et al., 2016; Jackson et al., 2014; Mulepati, Heroux, & Bailey, 2014; Wiedenheft et al., 2011). The Cascade of subtype I-F systems has a similar architecture, but lacks the small subunit protein Cas11 (Chowdhury et al., 2017; Makarova et al., 2015). Nonetheless, both subtypes exhibit similar structures of shared Cas proteins and comparable PAM recognition mechanisms via dsDNA interactions by the large subunit (Cas8).

A subtype I-Fv Cascade was identified in *Shewanella putrefaciens* CN-32 and shown to lack both Cas11 and Cas8, resulting in a minimal Cascade architecture of three different proteins and one mature crRNA (Dwarakanath et al., 2015; Gleditzsch et al., 2016; Pausch et al., 2017) (Fig. 1).

The variant structures of Cas5fv and Cas7fv proteins of subtype I-Fv systems result in an "open" Cascade formation that resembles subtype I-E Cascade. The small and large subunits are functionally replaced by Cas7fv and Cas5fv, respectively. Cas5fv interacts with the 8 nt long 5′ handle of the crRNA, whereas Cas6f binds to the 20 nt long 3′ terminal hairpin and interacts with the Cas7fv backbone (Pausch et al., 2017). A single Cas7fv backbone subunit covers a 6 nt sequence stretch of the spacer and extending or shortening of the spacer results in altered Cas7fv subunit amounts. The *S. putrefaciens* subtype I-Fv system relies on the recognition of a two nucleotide "GG"-PAM to distinguish between target and self DNA (Dwarakanath et al., 2015). In contrast to other Type I systems, PAM recognition is performed from the DNA major groove side by a protruding alpha-helical domain of Cas5fv (Pausch et al., 2017). Cascade effector complexes of Type I CRISPR–Cas systems are able to bind invading nucleic acids by generating R-loop structures as a result of hybridization between crRNA spacers and

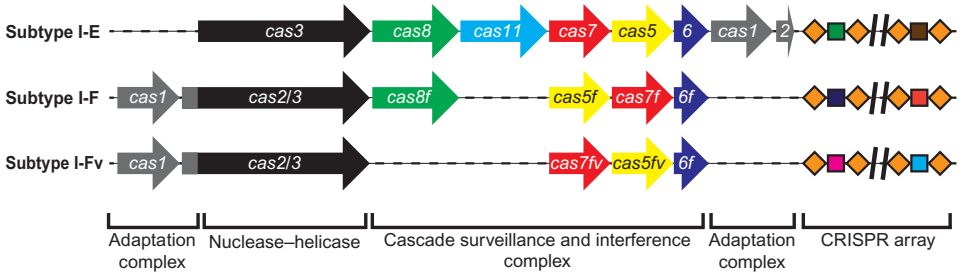

Fig. 1 Gene and CRISPR array arrangement of subtype I-E, I-F, and I-Fv CRISPR–Cas systems. A schematic representation of CRISPR–Cas loci is shown. *Arrows* indicate *cas* genes of comparative length. The Cascade surveillance and interference complex genes are multicolored and consist of five, four, and three different genes, respectively. The helicase–nuclease Cas3 is fused to Cas2 in subtypes I-F and I-Fv. The CRISPR arrays are indicated as alternating *rhombi* (*orange*, CRISPR–DNA (crDNA) repeats) and *squares* of *various colors* (different crDNA spacers).

target DNA protospacers (Garneau et al., 2010; Jore et al., 2011; Westra et al., 2012). Subsequently, the Cas3 helicase–nuclease is recruited to the R-loop region to unwind and finally degrade the foreign nucleic acids (Hochstrasser et al., 2014; van der Oost et al., 2014).

1.1 Dynamics of Cas protein-mediated DNA targeting

CRISPR–Cas systems, both Type I and II, were studied on a single-molecule level in vitro, e.g., by DNA curtains, single-molecule FRET assays, or using magnetic tweezers, providing detailed knowledge about their kinetics and the underlying molecular mechanisms. Here, it could be shown that target binding and R-loop formation proceed directionally along the target sequence and that full target sequences with incorrect PAMs are ignored (Sternberg, Redding, Jinek, Greene, & Doudna, 2014) and that PAM proximal sequences affect the R-loop formation rate, whereas PAM distal sequences are involved in R-loop stabilization (Szczelkun et al., 2014). Further studies revealed that Cas9–RNA/DNA association rates are only weakly dependent on the spacer sequence but the dissociation rates increase significantly upon introduction of mismatches in PAM proximity (Singh, Sternberg, Fei, Doudna, & Ha, 2016), R-loop formation was shown to respond to sequence mismatches and that when the R-loop formation reaches the protospacer end, complexes enter a locked state until Cas3 nuclease recruitment (Rutkauskas et al., 2015). Furthermore, quantitative bionumbers could be retrieved, e.g., single-molecule FRET studies revealed the binding times of Type I-E Cascade during interference. Here, the authors found two binding modes, one longer than 30 min, which is considered being an interference mode, and the second with ~25 s lifetime being connected to partial R-loop formation (Blosser et al., 2015). DNA curtains experiments showed that Cascade complexes remain in their locked state for more than 57 min and for only approximately 25 s, when bound to a partially complementary sequence (Redding et al., 2015). Finally, in both studies, the authors evaluated the DNA-probing time to be in the second range: 0.75–3 s (Redding et al., 2015) and 1.6 ± 0.4 s (Blosser et al., 2015). In summary, the in vitro measurements of CRISPR–Cas interference show that Cascade–DNA interaction times cover a wide range: from seconds to tens of minutes. However, in vitro conditions investigate CRISPR–Cas systems in isolation from their intracellular environment. Thus, it is important to explore CRISPR–Cas interference in vivo as well. Until now, only two in vivo studies were published, one investigating

Cas9 target search in living mammalian cells (Knight et al., 2015) and one in *E. coli* cells (Jones et al., 2017).

In the following sections, we will provide the methodological details for performing live-cell single-particle tracking of the molecular dynamics of Cas protein-mediated DNA surveillance. Single-molecule localization microscopy (SMLM) techniques (Betzig et al., 2006; Folling et al., 2008; Heilemann et al., 2008; Hess, Girirajan, & Mason, 2006; Rust, Bates, & Zhuang, 2006) can bypass the diffraction limit of light by utilizing photochromic fluorophores that can be photoswitched between different molecular states. This allows switching a small, spatially separated subset of fluorophores into their fluorescent on-state, resulting in spatially well-separated single fluorescent spots, characteristic point spread function (PSF) profiles that are resolvable within the diffraction limit. After the full readout of this subset, a new subset is switched on and readout. Repeating this procedure over time leads to a read-out of all fluorophores (Fig. 2A). As PSFs are spatiotemporally separated, each centroid can be estimated with nanometer precision (Fig. 2B). This procedure enables high-density mapping of fast single-protein dynamics by single-particle tracking photoactivated localization microscopy (sptPALM) (Manley et al., 2008) as sptPALM combines single-molecule tracking with the spatiotemporal separation of fluorophores of SMLM techniques (Fig. 2C).

The described minimal Type I-Fv Cascade of *S. putrefaciens* serves as a model system and is studied in a heterologous *E. coli* host. Particularly, this protocol allows to investigate the different time scales of Cascade interference and to probe their dynamics depending on the complementarity of different crRNAs, as sketched in Fig. 3. For example, when imaging the Cascade dynamics using long camera integration times of several seconds, only fluorescence signals from stable interference complexes are detected. The nucleoid, due to its size, is virtually immobile on these time scales, thus complexes bound to genomic targets appear immobile (Fig. 3, Cascade (anti-REP), 16 genomic targets, see Section 2.1). Cascade complexes which are only transiently binding or carrying a noncomplementary crRNA only show diffusive signals since the transient DNA interactions during target search processes are too short-lived to be visible as clear fluorescent spots at seconds-long exposure times (Fig. 3, Cascade (antilambda), no genomic targets, see Section 2.1). A fast imaging rate of 30 ms per frame allows to also detect the diffusive molecules. Thereby it is possible to also investigate the transient dynamics of Cascade complexes (Fig. 3, right).

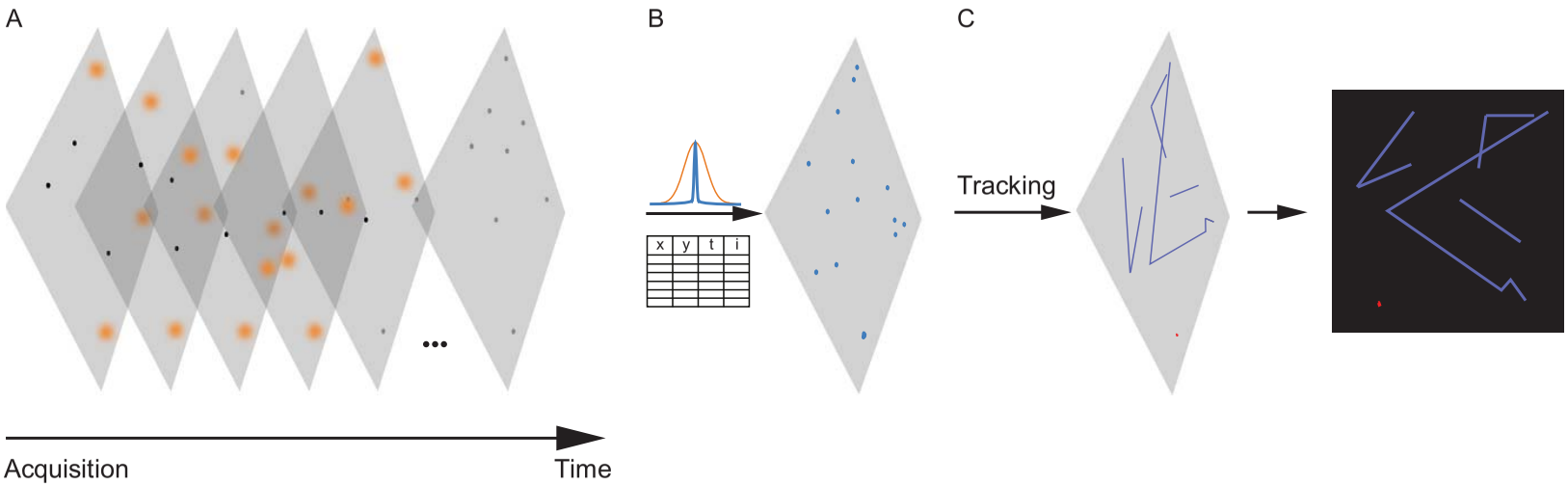

Fig. 2 Workflow of sptPALM. (A) Image acquisition: fluorescence signals of individual molecules are collected in an acquisition sequence. Fluorophores are photoswitched sequentially to spatially separate the individual signals; (B) localization routine: each fluorescent spot in form of a PSF is fitted by a localization algorithm to extract its centroid, which determines the fluorophores localization with nanometer precision; (C) tracking routine: localizations are classified into single-molecule trajectories by a tracking algorithm. The dynamics of the single proteins can be inferred from the obtained trajectories.

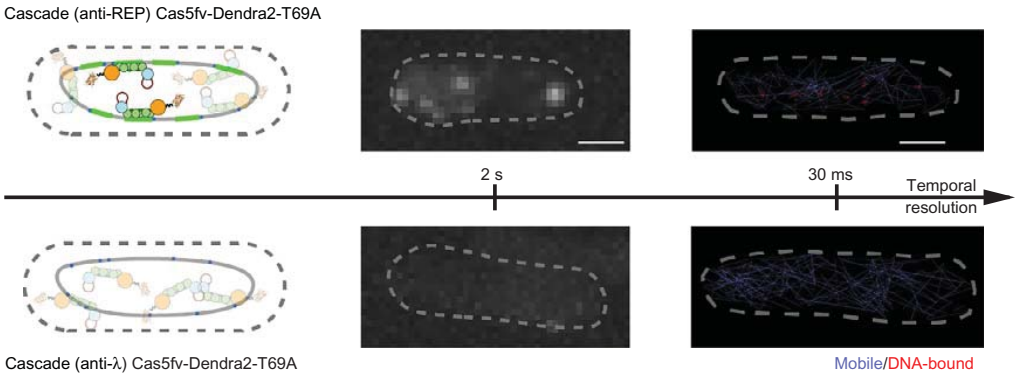

Fig. 3 Two *E. coli* strains expressing Cascade I-Fv complexes carrying different crRNAs. Here, the anti-REP crRNA is targeted against 16 sequences in the genome (*top panel*), the antilambda crRNA has no target sequence present in the host (*bottom panel*). Imaging with long integration times reveals Cascade complexes bound to their genomic targets while unbound Cascades are not detected. Faster imaging rates at higher temporal resolution visualize the DNA-bound and the mobile fractions of transient Cascade interference dynamics (*red* (JD $\leq$ 160 nm) and *blue* trajectories, respectively). Scale bars: 1 μm.

2. Generation of Cascade complexes with a fluorescent tag

In order to follow the dynamics of Type I CRISPR–Cas systems in vivo, the investigated crRNP complex needs to be tagged with a suitable photoswitchable fluorescent protein. For this purpose, two alternative strategies are possible. First, the CRISPR–Cas system can be studied in the native host organism which has to be suitable for direct imaging. Factors like low autofluorescence and the availability of genetic modification tools need to be considered. As a second option, it can be preferable to transfer the studied CRISPR–Cas system into a suitable host or model system. This protocol covers the imaging of heterologously expressed Type I-Fv CRISPR–Cas complexes from *S. putrefaciens* CN-32 in *E. coli* BL21-AI, which can be used to test a large variety of CRISPR–Cas systems from mesophilic organisms with similar codon usage. In this case, the transfer of the system was preferred due to the pink coloration of the host organism, a feature that interferes with fluorescent imaging. BL21-AI is a commonly used *E. coli* strain for the heterologous production of proteins and for studies on CRISPR–Cas activity, since it lacks endogenous *cas* genes (Brouns et al., 2008) and prophages. Furthermore, it carries the T7 polymerase gene under the control of the Ara promoter, allowing the use of T7 promoters for the controlled transcription of genes.

The selected fluorescent protein, Dendra2-T69A, has several advantages for sptPALM, such as high photon budget and well-controlled photophysics (Berardozzi, Adam, Martins, & Bourgeois, 2016), which is critical for precise localization and detection sensitivity when it comes to identifying highly mobile proteins. Additionally, it is a monomeric fluorescent protein like its direct ancestor Dendra2 and it is not suspected to oligomerize or form artificial aggregates (Wang, Moffitt, Dempsey, Xie, & Zhuang, 2014).

The Type I-Fv CRISPR–Cas system features a multiprotein effector complex and different Cas proteins are available for fluorescent tagging. In our approach, we determined the single Cas5fv subunit of Cascade to be optimal for tagging with Dendra2-T69A. Proteins with more than one copy per complex should not be selected for fusion, as this setup might lead to errors during data analysis. For example, if Cas7fv subunits were to be tagged, it would not be possible to discern two close-by fluorescent signals as separate Cascades or a single Cascade that was activated more than once.

Due to the large size of the *cas* gene operon of *S. putrefaciens* CN-32, we separated the genes into two different constructs to facilitate cloning into Duet vectors. Furthermore, the parallel generation of both amino- and carboxy-terminal protein fusions is suggested, since both the Cas protein and the fluorophore activity depends on proper folding, a property that is difficult to predict in silico. To minimize the risk of misfolding, we introduced a "GGGGS"-linker between the two proteins. Other linker options can be assessed if none of the fusions exhibits appropriate activity (Chen, Zaro, & Shen, 2013).

The use of genomic targets requires the generation of a nuclease-deficient system for in vivo imaging. For Type I systems, the HD nuclease domain is highly conserved for Cas3 proteins (Koonin et al., 2017), and the disruption of it is sufficient to abolish target cleavage for the Type I-Fv system (Dwarakanath et al., 2015).

Finally, for the successful imaging of target-bound Cascade, previous knowledge on the crRNA and target requirements of the complex is needed. The length of the spacer, the nature of the targeted molecule (DNA or RNA), and PAM specificity are essential variables to consider during experiment preparation. Further information on seed length and mismatch tolerance is extremely useful, as these parameters are directly related to Cascade retention time on the target and should be taken into account, both for experimental design (e.g., target selection) and data interpretation.

2.1 Target selection and oligonucleotide design for the cloning of CRISPR arrays

In order to study the target-binding dynamics of Cascade, three types of spacers were designed:

2.1.1 Control spacer with no targets on the genome

For this purpose, a 32 nt sequence that is complementary to a region of gene E from phage lambda flanked by the I-Fv PAM GG at the 3′ end of the target strand was selected (Gleditzsch et al., 2016). This spacer has no targets in the *E. coli* BL21-AI host genome and the longest observed stretch of complementarity spans only 9 nts. This crRNA can be used to determine the basal target search dynamics of Cascade and allows for testing the activity of the fluorescently labeled complex via efficiency of plaquing assays. The following spacer sequence was used: 5′-GGCGGCACGGAGTGGAGCAAGCGTGACAAGTC-3′.

2.1.2 Targeting spacer with full complementarity to the host genome

In order to study the DNA-binding dynamics of Cascade complexes, selection of appropriate targets is needed. These sites should be abundant, as it is difficult to study a single-binding event in the presence of noise from a larger pool of nonbinding complexes looking for targets. The use of plasmid targets is not recommended, as their polar localization in the cell might overlap with inclusion bodies due to protein overexpression. Furthermore, the reduced cellular size at this position poses a challenge for single-particle tracking, due to higher "bouncing" of the molecules against the cell membrane. An alternative solution is the generation of synthetic target arrays by insertion of large repeat-constructs into the *E. coli* genome, as this allows controlling the number and position of targets. A previous study on Cas9 dynamics utilized an array of LacO sites (Jones et al., 2017); however, the short length of these elements (23 bp) makes it inapplicable for Type I CRISPR–Cas systems, where spacers are longer than 30 bp. The insertion of target arrays with longer protospacers would constitute a challenge for genome stability, as repeat sequences over 27 bp are subject to homologous recombination by RecBC (Shen & Huang, 1986). Insertion of individual targets throughout the genome is also a possibility, although very arduous and time-consuming.

A simpler option, suitable for Cascade targeting, is the use of the repetitive elements already present in the *E. coli* genome. Due to the size constrains previously described, we selected the 35-bp long repetitive extragenic palindromic (REP) elements (Tobes & Ramos, 2005). These elements are highly suitable targets, since they are of the appropriate size,

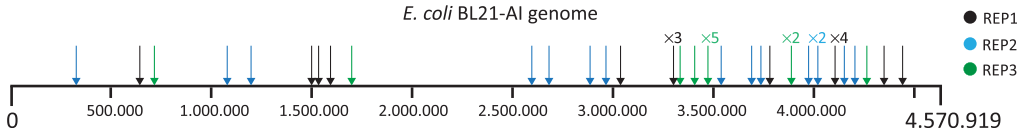

Fig. 4 Distribution of targeted REP elements throughout the *E. coli* BL21-AI genome. Schematic representation of the *E. coli* BL21-AI genome, with *arrows* indicating the positions of the protospacers targeted by the different spacers used to study the dynamics of Cascade complexes. *Black arrows* represent the targets for spacer REP1, *blue arrows* for REP2, and *green arrows* for REP 3.

contain a GG to act as PAM and are distributed throughout the genome (Fig. 4). The natural distribution of targets provides variability, since not all of them might be available for targeting at all times in live cells.

The crRNP complex vs target ratio should be taken into consideration when determining the amount of spacers that the CRISPR array should carry. As an optimal ratio of 1:1 is difficult to accomplish, it is suggested to utilize a maximum number of targets to then control the ratio by modulating the induction levels of Cascade. When targeting REP elements with a 32 nt spacer, full targets can be increased from 16, with a single spacer (REP1: 5′-GGATGCGGCGTAAACGCCTTATCCGGCCTACG-3′), to 42 with 3 spacers (REP2: 5′-GGATGCGGCGTAAACGCCTTATCCGGCCTACA-3′, REP3: 5′-GGATGCGGCGTGAACGCCTTATCCGGCCTACG-3′), due to the presence of mismatches at positions 32 and 12 of the protospacers. Imaging of Cascades carrying only 1 spacer variant or all 3 variants gives further insights into the dynamics of the complex, as not only the total number of targets increases, but also the number of incomplete intermediates. Furthermore, as the crRNA is the limiting component for Cascade formation, the increase of spacer number would also promote Cascade formation.

2.1.3 Targeting spacer with reduced complementarity to regions of the genome

The design of spacers with partial complementarity allows for studying the stability of the DNA-binding events and the retention time of the complex. Since Cas7 subunits cover 6 nt intervals of the crRNA for Cascade and other Class I CRISPR–Cas system, the design of spacers with 6 nt increasing complementarity to the REP elements allows for the study of possible R-loop variants. For this, spacers REP1, REP2, and REP3 were modified to have complementarities of 30, 24, 18, and 12 nt to the genomic targets, including randomized sequences with no complementarity to the host DNA to

complete the 32 nt spacer stretch. Since REP1 and REP2 sequences are identical apart from the last nucleotide of the spacer (in order to cover targets with a mismatch at position 32), when designing crRNAs with 30 bp of complementarity or less, the CRISPR array can be reduced to only two spacers. Table 1 shows all the intermediate spacers and the total amount of incomplete targets in the genome. By shifting the spacer toward an appropriate PAM and modulating the spacer length, the presented sequences can be adjusted to guide other interference complexes, with the REP sequence length of 35 bp as only constraint.

For *S. putrefaciens* CN-32 Type I-Fv systems, the repeat sequence has been defined as 5′-GTTCACCGCCGCACAGGCGGCTTAGAAA-3′ (Dwarakanath et al., 2015). When studying other systems, the repeat sequence can be predicted using the CRISPRFinder tool (Couvin et al., 2018; Grissa et al., 2007b), if the organism is not already listed in the CRISPRdb database (Grissa, Vergnaud, & Pourcel, 2007a). Array directionality is relevant for determining the proper repeat sequence and can be predicted using CRISPRDetect (Biswas, Staals, Morales, Fineran, & Brown, 2016). Type I repeats usually carry a short adenine stretch at the 3′ end, providing additional support for the correct directionality prediction of the repeat.

For the cloning of the previously selected spacers as CRISPR arrays, two different strategies were utilized. Single spacer arrays were designed on complementary oligonucleotides pairs carrying corresponding restriction sites at their ends (Fig. 5, bottom). For multiplexed sequences, synthesis of the arrays was necessary in order to avoid assembly errors due to the amount of repeats. For these constructs, the same restriction sites as for the minimal CRISPR were added to flank the array.

2.2 Oligonucleotide design for the cloning of *cas* genes

Cas genes are encoded in large operons. The *S. putrefaciens* CN-32 *cas* gene operon comprises genes encoding for Cas1, Cas2–3, Cas7fv, Cas5fv, and Cas6f, at a total size of 6.457 bp. As Cas1 is needed for adaptation, but its role in interference was deemed negligible (Brouns et al., 2008; Dwarakanath et al., 2015), this gene was excluded from the cloning strategy. In order to facilitate the assembly of the required plasmids, the operon was split and oligonucleotides were designed to introduce all the components into two multiple cloning sites of Duet vectors. In order to promote complex formation in *E. coli*, the genes *cas7fv* and *cas6f* were introduced into pRSFDuet-1, a high-copy plasmid (around 100 copies per cell), while

Table 1 Sequence and target number of spacers with partial complementarity to REP elements on the *E. coli* BL21-AI genome

crRNA–DNA complementarity (bp)	Sequence REP1	Sequence REP2	Number of genomic targets
30	GGATGCGGCGTAAACGCCTTATCCGGCCTAAT	GGATGCGGCGTGAACGCCTTATCCGGCCTAGC	75
24	GGATGCGGCGTAAACGCCTTATCCGAAACGTT	GGATGCGGCGTGAACGCCTTATCCCGATAGGT	99
18	GGATGCGGCGTAAACGCCCCTGTTCGTGTCGT	GGATGCGGCGTGAACGCCATCGGTAAATAGCC	107
12	GGATGCGGCGTACCGCGGAGCCATGTGCCATA	GGATGCGGCGTGCTCGTCTGCGGAGCACTCTG	133

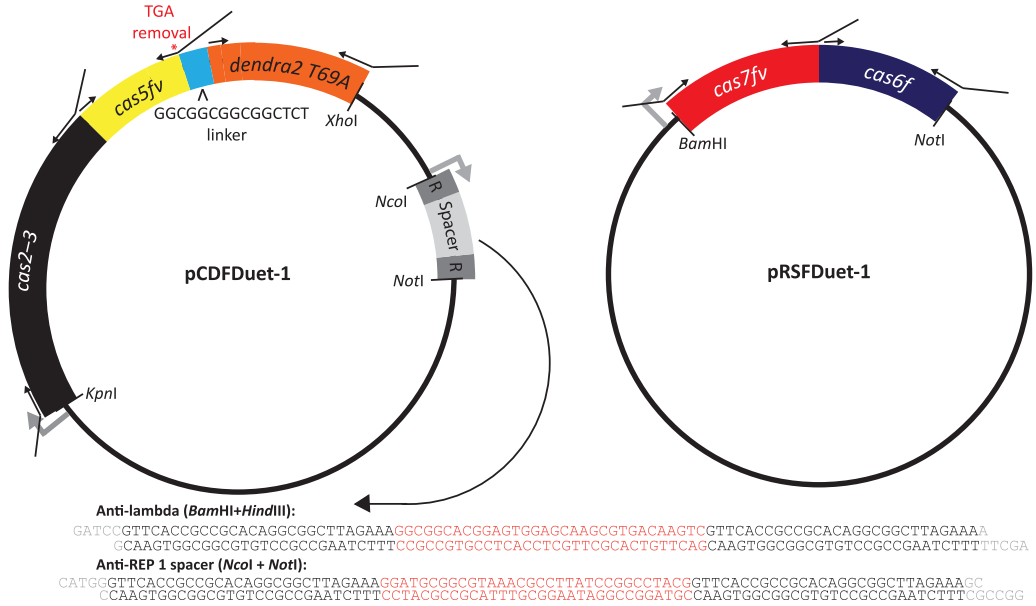

Fig. 5 Cloning strategy for the generation of fluorescently labeled Cascade. T7 promoters are shown as *light gray arrows*, while Gibson Assembly primers are shown as *small black arrows* including in diagonal the overlapping regions needed for assembly. R stands for repeat sequence. Due to size constraints, the *cas* operon was divided and rearranged into two fragments. *Left*: *cas2–3* and the *cas5fv-dendra2-T69A* fusion (carboxy-terminus with the corresponding linker shown as example) was introduced into the second multiple cloning site of pCDFDuet-1. On the first multiple cloning site of the same backbone, variants of a minimal CRISPR array were introduced either by oligonucleotide annealing or restriction enzyme digestion and ligation. Both array versions generated by the first technique are shown, with the generated restriction sites in *light gray*, the repeat sequence in *black* and the spacer in *red* (*bottom*). *Right*: *cas7fv* and *cas6f* were cloned together as an operon by Gibson Assembly onto the first multiple cloning site of pRSFDuet-1.

cas2–3 and the *cas5fv-dendra2-T69A* fusion was designed to be inserted in the second multiple cloning site of pCDFDuet-1, a plasmid of lower copy number (approximately 20 copies per cell). This plasmid was also designed to carry the minimal CRISPR arrays. For the fluorescent fusion, the sequence coding for a "GGGGS" linker was added to the corresponding oligonucleotides for amplifying *cas5fv* and *dendra2-T69A*, either upstream or downstream of the *cas* gene to generate amino- or carboxy-tagged versions, respectively.

An overview of the oligonucleotides designed for cloning these constructs, as well as the resulting plasmids, is shown in Fig. 5. Gibson assembly (Gibson et al., 2009) requires a cleaved backbone in addition to PCR fragments of the components to be assembled together. The proper arrangement of the fragments is achieved by annealing of the fragments with overlapping regions of at least 30 bp. Incorporation of these sequences occurs during the

PCR reaction, since the oligonucleotides used to amplify each unit carry these extra nucleotides. For oligonucleotide design, corresponding 30 nt overlapping sequences (diagonal sections of the black arrows in Fig. 5) were added to the 20 nt sequence stretch needed for regular PCR amplification. Randomized nucleotides were added between genes, in addition to ribosome-binding sites to ensure translation of all the components in the operon. Restriction sites were chosen to not cleave the previously designed CRISPR arrays, since these would be cloned first into the plasmids, and added to the corresponding oligonucleotides.

As genomic targeting requires the expression of a nuclease-deficient Cas2–3 protein, oligonucleotides for site-directed mutagenesis were designed by using the online tool "QuikChange primer design" from Agilent (https://www.agilent.com/store/primerDesignProgram.jsp), in order to mutate the HD domain by alanine replacement (H156A/D157A). These mutations were previously described to be sufficient for abolishing CRISPR–Cas interference activity (Dwarakanath et al., 2015).

2.3 Plasmid generation

As a first approach, the antilambda CRISPR array was introduced into the *Bam*HI and *Hind*III sites of pCDFDuet-1 by oligonucleotide annealing (Fig. 5, bottom) (Zoephel, Dwarakanath, Richter, Plagens, & Randau, 2012). Synthesized oligonucleotides were phosphorylated, mixed at equal molar ratio, heated up to remove secondary structures, and cooled down slowly to promote annealing. The duplex, which carries sticky ends generated by incomplete annealing at the oligonucleotide termini, was then ligated into a restricted pCDFDuet-1 vector. Array insertion was corroborated by Sanger sequencing, and downstream cloning of *cas2–3* and the *cas5fv* fluorescent fusions was performed by Gibson assembly. In order to determine the activity of amino- and carboxy-fusions of Cas5fv and Dendra2-T69A and to select the most appropriate option, both constructs and *cas2–3* were cloned into the second multiple cloning site of the antilambda pCDFDuet-1 using *Kpn*I and *Xho*I restriction sites. The genes were amplified with the corresponding oligonucleotides carrying overlapping regions, and the resulting PCR fragments were mixed with the cleaved backbone at a ratio of 3:1. After addition of 2 × Gibson Assembly Master Mix (NEB), samples were incubated for 1 h at 50°C and transformed into chemically competent *E. coli* DH5α cells. Following overnight growth at 37°C, plasmids were extracted and correct plasmid assembly was confirmed by Sanger sequencing.

Cas2–3 nuclease deficient constructs were generated by site-directed mutagenesis by use of the QuikChange Site Directed Mutagenesis Kit (Agilent) and the previously described oligonucleotides, following the manufacturer's protocol.

Once fluorescence readout and Cascade interference were determined, the best performing fusion plasmid was modified by insertion of the remaining REP-targeting arrays into the plasmid encoding for the Cas2–3 HD mutant.

The CRISPR array carrying a single spacer against the REP elements was cloned by oligonucleotide annealing (Fig. 5, bottom), while multiplexed arrays previously synthesized (Sigma-Aldrich) were introduced by restriction enzyme digestion and ligation. These constructs were cloned into the first multiple cloning site of pCDFDuet-1 using the restriction sites *Nco*I and *Not*I, excluding the ribosome-binding site and the His-tag present on the empty backbone. Array insertions were corroborated by Sanger sequencing.

In parallel, empty pRSFDuet-1 was digested by *Bam*HI and *Not*I restriction enzymes, and *cas7fv* plus *cas6f* were cloned by Gibson Assembly into this site, as depicted in Fig. 5, right.

3. Heterologous expression of Cascade

The described plasmids were used to transform the expression strain, in order to test the activity of the fluorescent protein and Cascade. In addition, optimal expression conditions were screened.

3.1 Transformation into BL21-AI

3.1.1 Generation of strains for the evaluation of Cascade activity

In order to determine the activity of the tagged complex, 100 ng of plasmid combinations were introduced by heat shock into 100 μL aliquots of chemically competent *E. coli* BL21-AI (Invitrogen). Strains were designed to carry one version of pRSFDuet-1 and one of pCDFDuet-1, which exhibit compatible antibiotic resistance against kanamycin and spectinomycin.

i. Positive lambda control: pCDFDuet-1 and pRSFDuet-1 empty backbones. This strain, when subjected to infection, displays the full plaquing activity of the bacteriophage and was utilized as a normalization strain for the experiment and imaging.
ii. Positive wild-type Cascade control: pCDFDuet-1 carrying the anti-lambda CRISPR array and pRSFDuet-1 encoding for the nontagged

Cas operon (excluding Cas1). This strain was utilized as a comparison point for the activity of the Cascades carrying a fluorescent fusion of Cas5fv.

iii. Negative wild-type Cascade control: pCDFDuet-1 carrying the anti-lambda CRISPR array and pRSFDuet-1 encoding for the nontagged Cas operon with the Cas2–3 HD mutant (excluding Cas1). This strain allows linking the reduction of plaquing efficiency (if any) to Cascade activity.

iv. Positive Cascade-Dendra2-T69A: pCDFDuet-1 carrying the anti-lambda CRISPR array plus one of the Cas2–3/Cas5fv-Dendra2-T69A fusion version (Cas5fv amino- or carboxy-tagged), in addition to pRSFDuet-1 encoding for Cas7fv and Cas6f.

v. Negative Cascade-Dendra2-T69A: pCDFDuet-1 carrying the anti-lambda CRISPR array plus one of the Cas2–3 HD mutant/Cas5fv-Dendra2-T69A fusion version (Cas5fv amino- or carboxy-tagged), in addition to pRSFDuet-1 encoding for Cas7fv and Cas6f.

3.1.2 Generation of strains for sptPALM imaging

100 μL aliquots of chemically competent *E. coli* BL21-AI cells were transformed by heat shock with 100 ng of a pCDFDuet-1 plasmid variant carrying the different CRISPR arrays and the *cas2–3* HD mutant/*cas5fv-dendra2-T69A* cassette; plus 100 ng of pRSFDuet-1 plasmid encoding for Cas7fv and Cas6f. A total of six strains were generated, one per each pCDFDuet-1 plasmid with a CRISPR array described in Section 2.1.1: four with partial complementarity to the REP elements, one with full complementarity, and one complementary to gene E of the bacteriophage lambda.

3.2 Evaluation of the fluorescent signal of Cascade-Dendra2-T69A

As a first approach to corroborate the activity of the tagged complex, the fluorescence signal of the fusions was tested by fluorescence microscopy, taking advantage of the preconverted state of Dendra2-T69A. In this conformation, the fluorescent protein exhibits a similar excitation and emission spectrum as GFP (excitation: 502 nm, emission: 518 nm) (Berardozzi et al., 2016), allowing for the imaging with microscope setups programmed to visualize this commonly used reporter protein.

To guarantee that the obtained signal is Dendra2-T69A dependent, strains carrying empty plasmids and expressing the fluorescent protein alone were generated as negative and positive controls, respectively. Single

colonies of the strains expressing both plasmids necessary for fluorescent Cascade formation plus the controls were grown overnight at 37°C, with shaking at 200 rpm in 5 mL of 2YTL media (16 g/L tryptone, 10 g/L yeast extract, 5 g/L NaCl, 10 m*M* $MgSO_4$, 0.2% maltose) plus 25 μg/mL of spectinomycin and kanamycin.

Cells were reinoculated at a ratio of 1:100 into 20 mL of fresh 2YTL media with antibiotics and grown at 37°C, 200 rpm, until $OD_{600nm} = 0.3$. All cultures were induced by addition of 0.2% of arabinose and 0.1 m*M* of IPTG (Sigma-Aldrich) and grown until $OD_{600nm} = 0.6$. For all strains, 1 mL of culture was pelleted at 4000 × *g* for 2 min and resuspended in 50 μL of 1 × phosphate-buffered saline (PBS, NaCl 137 m*M*, KCl 2.7 m*M*, Na_2HPO_4 10 m*M*, KH_2PO_4 1.8 m*M*).

Agarose pads were prepared by pipetting 300 μL of 2% agarose in 1 × PBS into a glass slide, avoiding bubbles, and then covering it with an extra glass slide. When dried, the top slide was removed and 10 μL of the cell suspension was placed on the middle of the pad and covered with a glass slip, avoiding bubble formation.

Cells were imaged at 100 × magnification with the Zeiss Axioplan II microscope with filter sets for GFP detection (bandpass 470/20, beam splitter 493, bandpass 505–530 nm; Zeiss), using the negative control to set the background noise and the positive control to test the proper selection of excitation and emission wavelengths. Photographs were taken with the charged-coupled camera CoolSNAPHQ (Photometrics). Image processing was done with MetaMorph software, version 6.2r6 (Universal Imaging). For Type I-Fv Cascade-Dendra2-T69A, both amino- and carboxy fusions displayed the expected fluorescent emission. Imaged cells presented fluorescent cell poles, indicating the formation of inclusion bodies, likely caused by protein overexpression. To minimize this issue, decreased induction conditions were tested, with expression induced by the addition of only 0.1% arabinose (inducing T7 polymerase production, but not lifting *Lac*I repression) was deemed to be optimal for further sptPALM experiments, with clear fluorescence signals and good cell morphology.

3.3 Evaluation of Cascade activity by efficiency of plaquing assays

To confirm the activity of fluorescent Cascade variants, strains described in Section 3.1.1 were challenged in efficiency of plaquing (EOP) assays with a lytic version of phage lambda (NCCB 3467) carrying an unaltered protospacer targeted by the CRISPR arrays present on the strains.

Single colonies from the required strains were grown overnight at 37°C, 200 rpm shaking, in 5 mL of 2YTL media supplemented with 25 μg/mL of spectinomycin and kanamycin.

Cells were reinoculated into 20 mL of fresh 2YTL media (with antibiotics) at a ratio of 1:100 and grown at 37°C, 200 rpm, until $OD_{600nm} = 0.3$. All cultures were induced by addition of 0.2% of arabinose and 0.1 m*M* of IPTG and grown for 30 min under consistent conditions.

During incubation, serial dilutions of the lambda phage were prepared by dilution of the initial stock on SM buffer (NaCl 100 m*M*, $MgSO_4 \times 7\ H_2O$ 8 m*M*, Tris–HCl pH 7.5 50 m*M*, Gelatin 0.01% (w/v)) and stored at 4°C. Dilutions were determined according to the phage titer of the stock in order to obtain a quantifiable amount of plaques on the final plates.

Cell cultures were pelleted by centrifugation at 4000 × *g* for 10 min at 4°C, the supernatant was discarded and pellets were resuspended in 8 mL of 10 m*M* $MgSO_4$. 100 μL of phage dilutions were mixed with 100 μL of cell suspension in 1.5 mL reaction tubes for all of the tested strains/phage dilutions. As controls, 100 μL of 10^{-1} phage dilution was mixed with 100 μL of cell-free 10 m*M* $MgSO_4$, while 100 μL of the empty plasmid control strain was mixed with 100 μL of phage-free SM buffer. In order to promote phage absorption, samples were incubated for 20 min at 37°C without shaking.

During this interval, 2YTL soft agar (2YTL media with 7.5 g/L of agar), supplemented with inducers (0.2% arabinose and 0.1 m*M* IPTG), was aliquoted into 15-mL glass culture tubes that were prewarmed at 49°C. Each tube was filled with 3 mL of soft agar and stored at 49°C in a water bath until samples were ready. After incubation, 200 μL of phage-cell mixes were added to 3 mL of soft agar, lightly vortexed and poured on top of 2YTL agar plates supplemented with antibiotics. After drying of the soft agar, plates were incubated upside down at 37°C overnight.

The following day, growth was assessed on control plates and, when no cross-contamination was detected, plaque numbers were determined for plates with appropriate phage dilution. Efficiency of plaquing was determined as the ratio of plaques formed on the lawn of the strain of interest vs the number of plaques for the strain carrying empty plasmids.

In order to confirm the activity of the fluorescent Cascade, this assay was performed in triplicates starting from three different colonies of the initial strains.

For Type I-Fv Cascade, the carboxy-terminal Cas5fv fusion revealed activity that resembled wild-type Cascade activity and this construct was chosen for subsequent single-particle tracking experiments.

4. sptPALM imaging of Cascade interference

4.1 Sample preparation for sptPALM imaging

Imaging of single fluorophores in sptPALM experiments demands for highly optimized sample preparations as the sensitivity of the method makes it prone to detect background signals. Background signals stemming from the imaged organism itself are common, e.g., due to colorful pigments (e.g., cyanobacteria possessing chlorophyll or bacteria producing red pigments like *S. putrefaciens* or *Serratia marcescens*). Other background signals can be commonly traced back to particular growth conditions. For sptPALM, only high-purity grade chemicals and defined colorless growth media such as EZ Rich-defined medium (EZRDM, Teknova-M2105) should be used (Fig. 6A). Furthermore, changing the growth temperature might reduce the background as dying cells become highly autofluorescent (Fig. 6B).

Impurities on coverslips and microscope slides are removed before using them. Commonly used cleaning protocols include cleaning with KOH (optionally with sonication) (Stehbens, Pemble, Murrow, & Wittmann, 2012; Turkowyd et al., 2017; Virant, Turkowyd, Balinovic, & Endesfelder, 2017), sonication in different organic solvents or detergents (Preciado Lopez et al., 2014; Stehbens et al., 2012), plasma cleaning (Lelek, Di Nunzio, & Zimmer, 2014), and cleaning with piranha solution (Simms, Bowman, & Anseth, 2008) or base piranha solution (Preciado Lopez et al., 2014). For this study, overnight cleaning in 1 *M* KOH (Sigma-221473) was selected. It is strongly recommended to use high-precision coverslips of well-defined thickness of 170 μm (matching the objective working distance), critical for undistorted PSF detection. Cleaned microscope slides and coverslips (Carl Roth H884.1 and LH25.1, respectively) were prepared in a ratio of 2:1 and were stored in ddH_2O (Fig. 7).

Cellular stress leads to the production of metabolites that are often autofluorescent. In order to avoid stress while imaging, the agarose solution for cell mounting was prepared by dilution in growth medium. Here, 1% agarose pads were prepared with EZRDM. Pads can be prepared in two ways: (i) 2% agarose solution in ultrapure water is heated up to melt the agarose and afterward mixed with a room temperature 2× media stock (Uphoff, Reyes-Lamothe, Garza de Leon, Sherratt, & Kapanidis, 2013; Zawadzki et al., 2015). This procedure avoids heating the media, avoiding thermal degradation; (ii) 1% of low gelling and fluorescence-free agarose is suspended in media and heated up to 70°C until agarose melts (Turkowyd et al., 2017; Virant et al., 2017).

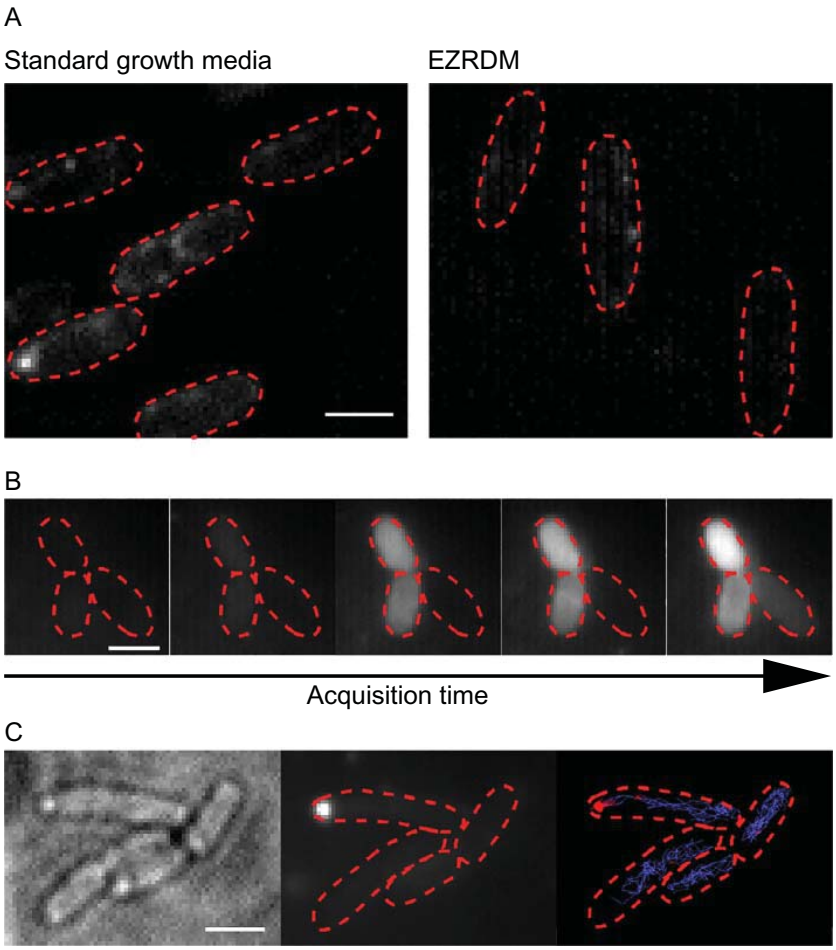

Fig. 6 Background noise and artifacts of different causes. (A) Using colorful growth media might cause cellular background noise (*left*), defined colorless media reduces unwanted signal (*right*). (B) High laser intensity might lead to cell death during imaging which is manifested by increasing background intensity over time (*left to right*, each image is a fluorescence average of each 1000 imaging frames); the cell in the lower right corner reacts later than the other two cells. (C) Overexpression of Cas proteins can cause aggregation of these proteins in inclusion bodies at cell pole, which is clearly visible in bright light (*left*) as well as in the fluorescence readout channel (*middle*) and finally in an unfiltered trajectory map (*right*). Scale bars: 2 μm.

The second approach has the advantage of a homogenous consistence (mixing hot agarose with room temperature media can cause agarose clumps) and the solution can be stored at 37°C after melting without the risk of gelling, which is convenient when preparing more agarose pads. In this study, the second approach with low-gelling agarose (Sigma-A9414) was used. Cooled down agarose was loaded onto a cleaned microscope slide with mold and covered with a clean coverslip. Agarose pads should be incubated for 90 min before use, in order to allow the agarose to settle. They can be used up to 5 h after preparation.

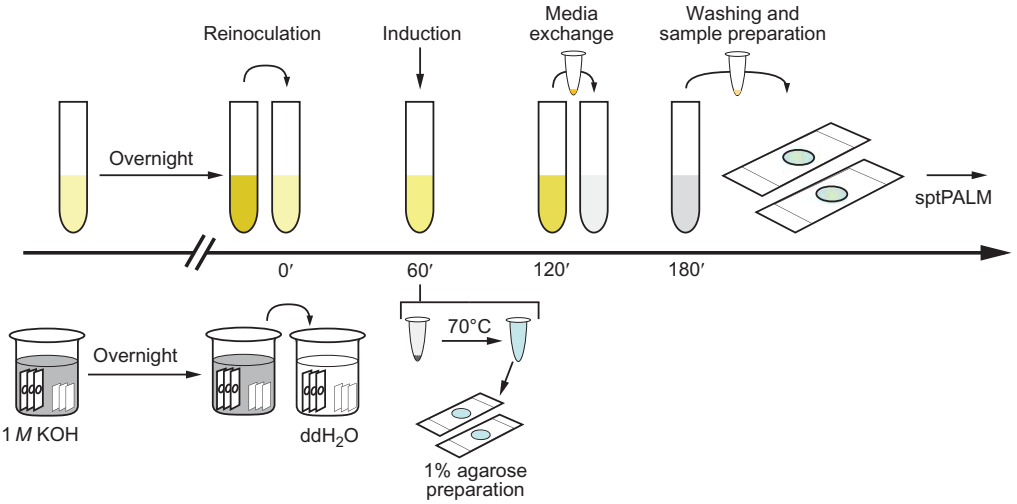

Fig. 7 Timeline of sptPALM sample preparation. *Top*: culture incubation, induction, and cell washing steps. *Bottom*: cleaning microscope slides and coverslips, and agarose pads preparation.

Controlled culture cultivation and induction conditions are essential for reproducible sptPALM experiments (Fig. 7). Here, initial cultures were prepared in liquid 2YTL media with spectinomycin and kanamycin (both 25 μg/mL) and grown overnight at 37°C under shaking at 210 rpm. On the next day, cells were reinoculated in 1:100 dilutions into fresh 2YTL without drugs and incubated at 37°C. At $OD_{600nm} = 0.05$, the expression of Cascade proteins and crRNA was induced by adding arabinose to a final concentration 0.1% (w/v) to prevent Cascade proteins accumulation in inclusion bodies at the cell poles (Fig. 6C). After incubation for 1 h, cultures were pelleted, 2YTL supernatant discarded and replaced by EZRDM with 2% glucose. This sugar inhibits the Ara promoter, blocking induction and hindering protein overexpression. Subsequently, cells were grown for another hour to allow the fluorescent proteins to mature as well as the Cascade complexes to assemble. This is the last step where it is possible to transfer the cells to a defined media suitable for sptPALM imaging (see Fig. 6A). 500 μL of culture was centrifuged (3000 × *g*, 2 min), pellet was washed twice with fresh EZRDM and suspended in 50 μL of EZRDM. After removing the coverslip from an earlier prepared agarose pad, 2 μL of cell suspension was loaded onto the pad, sealed with a new coverslip, and gently pressed to remove any excess of liquid. Slides were incubated for 15 min on the bench in darkness to allow cells to settle down on the pad. Afterward, the sample was gently pressed with a wipe to fully dry the coverslip. Avoid applying too much pressure on the slide, as the coverslip could be invaginated toward the pad, which will cause tension in the agarose and subsequently lead to sample drift while imaging.

4.2 Microscope settings and sptPALM imaging routines

For this study, a SMLM setup consisting of a Nikon Ti Eclipse inverted microscope equipped with a custom-build excitation path and a custom-build heating chamber and heating objective ring was used. 50 mW 405 nm and 150 mW 561 nm lasers (both OBIS Free-space Beam, Coherent Inc.) were controlled by OBIS LX/LS Scientific Remote and were coupled into the microscope optical excitation pathway by using Thorlabs-BB1-E02 set of mirrors and AHF Analysentechnik-F38-M01 and F38-M05 dichroic mirrors. Illumination was controlled (wavelength and intensities) via an acousto-optical tunable filter (AOTF TF525-250-6-3-GH18A, Gooch & Housego) in combination with the ESio AOTF controller (ESio). Beams passing the AOTF were adjusted in spot size using a 10× telescope of two lenses (25 mm focal length and 250 mm focal length). After passing a piezo sensor-controlled TIRF mirror (piezo KC1-PZ/M with MDT693B controller, Thorlabs), the laser beam was focused on the backfocal plane of the objective by a focusing lens (50.8 mm diameter, 300 mm focal length) being reflected by dichroic mirror (AHF Analysentechnik-F68-010) into the immersion objective (CFI Apo TIRF 100× oil objective, NA 1.49, Nikon, immersion oil Type F, Nikon). For detection, fluorescence signals passed through the above-mentioned dichroic mirror, a rejection filter (AHF Analysentechnik-F67-408), and bandpass filter (AHF Analysentechnik-F49-617) and were directed to the EM-CCD camera (iXon Ultra 888, Andor). Most of the setup, except heating chamber and ring and laser remote controller, was controlled via a customized version of Micro-Manager (Edelstein et al., 2014), an open source plugin for Fiji (ImageJ) (Schindelin et al., 2012).

The fluorescence signal readout quality can be improved by enhancing the signal-to-noise ratio using different illumination modes. For normal epi-fluorescence illuminations, the laser light passes throughout the entire sample and could induce background signal. To avoid this, one option is the optical sectioning by total internal reflection fluorescence microscopy (TIRF), where laser beam is totally internally reflected at the coverslip-sample boundary (Axelrod, 2003). Only fluorophores in a thin layer above the coverslip (approximately 200 nm) are illuminated and thus fluoresce. Another approach is to use a highly illuminated and laminated optical sheet (HiLo), where laser light passes through the coverslip at a narrow angle (Tokunaga, Imamoto, & Sakata-Sogawa, 2008). For our studies, HiLo mode was selected, as Cascade complexes can diffuse throughout the whole cellular thickness of about 1 μm.

As already indicated by in vitro single-molecule studies on CRISPR–Cas systems, Cascade–DNA interactions can span from seconds (DNA probing for PAM recognition, R-loop formation) to minutes (locked Cascade state recruiting Cas3) (Blosser et al., 2015). Thereby, to investigate all these interactions, multiple sptPALM imaging experiments spanning different temporal ranges were designed. Fast sptPALM imaging with frame rates of 30–100 Hz enables to detect Cascade complexes in different diffusive and binding states. From all trajectories, a spatial diffusion map of each individual cell can be reconstructed, which visualizes the different dynamics within the cellular volume (e.g., shown in Fig. 3). sptPALM imaging at slow speed and long camera integration time enables to visualize only immobile and slowly diffusing Cascades as fast diffusive signals blur out. The total fluorescence budget of the fluorophore can be flexibly adjusted to resolve the protein dynamics at different temporal scales: by increasing the imaging interval times introducing a variable gap time without prolonging the camera integration and laser excitation times, it is possible to track individual molecules for a longer time range. Thus, second-long bound times of Cascade complexes on full DNA–targets can also be determined. With this imaging mode, Cascades bound to genomic targets are easily traced until unbinding due to the nearly immobile nature of the nucleoid.

4.2.1 Measuring transient Cascade–target interactions at a high spatiotemporal resolution

1. The sample was placed on the heating stage and incubated for 15 min to equilibrate the temperature, since diffusion is dependent on this parameter. Before imaging, the stage was switched on for 2 h to equilibrate at 25°C.
2. Camera integration times were set to 13 and 30 ms on independent imaging experiments. Recording two temporal regimes is recommended, as this can reveal different diffusive states and different natures of several interactions by changes in the observed dynamics (e.g., the displacement between frames) of stable and transient states with different kinetics.
3. Intensities for 405 and 561 nm lasers were set to 5 and 800 W/cm^2, respectively, for 13 ms integration time and to 5 and 450 W/cm^2, respectively, for 30 ms integration time. For fluorescence readout (561 nm laser), continuous illumination was used. Faster acquisitions require higher readout laser intensities to obtain sufficient signal-to-noise ratios.

Excessive intensity, however, should be avoided, as it causes faster bleaching and pronounced blinking of fluorescent proteins, which leads to shorter trajectories (typically, the fluorescence budget of a fluorescent protein can be spread onto on average 10–20 imaging frames). Additionally, this setup might be phototoxic to cells. Photoconversion laser (405 nm) should be used at the lowest suitable intensity and in a pulsed mode (e.g., every 10th frame) to keep the localizations per cell sparse. Importantly, different species in different environmental conditions have different sensitivity to intensive light. Thus, maximal imaging time ranges should be tested beforehand on wild-type strains (Turkowyd et al., 2017).

4. A series of controls were prepared and imaged under sptPALM conditions for 10,000–20,000 frames:
   i. Negative control without a fluorescent marker. It is mandatory to evaluate if any fluorescent signal from the cells themselves or within the agarose pad might mimic the fluorescence signal of the marker.
   ii. Cytosolic, free diffusing fluorescent marker. This is recommended for two reasons: (a) to check if the chosen fluorescent marker performs well in the cellular environment of the specific organism, as fluorescence signal depends on pH, redox potentials, and oxygen; and (b) to evaluate how fast the fluorescent protein, when not interacting with any cellular compound, diffuses freely. The latter is especially important, as any diffusion distribution of the tagged proteins of interest can be compared to the free diffusing fluorophore.
   iii. Immobile fluorescent marker (e.g., fixed cells). Despite the fact that the fluorophore is immobile under this condition, the obtained single-molecule trajectories will show a small residual oscillation due to the finite localization precision of the technique. Like the freely diffusive control, this serves as a suitable reference for nucleoid- or membrane-bound states, and thus immobile distributions of proteins of interest (lower limit of diffusion).
5. Regions of interest (ROIs) were imaged first for 20 frames in bright light mode, to obtain images of the cell outlines needed for cell segmentation (see Section 4.3.1) and afterward for 10.000–20.000 frames under sptPALM conditions. Multiple ROIs were obtained per sample to maximize the number of imaged cells. Frame number was selected in order to reduce phototoxicity effects, as it is better to collect shorter movies from multiple regions rather than long movies from fewer fields of view.

4.2.2 Measuring bound times of DNA–Cascade interference

1. The sample was placed on the heating stage and incubated for 15 min to equilibrate the temperature.
2. Interval time was adjusted in reference to the order of magnitude (milliseconds, seconds, etc.) expected for the investigated bound state. Camera integration time was set long enough to blur any mobile molecule, but also short enough to keep the readout time as minimal as possible to prevent early fluorescent protein bleaching. For measuring Cascade interference on full targets, the integration time was set to 200 ms with a 500 ms interval.
3. Laser readout intensity was adjusted to the lowest possible intensity which still provided a clear single-molecule fluorescence signal. As before, this prevents fluorophore bleaching and reduces blinking events. 30 W/cm^2 for the 561 nm laser was used. Intensity of the UV photoconversion laser was set to a minimum (1 W/cm^2) and in pulsed mode (every 50 frames).
4. The following controls were prepared and imaged:
   i. Negative control without fluorescent marker to ensure that cells themselves are not generating any background signal.
   ii. Cytosolic, free diffusing fluorescent marker. Useful to adjust imaging parameters, as camera integration times should be set at a slow speed which only shows homogenously fluorescent signal building up from freely diffusive molecules within the entire cell but should not reveal any defined fluorescent spots.
   iii. Immobile fluorescent marker. Since it is not possible to distinguish whether the disappearance of the fluorescence signal is due to fluorophore bleaching or to an unbinding event, the bleaching probability of the fluorophore under the readout conditions used has to be measured and used for bleaching correction. Furthermore, as fluorophores still might experience blinking events, these can be characterized on immobilized fluorescent proteins and be used as a parameter for tracking analysis.
5. Cells of interest were imaged for 4000 frames and several ROIs were taken per sample.

4.3 Localization and tracking routines

Data analysis to obtain single-molecule trajectories consists of the following steps (Fig. 8):

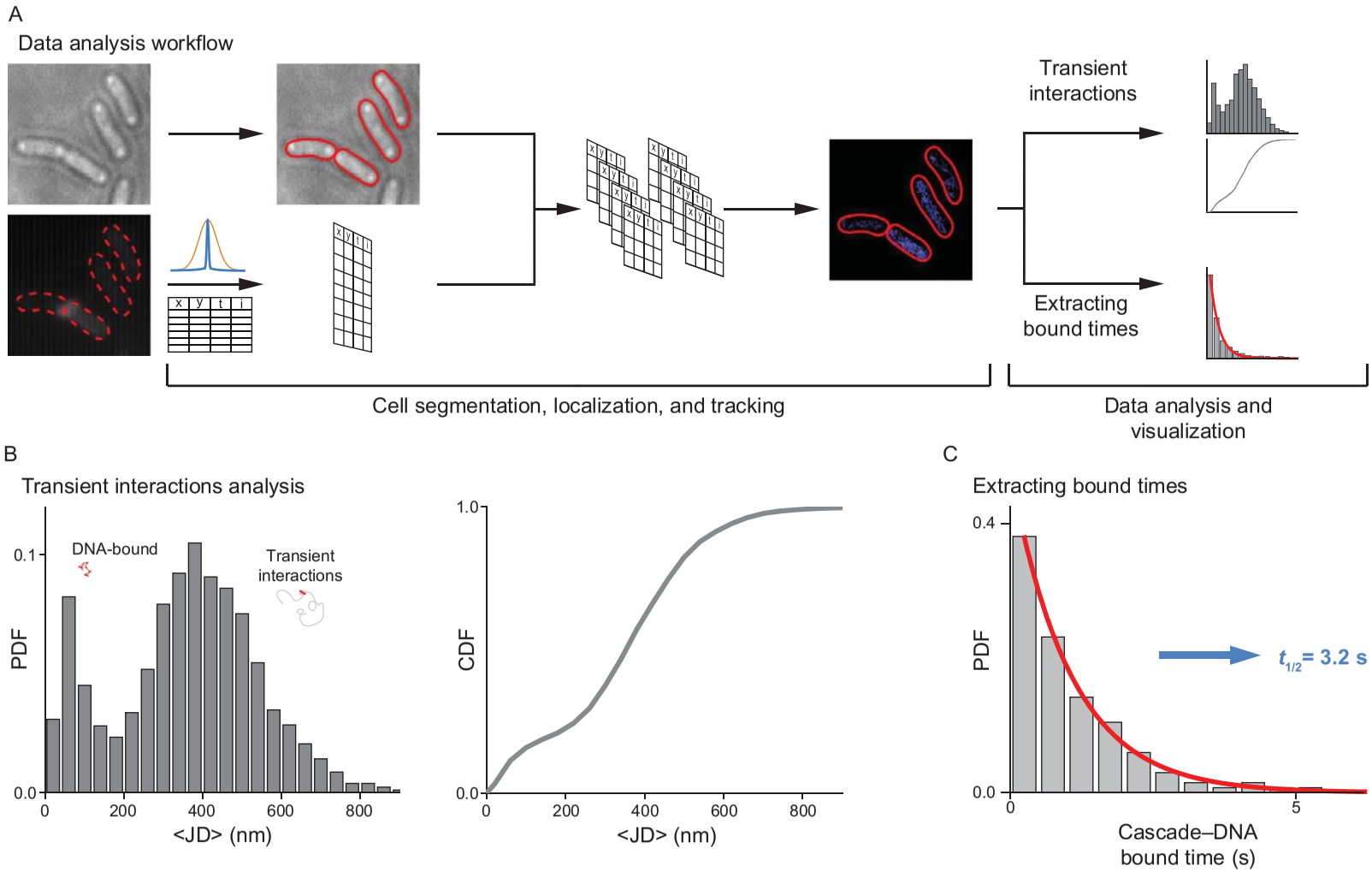

Fig. 8 See figure legend on opposite page.

4.3.1 Cell segmentation

This step is recommended for two reasons: (i) segmented cells provide some useful information about the sample (number of imaged cells, cell dimensions) and allow for sorting cells by their size/cell-cycle stage, number of localizations/trajectories per cell, cell heatmaps, etc.; (ii) cell segmentation prevents tracking artifacts by wrongly joining localizations from different, but spatially close cells into a single trajectory. Further, tracking is a computationally demanding process, and segmentation can reduce calculation times. Cell segmentation can be performed with multiple tools. The simplest, most accurate, but also time-consuming option is a manual segmentation: drawing ROIs from bright light images by hand in ImageJ (Fiji) (Schindelin et al., 2012). Segmentation can also be automatized by using different softwares like 3D Object Counter (ImageJ) (Bolte & Cordelieres, 2006), MorphoLibJ (Legland, Arganda-Carreras, & Andrey, 2016), or Oufti (Paintdakhi et al., 2016). Recently, machine learning and neural networks have been applied for image segmentation, with the use of softwares like DeepCell (Van Valen et al., 2016) or CDeep3M (Haberl et al., 2018). However, it should be pointed out that automatized segmentation might need manual correction. For this protocol, manual selection in Fiji was chosen as the most appropriate option.

4.3.2 Localization

SMLM is a localization-based method, which means that all data analyses are performed on localization coordinates having nanometer precision instead of being image based. This enables a wide range of analysis approaches like super-resolved image reconstruction, molecule-counting, clustering analysis, colocalization analysis, particle averaging, and particle

Fig. 8 Data processing workflow. (A) Cells were segmented based on bright light snapshots taken before sptPALM imaging (*top left*). In parallel, localizations were extracted based on PSF fitting (*bottom left*). Next, localizations were split into subarrays representing single cells and tracking was performed (*middle*). In case of fast imaging data were represented as histograms or cumulative distributions of averaged jump distances (*top right*). For slow imaging accessing the bound-time of complexes, data histograms representing fluorescence spot bound times were fitted to retrieve the average event lifetime (*bottom right*). (B) Data from transient interaction analysis represented in the form of probability density function (PDF) histogram (bin size = 40 nm) and cumulative distribution function (CDF). Exemplary trajectories for DNA-bound Cascade (*red trajectory*) and transiently interacting Cascade (*blue-red trajectory*). (C) PDF representing Cascade bound-time (bin size = 0.5 s) and single exponential model fitted to PDF.

tracking (Endesfelder et al., 2013; Lando et al., 2012; Loschberger, Franke, Krohne, van de Linde, & Sauer, 2014; Malkusch et al., 2012; Manley et al., 2008). Localization coordinates can be extracted from the imaging sequences by many different localization algorithms, which are discussed and compared in the following publications: (Sage et al., 2015; Small & Stahlheber, 2014). In this work, we use two localization software packages: rapidStorm (Wolter et al., 2012) and ThunderStorm (Ovesny, Krizek, Borkovec, Svindrych, & Hagen, 2014). In this step, it is important to select appropriate fitting and filtering parameters and thresholds, to sieve most of the noise signal, e.g., by an intensity threshold, as noise usually possesses lower intensities than fluorescence signals from fluorophores. On the other hand, too strong filtering might cause a huge loss of fluorophore detections, which might severely impact obtaining proper single-molecule trajectories. Furthermore, especially for slow frame rate data, where only immobile complexes are investigated, PSFs shape and dimensions are helpful filters. Signals from immobile particles have round PSFs of a typical diffracted spot size. Any asymmetric, elliptic, or differently sized PSF can be discarded as it can be attributed either to noise, multiple proximal fluorophores activated at the same time, or moving Cascade complexes.

4.3.3 Tracking

From the list of localizations, single-molecule trajectories of individual Cas proteins or Cascade complexes can be retrieved. The simplest and fastest method for single-particle tracking is the nearest neighbor (NN) algorithm, in which connections are made between localizations in adjacent frames and the distance between them is the lowest from all possible connections. This solution is sufficient when the density of localizations is low (around 1 event per frame per cell). For higher densities NN might wrongly connect different particles, thus bias the diffusion statistics when mixing different molecular states. This obstacle might be omitted by a simple filtering step, in which only localizations that have a sufficiently low density and thus only one possible neighbor in reach are connected. However, in this way some readout is lost, in effect decreasing the statistics. More sophisticated approaches, e.g., based on a priori knowledge about fluorophore photophysics and protein behavior (transition probability from immobile to mobile, etc.) can be a solution for dense data and is for this reason implemented into our routine. There are also other tracking algorithms which are used in sptPALM (Chenouard et al., 2014); however, a majority of these algorithms were developed for classical single-particle tracking of bright quantum dots

for long observation times or for cell lineage tracking, which differs from sptPALM with fluorescent proteins as markers.

4.3.4 Data quality assessment

Despite optimal conditions, initial data can still contain some false trajectories. Thus, it is recommended to visually inspect the retrieved data. For obtaining diffusion statistics of high quality, a selection of trajectories of sufficient length can be advisable. Short trajectories might have multiple sources: detection loss due to molecules leaving the focal plane, fluorescent protein blinking, or residual noise. Filtering against very long trajectories can also improve data quality, as unusually long trajectories are often caused by impurities in the sample or by aggregates in which multiple fluorescent proteins are brought to their fluorescent state one after another. Finally, trajectories which appear as obvious artifacts, like inclusion bodies caused by protein accumulation (see Fig. 6C) and trajectories "sliding" on cell membrane (impurities from the buffer transiently binding to the cell) or protruding the cellular area must be excluded. When inspecting trajectories from slow imaging schemes exploring the complex bound times, most noise can be easily identified by residual, mobile trajectories.

4.4 Data analysis and visualization

When recording sptPALM movies at fast readout rates, the high spatiotemporal data reveal different and highly transient subpopulations of Cascade interactions based on their apparent mobility. In contrast, for slow readout rates, the fluorescence lifetime of the fluorescent marker is spread over longer imaging times by introducing gap times and thus lowering the spatiotemporal resolution. By doing so, bound times of several seconds for the investigated interactions can be observed, but can only be registered for immobile complexes, e.g., bound to the nucleoid.

4.4.1 Obtaining molecule mobilities

There are different metrics to represent molecule motilities. One method is extracting the diffusion coefficient (D) by plotting mean square displacements (MSD) for given time lags Δt (Oswald, Bank, Bollen, & Peterman, 2014; Weimann et al., 2013):

$$MSD(n\Delta t) = 4D * n\Delta t + 4\sigma^2$$

with σ being the localization precision. The diffusion coefficient is calculated individually for each trajectory (usually by using the first four MSD

time steps, as otherwise confinement effects become too large) and a distribution of diffusions can be later visualized in histograms as a probability density function (PDF) or as cumulative distribution functions (CDFs). The MSD method is a common approach to analyze sptPALM data (Sanamrad et al., 2014; Stracy et al., 2015; Uphoff et al., 2013).

Another way to represent the dynamics of the protein is by the average displacement between adjacent time points within each trajectory (also called jump distances (JDs)) (Grunwald et al., 2008; Oswald, et al., 2014; Schutz, Schindler, & Schmidt, 1997; Weimann et al., 2013):

$$JD = |r(t + \Delta t) - r(t)|$$

with r being the position of the particle at times t and $t + \Delta t$. Once the JDs or an average JD for every trajectory (or segment of a trajectory if a change of diffusive state divides the trajectory in several segments) are calculated, they can be as well represented as a PDF or CDF in which different mobile fractions can be distinguished (Fig. 8B).

In this study, the second approach was selected. As sptPALM trajectories are generally rather short, MSD values for larger time lag values have poor statistics (Flier et al., 2011; Saxton, 1997). Furthermore, due to the small volume of the bacterial cell, the strong confinement of diffusion affects the diffusion values obtained by MSD analyses (Oswald, et al., 2014; Qian, Sheetz, & Elson, 1991). JD values behave more robust for these issues (Chen et al., 2015; Mazza, Abernathy, Golob, Morisaki, & McNally, 2012). Nevertheless, due to confinement and two-dimensional projections of the diffusion (if not imaged in 3D using a microscope with isotropic resolution in all three dimensions), only apparent diffusion coefficients can be retrieved.

Finally, trajectories can be visualized in form of a tracking map per cell, where trajectories are color coded for their dynamics. In this study, fast dynamical sptPALM data were visualized as a function of JD where different fractions of Cascades can be identified (Fig. 8B). Peaks at lower JD values resemble complexes which were stably bound to the DNA target, while the broad fast diffusing fraction is attributed to transiently interacting and free diffusing Cascades.

4.4.2 Extracting molecular bound times

The dynamics of the target bound Cascade can be extracted by the length of each immobile trajectory, and data can be plotted as a histogram. Correctly filtered data should show a histogram of single exponential decay

(assuming only one possible interaction). This histogram can be described with the following equation:

$$k_{\text{lifetime}} e^{-k_{\text{lifetime}} t} = (k_{\text{unb}} + k_{\text{bl}}) e^{-(k_{\text{unb}} + k_{\text{bl}})t}$$

with k_{lifetime} being the rate of the average lifetime of the fluorescence signals, k_{unb} is the rate of Cascade unbinding events, and k_{bl} the rate of fluorophore bleaching (Beattie et al., 2017). To extract the unbinding rate, the bleaching rate has to be evaluated. Here, an immobile fluorescent marker control has to be used, e.g., fusing the marker to a protein forming highly stable complexes (significantly longer than imaging times) or by chemically fixing the sample. For fixed samples, as no unbinding events occur, the lifetime rate is equivalent to the bleaching rate. Thus, k_{unb} can be retrieved (Fig. 8C). Experiments like this are time-consuming and thus may suffer from low statistics. Measurement errors can be determined by subsampling (bootstrapping) and performing multiple fits on these subsets (Beattie et al., 2017).

5. Conclusions

The ability to study Cascade dynamics in vivo at high spatiotemporal resolution allows for analyzing target requirements for Cascade binding in parallel with other DNA-interacting proteins, e.g., the replisome, in their natural environment. The observed parameters can be compared with in vitro studies to obtain a more complete picture of Cascade-mediated target search processes. Quantitative sptPALM analyses of CRISPR–Cas/DNA interactions could also help to unveil levels of regulation imposed on interference, but also adaptation or crRNP complex assembly stages.

Acknowledgments

We would like to thank Marco Hui for benchmarking some sptPALM parameters and for establishing parts of the data analysis workflow. This work was supported by the Max Planck Society (L.R., U.E.), by SYNMIKRO (U.E.), SPP 2141 from the Deutsche Forschungsgemeinschaft (L.R., U.E.), by the Fonds der Chemischen Industrie (U.E.), and by IMPRS-Mic (H.M.E.).

References

Amitai, G., & Sorek, R. (2016). CRISPR-Cas adaptation: Insights into the mechanism of action. *Nature Reviews. Microbiology*, *14*(2), 67–76.

Axelrod, D. (2003). Total internal reflection fluorescence microscopy in cell biology. *Methods in Enzymology*, *361*, 1–33.

Barrangou, R., Fremaux, C., Deveau, H., Richards, M., Boyaval, P., Moineau, S., et al. (2007). CRISPR provides acquired resistance against viruses in prokaryotes. *Science*, *315*(5819), 1709–1712.

Beattie, T. R., Kapadia, N., Nicolas, E., Uphoff, S., Wollman, A. J., Leake, M. C., et al. (2017). Frequent exchange of the DNA polymerase during bacterial chromosome replication. *eLife*, *6*, e21763.

Berardozzi, R., Adam, V., Martins, A., & Bourgeois, D. (2016). Arginine 66 controls dark-state formation in green-to-red photoconvertible fluorescent proteins. *Journal of the American Chemical Society*, *138*(2), 558–565.

Betzig, E., Patterson, G. H., Sougrat, R., Lindwasser, O. W., Olenych, S., Bonifacino, J. S., et al. (2006). Imaging intracellular fluorescent proteins at nanometer resolution. *Science*, *313*(5793), 1642–1645.

Biswas, A., Staals, R. H., Morales, S. E., Fineran, P. C., & Brown, C. M. (2016). CRISPRDetect: A flexible algorithm to define CRISPR arrays. *BMC Genomics*, *17*, 356.

Blosser, T. R., Loeff, L., Westra, E. R., Vlot, M., Kunne, T., Sobota, M., et al. (2015). Two distinct DNA binding modes guide dual roles of a CRISPR-Cas protein complex. *Molecular Cell*, *58*(1), 60–70.

Bolte, S., & Cordelieres, F. P. (2006). A guided tour into subcellular colocalization analysis in light microscopy. *Journal of Microscopy*, *224*(Pt. 3), 213–232.

Brouns, S. J., Jore, M. M., Lundgren, M., Westra, E. R., Slijkhuis, R. J., Snijders, A. P., et al. (2008). Small CRISPR RNAs guide antiviral defense in prokaryotes. *Science*, *321*(5891), 960–964.

Carte, J., Wang, R., Li, H., Terns, R. M., & Terns, M. P. (2008). Cas6 is an endoribonuclease that generates guide RNAs for invader defense in prokaryotes. *Genes & Development*, *22*(24), 3489–3496.

Chen, T. Y., Santiago, A. G., Jung, W., Krzeminski, L., Yang, F., Martell, D. J., et al. (2015). Concentration- and chromosome-organization-dependent regulator unbinding from DNA for transcription regulation in living cells. *Nature Communications*, *6*, 7445.

Chen, X., Zaro, J. L., & Shen, W. C. (2013). Fusion protein linkers: Property, design and functionality. *Advanced Drug Delivery Reviews*, *65*(10), 1357–1369.

Chenouard, N., Smal, I., de Chaumont, F., Maska, M., Sbalzarini, I. F., Gong, Y., et al. (2014). Objective comparison of particle tracking methods. *Nature Methods*, *11*(3), 281–289.

Chowdhury, S., Carter, J., Rollins, M. F., Golden, S. M., Jackson, R. N., Hoffmann, C., et al. (2017). Structure reveals mechanisms of viral suppressors that intercept a CRISPR RNA-guided surveillance complex. *Cell*, *169*(1). 47-57.e11.

Chylinski, K., Makarova, K. S., Charpentier, E., & Koonin, E. V. (2014). Classification and evolution of type II CRISPR-Cas systems. *Nucleic Acids Research*, *42*(10), 6091–6105.

Cong, L., Ran, F. A., Cox, D., Lin, S., Barretto, R., Habib, N., et al. (2013). Multiplex genome engineering using CRISPR/Cas systems. *Science*, *339*(6121), 819–823.

Couvin, D., Bernheim, A., Toffano-Nioche, C., Touchon, M., Michalik, J., Neron, B., et al. (2018). CRISPRCasFinder, an update of CRISRFinder, includes a portable version, enhanced performance and integrates search for Cas proteins. *Nucleic Acids Research*, *46*(1), 246–251.

Dwarakanath, S., Brenzinger, S., Gleditzsch, D., Plagens, A., Klingl, A., Thormann, K., et al. (2015). Interference activity of a minimal type I CRISPR-Cas system from *Shewanella putrefaciens*. *Nucleic Acids Research*, *43*(18), 8913–8923.

Edelstein, A. D., Tsuchida, M. A., Amodaj, N., Pinkard, H., Vale, R. D., & Stuurman, N. (2014). Advanced methods of microscope control using μManager software. *Journal of Biological Methods*, *1*(2), e10.

Edgar, R., & Qimron, U. (2010). The *Escherichia coli* CRISPR system protects from lambda lysogenization, lysogens, and prophage induction. *Journal of Bacteriology*, *192*(23), 6291–6294.

Endesfelder, U., Finan, K., Holden, S. J., Cook, P. R., Kapanidis, A. N., & Heilemann, M. (2013). Multiscale spatial organization of RNA polymerase in *Escherichia coli*. *Biophysical Journal*, *105*(1), 172–181.

Flier, B. M., Baier, M., Huber, J., Mullen, K., Mecking, S., Zumbusch, A., et al. (2011). Single molecule fluorescence microscopy investigations on heterogeneity of translational diffusion in thin polymer films. *Physical Chemistry Chemical Physics*, *13*(5), 1770–1775.

Folling, J., Bossi, M., Bock, H., Medda, R., Wurm, C. A., Hein, B., et al. (2008). Fluorescence nanoscopy by ground-state depletion and single-molecule return. *Nature Methods*, *5*(11), 943–945.

Garneau, J. E., Dupuis, M. E., Villion, M., Romero, D. A., Barrangou, R., Boyaval, P., et al. (2010). The CRISPR/Cas bacterial immune system cleaves bacteriophage and plasmid DNA. *Nature*, *468*, 67.

Gibson, D. G., Young, L., Chuang, R. Y., Venter, J. C., Hutchison, C. A., 3rd, & Smith, H. O. (2009). Enzymatic assembly of DNA molecules up to several hundred kilobases. *Nature Methods*, *6*(5), 343–345.

Gleditzsch, D., Muller-Esparza, H., Pausch, P., Sharma, K., Dwarakanath, S., Urlaub, H., et al. (2016). Modulating the Cascade architecture of a minimal type I-F CRISPR-Cas system. *Nucleic Acids Research*, *44*(12), 5872–5882.

Grissa, I., Vergnaud, G., & Pourcel, C. (2007a). The CRISPRdb database and tools to display CRISPRs and to generate dictionaries of spacers and repeats. *BMC Bioinformatics*, *8*, 172.

Grissa, I., Vergnaud, G., & Pourcel, C. (2007b). CRISPRFinder: A web tool to identify clustered regularly interspaced short palindromic repeats. *Nucleic Acids Research*, *35*(web server issue), W52–W57.

Grunwald, D., Martin, R. M., Buschmann, V., Bazett-Jones, D. P., Leonhardt, H., Kubitscheck, U., et al. (2008). Probing intranuclear environments at the single-molecule level. *Biophysical Journal*, *94*(7), 2847–2858.

Haberl, M. G., Churas, C., Tindall, L., Boassa, D., Phan, S., Bushong, E. A., et al. (2018). CDeep3M-plug-and-play cloud-based deep learning for image segmentation. *Nature Methods*, *15*(9), 677–680.

Haurwitz, R. E., Jinek, M., Wiedenheft, B., Zhou, K., & Doudna, J. A. (2010). Sequence- and structure-specific RNA processing by a CRISPR endonuclease. *Science*, *329*(5997), 1355–1358.

Hayes, R. P., Xiao, Y., Ding, F., van Erp, P. B., Rajashankar, K., Bailey, S., et al. (2016). Structural basis for promiscuous PAM recognition in type I-E Cascade from *E. coli*. *Nature*, *530*(7591), 499–503.

Heilemann, M., van de Linde, S., Schuttpelz, M., Kasper, R., Seefeldt, B., Mukherjee, A., et al. (2008). Subdiffraction-resolution fluorescence imaging with conventional fluorescent probes. *Angewandte Chemie (International Ed. in English)*, *47*(33), 6172–6176.

Hess, S. T., Girirajan, T. P., & Mason, M. D. (2006). Ultra-high resolution imaging by fluorescence photoactivation localization microscopy. *Biophysical Journal*, *91*(11), 4258–4272.

Hochstrasser, M. L., Taylor, D. W., Bhat, P., Guegler, C. K., Sternberg, S. H., Nogales, E., et al. (2014). CasA mediates Cas3-catalyzed target degradation during CRISPR RNA-guided interference. *Proceedings of the National Academy of Sciences of the United States of America*, *111*(18), 6618–6623.

Ishino, Y., Shinagawa, H., Makino, K., Amemura, M., & Nakata, A. (1987). Nucleotide sequence of the iap gene, responsible for alkaline phosphatase isozyme conversion in *Escherichia coli*, and identification of the gene product. *Journal of Bacteriology*, *169*(12), 5429–5433.

Jackson, R. N., Golden, S. M., van Erp, P. B. G., Carter, J., Westra, E. R., Brouns, S. J. J., et al. (2014). Crystal structure of the CRISPR RNA-guided surveillance complex from *Escherichia coli*. *Science*, *345*(6203), 1473–1479.

Jansen, R., van Embden, J. D. A., Gaastra, W., & Schouls, L. M. (2002). Identification of genes that are associated with DNA repeats in prokaryotes. *Molecular Microbiology*, *43*(6), 1565–1575.

Jones, D. L., Leroy, P., Unoson, C., Fange, D., Curic, V., Lawson, M. J., et al. (2017). Kinetics of dCas9 target search in *Escherichia coli*. *Science*, *357*(6358), 1420–1424.

Jore, M. M., Lundgren, M., van Duijn, E., Bultema, J. B., Westra, E. R., Waghmare, S. P., et al. (2011). Structural basis for CRISPR RNA-guided DNA recognition by Cascade. *Nature Structural & Molecular Biology*, *18*(5), 529–536.

Knight, S. C., Xie, L., Deng, W., Guglielmi, B., Witkowsky, L. B., Bosanac, L., et al. (2015). Dynamics of CRISPR-Cas9 genome interrogation in living cells. *Science*, *350*(6262), 823–826.

Komor, A. C., Badran, A. H., & Liu, D. R. (2017). CRISPR-based technologies for the manipulation of eukaryotic genomes. *Cell*, *168*(1–2), 20–36.

Koonin, E. V., Makarova, K. S., & Zhang, F. (2017). Diversity, classification and evolution of CRISPR-Cas systems. *Current Opinion in Microbiology*, *37*, 67–78.

Lando, D., Endesfelder, U., Berger, H., Subramanian, L., Dunne, P. D., McColl, J., et al. (2012). Quantitative single-molecule microscopy reveals that CENP-A(Cnp1) deposition occurs during G2 in fission yeast. *Open Biology*, *2*(7), 120078.

Legland, D., Arganda-Carreras, I., & Andrey, P. (2016). MorphoLibJ: Integrated library and plugins for mathematical morphology with ImageJ. *Bioinformatics*, *32*(22), 3532–3534.

Lelek, M., Di Nunzio, F., & Zimmer, C. (2014). FlAsH-PALM: Super-resolution pointillist imaging with FlAsH-tetracysteine labeling. *Methods in Molecular Biology*, *1174*, 183–193.

Loschberger, A., Franke, C., Krohne, G., van de Linde, S., & Sauer, M. (2014). Correlative super-resolution fluorescence and electron microscopy of the nuclear pore complex with molecular resolution. *Journal of Cell Science*, *127*(Pt. 20), 4351–4355.

Makarova, K. S., Haft, D. H., Barrangou, R., Brouns, S. J., Charpentier, E., Horvath, P., et al. (2011). Evolution and classification of the CRISPR-Cas systems. *Nature Reviews. Microbiology*, *9*(6), 467–477.

Makarova, K. S., Wolf, Y. I., Alkhnbashi, O. S., Costa, F., Shah, S. A., Saunders, S. J., et al. (2015). An updated evolutionary classification of CRISPR-Cas systems. *Nature Reviews. Microbiology*, *13*(11), 722–736.

Malkusch, S., Endesfelder, U., Mondry, J., Gelleri, M., Verveer, P. J., & Heilemann, M. (2012). Coordinate-based colocalization analysis of single-molecule localization microscopy data. *Histochemistry and Cell Biology*, *137*(1), 1–10.

Manley, S., Gillette, J. M., Patterson, G. H., Shroff, H., Hess, H. F., Betzig, E., et al. (2008). High-density mapping of single-molecule trajectories with photoactivated localization microscopy. *Nature Methods*, *5*(2), 155–157.

Marraffini, L. A., & Sontheimer, E. J. (2008). CRISPR interference limits horizontal gene transfer in staphylococci by targeting DNA. *Science*, *322*(5909), 1843–1845.

Marraffini, L. A., & Sontheimer, E. J. (2010). Self versus non-self discrimination during CRISPR RNA-directed immunity. *Nature*, *463*(7280), 568–571.

Mazza, D., Abernathy, A., Golob, N., Morisaki, T., & McNally, J. G. (2012). A benchmark for chromatin binding measurements in live cells. *Nucleic Acids Research*, *40*(15), e119.

Mohanraju, P., Makarova, K. S., Zetsche, B., Zhang, F., Koonin, E. V., & van der Oost, J. (2016). Diverse evolutionary roots and mechanistic variations of the CRISPR-Cas systems. *Science*, *353*(6299), aad5147.

Mojica, F. J. M., Díez-Villaseñor, C. s., García-Martínez, J., & Soria, E. (2005). Intervening sequences of regularly spaced prokaryotic repeats derive from foreign genetic elements. *Journal of Molecular Evolution*, *60*(2), 174–182.

Mulepati, S., Heroux, A., & Bailey, S. (2014). Structural biology. Crystal structure of a CRISPR RNA-guided surveillance complex bound to a ssDNA target. *Science*, *345*(6203), 1479–1484.

Nunez, J. K., Kranzusch, P. J., Noeske, J., Wright, A. V., Davies, C. W., & Doudna, J. A. (2014). Cas1-Cas2 complex formation mediates spacer acquisition during CRISPR-Cas adaptive immunity. *Nature Structural & Molecular Biology*, *21*(6), 528–534.

Oswald, F., Bank, E. L. M., Bollen, Y. J., & Peterman, E. J. (2014). Imaging and quantification of trans-membrane protein diffusion in living bacteria. *Physical Chemistry Chemical Physics*, *16*(25), 12625–12634.

Ovesny, M., Krizek, P., Borkovec, J., Svindrych, Z., & Hagen, G. M. (2014). ThunderSTORM: A comprehensive ImageJ plug-in for PALM and STORM data analysis and super-resolution imaging. *Bioinformatics*, *30*(16), 2389–2390.

Paintdakhi, A., Parry, B., Campos, M., Irnov, I., Elf, J., Surovtsev, I., et al. (2016). Oufti: An integrated software package for high-accuracy, high-throughput quantitative microscopy analysis. *Molecular Microbiology*, *99*(4), 767–777.

Pausch, P., Muller-Esparza, H., Gleditzsch, D., Altegoer, F., Randau, L., & Bange, G. (2017). Structural variation of type I-F CRISPR RNA guided DNA surveillance. *Molecular Cell*, *67*(4). 622-632.e624.

Pingoud, A., Fuxreiter, M., Pingoud, V., & Wende, W. (2005). Type II restriction endonucleases: Structure and mechanism. *Cellular and Molecular Life Sciences*, *62*(6), 685–707.

Pourcel, C., Salvignol, G., & Vergnaud, G. (2005). CRISPR elements in Yersinia pestis acquire new repeats by preferential uptake of bacteriophage DNA, and provide additional tools for evolutionary studies. *Microbiology*, *151*(Pt. 3), 653–663.

Preciado Lopez, M., Huber, F., Grigoriev, I., Steinmetz, M. O., Akhmanova, A., Dogterom, M., et al. (2014). In vitro reconstitution of dynamic microtubules interacting with actin filament networks. *Methods in Enzymology*, *540*, 301–320.

Qian, H., Sheetz, M. P., & Elson, E. L. (1991). Single particle tracking. Analysis of diffusion and flow in two-dimensional systems. *Biophysical Journal*, *60*(4), 910–921.

Redding, S., Sternberg, S. H., Marshall, M., Gibb, B., Bhat, P., Guegler, C. K., et al. (2015). Surveillance and processing of foreign DNA by the *Escherichia coli* CRISPR-Cas system. *Cell*, *163*(4), 854–865.

Rust, M. J., Bates, M., & Zhuang, X. (2006). Sub-diffraction-limit imaging by stochastic optical reconstruction microscopy (STORM). *Nature Methods*, *3*(10), 793–795.

Rutkauskas, M., Sinkunas, T., Songailiene, I., Tikhomirova, M. S., Siksnys, V., & Seidel, R. (2015). Directional R-loop formation by the CRISPR-Cas surveillance complex Cascade provides efficient off-target site rejection. *Cell Reports*, *10*(9), 1534–1543.

Sage, D., Kirshner, H., Pengo, T., Stuurman, N., Min, J., Manley, S., et al. (2015). Quantitative evaluation of software packages for single-molecule localization microscopy. *Nature Methods*, *12*(8), 717–724.

Sanamrad, A., Persson, F., Lundius, E. G., Fange, D., Gynna, A. H., & Elf, J. (2014). Single-particle tracking reveals that free ribosomal subunits are not excluded from the *Escherichia coli* nucleoid. *Proceedings of the National Academy of Sciences of the United States of America*, *111*(31), 11413–11418.

Saxton, M. J. (1997). Single-particle tracking: The distribution of diffusion coefficients. *Biophysical Journal*, *72*(4), 1744–1753.

Schindelin, J., Arganda-Carreras, I., Frise, E., Kaynig, V., Longair, M., Pietzsch, T., et al. (2012). Fiji: An open-source platform for biological-image analysis. *Nature Methods*, *9*(7), 676–682.

Schutz, G. J., Schindler, H., & Schmidt, T. (1997). Single-molecule microscopy on model membranes reveals anomalous diffusion. *Biophysical Journal*, *73*(2), 1073–1080.

Shen, P., & Huang, H. V. (1986). Homologous recombination in Escherichia coli: Dependence on substrate length and homology. *Genetics*, *112*(3), 441–457.

Simms, H. M., Bowman, C. M., & Anseth, K. S. (2008). Using living radical polymerization to enable facile incorporation of materials in microfluidic cell culture devices. *Biomaterials*, *29*(14), 2228–2236.
Singh, D., Sternberg, S. H., Fei, J., Doudna, J. A., & Ha, T. (2016). Real-time observation of DNA recognition and rejection by the RNA-guided endonuclease Cas9. *Nature Communications*, *7*, 12778.
Small, A., & Stahlheber, S. (2014). Fluorophore localization algorithms for super-resolution microscopy. *Nature Methods*, *11*(3), 267–279.
Staals, R. H., Zhu, Y., Taylor, D. W., Kornfeld, J. E., Sharma, K., Barendregt, A., et al. (2014). RNA targeting by the type III-A CRISPR-Cas Csm complex of Thermus thermophilus. *Molecular Cell*, *56*(4), 518–530.
Stehbens, S., Pemble, H., Murrow, L., & Wittmann, T. (2012). Imaging intracellular protein dynamics by spinning disk confocal microscopy. *Methods in Enzymology*, *504*, 293–313.
Sternberg, S. H., Redding, S., Jinek, M., Greene, E. C., & Doudna, J. A. (2014). DNA interrogation by the CRISPR RNA-guided endonuclease Cas9. *Nature*, *507*(7490), 62–67.
Stracy, M., Lesterlin, C., Garza de Leon, F., Uphoff, S., Zawadzki, P., & Kapanidis, A. N. (2015). Live-cell superresolution microscopy reveals the organization of RNA polymerase in the bacterial nucleoid. *Proceedings of the National Academy of Sciences of the United States of America*, *112*(32), E4390–E4399.
Sun, C. L., Barrangou, R., Thomas, B. C., Horvath, P., Fremaux, C., & Banfield, J. F. (2013). Phage mutations in response to CRISPR diversification in a bacterial population. *Environmental Microbiology*, *15*(2), 463–470.
Szczelkun, M. D., Tikhomirova, M. S., Sinkunas, T., Gasiunas, G., Karvelis, T., Pschera, P., et al. (2014). Direct observation of R-loop formation by single RNA-guided Cas9 and Cascade effector complexes. *Proceedings of the National Academy of Sciences of the United States of America*, *111*(27), 9798–9803.
Tobes, R., & Ramos, J. L. (2005). REP code: Defining bacterial identity in extragenic space. *Environmental Microbiology*, *7*(2), 225–228.
Tokunaga, M., Imamoto, N., & Sakata-Sogawa, K. (2008). Highly inclined thin illumination enables clear single-molecule imaging in cells. *Nature Methods*, *5*(2), 159–161.
Turkowyd, B., Balinovic, A., Virant, D., Carnero, H. G. G., Caldana, F., Endesfelder, M., et al. (2017). A general mechanism of photoconversion of green-to-red fluorescent proteins based on blue and infrared light reduces phototoxicity in live-cell single-molecule imaging. *Angewandte Chemie (International Ed. in English)*, *56*(38), 11634–11639.
Unterholzner, S. J., Poppenberger, B., & Rozhon, W. (2013). Toxin-antitoxin systems: Biology, identification, and application. *Mobile Genetic Elements*, *3*(5), e26219.
Uphoff, S., Reyes-Lamothe, R., Garza de Leon, F., Sherratt, D. J., & Kapanidis, A. N. (2013). Single-molecule DNA repair in live bacteria. *Proceedings of the National Academy of Sciences of the United States of America*, *110*(20), 8063–8068.
van der Oost, J., Westra, E. R., Jackson, R. N., & Wiedenheft, B. (2014). Unravelling the structural and mechanistic basis of CRISPR-Cas systems. *Nature Reviews Microbiology*, *12*(7), 479–492.
Van Valen, D. A., Kudo, T., Lane, K. M., Macklin, D. N., Quach, N. T., DeFelice, M. M., et al. (2016). Deep learning automates the quantitative analysis of individual cells in live-cell imaging experiments. *PLoS Computational Biology*, *12*(11), e1005177.
Virant, D., Turkowyd, B., Balinovic, A., & Endesfelder, U. (2017). Combining primed photoconversion and UV-photoactivation for aberration-free, live-cell compliant multi-color single-molecule localization microscopy imaging. *International Journal of Molecular Sciences*, *18*(7), E1524.
Wang, J., Li, J., Zhao, H., Sheng, G., Wang, M., Yin, M., et al. (2015). Structural and mechanistic basis of PAM-dependent spacer acquisition in CRISPR-Cas systems. *Cell*, *163*(4), 840–853.

Wang, S., Moffitt, J. R., Dempsey, G. T., Xie, X. S., & Zhuang, X. (2014). Characterization and development of photoactivatable fluorescent proteins for single-molecule-based superresolution imaging. *Proceedings of the National Academy of Sciences of the United States of America*, *111*(23), 8452–8457.

Weimann, L., Ganzinger, K. A., McColl, J., Irvine, K. L., Davis, S. J., Gay, N. J., et al. (2013). A quantitative comparison of single-dye tracking analysis tools using Monte Carlo simulations. *PLoS One*, *8*(5), e64287.

Westra, E. R., van Erp, P. B., Kunne, T., Wong, S. P., Staals, R. H., Seegers, C. L., et al. (2012). CRISPR immunity relies on the consecutive binding and degradation of negatively supercoiled invader DNA by Cascade and Cas3. *Molecular Cell*, *46*(5), 595–605.

Wiedenheft, B., Lander, G. C., Zhou, K., Jore, M. M., Brouns, S. J. J., van der Oost, J., et al. (2011). Structures of the RNA-guided surveillance complex from a bacterial immune system. *Nature*, *477*(7365), 486–489.

Wolter, S., Loschberger, A., Holm, T., Aufmkolk, S., Dabauvalle, M. C., van de Linde, S., et al. (2012). rapidSTORM: Accurate, fast open-source software for localization microscopy. *Nature Methods*, *9*(11), 1040–1041.

Zawadzki, P., Stracy, M., Ginda, K., Zawadzka, K., Lesterlin, C., Kapanidis, A. N., et al. (2015). The localization and action of topoisomerase IV in *Escherichia coli* chromosome segregation is coordinated by the SMC complex, MukBEF. *Cell Reports*, *13*(11), 2587–2596.

Zhao, H., Sheng, G., Wang, J., Wang, M., Bunkoczi, G., Gong, W., et al. (2014). Crystal structure of the RNA-guided immune surveillance Cascade complex in *Escherichia coli*. *Nature*, *515*(7525), 147–150.

Zoephel, J., Dwarakanath, S., Richter, H., Plagens, A., & Randau, L. (2012). Substrate generation for endonucleases of CRISPR/cas systems. *Journal of Visualized Experiments*, *67*, e4277.

3.2 Studying the *in vivo* Protein Organization and Dynamics of the Type I-Fv CRISPR-Cas System of *Shewanella putrefaciens* CN-32 at a High Spatiotemporal Resolution

In this work, we study the CRISPR-Cas Type I-Fv system from *Shewanella putrefaciens* CN-32 *in vivo* using sptPALM methods. We have visualized the DNA scanning of individual Cas assemblies in great detail, providing insights into the native target detection by the complex and the independent functions of the individual Cas proteins under different conditions and target affinities.

This work has been done in a collaboration with Dr. Lennart Randau and Hanna Müller-Esparza. The following text is part of a manuscript currently in preparation for submission. I contributed in this work by designing and performing sptPALM experiments, analyzing sptPALM data and by preparing figures and parts of the manuscript.

3.2.1 Materials and Methods

Generating *E. coli* Strains

Details of the strain generation as well as assessing Cascade activity are described in Section 3.1, chapter 3 and briefly shown in Figure 3.1. Efficiency of Plaquing (EOP) assay, shown in Figure 3.1a, is described in detail Section 3.1, chapter 3.3.

Cell Culture Preparation

Cells were inoculated from the cryo stock into fresh LB medium supplied with kanamycin and spectinomycin (both 25 μg/mL) and grown overnight at 37 °C. On the next day, cultures were reinoculated into fresh 2YTL (1:100 dilution, 3 mL final culture volume), grown for one hour at 37 °C and induced with 0.1 % arabinose for another hour afterwards. The induction of Cas proteins expression was stopped by exchanging medium into 3 mL EZRDM (Teknova, USA). Cells grew in this medium for one hour to enable protein maturation and Cascade assembly. 500 μL of each culture was centrifuged (2 min, 3000 $\times$ g), washed twice with fresh EZRDM and suspended in residual 50 μL medium. 2 μL of suspended cells were placed on agarose pads covered with the cleaned coverslip and incubated for 15 minutes on a bench to settle them down on the pad (Figure 3.2).

BL21-AI carrying the pRSETb-Dendra2-T69A plasmid were inoculated from the cryo stock into fresh LB medium (100 μg/mL ampicillin) and grown overnight at 37 °C. On the next day, the culture was reinoculated into fresh 2YTL medium (1:100 dilution, 3 mL) and after one hour growth at 37 °C induced with 0.05 % arabinose for another hour. Expression was stopped by replacing medium into 3 mL EZRDM and cells grew for one hour. Two subcultures, 500 μL each, were washed twice with fresh EZRDM and one of them was suspended in residual 50 μL EZRDM, while another one was suspended in 500 μL EZRDM and chemically fixed with 3 % formaldehyde for 15 minutes. After fixation, the culture was washed twice and suspended in 50 μL medium. 2

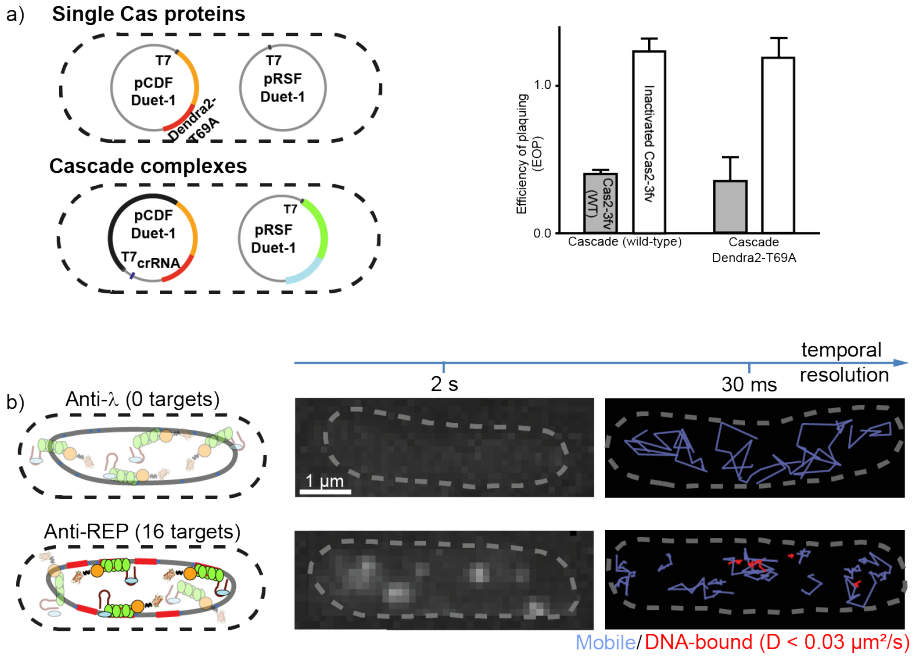

Figure 3.1: Experimental strategy used in this research. (a) Cas proteins tagged with Dendra2-T69A and crRNA were heterologously expressed from plasmids in *E. coli* cells. We evaluated the effector complex interference activity by the EOP assay and also Cascade complex assembly efficiency when one of the Cas proteins is tagged with a fluoroescent protein. (b) When imaging the complexes in living *E. coli* cells at a slow imaging speed, a significant fraction of Cascade (Anti-REP) shows up as immobile spots, being tightly bound to DNA targets, whereas Cascade (Anti-λ) only shows a diffuse fluorescent signal (left). The transient DNA interactions during target search processes only become visible at high imaging rates with exposure times under 30 ms (right).

μL of suspended cells were placed on agarose pads covered with a cleaned coverslip and incubated for 15 minutes on a bench to settle them down on the pad (Figure 3.2).

Agarose Pads Preparation

Low-temperature gelling agarose (Sigma-Aldrich, Germany) was suspended in freshly prepared EZRDM to a final concentration 1 % (w/v) and heated up to 70 °C until agarose melted completely, and stored later at 37 °C. Cooled to 37 °C agarose was placed on indented microscope slide (Thermo Fisher, Germany) and sealed with a coverslip cleaned overnight in 1 M KOH (Sigma-Aldrich, Germany). After two hours EZRDM-agarose pads were ready to use (Figure 3.2).

SMLM Setup

Imaging was performed on a custom built setup based on an automated Nikon Ti Eclipse microscope, equipped with appropriate dichroic and filters (ET dapi/Fitc/cy3 dichroic, ZT405/488/561rpc rejection filter, ET610/75 bandpass, all AHF Analysentechnik, Germany) and a CFI Apo TIRF 100x oil objective (NA 1.49, Nikon). 405 and 561 nm laser devices (OBIS, Coherent Inc., Santa Clara, California USA) were modulated via an acousto-optical tunable filter (AOTF, Gooch & Housego, UK). Fluorescence was detected by an emCCD (iXON Ultra 888;

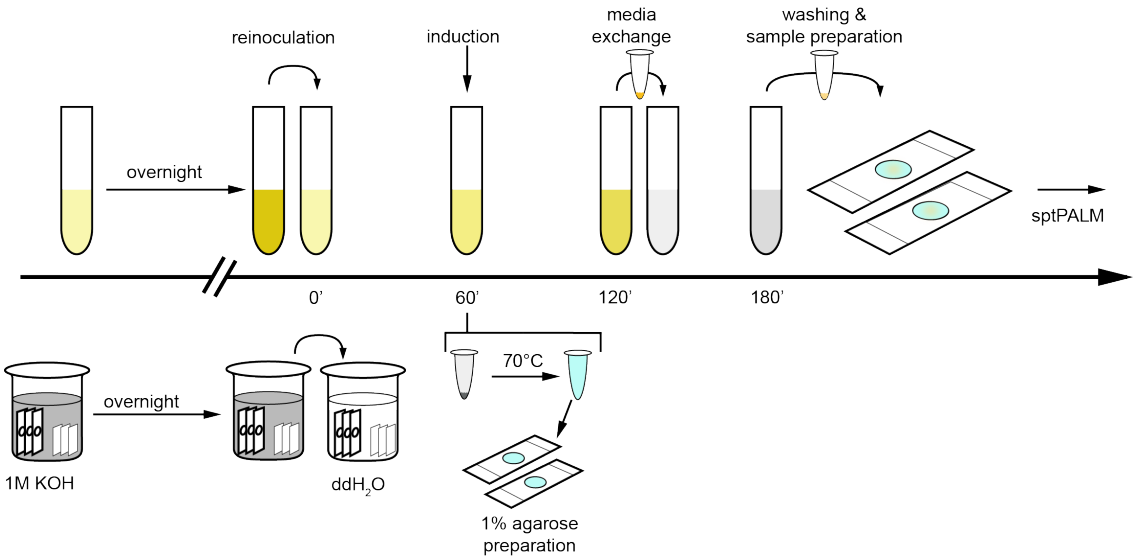

Figure 3.2: Timeline of sptPALM sample preparation. Top: culture incubation, induction, and cell washing steps. Bottom: cleaning microscope slides and coverslips, and agarose pads preparation. Adapted with permission from [23].

Andor, UK) adjusted to 129 nm pixel size. The z-focus was controlled by a commercial perfect focus system (Nikon, Düsseldorf, Germany). Acquisitions were controlled by Micro-Manager [96]. Live cell experiments were performed on a customized heating stage at 25 °C.

sptPALM Data Acquisition

Measuring fast in vivo kinetics.

Living *E. coli* cells growing on EZRDM-agarose pads were placed into the heating chamber of the microscope and imaged with 77 and 33 Hz frame rate for 20.000 frames in HILO illumination mode [97]. During the image acquisition, samples were exposed to 561 nm illumination (800 W/cm^2) continuously, while a 405 nm laser was pulsed every 20^{th} frame with the intensity of 1-3 W/cm^2. Before recording the sptPALM movie bright light snapshots of cells were taken.

Measuring in vivo binding kinetics of Cascades.

Cells on agarose pads were imaged with different time intervals (τ_{tl}) (0.2 to 10 s) due the rather low photostability of fluorescent proteins (see Section 1.2). The integration time (τ_{int}) was extended to (200 ms) to collect fluorescent signals only from stably DNA-bound Cascades (Figure 3.1 and Figure 3.3). To prevent Dendra2-T69A from rapid photobleaching, 561 nm laser intensity was set to 30 W/cm^2. 405 nm laser was pulsed every 25^{th} frame with the intensity of 1-3 W/cm^2. Before sptPALM imaging, bright light snapshots were taken. To mimic the fluorescent signal coming from stably bound Cascade-DNA complexes, a chemically fixed *E. coli* BL21-AI strain, expressing LacY-Dendra2-T69A was imaged under the same conditions. With this control we can correct for photobleaching effects of the measurements.

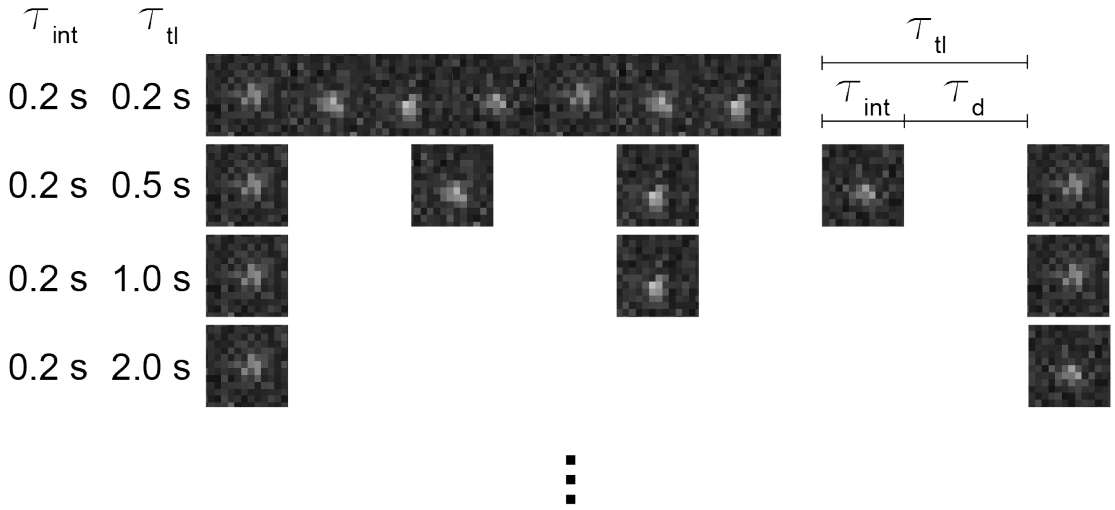

Figure 3.3: Imaging Cascade-DNA interactions by using time-lapse imaging with various dark times (τ_{d}). The camera integration time (τ_{int}) is kept constant, thus in all experiments Dendra2-T69A is bleached in a same manner. By increasing τ_{d} values we are elongating the imaging interval (τ_{tl}), in consequence we visualize events with longer lifetimes.

sptPALM Data Analysis

All imaging procedures and data analysis steps described below were shown in Figure 3.4.

Measuring fast in vivo kinetics.

Cells were segmented manually from bright light images using the open source software Fiji [98] and stored as ROI areas in zip files. Nanometer precise localizations of diffusing fluorophores were obtained with the rapidSTORM 3.3 software [99]. Tracking was performed using custom software, developed in our lab (unpublished), written in C++. For further analysis, only trajectories longer than six steps and shorter than 20 steps were taken. Furthermore, highly autofluorescent cells and obvious noise (e.g. from inclusion bodies at cell poles) were manually discarded from the dataset. For all trajectories which passed the filtering, the average displacement between adjacent frames (<JD>) was extracted and weighted by the number of steps. Weighted <JD> values were plotted in histogram plots using the software OriginPro 2017 (OriginLab Corporation).

Measuring in vivo binding kinetics of Cascades

In a first step, nanometer precise localizations of chemically fixed LacY-Dendra2-T69A proteins were obtained with the ThunderSTORM software [100]. As chemically fixed LacY-Dendra2-T69A are immobile, and thus resemble stable Cascade-DNA interactions, parameters characterizing their PSF architecture, like the intensity, xy-dimensions, and uncertainty were used later in the filtering step to exclude mobile Cascade fractions.

Filtered localizations were then connected into trajectories using customized software written in C++. Here, the tracking software makes use of *a priori* knowledge about the fluorophore blinking and bleaching rates, which were obtained from a manual first analysis of the control strain measurements. Additionally, we provided an expected average displacement value for the immobile molecule. Given these *a priori* parameters, tracking software can evaluate whether a tracked molecule is either static (immobile) or freely diffusing. For further analysis, only the immobile trajectories were taken into consideration. Trajectories coming from inclusion bodies and other artifacts were manually excluded from the dataset. For all trajectories which pass the filtering, trajectory lifetimes (number of frames between first and last localization in a trajectory), representing fluorescence lifetimes, were plotted in histograms, to which single exponential decay model was fitted:

$$PDF(t) = Ae^{-k_{\mathrm{eff}(\tau_{\mathrm{tl}})}t}$$

Where *PDF(t)* is a probability density function, A is the amplitude at $t = 0$, t is the fluorescence lifetime and $k_{eff(\tau_{tl})}$ is the fluorescence lifetime decay effective rate for a given τ_{tl}. $k_{eff(\tau_{tl})}$ values for all tested crRNA variants were plotted in $k_{eff}\tau_{\mathrm{tl}}(\tau_{\mathrm{tl}})$ graphs. Linear fits on plotted data were performed. For fitting, each data point was weighted by its Standard Error (SE) to put more significance on data with a better statistics. Slope values of fits are equal to an effective rate (k_{eff}) for given crRNA variants.

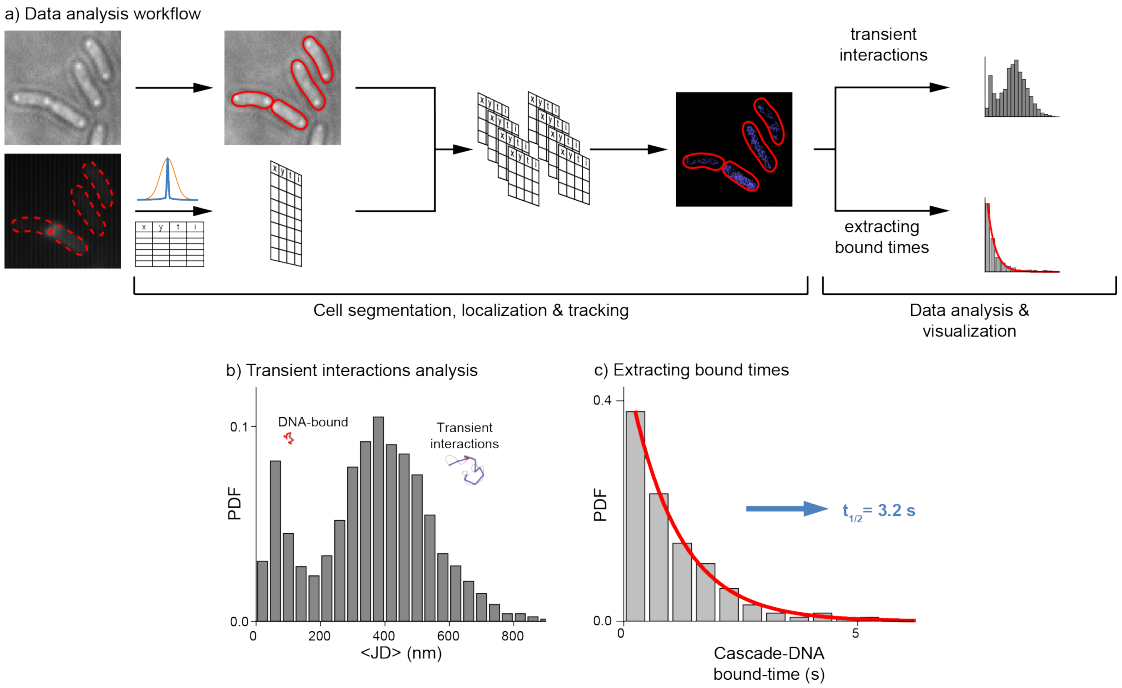

Figure 3.4: Data processing workflow. (a) Cells were segmented based on bright light snapshots taken before sptPALM imaging (top left). In parallel, localizations were extracted based on PSF fitting (bottom left). Next, localizations were split into subarrays representing single cells and tracking was performed (middle). In case of fast imaging, data were represented as histograms (top right). For slow imaging accessing the bound-time of complexes, data histograms representing fluorescence spot bound times were fitted to retrieve the average event lifetime (bottom right). (b) Data from transient interaction analysis represented in the form of probability density function (PDF) histogram (bin size- 40nm). Exemplary trajectories for DNA-bound Cascade (red trajectory) and transiently interacting Cascade (blue-red trajectory). (c) PDF representing Cascade bound-time (bin size- 0.5 s) and single exponential model fitted to PDF. Adapted with permision from [23].

3.2.2 Results and Discussion

Studying the *in vivo* Kinetics of the CRISPR-Cas Type I-Fv System

For our experiments, we heterologously expressed from a pair of plasmids (pCDFDuet-1/pRSFDuet-1) the Cascade proteins: inactivated Cas2-3fv (H156A/D157A mutation in the HD nuclease domain), a fluorescently labeled Cas5fv, Cas6f and Cas7fv, and a short CRISPR array carrying one, two or three spacers in *E. coli* BL21-AI cells. Notably, *E. coli* is a well-established prokaryotic model organism for SMLM [101] and furthermore, BL21-AI lacks its own CRISPR-Cas system. Cas5fv was C-terminally fused to the green-to-red photoconvertible fluorescent protein Dendra2, carrying the mutation T69A which optimizes its performance for SPT studies [102]. We assessed the activity of the Cascade complexes, including the Cas5fv-Dendra2-T69A fusion by EOP assays (using an active Cas2-3fv) against the λ phage, which were comparable to wild-type Cascade complexes (Figure 3.1a- right).

We designed two crRNAs targeting either repetitive extragenic palindromic sequences of *E. coli* [103] to obtain a Cascade complex with targets in the *E. coli* genome (termed Anti-REP) or

targeting the λ phage genome not present in our experiments yielding a Cascade without genomic targets (termed Anti-λ). For the Anti-REP crRNA, we further designed different versions of varying complementarity and using either a single, dual or triple array of spacers (Table 3.1).

Table 3.1: Number of targets with different complementarities which can be targeted by Cascades carrying different crRNA variants

Target compl. (bp)	**Anti-λ**	**Anti-REP 12 bp**	**Anti-REP 18 bp**	**Anti-REP 30 bp**	**Anti-REP (three spacer)**	**Anti-REP (one spacer)**
>31	0	0	0	0	42	16
25-30	0	0	0	75	33	14
19-24	0	0	0	24	24	12
13-18	0	0	107	8	8	0
12	0	133	26	26	26	9
<11	0	3	3	3	3	85

As we were also interested in the interations of individual Cas proteins, we constructed strains carrying pCDFDuet-1 plasmids either only encoding for Cas5fv-Dendra2-T69A, Cas6f-Dendra2-T69A or Cas5fv-ΔAH (deletion of the AH domain). In all three cases we co-transformed three strains with an empty pRSFDuet-1. Finally, we constructed a strain co-expressing Cas5fv, Cas6f and Anti-λ crRNA.

By fine-tuning imaging frequency, frame duration and laser intensity of our pulsed fluorescence read-out to budget the overall fluorescence lifetime, we can observe DNA-Cascade interactions in individual protein complexes at different timescales from the millisecond range to several seconds (details in Materials and Methods) and thus can probe the system for the different interactions as sketched in Figure 1.6. Furthermore, we can probe their dynamics depending on their complementarity of the different crRNAs. For example, when imaging Cascade complexes in living cells at a slow imaging speed (2 seconds long exposure), a significant fraction of Cascade Anti-REP complexes shows as immobile spots, being tightly bound to DNA targets whereas Cascade Anti-λ only show diffusive fluorescent signal (Figure 3.1b). This is expected as the Anti-REP (single spacer) crRNA has 16 potential targets of 100% complementarity) per *E. coli* genome, whereas Anti-λ has none and the transient DNA interactions during target search processes are expected to be too short-lived to be visible as clear fluorescent spots at seconds-long exposure times. Using the higher temporal resolution of faster imaging rates with exposure times under 30 ms, the fast diffusing Cascades (for both crRNAs) as well as the DNA-bound, immobile fraction of Cascade Anti-REP complexes are revealed (Figure 3.1b, blue color-coded trajectories have a diffusion of D $> 0.03\ \mu m^2/s$, red color-coded trajectories are below this threshold).

Cas5fv Protein Alone Interacts With DNA and RNA *in vivo*

To investigate the dynamics of the CRISPR Type I-Fv system in detail, we first focused on individual Cas5fv proteins and performed sptPALM imaging of the protein Cas5fv alone at

a fast imaging rate of 77 Hz (Figure 3.6a). For all conditions measured, we summarized our single-molecule trajectory statistics in histograms (Materials and Methods). As a sptPALM calibration we measured a free diffusion of the cytosolic Dendra2-T69A (Figure 3.5- left) with <JD> medians at 370 nm (77 Hz frame rate) and 400 nm (33 Hz). Additionally we mimicked, by a chemical fixation of cells, to immobilize cellular compounds, a <JD> distribution of immobile molecules which only show a residual median displacement of about 60 nm which is only larger than zero due to the finite localization precision of the technique (Figure 3.5- middle).

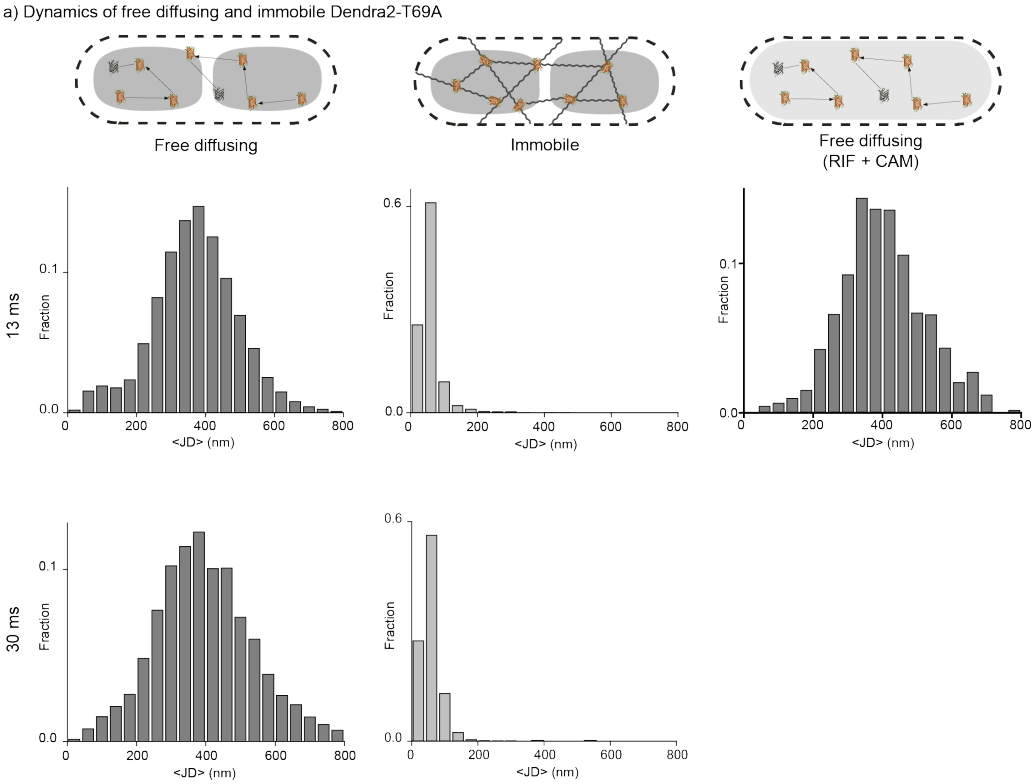

Figure 3.5: Dynamics of freely diffusing and immobile Dendra2-T69A. <JD> histograms for cytosolic Dendra2-T69A (left), immobile Dendra2-T69A in chemically fixed cells (middle) and cytosolic Dendra2-T69A in cells treated simultaneously with rifampicin and chloramphenicol.

For Cas5fv proteins, the <JD> distribution exhibits two fractions, one minor slow one at about 80-120 nm <JD> displacement and a major faster one at 240-360 nm (Figure 3.6a). Interestingly, when compared to our Dendra2-T69A controls (grey outlines, Figure 3.6a and Figure 3.5- left), the slow fraction is not fully immobile and the faster fraction is significantly slower than the freely diffusing fluorophore. As Cas5fv is responsible for 'GG' PAM recognition, we expected to observe one DNA-interacting fraction and maybe one freely diffusive fraction. As the two measured fractions on a first glance cannot be directly assigned to either of both, we set out to further explore the nature of the two observed fractions and performed several additional experiments.

From the crystal structure of Cas5fv as well as interference assays it is known that Cas5fv recognizes PAM sequences through its AH domain [75]. Thus, we constructed a deletion mutant, Cas5fv-ΔAH, which we expected to show no major interaction with DNA. Interestingly, in our

sptPALM data, we observed a shift of the faster fraction from 240-360 nm for Cas5fv to 280-440 nm for Cas5fv-ΔAH (Figure 3.6b). By this shift, this fraction of Cas5fv-ΔAH molecules shows a similar diffusion as cytosolic Dendra2-T69A (grey outline in Figure 3.6b) and strongly suggests that for Cas5fv-ΔAH, transient PAM recognitions are strongly reduced (in agreement with the structural data [75]). Consequently, Cas5fv-ΔAH does not interact with the nucleoid and the main, mobile fraction resembles the cytosolic Dendra2-T69A dynamics. This also lets us suppose that the fast fraction observed for Cas5fv could be explained by a highly short-lived DNA-protein interaction. Here, as the nucleoid is a large macromolecule which at our imaging speed of 13 ms per imaging frame does not exhibit any significant diffusion [104, 94], a stable Cas5fv interaction with a bound time in the range of our imaging resolution would result in an immobile particle. Thus, the timescale of transient Cas5fv-DNA interactions is significantly below our temporal imaging resolution. In consequence, Cas5fv molecules transiently interacting with the nucleoid show a slowed down (as compared to the full free diffusion), but still rather fast apparent diffusion.

For both proteins, Cas5fv and its mutant, the minor fraction with a <JD> of about 80 -120 nm is present. As the Cas5fv is expressed in our experiment is not supplied with a crRNA, we speculated that this fraction could be actually explained by a possible affinity of Cas5fv to RNA, and in our growth conditions most likely Messenger RNA (mRNA). This RNA interaction could then lead to a co-diffusion of Cas5fv with RNA, which could explain the slow diffusive behavior for both, Cas5fv and Cas5fv-ΔAH. To test this hypothesis, we thus performed experiments relying on drug treatments.

First, we treated the cells with 10 μg/mL chloramphenicol for 60 minutes, which blocks translation by tethering translating ribosomes to the mRNA [105]. As the cell tries to counteract the increasing fraction of non-functional ribosomes, this leads to a strongly increased transcription and thus increased RNA/protein ratio, in particular to an unusual high amount of ribosomal RNA ([105, 106]). Furthermore, the nucleoid is strongly compacted (Figure 3.6c, inset, and [107]). In consequence, cells contain large DNA-free regions enriched with RNAs. By selectively analyzing only trajectories from these areas (as indicated by the yellow box in the inset of Figure 3.6c), we observed an only slow diffusive fraction of Cas5fv (Figure 3.6c) which in its nature overlaps with the slow diffusive fraction of Cas5fv in untreated cells (orange outline in Figure 3.6c). Importantly, under chloramphenicol treatment, a large fraction of this RNA is Ribosomal RNA (rRNA), which is not translated and thus free from ribosomes and accessible for Cas5fv.

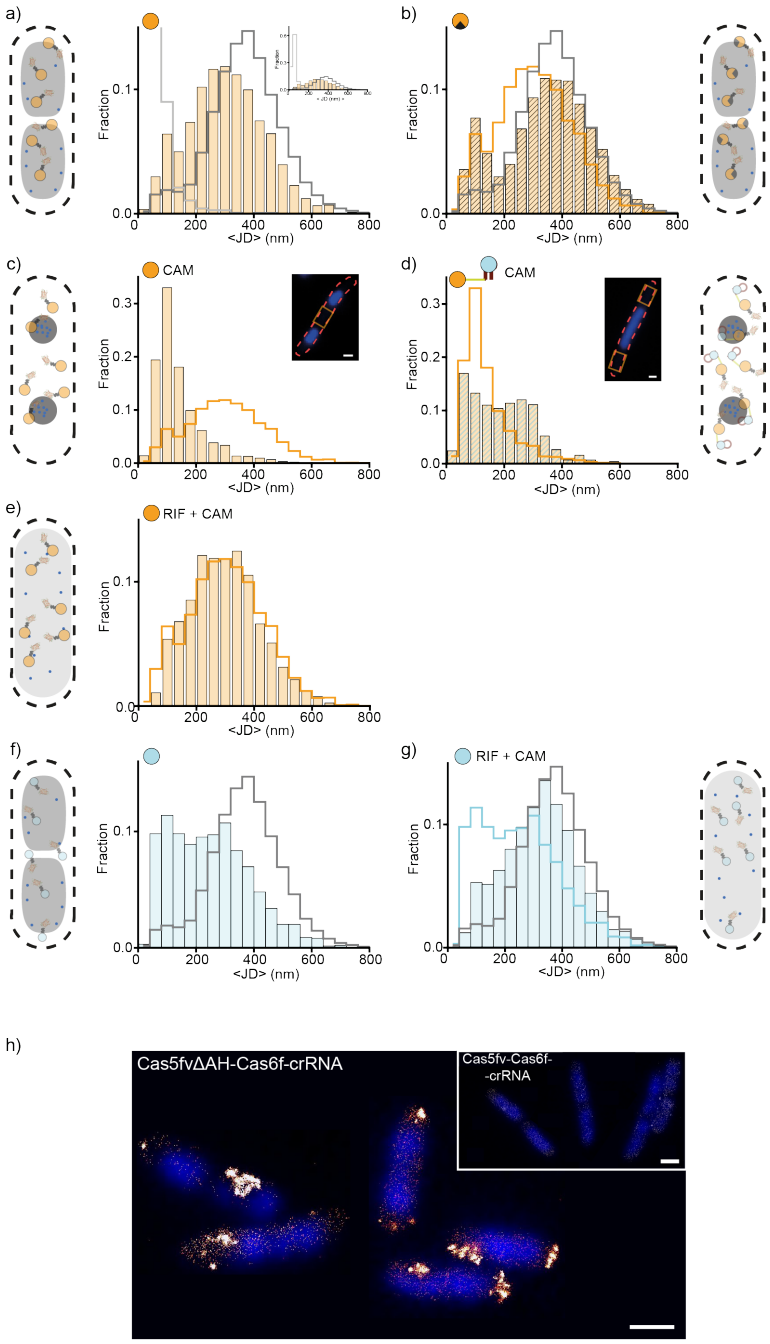

Figure 3.6: Dynamics of individual Cas proteins. (a) Cas5fv has two fractions showing transient interactions. (b) Cas5-ΔAH is mainly freely diffusing but one fraction remains unchanged. (c) In DNA-free, RNA-enriched areas (orange box in the inset) Cas5fv exists mostly as a slowly diffusing protein. (d) When Cas5fv is loaded with the crRNA, the slowly diffusing fraction is decreased, when compared to (c). (e) In RNA-free cells, Cas5fv exists in a fast, only transiently interacting fraction, similarly to Cas5fv in untreated cells. (f) Cas6f exists in two slowly diffusing fractions. (g) These fractions are not present in RNA-free cells. (h) Cas5-ΔAH carrying crRNA is perfectly excluded from the DNA area (blue signal) and forms clusters at cell poles and in the middle of the cell (yellow signal). Scale bars: 1 μm

We then co-expressed Cas5fv together with Cas6f and the Anti-λ crRNA which does not match any cellular target. Here, Cas5fv and Cas6f very efficiently together with the crRNA form stable preassembled complexes which in some cases are cleaved in two parts by intracellular nucleases. For both, the full Cas5fv/Cas6f/crRNA complex as well as its cleaved version, the RNA binding site of Casf5v is occupied with the crRNA. Under chloramphenicol treatment, this should lead to a large fraction of freely diffusing Cas5fv/Cas6f/crRNA complexes and possibly Cas5fv/crRNA in the DNA-free areas of the cells, which thus cannot interact anymore with the RNAs present. Indeed, next to a similar slow fraction we observed for Cas5fv which interacts with RNA in these DNA-free areas (Figure 3.6d, orange outline Cas5fv under chloramphenicol), we measured a second, significantly faster fraction of mobile complexes (Figure 3.6d), albeit at a bit slower apparent <JD> peak of 200-320 nm compared to freely diffusive Cas5fv-ΔAH and Dendra2-T69A. This indicates that this second fast peak resembles successfully formed Cas5fv/Cas6f/crRNA complexes which indeed cannot interact with RNA and furthermore, as they diffuse a bit slower than single proteins, most likely stay intact and are not cleaved in two parts.

We then evaluated the Cas5fv dynamics after the simultaneous treatment with 10 μg/mL chloramphenicol and 5 μg/mL rifampicin for one hour (Figure 3.6e). Here, rifampicin efficiently blocks the transcription of the bacterial RNA polymerase by inhibiting its elongation along the DNA [108, 109]. This causes a rapid mRNA depletion in the cells, as the average mRNA lifetime is about 2.5 minutes [110, 111, 112]. Importantly, our expression system used to express Cas5fv from our plasmid system is under the control of the T7 promoter. The viral T7 RNA polymerase is not inhibited by rifampicin [113], thus mRNA encoding for Cas5fv can still be synthesized. Moreover, the T7 RNA polymerase yield has been shown to be positively affected under rifampicin influence [114]. Nevertheless, this mRNA pool should be largely inaccessible due to stalling ribosomes on it by chloramphenicol treatment [105]. The action of chloramphenicol is rapid, as *de novo* synthesized mRNA reaches a ribosome-rich area in less than one second [115]. Thus, we expected a lowered slow fraction, with the faster DNA-interacting fraction remaining unchanged. Our data is in agreement with these assumptions as the minor peak vanished (Figure 3.6e). Nevertheless, as this minor peak is not very significant for Cas5fv, we strived at showing this effect in a more pronounced manner and probed Cas6f dynamics. As Cas6f is involved in pre-crRNA maturation to obtain final crRNA protospacers, an initial step of Cascade complex formation [65, 68], we hypothesized it to strongly interact with cellular RNA when trying to find its substrate. Indeed, we found Cas6f to reveal a rather slowly diffusing <JD> distribution which seems to be explained by at least two diffusive fractions (Figure 3.6f). Thus, we attribute both to RNA interactions but did not further investigate them (as there exists a multitude of possible RNA interactions, e.g. with RNA of diverse diffusion dynamics due to different lengths and secondary structures, tethered to the transcription complex or to the membrane, etc.). More importantly, the simultaneous drug treatment led to a significant and clearly visible reduction of slow diffusing Cas6f and the overall diffusion dynamics became similar to free diffusing Dendra2-T69A (Figure 3.6g). As a control, rifampicin and chloramphenicol treatment on cytosolic Dendra2-T69A showed no effect (Figure 3.5- right). This hints at a strong shortage of RNA interactions. Thus, this strong phenotype of Cas6f dynamics substantiates our hypothesis of almost complete RNA depletion or blockage under double drug treatment and confirms our observations of the diffusive Cas5fv distributions.

We additionally tried to measure the dynamics of Cas5fv-ΔAH/Cas6f/crRNA complexes as these should neither interact with DNA nor RNA and should therefore be freely diffusive. Remarkably, we were not able to measure possible Cas5fv-ΔAH/Cas6f/crRNA dynamics, as these complexes were highly excluded from the nucleoid area as indicated by DAPI staining (Figure 3.6h, blue signal) and formed concentrated clusters at cell poles or in between nucleoids (Figure 3.6h, yellow signal). This effect cannot be explained by a lack of DNA-interaction only, as we then should observe a similar effect for Cas5fv-ΔAH alone which we found normally distributed and thus present in the nucleoid-rich areas interacting with *de novo* synthesized RNA (Figure 3.6b). Together, this strongly indicates that Cas5fv-ΔAH/Cas6f/crRNA also lacks RNA-interaction. In consequence, it is excluded from the denser mid-cell area by entropic forces and then, most likely caused by its high crowding in those excluded areas, aggregates.

In summary, our observations strongly indicate that the slowly diffusing native Cas5fv dynamics as measured in (Figure 3.6a) can be attributed to RNA-interacting Cas5fv molecules, whereas the majority of Cas5fv molecules in the main, fast fraction transiently interacts with DNA.

Fast *in vivo* Kinetics of Type I-Fv Cascade

We then set out to elucidate the details of the different kinetic sub-populations of Cascade complexes to assess their interaction dynamics and variations within, depending on their crRNA complementarity. We performed detailed sptPALM experiments of Cascades carrying diverse crRNA (Table 3.1) and measured 2-4 biological repeats from different cultures and imaging days at large single-molecule statistics for 13 and 30 ms camera exposure times (Figure 3.7a). Here, the obtained <JD> distributions are more complex than for single Cas proteins and vary according to the complementarity of the provided crRNA but for each crRNA revealed an individual and for all imaging repetitions distinctly reproducible fingerprint of interaction dynamics (Figure 3.7a).

For 13 ms exposures, Cascade Anti-λ, which has no DNA-targets, is respectively missing a stationary fraction (compared to the grey overlaid outline of immobile Dendra2-T69A) but shows a large peak of high mobility with a maximum around 240-320 nm and a smaller peak at slower diffusion with displacements around 80-160 nm (Figure 3.7a, first column). Importantly, both fractions neither resemble the immobile, fixed Dendra2-T69A, nor the freely diffusing Dendra2-T69A distribution. This suggests that we observe some transient interactions we cannot directly resolve at our temporal resolution (as fully resolved interactions would appear as stably bound fractions similar to chemically fixed Dendra2-T69A). Furthermore, from the slower 30 ms exposures, we can infer that the more mobile fraction seems to be indeed a highly transient state frequently cycling between on- and off-binding at high rates as the whole fraction shifts to larger <JD> values with a maximum peak at about 320-360 nm. Contrarily, the slower transient fraction is not resolvable anymore. This hints either i) at a rather slowly frequented state with bound times within the lower millisecond range, a state that we expect to resolve if we would be able to image at an about 10 times faster imaging rate (technically not possible) or ii) at an itself freely, but slowly diffusive state of a molecule or complex (e.g. large hydrodynamic radius or big mass) which for slower 30 ms exposures possesses a higher increase in <JD> as compared to the transiently interacting fraction and thus consequently fully overlaps with it. We therefore

controlled if this fraction of complexes are bound to DNA or to RNA by depleting the free mRNA pool by a simultaneous treatment with chloramphenicol and rifampicin like for the single Cas proteins before. Indeed, for Cascade Anti-λ, the transient peak diminishes like for Casf5v molecules before (Figure 3.7b, first column).

We then allowed for partial complementarity with 133 targets (per *E. coli* genome) of 12 base pair complementarity for Cascade (Anti-REP 12bp) (Figure 3.7a, second column). Here, these partial targets should spatially allow for the first two Cas7 molecules to participate in the Cascade-DNA interference and to stabilize the base-pairing of the crRNA with the target by displacing the complementary DNA strand. We indeed see a stabilizing effect of the Cascade interference, as an immobile fraction appears. Furthermore, this fraction in a large extent also stays stably bound at slower imaging speeds of 30 ms exposures. Nevertheless, we further also reveal a plateau of transient interactions (around 200 nm displacement), which we do not fully resolve anymore. Together, this indicates that the interaction time of Cascade (Anti-REP 12bp) with the DNA is indeed in the tens of millisecond range.

Next, we explored the dynamics of Cascade Anti-REP possessing full targets (Figure 3.7a, third column). We adjusted the 12 base pairs-complementary crRNA in a way that by tripling it to 3 similar but different crRNAs, the previously 133 targets of only 12 bp complementarity now span the range of 42 full targets, 33 targets with 25-30 bp complementarity and 24 (19-24 bp), 8 (13-18 bp) and 26 (12 bp) targets of lower complementarity (Table 3.1). As the total number of targets is still 133 but the complementarity is highly shifted towards higher base pair matching, the ratio of the different fractions shifts in favor of a significantly higher peak of stable DNA interactions, whereas the plateau of transient interactions remains at similar levels but the fast fraction at highest mobility accordingly drastically decreases (Figure 3.7a, third column).

This distribution can be made almost bimodal by changing the crRNAs once more to drastically reduce the middle (plateau) fraction of transiently interacting complexes. Thus, for our last strain (Figure 3.7a, last column), we can resolve two clear peaks resembling Cascade complexes which can either stably interfere with DNA due to a high complementarity or do interact only very transiently with the DNA and thus similarly to the Cascade Anti-λ strain with a majority of 85 targets possessing no higher match than 11 base pairs of complementarity. Finally, also controlling this strain for the nature of its interactions by depleting the RNA levels, we cannot detect any significant changes in the distribution (except of a small decrease in the middle, transiently interacting, fraction) which substantiates its strong DNA-binding nature (Figure 3.7b, last column).

In summary, the interactions of Cascade complexes with the variety of possible genomic targets is very diverse and consequently leads to multi-layered and highly overlapping diffusion statistics, which nevertheless are highly characteristic fingerprints of the respective crRNA throughout all repetitions of our experiments. Clearly distinguishable from all other components is only the, under the respective temporal resolution, stably bound fraction. We thus figured that it could be possible to measure the absolute bound-time of Cascades to their targets in relation to their crRNA complementarity by ingeniously varying the imaging frequencies as investigated in the next section.

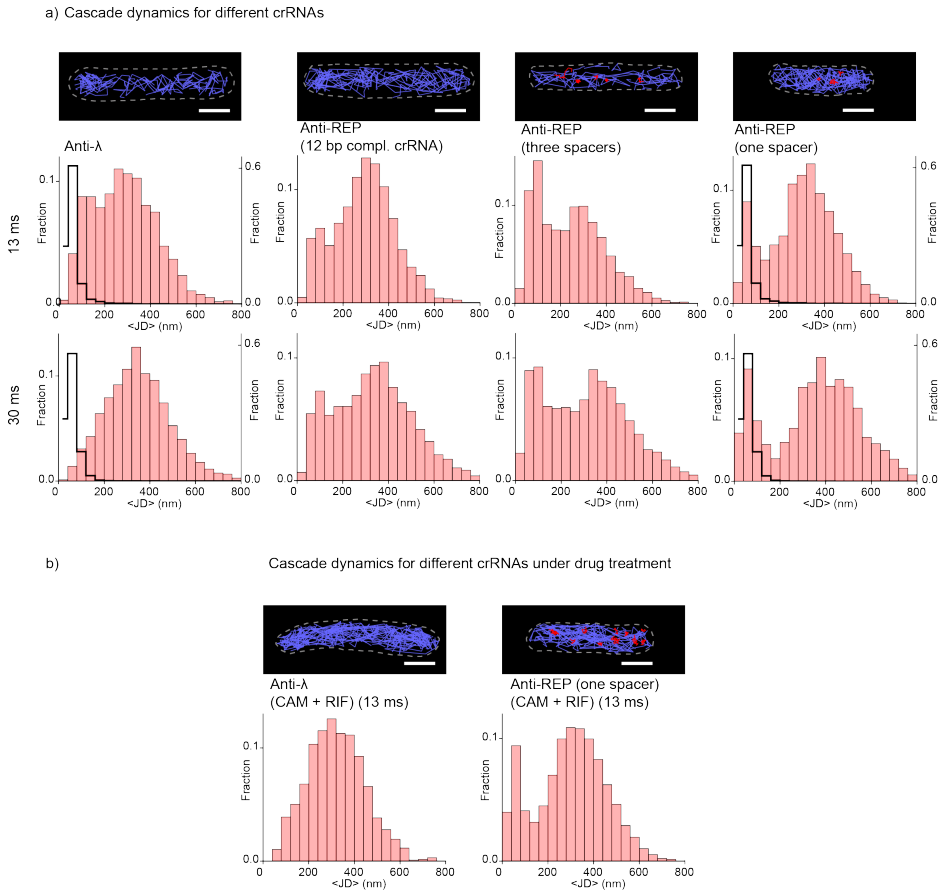

Figure 3.7: Fast *in vivo* kinetics of type I-Fv Cascade. (a) Cascades with different crRNA variants have a unique <JD> distribution. Cascade (Anti-λ) (first column) lacks the immobile fraction (compared to grey overlaid outline of immobile Dendra2-T69A) in both, 13 and 30 ms, imaging intervals. Two fractions showing transient interactions are visible with the 13 ms imaging interval and merge into the one fraction under 30 ms exposure. When Cascades can match partial targets (Cascade (Anti-REP 12bp), second column) the immobile fraction appears in the 13 ms imaging interval and remains unchanged when the imaging interval is increased to 30 ms. By providing crRNAs which in most cases can match full (>31 bp complementarity) or almost full (24-30 bp complementarity) targets (Cascade (Anti-REP three spacers), third column), immobile fraction becomes more prominent as well as fraction of the transienly interacting Cascades is significant. When Cascade is supplied with the crRNA which can not match partial (12-24 bp complementarity) targets, <JD> distribution becomes almost bimodal (Cascade (Anti-REP one spacer), last column). (b) <JD> distributions for Cascade (Anti-λ) and Cascade (Anti-REP (one spacer)) imaged with the 13 ms imaging interval in cells lacking mRNA. In Cascade (Anti-λ) slower fraction is not visible anymore, while in Cascade Anti-REP, the <JD> distribution remains unchanged. In (b) and (c) for each strain trajectory maps for exemplary cells are shown (color coding as in Figure 3.1). Scale bars: 1 μm.

Long-exposure sptPALM Tracking to Measure *in vivo* Binding Kinetics

By varying the imaging and read-out frequencies to long-exposure sptPALM tracking, we expect to observe different k_{eff} values, which are inverse of interaction lifetimes, for Cascades carrying different crRNA variants, where lower k_{eff} values are expected for Cascades capable of finding fully complementary targets and higher values for Cascades matching only partial targets.

To evaluate these assumptions, in the first part of the experiment we imaged two conditions: chemically fixed cells expressing LacY-Dendra2-T69A and the Cascade (Anti-λ) strain (Figure

3.8- black and grey data, respectively). In the first case, as proteins are permanently immobile, the $k_{eff\text{-}fixed}$ is equal to the fluorescent protein bleaching rate. In consequence, the k_{eff} for any dynamic system cannot be lower than this value, thus slopes should be steeper than for chemically fixed proteins. Contrarily to that, Cascade (Anti-λ) can not match any targets in the host and Cascade-DNA interactions are very short, which results in a high $k_{eff\text{-}Anti\text{-}\lambda}$ value and marks an upper limit for other Cascade variants.

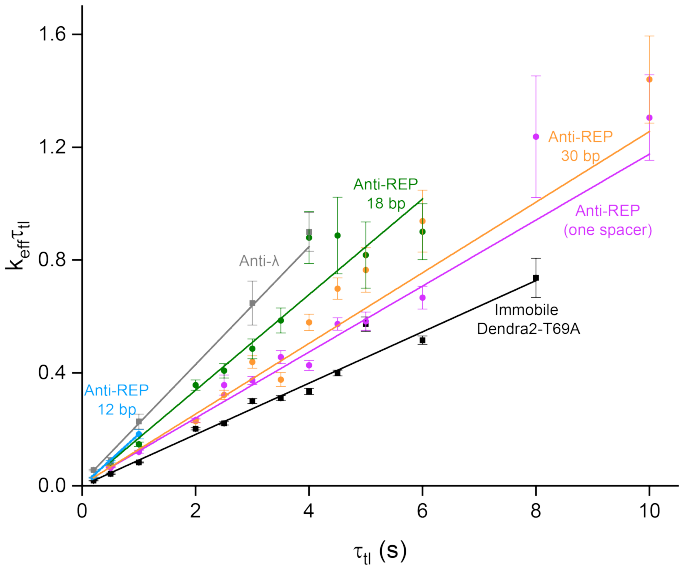

Figure 3.8: Effective unbinding rates (k_{eff}) multiplied by the imaging interval (τ_{tl}) in function of τ_{tl}. Efficient rates (k_{eff}) are proportional to the slope of the linear fit. k_{eff} values are decreasing for crRNAs matching more complementary targets. Error bars represent SE.

In the second part of the experiment we imaged other Cascades carrying different crRNA variants which can match: from the PAM sequence up to 12 more base pairs of possible targets, up to 18 and up to 30. Further, we also imaged full target binding by using Cascade (Anti-REP (one spacer)). (Figure 3.8- blue, green, orange and magenta points, respectively). As expected, for all four variants, data points are distributed between the two control conditions of bleaching rate and only transient binding. The slopes of the linear fits (reflecting k_{eff} values) show a clear trend. Their value decreases for crRNA with higher target complementarity. This indicates an increasing stability of the Cascade-DNA interference complex for better matching targets.

Table 3.2: Average target lengths in base pairs

crRNA variant	Average target compl. (bp)	k_{eff} (1/s)	SE
Anti-λ	0.00	0.236	0.0172
Anti-REP 12 bp	12.00	0.170	0.0117
Anti-REP 18 bp	16.82	0.156	0.0037
Anti-REP 30 bp	24.67	0.131	0.0046
Anti-REP (one spacer)	26.03	0.121	0.0025
Immobile Dendra2-T69A	-	0.090	0.0021

Next, we test whether the k_{eff} rate has a linear dependency to the target complementarity. For this purpose, we calculated the average target complementarity for each crRNA variant from the distribution of targets as given in Table 3.1. Plotting k_{eff} values as a function of the average target complementarity, we obtain a linear decrease in k_{eff} in respect to the target length (Figure 3.9). Unfortunately, our current preliminary data cannot answer the question whether the k_{eff} change occurs with every base pair match, or with every sixth base pair as it is suggested in [116] allowing for more Cas7 stabilizing the interference. Here, further experiments are required. Furthermore, at the current stage, data are not allowing to determine absolute bound-times of Cascades to their target in relation to their crRNA complementarity. To address this question, we need better statistics, as well as need to perform additional imaging with intermediate τ_{tl} values to accurately identify and resolve the multitude of different Cascade-DNA long-term interactions.

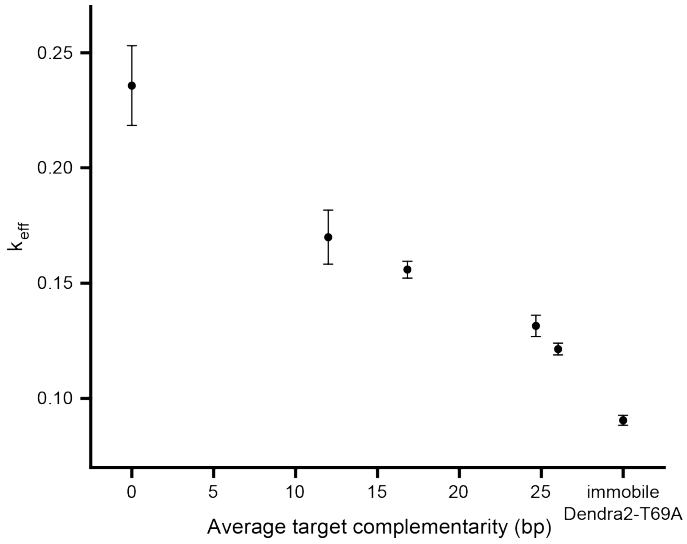

Figure 3.9: Effective unbinding rates (k_{eff}) in function of the average target length. k_{eff} values decrease linearly with increasing average target length.

To summarize, by imaging Cascade-DNA interference of Cascades carrying different crRNAs with varying interval times, we were able to qualitatively show the relationship between the Cascade-DNA complex stability and the crRNA carried by the Cascade. Stability of the Cascade-DNA complex increases with the complementarity of the crRNA. Moreover, our data suggest that this relationship has a linear correlation. Measuring absolute bound-times with the current dataset was yet not successful mainly due to insufficient statistics and sampling times. However, these rather preliminary results indicate, that after performing further measurements, the accurate bound-times can be resolved. In Section 4.2, further research directions to consider in the future are discussed.

4 | Discussion

4.1 Developed tools

4.1.1 Primed Conversion as a Novel Tool Reducing Phototoxicity in Live-Cell SMLM

pcFPs change their optical properties upon illumination with specific wavelengths. This property makes them a key tool in SMLM methods like sptPALM. Among different variants of pcFPs, especially green-to-red pcFPs gained popularity due to their brightness, photostability and high signal-to-noise ratio. In their initial form, they can absorb blue photons and emit green fluorescence light. When illuminated with near-UV light (wavelength approx. 380-410 nm), green-to-red pcFPs irreversibly change their absorption and emission spectra with a maxima in the orange/red range of the spectrum (550-580 nm). While using short wavelength light in structural PALM is not an issue, as usually these experiments are performed in fixed samples, illuminating living samples can however cause severe phototoxic damage. In 2015, an alternative photoconversion mechanism, called PC, was reported for Dendra2 [117], where near-UV light is replaced by the simultaneous illumination with blue and near-infrared light.

One task of this Ph.D. work was to investigate, whether PC can be successfully applied in sptPALM routines and in effect reduce the phototoxicity during imaging. Also, the question arises if this mechanism is unique for Dendra2, or if it can be also used in other green-to-red pcFPs. In our publication [94] we have shown that indeed, PC reduces the phototoxic effect and that a vast majority of *E. coli* cells survive six minutes of sptPALM illumination under PC regime. We showed that PC-sptPALM provides the same quantitative results as "classic" UV-sptPALM in terms of statistics and quantities. Thus, we concluded that PC can successfully replace the UV photoconversion in sptPALM experiments.

Furthermore, we have determined that the PC mechanism is not unique for Dendra2, but naturally also occurs for the mMaple protein family. Additionally, PC-ability can be introduced to other families such as EosFP, Monomeric Kik Green-to-Red Fluorescent Protein (mKikGR), and Photoconvertible Dronpa Fluorescent Protein (pcDronpa) by exchanging their 69th residue (GFP numbering) from an alanine to a threonine. Thus we generated new green-to-red pcFPs variants (e.g. mEos3.2-A69T, pcDronpa2-A69T), which we currently frequently use in our recent studies due to their superior performance.

In additional experiments reported in [94], we have shown a pH-dependence of the PC mechanism. PC seems to occur from the anionic form of the chromophore, while UV-photoconversion occurs from the neutral form of the chromophore. We also characterized the photoswitching behavior of both, primed-convertible and non-primed-convertible proteins.

4.1.2 Aberration-free Multi-color Imaging by Combining UV-photoactivation and PC

Multi-color PALM studies are limited by the fact that the vast majority of paFPs and pcFPs utilize UV-light as the photoactivation/photoconversion source and that most of best performing proteins emit fluorescence in the same orange-red emission channel. Other FPs which emit fluorescence in other spectral channels, e.g. Photoactivatable Green Fluorescent Protein (paGFP) [118], Photoswitchable Cyan Fluorescent Protein 2 (PS-CFP2) [119] or Dronpa [120] are less bright and show a less strict photophysical behavior. In effect, multi-color PALM is possible by combining pairs like Dronpa/EosFP or PS-CFP2/EosFP [121]. Nevertheless, different read-out spectras cause chromatic aberration, resulting in non-linear disturbances between read-out channels, which have to be corrected in a postprocessing step proving to be a non-trivial task and inferior photophysics and FP brightness lead to lower SMLM image qualities.

In our second publication, which resulted from my work [95], we proposed a new sptPALM multi-color approach, combining UV-photoactivation and PC in various organisms. Here, the read-out is performed sequentially, where first a primed-convertible pcFPs (e.g. Dendra2, mEos3.2-A69T) is fully read-out using a combined illumination of blue and infrared light, followed by the read-out of paFPs, e.g. PAmCherry, which can be photoactivated using UV-illumination. We verified that there is no crosstalk between both read-out channels and that the PC read-out is not affecting the paFPs, proving this method to be quantitative. Additionally, we demonstrated that this multi-color SMLM approach can be used in different prokaryotic and eukaryotic cell types, and that it is possible to perform dual-color sptPALM. Finally, we extended the read-out to four cellular targets in a single read-out channel by utilizing correlative imaging methods.

4.1.3 Outlook

We have shown that PC can be successfully used as a routine in SMLM and constructed pcFPs mutants that are capable of PC. Thus we expect it to be used advantageously in other studies (plasmids encoding PC pcFPs can be purchased from the Addgene plasmid repository). There are still open questions left which our attention should be directed next.

First, the full PC-mechanism is not yet fully elucidated. We were capable of showing a milliseconds lifetime of the transient state. Another research group has found this state to be a triplet state and they measured lifetimes match with our findings [122]. Byrdin et al. further investigated this long-lived triplet state for the Enhanced Green Fluorescent Protein (EGFP) [123] and for the green-to-red photoswitchable protein IrisFP [124] where they proposed a more complex mechanism of the triplet state formation [125]. Still, this field is in need of more investigation to fully understand the underlying mechanisms.

Since the developed PC mutants are able to undergo UV-photoconversion next to PC, the next task would be to design pcFPs that are bright and monomeric, but can only be photoconverted via PC. This would enable a simultaneous read-out in our dual-color approach, as for now, this has to be done in the proper order (first full read-out of primed-convertible, then UV-photoactivatable protein). So far, virtually all proteins capable of PC can be also photoconverted with UV-illumination [94, 122]. The only exception is pcDronpa-A69T [126] which poorly converts with UV and the conversion with PC is more prominent. There are however two obstacles, which are limiting the use of this protein in SMLM, such as an only moderate photoconversion efficiency of pcDronpa-A69T in general and the tetrameric nature of proteins from the pcDronpa family, in contrast to Dendra2 and mEos families, which are usually monomeric in lower and moderate protein concentrations. Moeyaert and colleagues generated a monomeric variant of pcDronpa2 (pcDronpa2-V123T-N158E-Y188A) which however showed no photoconversion at all [126].

Lastly, there is an open question, whether PC is limited to only green-to-red pcFPs, or if similar mechanisms can be found for other protein families, such as Photoswitchable Monomeric Orange Fluorescent Protein (PSmOrange) [127] and PSmOrange2 [128] which are photoconverting and emitting fluorescence at longer wavelengths, which makes them even more live-cell compatible.

4.2 CRISPR-Cas Type I-Fv System Dynamics in Living Cells

The role of the CRISPR surveillance complex is to find and disarm a potential viral threat. This task, however, is not as trivial as it sounds. A single effector complex has to correctly identify a short DNA target sequence in the crowded host DNA and at the same time, it has to avoid degradation of any other genetic material, e.g. the host genome. Furthermore, as the viral genetic material can mutate, and thus could evade the recognition by the surveillance complex, CRISPR-Cas complexes have to be able to adapt to new threats. To fulfill their role efficiently, Cascade complexes have to have a high performance in their surveillance process. In recent years, the CRISPR-Cas mechanism of action has been studied *in vitro* with single-molecule methods. Two studies reported independently that the DNA probing by the surveillance takes approx. one second and upon finding a partial target this interaction lasts for approx. 25 s. Finally, the interaction between the surveillance complex and its target is very stable in the range of tens of minutes [82, 77]. Despite an excellent agreement between these two *in vitro* studies, the open question is whether we can directly translate these quantities to *in vivo* systems. We can expect that contrary to isolated *in vitro* systems, surveillance complexes have to cooperate with other DNA-interacting systems like replication and transcription machinery, thus quantities can be altered when compared to *in vitro* measurements. With that reasoning, during my Ph.D. work I have studied the CRISPR-Cas type I-Fv protein dynamics *in vivo* by using sptPALM methods.

4.2.1 *In vivo* Dynamics of Cas5fv and Cas6f

As the surveillance complex of the type I-Fv is a multiprotein complex, we were first interested in studying the dynamics of single protein subunits forming the Cascade complex: Cas5fv and Cas6, which for this purpose were labeled with the Dendra2-T69A. With sptPALM imaging experiments, we have shown that Cas5fv interacts with the DNA and RNA in two dynamic modes. DNA-interactions are crucial to fulfilling its PAM recognition role as it has been shown in [75]. We have

also confirmed that this DNA-interaction is realized by its AH domain and mutants lacking this domain are losing this functionality. Additionally, we have reported the RNA-interaction function of Cas5fv, which is essential for the Cascade complex assembly process. Furthermore, we showed that Cas6f probes the RNA pool to find their substrate- pre-crRNA.

4.2.2 *In vivo* Kinetics of Type I-Fv Cascade

In the next part of my work I have studied the dynamics of Type I-Fv Cascade complexes. As mentioned previously in Section 1.3.5 and as has been shown in Figure 1.7, Cascade-DNA interactions range from milliseconds to minutes. In consequence, the investigation of these interactions was split into two parts. In the first part, we were focused on the fast kinetics of Cascades and this part was realized in the same way as for single Cas proteins. To study binding kinetics, we utilized an approach presented in [27, 28, 22, 19], where the same sample was imaged with a constant excitation but variable interval times.

To characterize the fast kinetics of Cascades, we have imaged effector complexes carrying four different crRNA variants (Figure 3.6a). We can clearly identify unique diffusion fingerprints for different crRNA variants. Cascade (Anti-λ), which cannot match any targets in the host genome, lacks a stationary fraction. Cascades supplied with crRNAs which can match targets in the host genome show immobile fractions. The diffusion distributions shown in Figure 3.6b strictly follow target distribution Figure 3.6a. When more fully matching targets are present in the host genome, immobile fractions are more prominent and fast diffusing fraction significantly decreases. Furthermore, for the Cascade (Anti-REP (one spacer)) which contains only long targets and almost no targets with the 12-18 bp length, diffusion fingerprint becomes almost perfectly bimodal.

In the second part of the Type I-Fv Cascade dynamics investigation, we aimed to measure absolute bound-times of Cascades with different crRNAs. At the current state, we were successful to show an increasing Cascade-DNA complex stability for higher target complementarity. Our data also indicate that the stability increases in a linear manner with the target complementarity. However, we cannot answer whether the stability increases with each single base pair match between the crRNA and target, or rather increases with each sixth base pair (one Cas7fv subunit covers six base pairs of the crRNA spacer sequence) as suggested in [116]. Unfortunately, due to insufficient statistics, we cannot provide absolute bound-time values at this moment and further experiments are required to answer this question which I will discuss in the next section.

4.2.3 Outlook

In this work we have shown that sptPALM methods can be successfully applied to investigate CRISPR-Cas protein dynamics in living cells. We can characterize the dynamics of Cascade complexes, as well as single Cas proteins. Nevertheless, there are open questions, which will be further addressed in this project.

The most critical part in this project is to investigate in more detail the absolute bound-time values for Cascades carrying different crRNAs. It has to be emphasized that CRISPR-Cas interactions are very complex in their nature and thus challenging to study *in vivo* when a lot of different targets are present and the cellular machineries can interfere. In our system, each tested

strain has targets with different complementarity, thus it is obvious we should expect multiple bound-time values, which can be represented as off-rates (k_{off}). However, due to insufficient statistics and missing data points, at this moment we can not resolve these k_{off} values. Thereby, in our preliminary data we have used the more robust average k_{eff} value, which yields the ensemble average of all interactions. This approach is sufficient enough to qualitatively show the trend of Cascade-DNA stabilities, as we have described in our results chapter but does not provide quantitative information. While having multiple k_{off} values should not be an issue to achieve our ultimate goal, as it has been shown in simulations by Ho et al. [129], this analysis demands large statistics. Therefore, during my wrap-up postdoc period, I will perform further experiments.

First, we want to evaluate the expression level of our CRISPR-Cas system. As we are expressing our Cas proteins and crRNAs from an inducible plasmid system, we want to keep the expression at a low level. Our reasoning is that keeping a low copy number of Cascades, significantly below the number of longest possible targets, Cascade complexes will all have the chance to find a target and maybe will mostly occupy better targets. In consequence, we might reduce the number of k_{off} states by populating those with highest affinity. Contrary, when the number of Cascades is higher than the number of longest possible targets, we expect the dataset to contain more k_{off} states. In effect, for different expression levels, we should observe different k_{eff} values within the same strain.

The second improvement requires introducing additional τ_{tl} values to our measurements. As it can be seen in Figure 3.8 for Cascade (Anti-REP 30 bp) and Cascade (Anti-REP one spacer), $k_{eff}\tau_{tl}$ values drop down at $\tau_{tl} = 3.5$ s and $\tau_{tl} = 4$ s, respectively. This trend is expected for systems with multiple unbinding rates, as shown in [129], however in our case these are single time points where this trend is observed. Despite having multiple biological repeats for these time points, it is recommended to image these strains with flanking τ_{tl} values to confirm that this trend is a real signal and not a measurement error.

Finally, as I stated previously, our data suffers from insufficient statistics, thus for already measured time points I will perform further measurements to improve statistics and to reduce the measurement error.

Another open question is what the exact interaction times between Cascade and random DNA sequences *in vivo* are and whether they differ from values measured *in vitro*. We can partially answer the second part of the question. *In vitro* data reports approximately one second lifetime for Cascades screening random DNA sequences [77, 82]. In our imaging conditions (milliseconds interval for fast sptPALM imaging), this is sufficiently long to visualize the Cascade complex as an immobile molecule. As we are not observing the stationary fraction in Cascade Anti-λ, we can argue that interaction lifetimes measured *in vivo* differ from *in vitro* measurements by at least an order of magnitude. These differences can be explained by two factors: (i) *in vitro* experiments are conducted in well-isolated conditions. On the one hand, these measurements are very precise as experimental conditions can be strictly controlled (including target choices). On the other hand, *in vitro* measures are conducted in an isolated system which might not fully reflect the cellular environment. As it has been reported by Dillard et al. in, paradoxically, *in vitro* experiments, Cascade activity is affected by protein roadblocks [81]. (ii) In our experimental

in vivo system, genomic DNA which carries targets is very compacted, compared to DNA used in *in vitro* experiments, which also might have an impact on Cascade activity. Very recently, Newton and colleagues reported that DNA stretching induces an off-target activity of Cas9, which leads to non-specific cuts [130]. This result might hint that different forces, which are applied to DNA in both experimental conditions, might significantly affect the Cascades behavior.

5 | Supplementary Materials

5.1 Appendix A

Supporting Information: A General Mechanism of Photoconversion of Green-to-Red Fluorescent Proteins Based on Blue and Infrared Light Reduces Phototoxicity in Live-Cell Single-Molecule Imaging

Bartosz Turkowyd, Alexander Balinovic, David Virant, Haruko G. Goelz Carnero, Fabienne Caldana, Marc Endesfelder, Dominique Bourgeois, Ulrike Endesfelder

Materials and Methods

Materials and Methods

Fluorescent protein plasmids

Plasmids carrying the sequences of the fluorescent proteins (FPs) were obtained from different sources or constructed as listed in **Table S1**. All plasmids were checked by sequencing (Eurofins Genomics, Germany) and heat-shock-transformed into expression-optimized BL21-AI (Thermo Fischer, Germany).

Plasmid construction

pRSETa-mMaple, pRSETa-mMaple3, pRSETa-mEos3.2 and pRSETa-mKikGR were generated by a customized CPEC protocol [1]. In short, the pRSETa backbone (from pRSETa-mEos2, addgene #20341) and the FP sequences (pBAD18 templates [2]) were amplified by PCR (Phusion, NEB) using the corresponding primers (**Table S3**). Purified PCR products were mixed in 1:10 molar ratio and ligated. CPEC reaction mixes were used for bacterial transformation directly after ligation.

pRSETb-pcDronpa-A69T, pRSETb-pcDronpa2-A69T, pRSETa-mEos3.2-A69T, pRSETa-mEos4b-A69T, pRSETa-mKikGR-V69T, pRSETa-mMaple3-V157I(V166I) were generated by site-directed mutagenesis PCR using the corresponding primers (**Table S3**). PCR reaction mixes were digested by DpnI (NEB, Germany) to remove residual template plasmids (2 h, 37°C) prior to the transformation. All primer were designed in Benchling (Benchling Inc.) and synthesized by Eurofins Genomics.

MG1655 rpoC-Dendra2 strain

MG1655 incorporating rpoC-Dendra2 was generated by homologous recombination using a modified lambda red recombination pKD46 protocol [3]. In short, the PCR-amplified Dendra2-sequence followed by the frt flanked chloramphenicol resistance gene from the codon-optimized Dendra2 pBAD18 template[2] with auxiliary homologous overhang sequences was electroporated (5ms, 1.8 kV) into MG1655 cells.

Samples with transiently expressed FPs in BL21ai cells

Strains from -80°C stocks were cultured overnight at 37°C, 210 rpm, LB with 100 µg/mL ampicillin, reinoculated, grown to OD 0.2 and induced by 0.5% w/v arabinose (Sigma-Aldrich, Germany). After 2 hours, cells were fixed for 15 minutes with 2% paraformaldehyde (Sigma-Aldrich, Germany) and washed twice in 100 mM PBS (*pH* 7.4). Samples were stored in 100 mM PBS (*pH* 7.4)/0.1% sodium azide at 4°C or immediately immobilized on 8-well slides (Ibidi, Germany) previously cleaned with 2% Hellmanex (Hellma, Germany) and coated with 0.05% poly-L-lysine (Sigma-Aldrich, Germany).

Live cell samples with MG1655 rpoC-Dendra2

Strains from -80°C stocks were cultured overnight at 37°C, 210 rpm, LB with 34 µg/mL chloramphenicol, reinoculated into 2% glucose EZ Rich Defined Medium (Teknova, USA) and grown at 32°C, 210 rpm to OD 0.2. Bacteria were placed on fresh agarose pads (1% low melting agarose (Sigma-Aldrich, USA) with EZRDM).

Purification of fluorescent proteins

Pellets of cultures overexpressing FPs from pRSET plasmids were suspended in 10 mM PBS (*pH* 7.4) with lysozyme (0.5 mg/mL) for 2h, homogenized by ultrasound (UP100H, Hielscher, Germany) and centrifuged for 15 minutes (17000 x g, 4°C). FPs were purified from the supernatant by Ni-NTA spin columns (Thermo Fischer, Germany) followed by a buffer exchange to 10 mM PBS (*pH* 7.4) (Nanosep columns, VWR, Germany).

Microscope Setup

Imaging was performed on a custom build setup based on an automated Nikon Ti Eclipse microscope equipped with appropriate dichroic and filters (ET dapi/Fitc/cy3 dichroic, ZT405/488/561rpc rejection filter, ET525/50 or ET610/75 bandpass, all AHF Analysentechnik, Germany), and a CFI Apo TIRF 100x oil objective

(NA 1.49, Nikon). For PC using 640 nm laser illumination, a zt405/488/561/640rpc dichroic and a ZET405/488/561/640 rejection filter were used (both AHF Analysentechnik, Germany). All lasers (405 nm OBIS, 561 nm OBIS, 640 nm OBIS, 730 nm OBIS, 488 nm Sapphire; all Coherent Inc. USA) except 730 nm were modulated via an acousto-optical tunable filter (AOTF) (Gooch and Housego, USA). Fluorescence was detected by an emCCD (iXON Ultra 888; Andor, UK). The z-focus was controlled by a commercial perfect focus system (Nikon, Germany). Acquisitions were controlled by µManager [4]. Live cell experiments were performed on a customized heating stage at 32°C.

Spectroscopy

Absorption spectra and fluorescence spectra (**Fig. S2**) were measured in V-750 and FP-8500 instruments (Jasco, Germany), respectively, using a 50µl UV-transparent quartz cuvette. Molar extinction coefficients (**Table 1 and Table S2**) were calculated as described [5]. pK_a values (**Fig. S2**) were determined as per previous description [6].

Photoconversion experiments

Photoconversion of the pcFPs variants by 405 nm and 488/ 730 nm illumination was measured in fixed BL21ai cells immobilized on 8-well slides (Ibidi, Germany) in 100 mM PBS equilibrated to different *pH* values (**Fig. S3 (c)**). In 405 nm-mediated photoconversion experiments, immobilized fixed cells were continuously illuminated by 2.5 W*cm^{-2} 405 nm light; in the PC experiments, cells were continuously illuminated by 450 W*cm^{-2} of 730 nm light and 488 nm laser pulses of 4 W*cm^{-2} were synchronized with every fifth imaging frame. In both modes, the fluorescence was read-out by a continuous illumination of 200 W*cm^{-2} of 561 nm laser irradiation. All regions of interests were imaged for 30 s with 30 ms exposure time making use of the frame transfer mode of the camera. For experiments measuring the PC efficiency for Dendra2 at different 488 and 730 nm light intensities, 100 mM PBS (*pH* 7.4) was used (**Fig. S3 (b)**). For PC experiments with 488 and 640 nm light, cells were imaged in 100 mM PBS (*pH* 8.5) and laser intensities were adjusted to 4 W*cm^{-2} of 488 nm light pulsed every fifth frame and 400 W*cm^{-2} of continuous 640 nm light (**Fig. S3 (e)**).

Experiments on the stability of fluorescence signals

Fluorescence of the green and red chromophore form of the photoconvertible FPs was measured in fixed BL21ai cells immobilized on 8-well slides (Ibidi, Germany) in 100 mM PBS (*pH* 7.5). For fluorescence intensity measurements in the green chromophore form, samples were illuminated by 3 W*cm^{-2} of 488 nm light. The red chromophore form was imaged after photoconverting the ROIs by illumination of 2.5 W*cm^{-2} 405 nm laser light for 15 seconds. ROIs were then illuminated by 200 W*cm^{-2} of 561 nm laser light. Intensity traces for both channels were recorded for 90 s with 30 ms exposure time in the frame transfer mode of the camera (**Fig. S3 (d)**).

Intermediate state lifetime measurements

Intermediate state half-life measurements were performed in fixed BL21ai cells immobilized on 8-well slides (Ibidi, Germany) in 100 mM PBS (*pH 7.5*). Samples were illuminated by alternating between 30 ms irradiation by 4 W*cm^{-2} of 488 nm light and 30 ms irradiation by 200 W*cm^{-2} of 561 nm and 2 kW*cm^{-2} of 640 nm light. Both channels were rapidly switched by an AOTF controller (ESTechnical, Kent, UK) with in between delays set from 0 to 30 ms (**Fig. S4 a (i)**). 640 nm light instead of 730 nm light had to be used due to the technical limitation of the AOTF, necessary for fast modulation, of only accepting wavelengths from 400 - 650 nm only. Intensity traces were measured over 1000 frames for each channel. Additionally, a UV photoconversion control was performed by illuminating the samples with alternations of 30 ms long irradiations of 2.5 W*cm^{-2} of 405 nm light and 200 W*cm^{-2} of 561 nm light (**Fig. S4 b (i)**).

Reversible photoswitching experiments of the green fluorophores

Fluorescence decay under 488 nm illumination and recovery upon 405 nm light were measured in fixed BL21ai cells immobilized on 8-well slides (Ibidi, Germany) in 100 mM PBS (*pH 7.5*). For fluorescence decrease measurements, samples were continuously illuminated by 4 W*cm^{-2} of 488 nm light. For fluorescence recovery, measurements samples were continuously illuminated by 2.5 W*cm^{-2} of 405 nm light and 488 nm laser pulses of 4 W*cm^{-2} were synchronized with every 20th imaging frame. Six cycles were recorded on the same ROI, both for 60 s with an exposure time of 30 ms exposure time (**Fig. S5 (a)**).

Post-processing and data analysis of ensemble measurements

All image stacks were post-processed by scripts in Fiji [7] as illustrated in **Fig. S3 (a)**. In short, ROIs were extracted by identifying individual bacterial shapes from fluorescence averages excluding overlapping or out-of-focus cells. The mean fluorescence intensity per pixel was measured as a function of time. For primed conversion experiments, frames including 488 nm illumination pulses were excluded from the analysis due to increased background of channel-leaking green fluorescence. For photoconversion efficiency experiments (**Fig. S3 (b,c)**), extracted data was fitted by equation (1).

$$I(t) = BG - Ae^{-kt} \quad (1)$$

Fitted conversion rates *k* and amplitudes *A* were taken only from fits of R-squared values of 0.95 or higher. For non-converting settings, where no curve could be fitted, the difference of the average intensity prior to the photoconversion and the maximum value reached during the illumination was plotted instead. To measure the photostability of the green fluorescence signal (**Fig. S3 (d)**), extracted data was fitted by equation (2).

$$I(t) = BG + Ae^{-kt} \quad (2)$$

Fitted conversion rates *k* were taken only from fits with R-squared values of 0.95 or higher, and their reciprocal multiplied by *ln(2)* yielded the fluorescence decrease time $t_{0.5}$. The red fluorescence decay cannot be fitted by a single exponential decay; instead $t_{0.5}$ was directly measured at the moment it reached 50% of intensity I_0.

Single-molecule experiments

Purified protein solutions were placed on 8-well slides (Ibidi, Germany) previously cleaned with 2% Hellmanex (Hellma, Germany) and rinsed twice with 100 mM PBS (*pH* 7.4) after 15 minutes. Surfaces were imaged under 405 nm and 488/730 nm photoconversion conditions in highly inclined and laminated optical sheet (HILO) illumination [8]. Additionally, a cleaned surface without single molecules was recorded as a purity control. Applied laser intensities were: 5 W*cm^{-2} of 405 nm, 4 W*cm^{-2} of 488 nm, 1 kW*cm^{-2} of 561 nm and 450 W*cm^{-2} of 730 nm. 405 nm and 488 nm lasers were pulsed every 25th frame. Movies were recorded at 33 Hz image acquisition rate for two minutes. Localizations of the fitted single fluorescent spots were obtained by the open source software rapidSTORM [9] and tracked with the help of customized tracking software written in C++. For analysis, only trajectories that started after 405 or 488 nm pulse frames and were visible for at least two frames were used (**Fig. S8 (a)**). Analysis was performed by using OriginPro software (Origin LAB Corporation). AD counts were converted to photon counts according to the emCCD camera sensitivity.

Single-particle-tracking PALM experiments followed by cell growth quantification

Living rpoC-Dendra2 MG1655 *E.coli* cells were imaged under 405 nm and 488/730 nm photoconversion sptPALM conditions for 2, 4, 6 and 8 minutes in HILO illumination mode. Additionally, two controls were

recorded: cells not illuminated by any laser light and cells illuminated for 6 minutes by the 561 nm read-out laser only. Applied laser intensities were: 690 mW*cm^{-2} of 405 nm, 400 mW*cm^{-2} of 488 nm, 450 W*cm^{-2} of 730 nm and 600 W*cm^{-2} of 561 nm. 405 nm and 488 nm lasers were pulsed every 12th frame. Movies were recorded at 77 Hz image acquisition rate to follow the diffusing RNA polymerase. After sptPALM imaging all illuminated regions and controls were imaged under bright light for 8 hours at 2 min intervals to quantify the cellular growth after the experiments. During sptPALM and overnight imaging, cells were incubated in 32°C. Localizations of the fitted single fluorescent spots were obtained by rapidSTORM [9], tracked with the help of customized tracking software written in C++ and visualized by customized software written in C++, to filter and group single molecule localizations or trajectories by their characteristics. The mean squared displacement (*MSD*) was calculated for all trajectories of at least four steps as per previous description [10]. (**Fig. 2** and **Fig. S7**)

Visualization software 3D protein structures taken from the Protein Data Bank (PDB) were visualized by Chimera (**Fig. S1 c**) [11]. All figures were prepared in Abobe Illustrator (Adobe Systems Inc.).

Table S1. Bacterial plasmids used for transient expression of fluorescent proteins.

FP	Backbone	Source
Dendra2	pRSETb	gift from Bourgeois lab, Grenoble, France[12]
Dendra2-T69A	pRSETb	gift from Bourgeois lab, Grenoble, France[12]
Dendra2-M159A	pRSETb	this work, created by David Virant using the pRSETb Dendra2 template
Dendra2-Q116N	pRSETb	this work, created by David Virant using the pRSETb Dendra2 template
Dendra2-Q116Y	pRSETb	this work, created by David Virant using the pRSETb Dendra2 template
Dendra2-S105N-Q116N	pRSETb	this work,created by David Virant using the pRSETb Dendra2 template
Dendra2-T104N-S105N-Q116N	pRSETb	this work,created by David Virant using the pRSETb Dendra2 template
IrisFP	pRSETa	gift from Bourgeois lab, Grenoble, France[5]
mEos2	pRSETa	Addgene #20341
mEos2-A69T	pRSETa	gift from Bourgeois lab, Grenoble, France[12]
mEos3.2	pRSETa	this work, created by Haruko Gölz using codon-optimized mEos3.2 [2]
mEos3.2-A69T	pRSETa	this work, created by Haruko Gölz using the pRSETa mEos3.2 template
mEos4b	pRSETa	Addgene #51073
mEos4b-V69T	pRSETa	this work, created by David Virant using the pRSETa mEos4b template
mKikGR	pRSETa	this work, created by Haruko Gölz using codon-optimized mKikGR [2]
mKikGR-V69T	pRSETa	this work, created by David Virant using the pRSETa mKikGR template
mMaple	pRSETa	this work, created by David Virant using codon-optimized mMaple[2]
mMaple3	pRSETa	this work, created by Alexander Balinovic using codon-optimized mMaple3[2]
mMaple3-V157I	pRSETa	this work, created by David Virant using the pRSETa mMaple3 template
NijiFP	pRSETb	gift from Bourgeois lab, Grenoble, France[13]
pcDronpa	pRSETb	gift from Dedecker lab, Leuven, Belgium[14]
pcDronpa-A69T	pRSETb	gift from Dedecker lab, Leuven, Belgium[14]
pcDronpa2	pRSETb	Addgene #78184
pcDronpa2-A69T	pRSETb	this work, created by Alexander Balinovic using the pRSETb pcDronpa2 template

Table S2. Properties of non-PC-converting green-to-red pcFPs

Name	Genetic background	λ_{exc} (nm)	λ_{em} (nm)	oligomeric state	ε ($M^{-1} * cm^{-1}$)	Φ	*pKa*	$t_{0.5*int}$ (s)	opt. pH_{405}	Refs
Dendra2-T69A	Dendra2 T69A	502[a]/563[a]	518[a]/578[a]	m	42000[a]/35400[a]	0.56[a]/0.64[a]	6.0[a]/7.0[a]	0.4/0.8	6-7.5	**a** [12]
Dendra2-M159A	Dendra2 M159A	471[b]/528[b]	504[b]/562[b]	m	51100[b]/42000[b]	0.55[b]/0.65[b]	6.5[b]/7.3[b]	ND/ND	ND	**b** [13]
NijiFP	Dendra2 F173S	469[b]/526[b]	507[b]/569[b]	m	41100[b]/42000[b]	0.64[b]/0.65[b]	7.0[b]/7.3[b]	ND/ND	6-7.5	**b** [13]
mEos2	EosFP N11K E70K H74N H121Y	508[a]/573[a]	519[a]/584[a]	m	79000[a]/34300[a]	0.66[a]/0.65[a]	5.0[a]/6.6[a]	0.8/0.1	5.5-7	**a** [12]
mEos3.2	mEos2 I102N H158E Y189A	507[c]/572[c]	516[c]/580[c]	m	63400[c]/32200[c]	0.84[c]/0.55[c]	6.5[c]/5.8[c]	1.1/0.1	6-7.5	**c** [6]
mEos4b	mEos3.2 K9R F34Y S39T A69V C195A	505[d]/570[d]	516[d]/580[d]	m	78200[d]/55500[d]	0.84[d]/0.71[d]	ND/ND	1.2/0.1	6-7.5	**d** [15]
IrisFP	EosFP F173S	488[b]/551[b]	516[b]/580[b]	t	57800[b]/27000[b]	0.48[b]/0.50[b]	5.7[b]/6.8[b]	ND/ND	5.5-7.5	**b** [13]
pcDronpa	Dronpa V60A C62H N94S N102I E218G	505[e]/569[e]	517[e]/581[e]	t	115000[e]/75000[e]	0.85[e]/0.68[e]	5.5[e]/6.3[e]	1.1/3.1	6.5-7.5	**e** [14]
pcDronpa2	pcDronpa Y116N	504[e]/569[e]	515[e]/583[e]	t	100000[e]/105000[e]	0.83[e]/0.68[e]	5.8[e]/6.1[e]	0.6/0.2	6.5-7.5	**e** [14]
mKikGR	KikGR A17S Q32R F34Y I37T N39T C116T V126T N161E Q167E F193Y L212A H219Y L222T P223Y L225G +228Y 229E 230F 231E 232A	505[f]/580[f]	515[f]/591[f]	m	49000[f]/28000[f]	0.69[f]/0.63[f]	6.6[f]/5.2[f]	0.6/0.3	5.5-6.5	**f** [16]

Table summarizing the properties of green-to-red pcFPs used in this study which can be photoconverted by 405 nm illumination but not by PC. Listed are their key photophysical properties with λ_{exc} – excitation wavelength; λ_{em} – emission wavelength; ε – molar extinction coefficient at pH 7.5; Φ – fluorescence quantum yield; $t_{0.5*int}$ – time of 50% intensity loss when irradiated by 488 nm or 561 nm light respectively at pH 7.5 in relation to Dendra2 (**Fig. S3e)**. Furthermore, their genetic background, oligomeric state (m – monomeric; t – tetrameric), the pKa values of the chromophores (**Fig. S2**) as well as the optimal pH for 405 nm light-mediated photoconversion are given (**Fig. S3**). Values are either from the literature as labeled or were measured in this study. ND - not determined.

Table S3. List of primers.

lambda red recombination primers (MG1655 rpoC-Dendra2)	
rpoC_Dendra2_FP	CCAGCCTGGCAGAACTGCTGAACGCAGGTCTGGGCGGTTCTGATAACGAGtctggtggcggcggttcta
rpoC_Dendra2_RP	CCCCCCATAAAAAAACCCGCCGAAGCGGGTTTTTACGTTATTTGCGGActagagaataggaacttcctgccactcatc
rpoc_FP_seq	CGTACCACCAGGATCGTATGCG
Dendra2_RP_seq	GGTGAAAGTTGGAACCTCTTACGTGC
CPEC primers	
F_mEos3.2-CPEC	GGATCGATGGGGATCCATGTCTGCCATTAAACCGGATATGAA
R_mEos3.2-CPEC	CCGGATCAAGCTTCGAATTCTTATTAGCGACGCGCATTATCC
F_mKikGR_CPEC	ATAAGGATCGATGGGGATCCATGAGCGTTATCACCAGCGAGATGA
R_mKikGR_CPEC	CCGGATCAAGCTTCGAATTCTTATTAGGCCTCGAATTCGTACTTGG
F_mMaple-CPEC	AGGATCGATGGGGATCCATGGTTAGCAAGGGCGAGGAGACC
R_mMaple-CPEC	CCGGATCAAGCTTCGAATTCTTATTTGTACAGCTCATCCATGCTGTC
F_mMaple3-CPEC	CGATAAGGATCGATGGGGATCCATGGTTAGCAAGGGCGAAGAAACCAT
R_mMaple3-CPEC	GCCGGATCAAGCTTCGAATTCTTATTATTTGTACAGCTCATCCATGCTGTC
F_pRSETa_CPEC	TAAGAATTCGAAGCTTGATCCG
R_pRSETa_CPEC	CATGGATCCCCATCGATCCTTAT
Site-directed mutagenesis primers	
F_Dendra2-M159A	CATCAACGCAGCCCTGCTGCTGGAGGGCGGC
R_Dendra2-M159A	AGGGCTGCGTTGATGTTGCCCACCAGCAGGCC
F_Dendra2-Q116N	CTTCTTCAACAACGTGCGCTTCAAGGGCACCAACTTCCC
R_Dendra2-Q116N	GCACGTTGTTGAAGAAGCAGTCGCCCTCCAGGCTGAT
F_Dendra2-Q116Y	TGCTTCTTCTATAACGTGCGCTTCAAGGGCACCAACTTCCCC
R_Dendra2-Q116Y	CGCACGTTATAGAAGAAGCAGTCGCCCTCCAGGCTGATG
F_Dendra2-R104T	CACCATCACTAACGACATCAGCCTGGAGGGCGACTGCTTCTT
R_Dendra2-R104T	CTGATGTCGTTAGTGATGGTGCAGATGCCCTTGTCCTCGAAGGTC
F_Dendra2-S105N	ACCATCCGCAACGACATCAGCCTGGAGGGCGACTGC
R_Dendra2-S105N	GATGTCGTTGCGGATGGTGCAGATGCCCTTGTCCTCGAAGGT
F_mEos3.2-A69T	GCGTTTTCACTAAATATCCGGATAATATCCAGGATTACTTTAAA
R_mEos3.2-A69T	GATATTTAGTGAAAACGCGGTTACCATAATGAAACGCC
F_mEos4b-V69T	GGGTATTCACGAAATATCCAGACAACATACAAGACTATTTTAAGCA
R_mEos4b-V69T	GATATTTCGTGAATACCCTGTTGCCGTAATGGAATGC
F_mKikGR-V69T	GCGTGTTCACTGAGTACCCGGAGGAGATCGTGGACTACTTC
R_mKikGR-V69T	GGTACTCAGTGAACACGCGGTTACCGTAGTGGAAGGCGG
F_mMaple3-V157I	GGGCGACATTAAGATGAAGCTGCTGCTGAAGGGTGGCAG
R_mMaple3-V157I	CTTCATCTTAATGTCGCCCTTCAGCACACCGTCGCGC
F_pcDronpa2-A69T	GGTATTCACTAAATACCCAGAAAATATAGTAGACTATTTCAAGCA
R_pcDronpa2-A69T	GGGTATTTAGTGAATACCCTGTTGCCGTAATGGAA

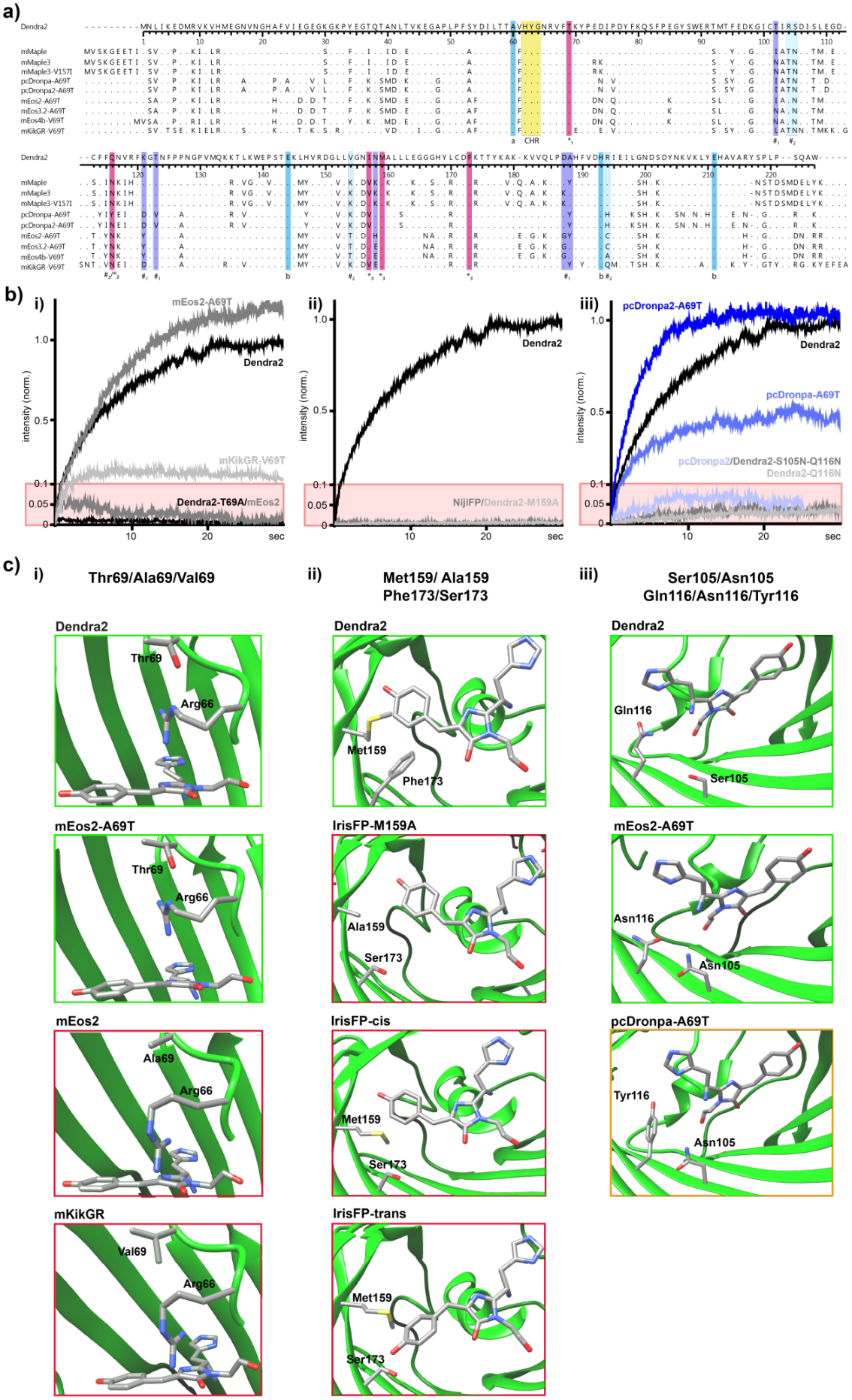
a)
Dendra2
mMaple
mMaple3
mMaple3-V157I
pcDronpa-A69T
pcDronpa2-A69T
mEos2-A69T
mEos3.2-A69T
mEos4b-V69T
mKikGR-V69T
b)
i)
ii)
iii)
mEos2-A69T
Dendra2
mKikGR-V69T
Dendra2-T69A/mEos2
NijiFP/Dendra2-M159A
pcDronpa2-A69T
pcDronpa-A69T
pcDronpa2/Dendra2-S105N-Q116N
Dendra2-Q116N
intensity (norm.)
sec
c)
i) Thr69/Ala69/Val69
ii) Met159/ Ala159
Phe173/Ser173
iii) Ser105/Asn105
Gln116/Asn116/Tyr116
Dendra2
Thr69
Arg66
Met159
Phe173
Gln116
Ser105
mEos2-A69T
IrisFP-M159A
Ala159
Ser173
Asn116
Asn105
mEos2
IrisFP-cis
pcDronpa-A69T
Ala69
Tyr116
mKikGR
IrisFP-trans
Val69

Figure S1. Influence of single amino-acid mutations on pcFP variants

a) Sequences of pcFP variants capable of PC in alignment with Dendra2.
a V60A yields shortened maturation times; **CHR** chromophore sequence HYG. Deviation from His62 is common for several reversibly green switching FPs [14, 17].
***$_1$** mEos2, mEos3.2, mEos4b, pcDronpa, pcDronpa2, mKikGR, Dendra2-T69A can be photoconverted by UV light but not by 488/730 nm illumination.
***$_2$** pcDronpa-A69T, a predecessor of pcDronpa2 (=pcDronpa-Y116N) has a low 488/730 nm photoconversion efficiency. Dendra2-Q116N and Dendra2-Q116Y cannot be photoconverted. Dendra2-S105N-Q116N and Dendra2-R104T-S105N-Q116N regain their photoconversion ability but only at very low efficiency.
***$_3$** Positions 157, 159 and 173 influence the photoswitching behavior of many pcFPs, e.g. NijiFP (=Dendra2-F173S) or Dendra2-M159A can be reversibly photoswitched [5, 13] but not converted by 488/730 nm light.
b amino acids critical for green GFP-like fluorescence [18].
#$_1$ amino acids influencing the oligomerization state [18].
#$_2$ amino acids critical for green-to-red pcFPs [18].

b) Exemplary photoconversion measurements for different pcFPs under PC conditions. All intensities were normalized to the intensity of red Dendra2 fluorescence. The y-axis within the red inset is stretched as indicated by the labels for better visibility.

c) Mutual organization of important amino acid residues in the chromophore environment. Colored boxes indicate the photoconversion characteristics of the different FPs: green, 405 & 488/730 nm converting; orange, moderately 488/730 nm converting but not 405 nm-converting and red, only UV converting.
(i) Residue 69 controls the orientation of the chromophore interacting residue Arg66. Only threonine variants can undergo PC.
(ii) Small residues at positions 159 (Ala159) and 173 (Ser173) increase the chromophore flexibilty and enable reversible conformation changes between *cis* and *trans* states which hinders PC.
(iii) Residues 105 and 116 are crucial for green-to-red photoconversion. Asn105/Tyr116 in pcDronpa-A69T prevents UV conversion, but allows for 488/730 nm conversion.
Structures were taken from the Protein Data Bank (PDB): Dendra2 (2VZX), mEos2 (3S05), mEos2-A69T (5DTL), mKikGR (4P76), IrisFP-M159A (4R6B), IrisFP-cis (2VVH), IrisFP-trans (2VVI), pcDronpa-A69T (4IZN).

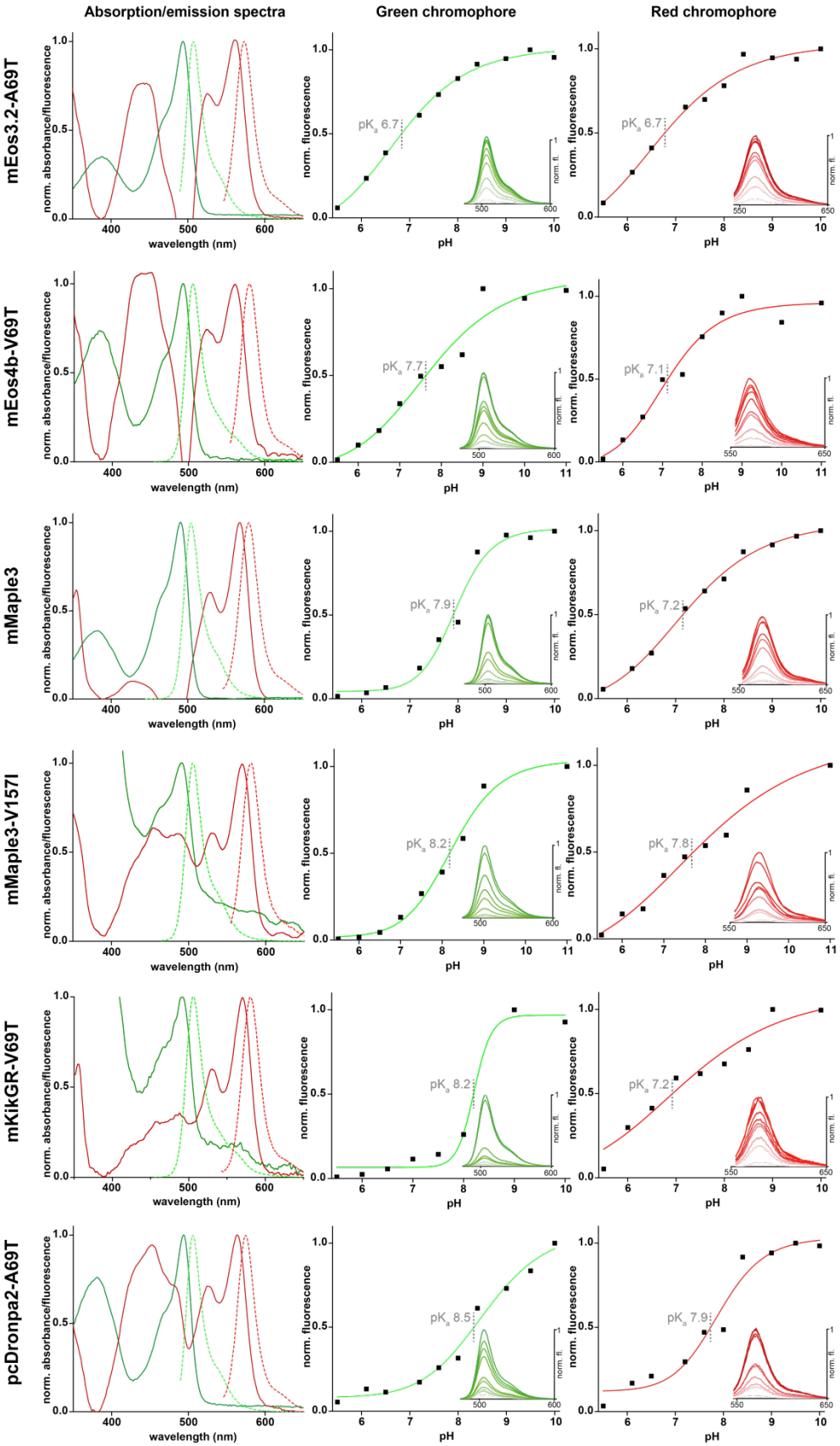

Figure S2. Absorption, fluorescence spectra and pKa measurements of pcFPs in their green and red form. Left: Absorption spectra (solid lines) and fluorescence spectra (dashed lines) of green and red chromophore forms. Middle and right: pH-dependency and fitted pK_a values of the FPs measured for the green and red chromophore form, respectively.

a) Analysis procedure

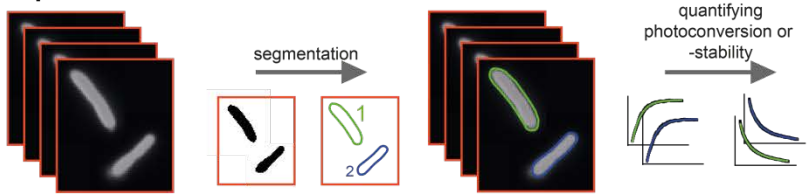

segment	rate (s^{-1})	intensity
1	0.25	35039
2	0.21	35043

b) Efficiency of PC for Dendra2 in relation to 488 and 730 nm light intensity

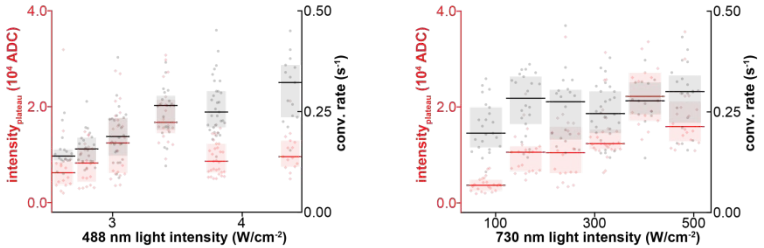

c) pH dependence of photoconversion mechanisms

i) Dendra family

ii) mEos family

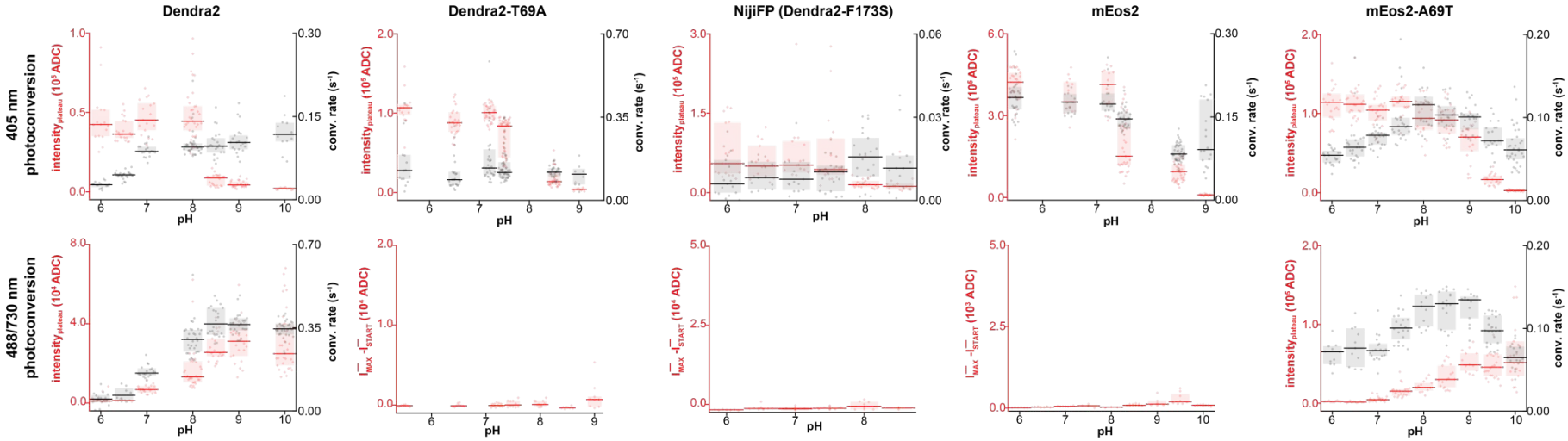

c) pH dependence of photoconversion mechanisms- continuation

ii) mEos family- continuation

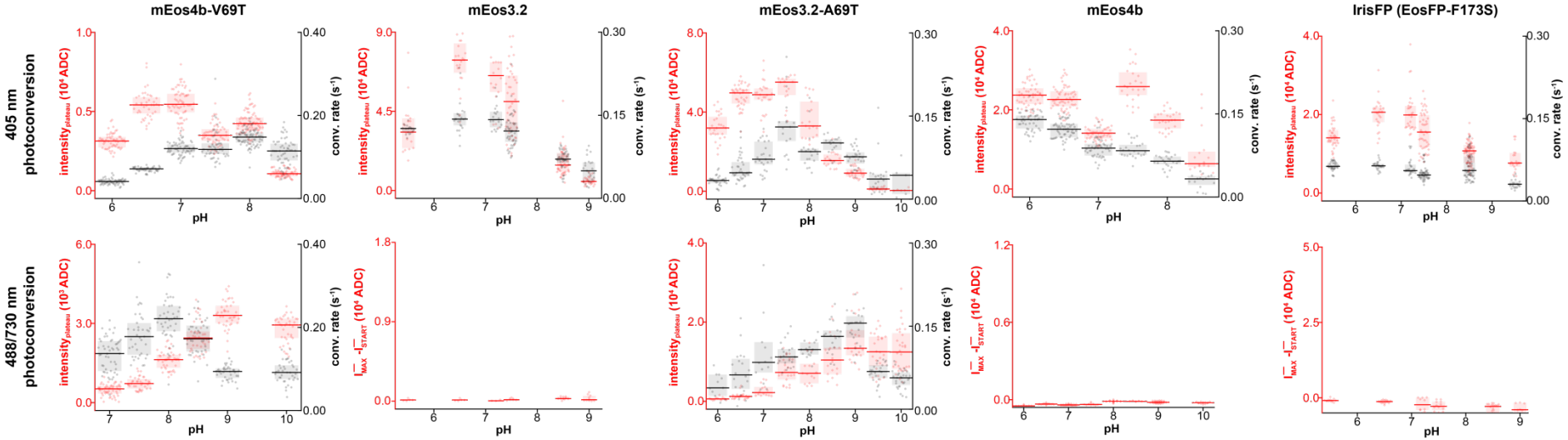

iii) mMaple family

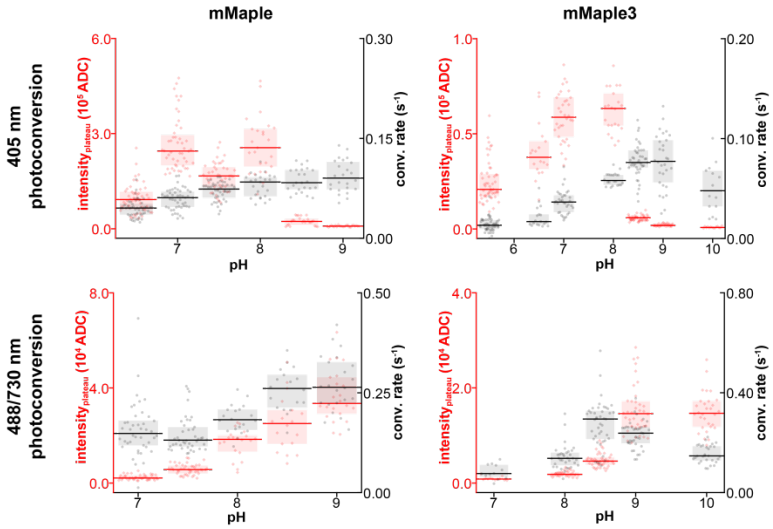

iv) mKikGR family

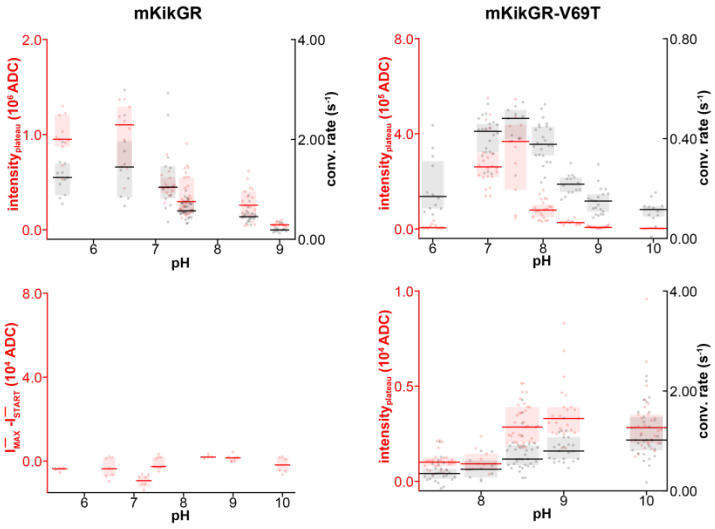

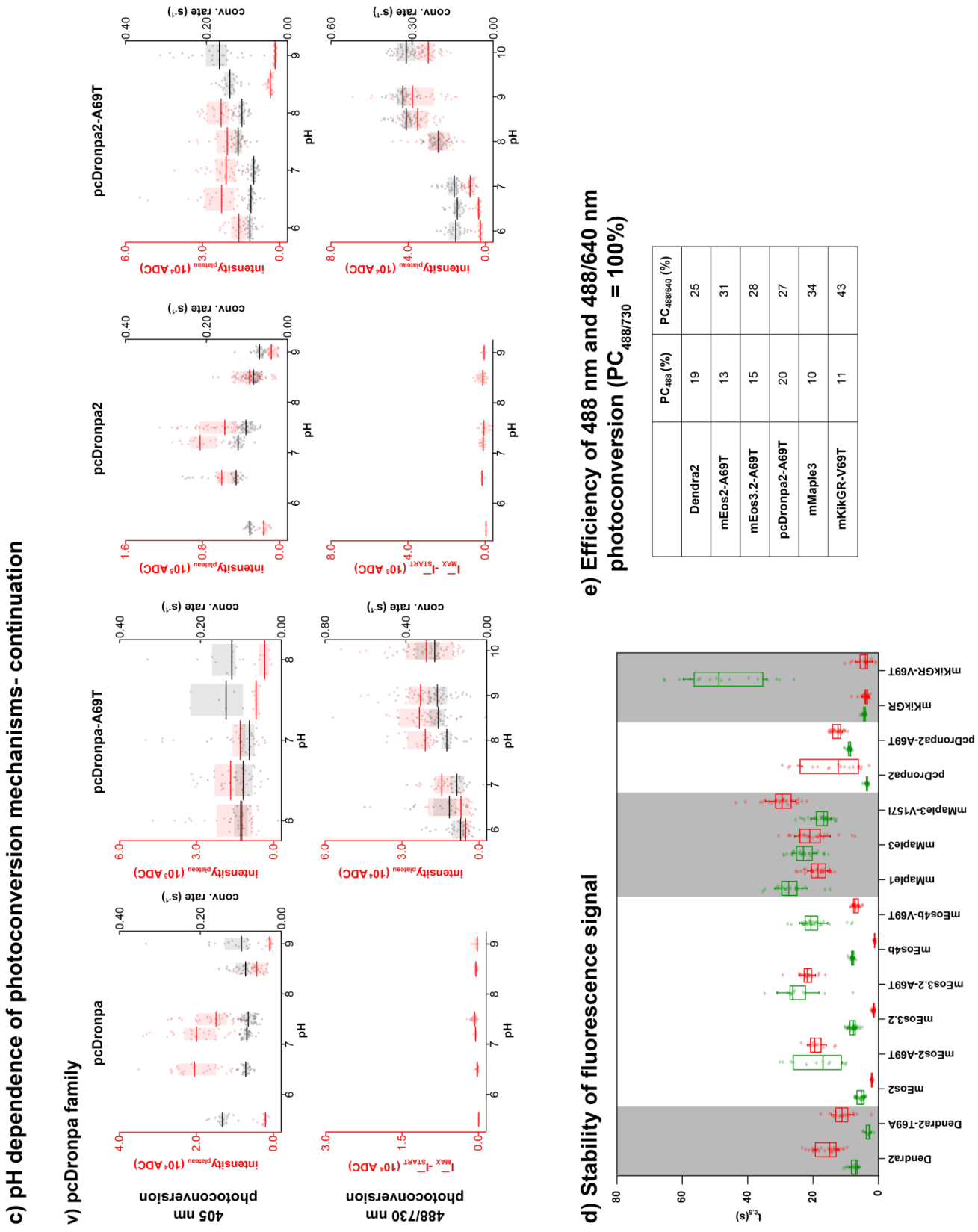

	PC_{488} (%)	$PC_{488/640}$ (%)
Dendra2	19	25
mEos2-A69T	13	31
mEos3.2-A69T	15	28
pcDronpa2-A69T	20	27
mMaple3	10	34
mKikGR-V69T	11	43

Figure S3. Photoconversion rates, red fluorescence yield and photostability of the green and red form for pcFPs are dependent on applied laser wavelengths, laser intensities and pH.

a) Analysis workflow for quantifying photoconversion and photostability of the pcFP variants as described in detail in the Materials and Methods section.

b) Impact of 488 nm and 730 nm light intensity on PC rate (grey) and red fluorescence intensity (red) measured for Dendra2. Increasing the 488 nm light intensity increases measured intensities (red bars and dots) as well as the conversion rate (gray bars and dots). For highest 488 nm laser intensities, the attained fluorescence intensity decreases, probably due to photobleaching of the green Dendra2 form. Increasing the 730 nm laser intensity increases the measured fluorescence intensities. The applied 730 nm light intensities do not alter the conversion rate significantly.

c) Green-to-red photoconversion efficiency and rates measured for pH values ranging from 6 to 10 by imaging overexpressed pcFPs in fixed *E.coli* cells and analyzed as depicted in a) and described in the Materials and Methods. 405 nm-mediated photoconversion and PC efficiencies were measured by the obtained red fluorescence intensities (red bars and dots) and photoconversion rates (gray bars and dots). Measurements were made for proteins from five different families: i) Dendra family; ii) mEos family; iii) mMaple family; iv) mKikGR family; v) pcDronpa family.

d) Stability of the fluorescence signal of the green and red chromophore forms for different proteins capable of 488/730 nm photoconversion and their non-PC-converting relatives. At time $t_{0.5}$, the fluorescence intensity had decreased to 50% of the initial intensity. All threonine 69 variants show a slower decrease of the intensity in both the green and red channel.

e) Comparison of the photoconversion efficiency for different PC-converting pcFPs under illumination of only 488 nm light (4 $W*cm^{-2}$) and additional 640 nm light (400 $W*cm^{-2}$). Intensities in table are represented as a percentage of the intensity obtained by 488/730 nm illumination (4 $W*cm^{-2}$ and 400 $W*cm^{-2}$ for 488 and 730 nm, respectively) for each protein.

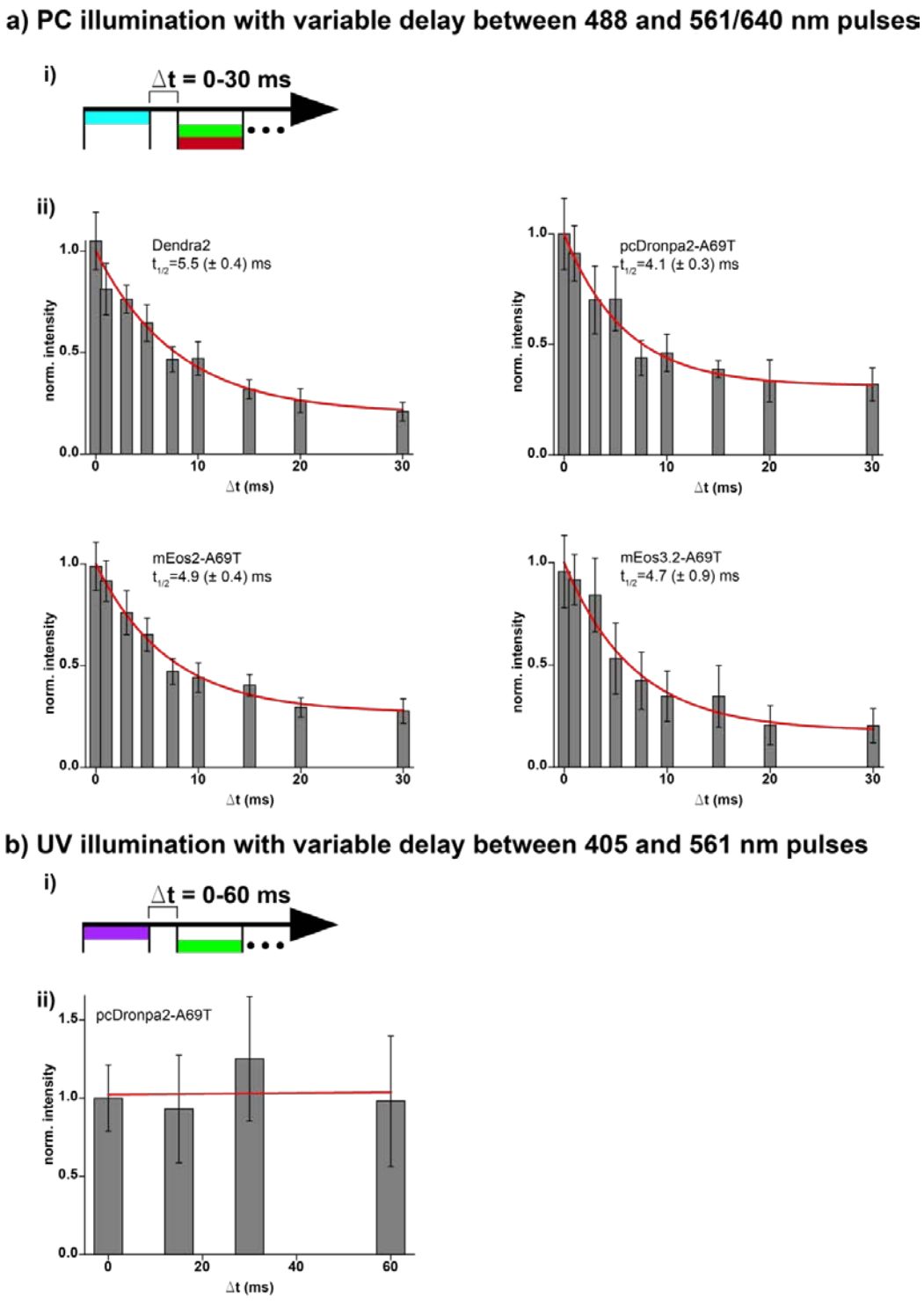

Figure S4. Dependency of the PC efficiency on a delay of 0-30 ms between priming and conversion laser illumination.

a) i) Scheme representing the applied illumination sequence with Δt being the delay between 488 laser pulses and 640 nm conversion/ 561 nm read-out. ii) The PC efficiency decreases exponentially for increasing delays between 488 and 640 nm light illuminations. Intensities, normalized to the intensity of Δt = 0 ms were fitted with a single exponential decay. Retrieved $t_{1/2}$ values represent the half-life of the presumed intermediate state, which is thought to be the entry state for PC by absorbing red/far red light.

b) i) Scheme representing illumination sequence for control experiments for 405 and 561 nm laser pulses. ii) Increasing the delay between 405 and 561 nm light does not affect the UV-photoconversion efficiency.

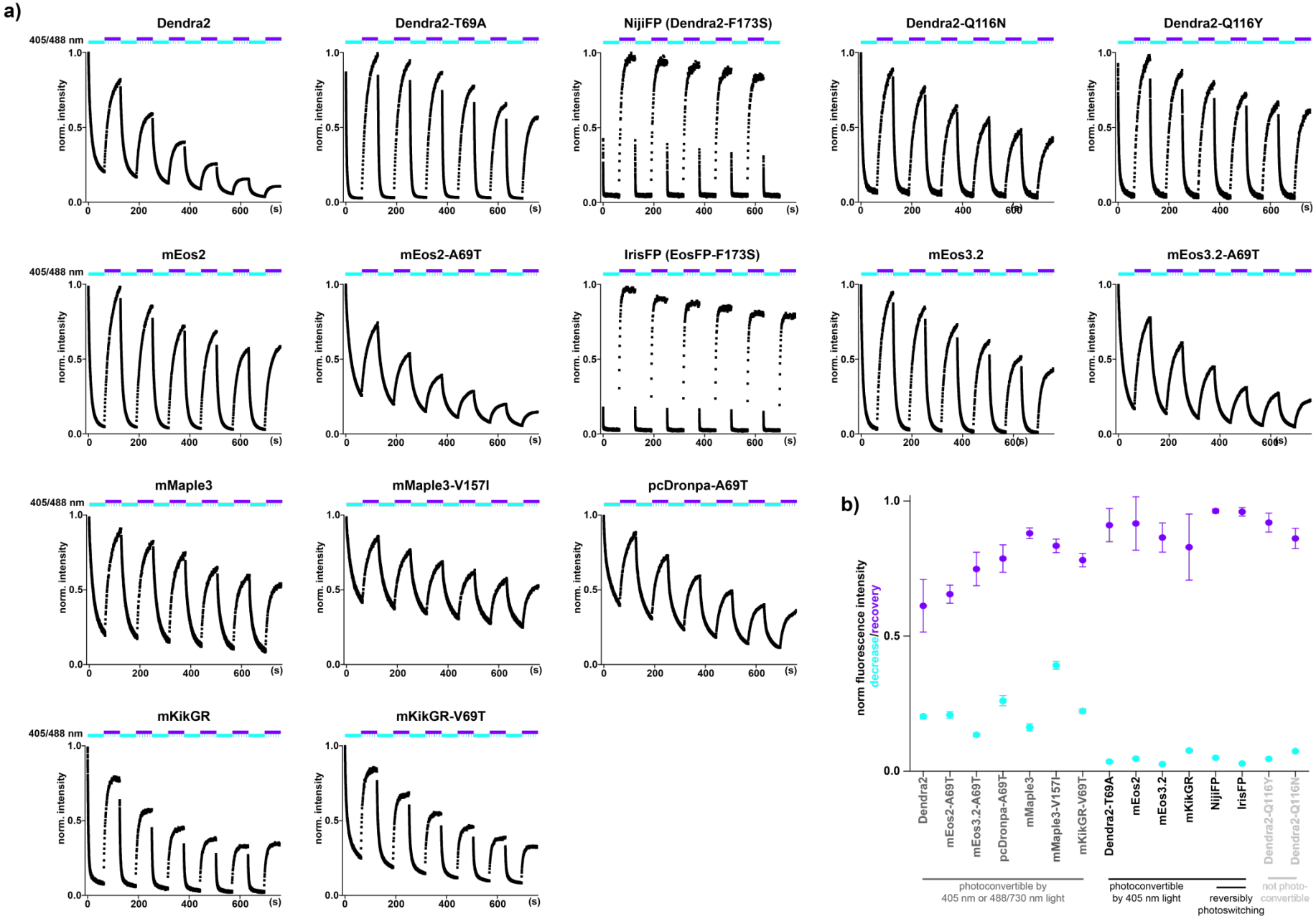
a)
Dendra2
Dendra2-T69A
NijiFP (Dendra2-F173S)
Dendra2-Q116N
Dendra2-Q116Y
mEos2
mEos2-A69T
IrisFP (EosFP-F173S)
mEos3.2
mEos3.2-A69T
mMaple3
mMaple3-V157I
pcDronpa-A69T
mKikGR
mKikGR-V69T
405/488 nm
norm. intensity
(s)
b)
norm fluorescence intensity
decrease/recovery
Dendra2
mEos2-A69T
mEos3.2-A69T
pcDronpa-A69T
mMaple3
mMaple3-V157I
mKikGR-V69T
Dendra2-T69A
mEos2
mEos3.2
mKikGR
NijiFP
IrisFP
Dendra2-Q116Y
Dendra2-Q116N
photoconvertible by 405 nm or 488/730 nm light
photoconvertible by 405 nm light
reversibly photoswitching
not photo-convertible

Figure S5. Reversible photoswitching of the green form of pcFPs by 488 nm and 405 nm illumination

a) Time traces of the green fluorescence intensity decrease under continuous 488 nm illumination for 60 s which is followed by continuous 405 nm illumination with probing 488 nm light pulses every 20th frame for another 60 s. This cycle was repeated six times on the same ROI. For all investigated proteins, recovery from non-fluorescent dark states was observed under 405 nm illumination. All pcFPs were overexpressed and measured in fixed E.coli cells as described in the Materials and Methods.

b) Evaluation of the green fluorescence intensity decrease levels (blue) and recovery levels (violet) of the pcFP-time traces in a): The fluorescence decrease level represents the fraction of FP molecules which remained fluorescent after one minute illumination by 488 nm light. The fluorescence recovery level shows the fraction of protein molecules which recovered their green fluorescent state after 60 s illumination with 405 nm light. All pcFPs capable of PC show a slower decrease in fluorescence under 488 nm illumination and thus a higher remaining fraction of molecules in their green fluorescent state after 60 s in comparison to the non-PC-converting FPs. Additionally, the fraction of molecules which recovers their green fluorescent state is lower in case of 488/730 nm photoconvertible proteins in comparison to proteins not capable of 488/730 nm photoconversion. NijiFP and IrisFP, which were designed for efficient reversible photoswitching show the highest contrast.

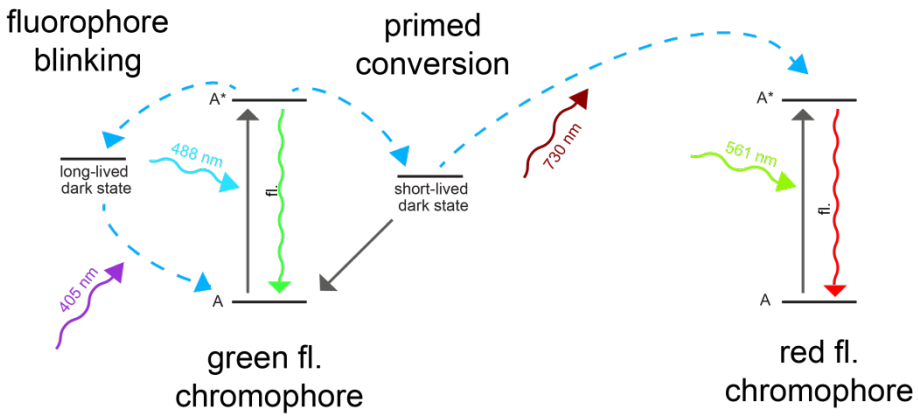

Figure S6. Model of photoconversion

Green-to-red pcFPs can populate different reversible dark states which might yield an explanation for the different PC efficiencies of different pcFPs. In this model, pcFPs which show strong blinking behavior and thus have a high tendency of populating long-lasting dark states, show only poor or non-detectable 488/730 nm photoconversion efficiency. Here, these dark states are thought to be directly competing with a short-lived intermediate state, which is suspected to be the entry point for PC by absorbing near-infra red light. Due to its estimated half-life, it is most likely a triplet or radical state. Both states are believed to be directly linked to the arginine 66 conformation and chromophore flexibility [12].

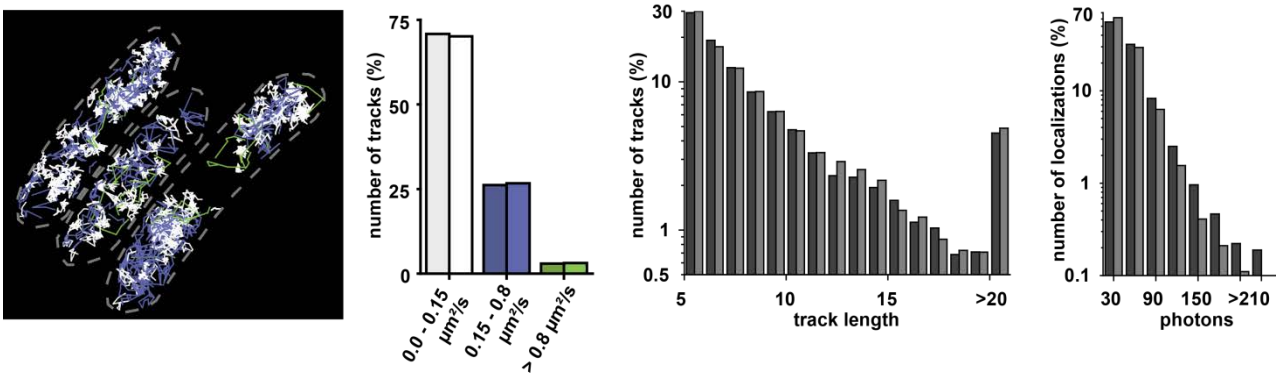

Figure S7. RNA polymerase dynamics in living *E.coli* cells by UV and PC photoconversion.
Examplary cells imaged by sptPALM using PC photoconversion (left) and diffusion coefficient distribution of RNA polymerase measured by 405 nm (left bars) and 488/730 nm (right bars) photoconversion. Trajectories are color coded by their apparent diffusion coefficient D: 0.0-0.15 $\mu m^2 * s^{-1}$ (white, ~ 70%), 0.15-0.8 $\mu m^2 * s^{-1}$ (blue, ~ 27%), faster than 0.8 $\mu m^2 * s^{-1}$ (green, ~3 %). PC was slightly more efficient and yielded more trajectories (with an average of 8 trajectories compared to 5 trajectories per μm^2 and minute) at lower conversion laser intensities (400 mW/cm^2 488 nm in comparison to 690 mW/cm^2 405 nm).

Statistics of single-particle track lengths (longer than 4 steps, middle right) obtained through 6 minute 405 nm or 488/730 nm-sptPALM imaging and statistics of single-molecule photon counts (right) of localizations in these trajectories are visualized by dark grey (UV-photoconversion: 5075 trajectories, 39913 localizations) and light grey (PC photoconversion: 7174 trajectories, 54127 localizations) histogram bars, bin size 1 (tracks) and 30 (photons). The average single-particle-trajectory lengths and spot intensities for both modes are comparable.

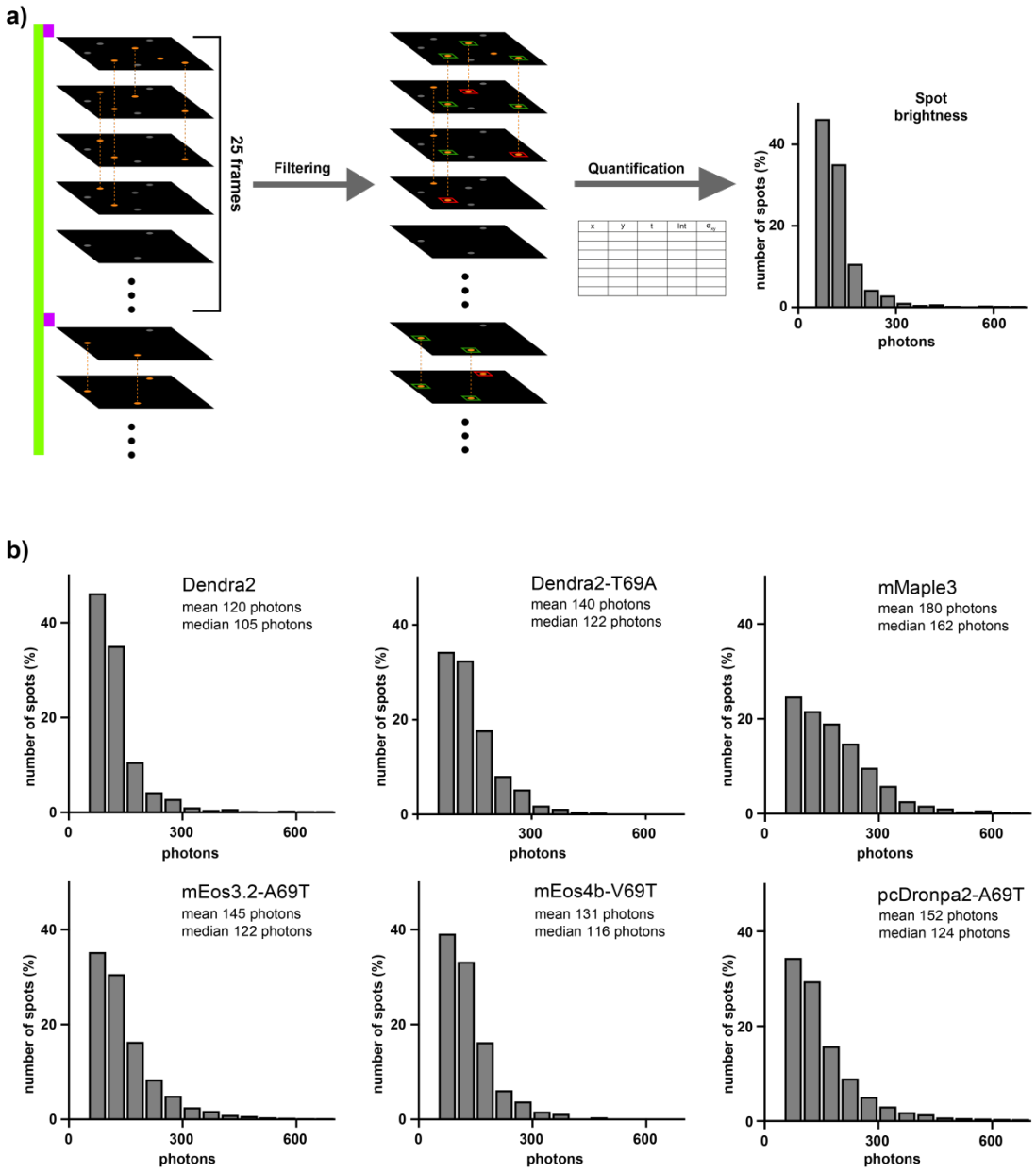

Figure S8. Photon counts of single pcFP molecules recorded on single-molecule surfaces.

a) Workflow of the single-molecule surfaces data analysis as described in the Materials and Methods section.

b) Photon counts of single fluorescent protein molecules recorded on single-molecule surfaces with 488/730 nm illumination at an imaging rate of 30 ms.

References

[1] J. Quan, J. Tian, *Nat Protoc* **2011**, *6*, 242-251.

[2] S. Wang, J. R. Moffitt, G. T. Dempsey, X. S. Xie, X. Zhuang, *PNAS* **2014**, *111*, 8452-8457.

[3] K. A. Datsenko, B. L. Wanner, *Proc Natl Acad Sci U S A* **2000**, *97*, 6640-6645.

[4] A. Edelstein, N. Amodaj, K. Hoover, R. Vale, N. Stuurman, *Curr Protoc Mol Biol* **2010**, *Chapter 14*, Unit14 20.

[5] V. Adam, M. Lelimousin, S. Boehme, G. Desfonds, K. Nienhaus, M. J. Field, J. Wiedenmann, S. McSweeney, G. U. Nienhaus, D. Bourgeois, *PNAS* **2008**, *105*, 18343-18348.

[6] M. Zhang, H. Chang, Y. Zhang, J. Yu, L. Wu, W. Ji, J. Chen, B. Liu, J. Lu, Y. Liu, J. Zhang, P. Xu, T. Xu, *Nat Methods* **2012**, *9*, 727-729.

[7] J. Schindelin, I. Arganda-Carreras, E. Frise, V. Kaynig, M. Longair, T. Pietzsch, S. Preibisch, C. Rueden, S. Saalfeld, B. Schmid, J. Y. Tinevez, D. J. White, V. Hartenstein, K. Eliceiri, P. Tomancak, A. Cardona, *Nat Methods* **2012**, *9*, 676-682.

[8] M. Tokunaga, N. Imamoto, K. Sakata-Sogawa, *Nat Methods* **2008**, *5*, 159-161.

[9] S. Wolter, A. Loschberger, T. Holm, S. Aufmkolk, M. C. Dabauvalle, S. van de Linde, M. Sauer, *Nat Methods* **2012**, *9*, 1040-1041.

[10] S. Wieser, G. J. Schutz, *Methods* **2008**, *46*, 131-140.

[11] E. F. Pettersen, T. D. Goddard, C. C. Huang, G. S. Couch, D. M. Greenblatt, E. C. Meng, T. E. Ferrin, *J Comput Chem* **2004**, *25*, 1605-1612.

[12] R. Berardozzi, V. Adam, A. Martins, D. Bourgeois, *J Am Chem Soc* **2016**, *138*, 558-565.

[13] V. Adam, B. Moeyaert, C. C. David, H. Mizuno, M. Lelimousin, P. Dedecker, R. Ando, A. Miyawaki, J. Michiels, Y. Engelborghs, J. Hofkens, *Chem Biol* **2011**, *18*, 1241-1251.

[14] B. Moeyaert, N. Nguyen Bich, E. De Zitter, S. Rocha, K. Clays, H. Mizuno, L. van Meervelt, J. Hofkens, P. Dedecker, *ACS Nano* **2014**, *8*, 1664-1673.

[15] M. G. Paez-Segala, M. G. Sun, G. Shtengel, S. Viswanathan, M. A. Baird, J. J. Macklin, R. Patel, J. R. Allen, E. S. Howe, G. Piszczek, H. F. Hess, M. W. Davidson, Y. Wang, L. L. Looger, *Nat Methods* **2015**, *12*, 215-218.

[16] S. Habuchi, H. Tsutsui, A. B. Kochaniak, A. Miyawaki, A. M. van Oijen, *Plos One* **2008**, *3*.

[17] aA. C. Stiel, S. Trowitzsch, G. Weber, M. Andresen, C. Eggeling, S. W. Hell, S. Jakobs, M. C. Wahl, *Biochem J* **2007**, *402*, 35-42; bX. Zhang, M. Zhang, D. Li, W. He, J. Peng, E. Betzig, P. Xu, *PNAS* **2016**, *113*, 10364-10369; cH. Chang, M. Zhang, W. Ji, J. Chen, Y. Zhang, B. Liu, J. Lu, J. Zhang, P. Xu, T. Xu, *PNAS* **2012**, *109*, 4455-4460; dR. Ando, C. Flors, H. Mizuno, J. Hofkens, A. Miyawaki, *Biophys J* **2007**, *92*, L97-99.

[18] aS. F. Field, M. V. Matz, *Mol Biol Evol* **2010**, *27*, 225-233; bH. Kim, T. J. Grunkemeyer, C. Modi, L. Chen, R. Fromme, M. V. Matz, R. M. Wachter, *Biochemistry* **2013**, *52*, 8048-8059.

5.2 Appendix B

Supplementary Information: Combining Primed Photoconversion and UV-Photoactivation for Aberration-Free, Live-Cell Compliant Multi-Color Single-Molecule Localization Microscopy Imaging

David Virant, Bartosz Turkowyd, Alexander Balinovic, Ulrike Endesfelder

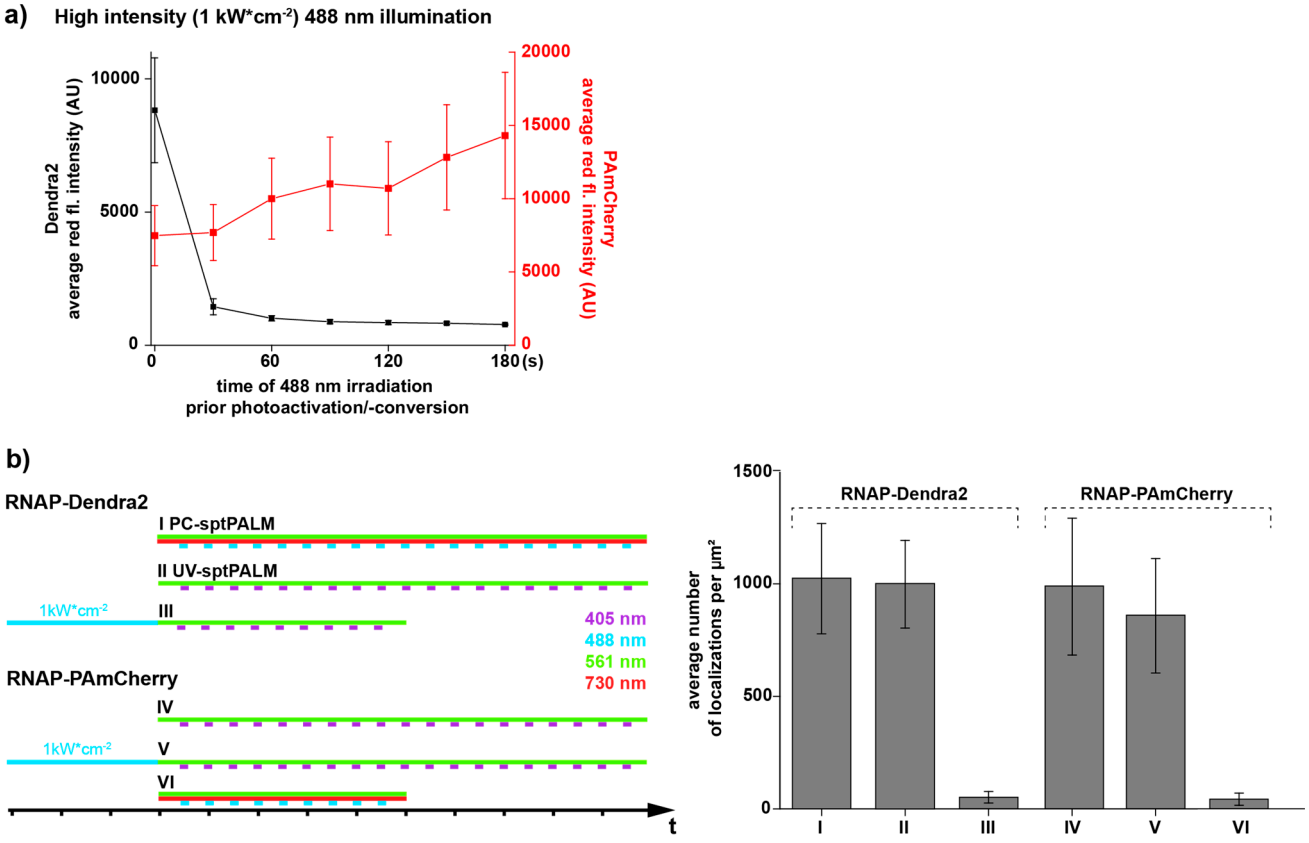

Figure S1: (a) Influence of high intensity (1 kW/cm²) 488 nm light illumination measured by the average red fluorescence intensity of PAmCherry and Dendra2 as a function of time of exposure by 488 nm light prior photoactivation/-conversion (for details, see materials and methods). Black graph: Dendra2 average fluorescence intensity; red graph: PAmCherry average fluorescence intensity. **(b) Left:** schemes representing illumination sequences for MG1655 RNAP-Dendra2 and MG1655 RNAP-PAmCherry samples serving as quantitative controls. Violet line: 405 nm light, blue line: 488 nm light, green line: 561 nm light, red line: 730 nm light. More details and laser intensities can be found in the materials and methods section. **Right:** average number of RNAP localizations per µm² identified during the imaging. **(I)** MG1655 RNAP-Dendra2 cells imaged with primed conversion-PALM. *n* = 13 cells; **(II)** MG1655 RNAP-Dendra2 cells imaged with UV-PALM. *n* = 21 cells; **(III)** MG1655 RNAP-Dendra2 cells illuminated with 488 nm light before imaging and imaged with UV-PALM. *n* = 21 cells; **(IV)** MG1655 RNAP-PAmCherry cells imaged with UV-PALM. *n* = 16 cells; **(V)** MG1655 RNAP-PAmCherry cells illuminated with 488 nm light before imaging and imaged with UV-PALM. *n* = 13 cells; **(VI)** MG1655 RNAP-PAmCherry cells imaged with primed conversion-PALM. *n* = 21 cells.

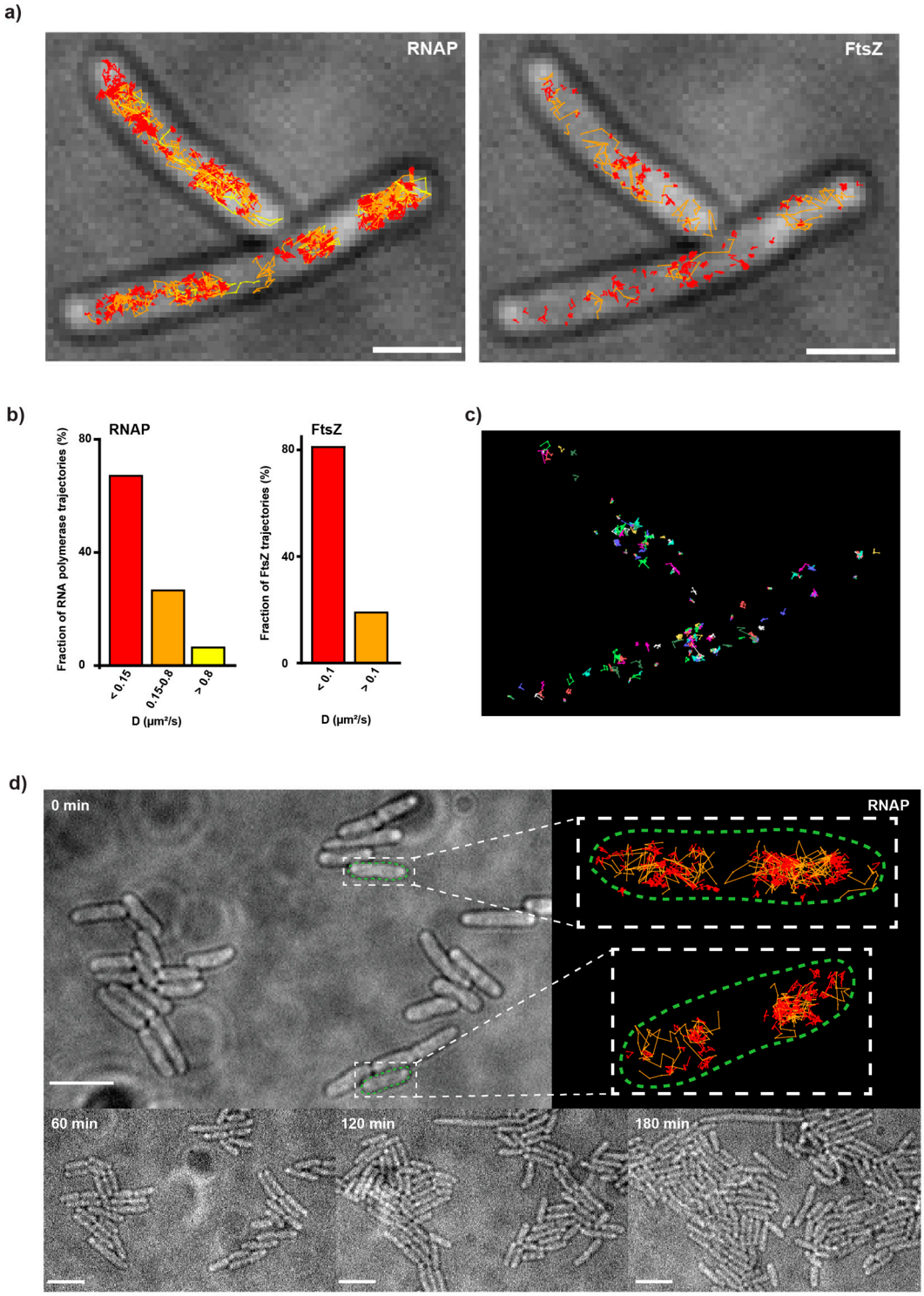

Figure S2: Live-cell single-particle tracking PALM (sptPALM) in *E. coli* cells. (a) Trajectories of RNAP molecules (left) and FtsZ (right). The individual trajectories are color coded by their apparent diffusion coefficient D and classified into categories. RNAP: 0.0–0.15 μm²/s (red), 0.15–0.8 μm²/s (orange), faster than 0.8 μm²/s (yellow) and FtsZ: 0.0–0.1 μm²/s (red), faster than 0.1 μm²/s (orange). This classification is based on recent literature on the protein dynamics [1,2] and chosen to be the same as in the histograms in **(b)**. Scale bar: 2 μm. **(b)** RNAP and FtsZ diffusion coefficient distribution histograms. RNAP molecules were classified by their diffusion coefficient as follows: slower than 0.15 μm²/s (67% of the whole population), faster than 0.15 and slower than 0.80 μm²/s (27%), and faster than 0.80 μm²/s (6%). $n = 471$ trajectories. This is in accordance with literature values [2,3]. FtsZ molecules were sorted into two classes: slower than 0.1 μm²/s (81% of the population- structural FtsZ) and faster than 0.1 μm²/s (19%). These values are also in

accordance with literature values [1]. n = 174 trajectories. **(c)** FtsZ trajectories of the structural FtsZ molecules (D < 0.1 μm²/s) shown by distinct colors to visualize individual trajectories. **(d)** Cell growth after dual-color sptPALM imaging. Cells are not affected by the in total 9-minute-read-out (2 min for RNAP-mEos3.2-A69T, 2 minutes of 488 nm bleaching of unconverted mEos3.2-A69T and 5 min for FtsZ-PAmCherry (due to the slower frame rate of 30 ms to obtain the same number of images as for RNAP-mEos3.2-A69T imaged by 13 ms frames) imaging procedure. Big bright light image: cells at the beginning of the experiment. On the right, two examples of RNAP trajectories in single cells are shown; red trajectories are for slowly diffusing RNAPs with D < 0.15 μm²/s and orange trajectories for RNAP with 0.15 μm²/s < D < 0.8 μm²/s. Bottom bright light images: cells after one, two and 3 h of growth. Scale bars: 5 μm.

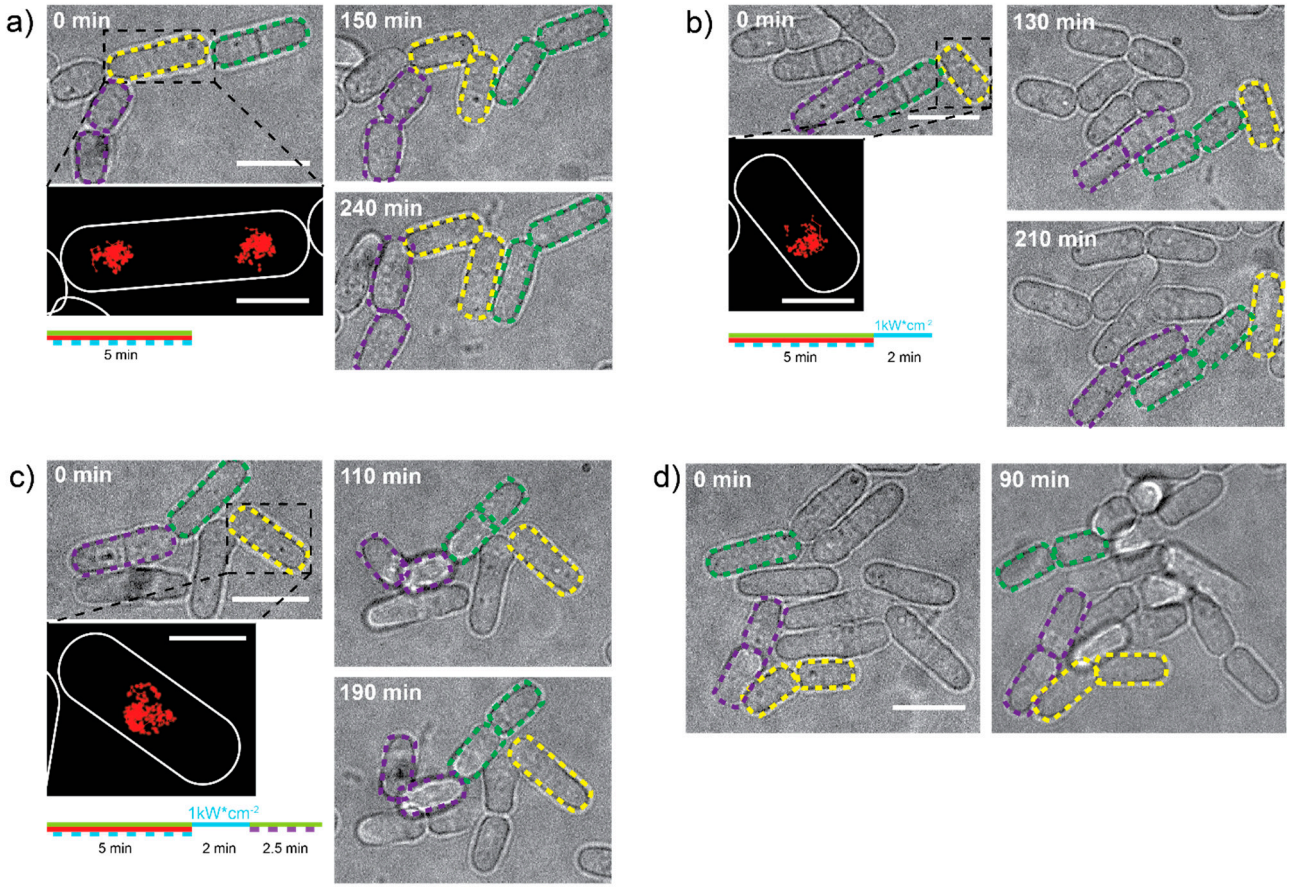

Figure S3: Comparison of *S. pombe* growth after different illumination schemes. Example cells are marked with dashed lines. Following the color-coded dashed lines, it is visible that the cells continue dividing and growing after imaging. Details experiment parameters are described in materials and methods. **(a)** Cell growth after 5 min of PC-PALM. **(b)** Cell growth after 5 min of PC-PALM and 2 min of 488 nm light post-bleaching. **(c)** Cell growth after 5 min of PC-PALM, 2 min of 488 nm light post-bleaching and 2.5 min of UV-PALM. The dose of UV light is not high enough to prevent cells from dividing/growing. **(d)** Control cells which were not illuminated by any laser light. Scale bars bright-field images 10 μm. Insets display examples of single-particle-trajectory data with a length >4 frames, obtained for cbp1-Dendra2, scale bars insets 4 μm. Colored lines beneath spt-PALM images represent the illumination scheme used in the experiment as described in **Figure S1**.

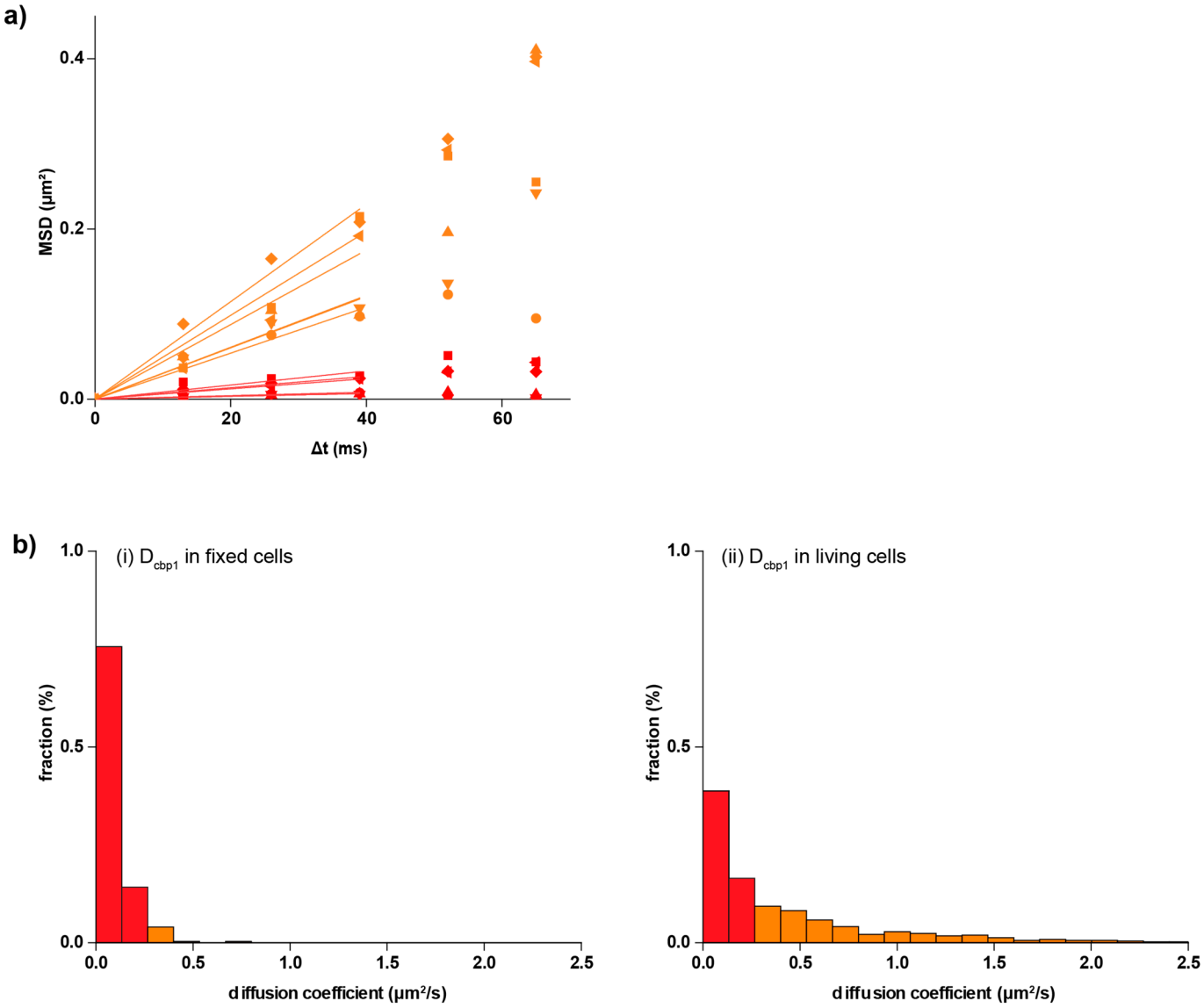

Figure S4: (a) Example fits of calculated MSD values, color coded red for MSDs corresponding to diffusion coefficients below 0.26 µm²/s and orange for MSDs corresponding to diffusion coefficients above 0.26 µm²/s. **(b)** Histograms of cbp1 diffusion coefficients in fixed **(i)** and living **(ii)** cells. Histogram bins are color coded as trajectories in **Figure 3b**, red for diffusion coefficients lower than 0.26 µm²/s and orange for diffusion coefficients above 0.26 µm²/s. **(i)** In fixed cells, the majority of analyzed trajectories displayed diffusion coefficients lower than 0.26 (~95%). All the present cbp1 molecules are expected to be immobilized by aldehyde fixation which results in a small, non-zero diffusion coefficient in agreement with the measurement error made within the localization precision. Some free-floating background may remain, resulting in a few detected mobile molecules with diffusion coefficients above 0.26 µm²/s. **(ii)** In live cells, a significant fraction (~55%) of immobile, DNA-bound cbp1 is clearly visible, while the rest of the protein moves with varying velocity. Only trajectories with a length of >4 frames and MSD-curves fitted with an R-squared value >0.85 were used in the analysis. The bin size of 0.13 was calculated using the Freedman-Diaconis rule. Number of diffusion coefficients plotted is 275 for fixed cells and 462 for live cells.

Table S1. Strains, plasmids and construction primers used in this study

Strain	Description	Reference
Escherichia coli strains		
MG1655 rpoC_mEos3.2-A69T	MG1655 RNAP-β′-mEos3.2-A69T, Cm^R	This study
MG1655 rpoC_mEos3.2-A69T+ pJB063	MG1655 RNAP-β′-mEos3.2-A69T + pJB063-FtsZ-PAmCherry, Cm^R, $Spect^R$	This study
MG1655 rpoC_Dendra2	MG1655 RNAP- β′-Dendra2, Cm^R	[2]
MG1655 rpoC_PAmCherry	MG1655 RNAP- β′-PAmCherry, Amp^R	[4]
MG1655 pBAD/HisB_pamcherry1	MG1655 pBAD/HisB_PAmCherry1, Amp^R	This study
Schizosaccharomyces pombe strains		
cbp1_Dendra2	C-terminal genomic integration, G418 resistance	This study
cnp1_PAmCherry	N-terminal genomic integration	[5]
cnp1_PAmCherry + cbp1_Dendra2	Combination of above strains	This study
Mammalian strains		
HeLa H2B-pDendra2(N)+ β-Actin-PAmCherry1	Transient expression from plasmid	This study
HeLa Dendra2-Keratin-17+ β-Actin-PAmCherry1	Transient expression from plasmid	This study

Plasmids for transient expression			
Plasmid	**Expression organism**	**Description**	**Reference**
H2B-pDendra2(N)	mammalian	H2B-pDendra2(N), Kan^R	Addgene 75283
Dendra2-Tubulin-6	mammalian	Dendra2-Tubulin-6, Kan^R	Addgene 57742
β-Actin-PAmCherry1	mammalian	β-Actin-PAmCherry1, Kan^R, Neo^R	[6]
Dendra2-Keratin-17	mammalian	KRT18-Dendra2, Kan^R	Addgene 57726
pJB063	bacteria	pBAD-FtsZ-pamcherry1, $Spect^R$	Gift from the Xiao Lab, USA
pBAD/HisB_PAmCherry	bacteria	pBAD/HisB_PAmCherry1, Amp^R	Addgene 31931

Construction primers	
Name	**Sequence**
rpoC_mEos3.2-A69T_F	CCAGCCTGGCAGAACTGCTGAACGCAGGTCTGGGCGGTTCTGATAACGAGgccattaaaccggatatgaaaatcaaactgcg
rpoC_mEos3.2-A69T_R	CCCCCCATAAAAAAACCCGCCGAAGCGGGTTTTTACGTTATTTGCGGActagagaataggaacttcctgccactcatc
F_KanR	GGCGCGCCAGATCTACTT
R_KanR	GACAGCAGTATAGCGACCAGC
F_Dendra2	GCCGGAGGCAGTGGTATGAACACCCCGGGAATTAA
R_Dendra2	AGAAGTAGATCTGGCGCGCCTTACCACACCTGGCTGGG
F1_cbp1	CAGCCTTGTAGTGAGGGTGTG
R1_cbp1	ACCACTGCCTCCGGCGGTGCTTCTCAAACGAGAAAGATTC

F2_cbp1	AATGCTGGTCGCTATACTGCTGTCTGTCTGTATTCGTTGTGCATATTTGAC
R2_cbp1	ACGAAGCAGTTAGCAAAAGAGAAGTACA

All primers were designed in Benchling (Benchling Inc.) and synthesized by Eurofins Genomics (Germany).

Supplementary Material & Methods

Strain constructions

***Escherichia coli* MG1655 rpoC-mEos3.2-A69T transformed with pJB063.** MG1655 expressing rpoC_mEos3.2-A69T was generated by homologous recombination using a modified lambda red recombination pKD46 protocol [7]. Briefly, the PCR-amplified (primers listed in **Table S1**) mEos3.2-A69T-sequence followed by the frt flanked chloramphenicol resistance gene from the codon-optimized mEos3.2-A69T pBAD18 plasmid [8] with auxiliary homologous overhang sequences was electroporated (5 ms, 1.8 kV) into MG1655 cells. After verifying the strain by sequencing (Eurofins, Ebersberg, Germany), the pJB063 plasmid (**Table S1**) containing an FtsZ sequence followed by the PAmCherry fluorescent protein and spectinomycin resistance gene sequences was introduced to MG1655 rpoC-mEos3.2-A69T via electroporation (5 ms, 1.8 kV). Transformed cells were selected under chloramphenicol and spectinomycin.

***Schizosaccharomyces pombe* cbp1-Dendra2**. The cloning strategy for tagging the C-terminus of the cbp1 was adapted from [9]. The *Saccharomyces cerevisiae* ADH1 terminator and kanamycin resistance gene were amplified from the PAW8 plasmid [10] using primers F_KanR and R_KanR. The Dendra2 fragment with the AGGSG linker was amplified from the pRSET-Dendra2 plasmid [11] using primers F_Dendra2 and R_Dendra2. The upstream (~600 bp) and downstream (~500 bp) *S. pombe* homologies were amplified from genomic DNA with the primer pairs F1_cbp1/ R1_cbp1 and F2_cbp1/ R2_cbp1 (all primers listed in **Table S1**). DNA fragments were assembled with overlap-extension PCR [12], using melting temperatures of the overlapping regions as the annealing temperature in the PCR. All PCRs were performed with Q5 High-Fidelity DNA polymerase (New England Biolabs, Frankfurt, Germany). 10 µL of the PCR product were transformed into wild type *S. pombe* using the Frozen-EZ Yeast Transformation II Kit (Zymo Research, Irvine, CA, USA), plated onto YES agar plates and incubated overnight at 30 °C, then replica plated onto 200 µg/mL G418 (Thermo Fisher Scientific, Darmstadt, Germany) YES agar plates and incubated at 30 °C until single colonies were visible. Genomic integration was confirmed by colony PCR and DNA sequencing.

***S. pombe* cnp1-PAmCherry1/cbp1-Dendra2.** The DNA fragment used for transformation was amplified from genomic DNA of the previously described cbp1-Dendra2 strain with the primer pair F1_cbp1/R2_cbp1 (**Table S1**). The fragment, containing upstream and downstream homologies, the Dendra2 sequence and the KanR gene was then transformed into an N-terminally tagged cnp1-PAmCherry *S. pombe* strain [5] as described earlier. Integration was confirmed by colony PCR and DNA sequencing.

Sample preparations

Escherichia coli. The strain MG1655 rpoC-mEos3.2-A69T+pJB063 was taken from a −80 °C stock and was cultured overnight at 37 °C, 210 rpm, LB with 34 µg/mL chloramphenicol and 100 µg/mL spectinomycin, reinoculated into fresh LB and grown to OD 0.1. Expression of FtsZ-PAmCherry from pJB063 plasmid was induced by arabinose (0.2% *w*/*v*). After 30 min of induction, the culture was centrifuged (2000× *g*, 3 min) to exchange the medium for fresh LB without inducer and again incubated in 37 °C, 210 rpm for two hours. Fixation was performed for 15 min with 1% paraformaldehyde (Sigma Aldrich, Munich, Germany) and cells were washed twice in 100 mM PBS (pH 7.4). Samples were stored in 100 mM PBS (pH 7.4) or immediately immobilized on 8-well slides (Ibidi, Munich, Germany) previously cleaned with 2% Hellmanex III (Hellma Analytivs, Muellheim, Germany) and coated with 0.05% poly-L-lysine.

MG1655 rpoC-Dendra2 and MG1655 rpoC-PAmCherry genomic strains were grown from −80 °C stocks overnight at 37 °C, 210 rpm in LB medium with appropriate antibiotic marker (**Table S1**), reinoculated and grown to OD 0.2. Fixation and cell immobilization were performed as above.

Prior to imaging, a 250 thousand fold dilution of FluoSphere dark red Carboxylate-Modified Microspheres (ThermoFisher, Munich, Germany) were added to the samples and allowed to settle for 5 min to serve as markers for drift correction.

For live-cell single-particle tracking of the strain MG1655 rpoC_mEos3.2A69T+pJB063, cells were inoculated into TB medium with chloramphenicol and spectinomycin (final concentration 34 and 100 μg/mL, respectively) and grown till OD 0.1. Then cells were induced for 45 min with 0.4% arabinose, washed with EZRDM medium (Teknova, Hollister, California, USA) and placed on 1% low melting agarose pads with EZRDM.

Schizosaccharomyces pombe. Yeast was grown in YES medium (5 g Yeast extract, 30 g glucose, 225 mg of each l-adenine, histidine, leucine, uracil, lysine-hydrochloride in 1 L of Milli-Q water) at 30 °C overnight, then inoculated into fresh YES to a starting OD of 0.1, grown to an OD of 1 and inoculated into EMM (Formedium, Hunstanton, UK) with 225 mg of each l-adenine, histidine, leucine, uracil, lysine-hydrochloride in 1 L of Milli-Q water to a starting OD of 0.1 and grown overnight at 30 °C. On the day of imaging, cells were inoculated into fresh EMM from the overnight culture to a starting OD of 0.1, grown at 30 °C until the cultures reached OD 0.4. For fixed cell experiments, yeast was fixed by adding 37% PFA to the growth medium to a final concentration of 1%, incubated for 10 min then washed three times with PBS. Cells were immobilized on poly-L-lysine coated Ibidi 8-well glass bottom slides, previously cleaned with a 2% solution of Hellmanex III , and then imaged at 30 °C.

HeLa cells. All cell culture reagents were obtained from ThermoFisher. HeLa cells were maintained in DMEM, supplemented with 10% fetal calf serum and 1% penicillin/streptomycin. Transfection of plasmid DNA was performed with FuGENE (Promega, Mannheim, Germany) according to the manufacturer's instruction. Two plasmid combinations were used, β-Actin-PAmCherry1 with Dendra2-Keratin-17 and β-Actin-PAmCherry1 with H2B-Dendra2 (**Table S1**). For each 6-well, 1 μg of plasmid DNA was diluted in 250 μL OptiMEM following addition of 4 μL FuGENE and incubation at room temperature for 30 min. 500 ng of each plasmid (250 ng in case of H2B-Dendra2) were used for co-transfections. Diluted plasmid DNA was then added to confluent Hela cells, and the culture medium was renewed after 3 h. Cells were subcultured in 8-well glass bottom slides (Ibidi, Germany) on the subsequent day. Fixation was performed with methanol (Carl Roth, Karlsruhe, Germany) at −20 °C for 15 min. Samples were washed with 1× PBS. Prior to imaging, a 250 thousand fold dilution of FluoSphere dark red Carboxylate-Modified Microspheres were added to the well and allowed to settle for 5 min to serve as markers for drift correction.

Purification of fluorescent proteins

The pellet of a culture overexpressing PAmCherry from a pBAD plasmid (**Table S1**) was suspended in 10 mM PBS (pH 7.4) with lysozyme (0.5 mg/mL) for 2 h, homogenized by ultrasound (UP100H, Hielscher, Germany) and centrifuged for 15 min (17000×*g*, 4 °C). FPs were purified from the supernatant by Ni-NTA spin columns followed by a buffer exchange to 10 mM PBS (pH 7.4) (Nanosep columns, VWR, Germany).

Microscope

Imaging was performed on a custom built setup based on an automated Nikon Ti Eclipse microscope, equipped with appropriate dichroic and filters (ET dapi/Fitc/cy3 dichroic, ZT405/488/561rpc rejection filter, ET525/50 or ET610/75 bandpass, all AHF Analysentechnik, Germany), and a CFI Apo TIRF 100× oil objective (NA 1.49, Nikon). All lasers (405 nm OBIS, 561 nm OBIS, 730 nm OBIS, 488 nm Sapphire; all Coherent Inc., Santa Clara, California USA) except 730 nm were modulated via an acousto-optical tunable

filter (AOTF) (Gooch and Housego, Eching, Germany). Fluorescence was detected by an emCCD (iXON Ultra 888; Andor, UK). The z-focus was controlled by a commercial perfect focus system (Nikon, Duesseldorf, Germany). Acquisitions were controlled by μManager [13].

Spectroscopy

Absorption spectra and fluorescence spectra (**Fig. 1a–d**) were measured in V-750 and FP-8500 instruments (Jasco, Gross-Umstadt, Germany), respectively, using purified PAmCherry protein with a final concentration 100 μM in 100 mM PBS (pH 7.5), NileRed diluted in acetone and Sytox Orange in ddH2O with final concentrations 1 μM for both in a 50μl UV-transparent quartz cuvette, except spectra of mEos3.2-A69T, which was taken from our previous work [2].

References

1. Niu, L.; Yu, J. Investigating intracellular dynamics of ftsz cytoskeleton with photoactivation single-molecule tracking. *Biophysical journal* **2008**, *95*, 2009–2016.
2. Turkowyd, B.; Balinovic, A.; Virant, D.; Golz Carnero, H.G.; Caldana, F.; Endesfelder, M.; Bourgeois, D.; Endesfelder, U. A general mechanism of photoconversion of green-to-red fluorescent proteins based on blue and infrared light reduces phototoxicity in live-cell single-molecule imaging. *Angewandte Chemie* **2017**.
3. Stracy, M.; Lesterlin, C.; Garza de Leon, F.; Uphoff, S.; Zawadzki, P.; Kapanidis, A.N. Live-cell superresolution microscopy reveals the organization of rna polymerase in the bacterial nucleoid. *PNAS* **2015**, *112*, E4390-E4399.
4. Endesfelder, U.; Finan, K.; Holden, S.J.; Cook, P.R.; Kapanidis, A.N.; Heilemann, M. Multiscale spatial organization of rna polymerase in escherichia coli. *Biophysical journal* **2013**, *105*, 172–181.
5. Lando, D.; Endesfelder, U.; Berger, H.; Subramanian, L.; Dunne, P.D.; McColl, J.; Klenerman, D.; Carr, A.M.; Sauer, M.; Allshire, R.C., *et al.* Quantitative single-molecule microscopy reveals that cenp-a(cnp1) deposition occurs during g2 in fission yeast. *Open biology* **2012**, *2*, 120078.
6. Endesfelder, U.; Malkusch, S.; Flottmann, B.; Mondry, J.; Liguzinski, P.; Verveer, P.J.; Heilemann, M. Chemically induced photoswitching of fluorescent probes--a general concept for super-resolution microscopy. *Molecules* **2011**, *16*, 3106–3118.
7. Datsenko, K.A.; Wanner, B.L. One-step inactivation of chromosomal genes in escherichia coli k-12 using pcr products. *Proceedings of the National Academy of Sciences of the United States of America* **2000**, *97*, 6640–6645.
8. Wang, S.; Moffitt, J.R.; Dempsey, G.T.; Xie, X.S.; Zhuang, X. Characterization and development of photoactivatable fluorescent proteins for single-molecule–based superresolution imaging. *PNAS* **2014**, *111*, 8452–8457.
9. Hayashi, A.; Ding, D.Q.; Tsutsumi, C.; Chikashige, Y.; Masuda, H.; Haraguchi, T.; Hiraoka, Y. Localization of gene products using a chromosomally tagged gfp-fusion library in the fission yeast schizosaccharomyces pombe. *Genes to cells : devoted to molecular & cellular mechanisms* **2009**, *14*, 217–225.
10. Watson, A.T.; Garcia, V.; Bone, N.; Carr, A.M.; Armstrong, J. Gene tagging and gene replacement using recombinase-mediated cassette exchange in schizosaccharomyces pombe. *Gene* **2008**, *407*, 63–74.
11. Berardozzi, R.; Adam, V.; Martins, A.; Bourgeois, D. Arginine 66 controls dark-state formation in green-to-red photoconvertible fluorescent proteins. *Journal of the American Chemical Society* **2016**, *138*, 558–565.
12. Bryksin, A.V.; Matsumura, I. Overlap extension pcr cloning: A simple and reliable way to create recombinant plasmids. *BioTechniques* **2010**, *48*, 463–465.
13. Edelstein, A.; Amodaj, N.; Hoover, K.; Vale, R.; Stuurman, N. Computer control of microscopes using micromanager. *Current protocols in molecular biology / edited by Frederick M. Ausubel [et al.]* **2010**, *Chapter 14*, Unit14 20.

6 | Bibliography

[1] B. Turkowyd, D. Virant, and U. Endesfelder, "From single molecules to life: microscopy at the nanoscale," Analytical and Bioanalytical Chemistry, vol. 408, pp. 6885–6911, Oct 2016.

[2] H. Geerts, M. D. Brabander, R. Nuydens, S. Geuens, M. Moeremans, J. D. Mey, and P. Hollenbeck, "Nanovid tracking: a new automatic method for the study of mobility in living cells based on colloidal gold and video microscopy," Biophysical Journal, vol. 52, no. 5, pp. 775 – 782, 1987.

[3] M. De Brabander, R. Nuydens, H. Geerts, and C. R. Hopkins, "Dynamic behavior of the transferrin receptor followed in living epidermoid carcinoma (a431) cells with nanovid microscopy," Cell Motility, vol. 9, no. 1, pp. 30–47, 1988.

[4] M. De Brabander, G. Geuens, R. Nuydens, M. Moeremans, and J. De Mey, "Probing microtubule-dependent intracellular motility with nanometre particle video ultramicroscopy (nanovid ultramicroscopy)," Cytobios, vol. 43, no. 174S, pp. 273–83, 1985.

[5] M. Edidin, S. C. Kuo, and M. P. Sheetz, "Lateral movements of membrane glycoproteins restricted by dynamic cytoplasmic barriers," Science, vol. 254, no. 5036, pp. 1379–82, 1991.

[6] A. Kusumi, Y. Sako, and M. Yamamoto, "Confined lateral diffusion of membrane receptors as studied by single particle tracking (nanovid microscopy). effects of calcium-induced differentiation in cultured epithelial cells," Biophys J, vol. 65, no. 5, pp. 2021–40, 1993.

[7] G. M. Lee, F. Zhang, A. Ishihara, C. L. McNeil, and K. A. Jacobson, "Unconfined lateral diffusion and an estimate of pericellular matrix viscosity revealed by measuring the mobility of gold-tagged lipids," J Cell Biol, vol. 120, no. 1, pp. 25–35, 1993.

[8] Y. Sako and A. Kusumi, "Barriers for lateral diffusion of transferrin receptor in the plasma membrane as characterized by receptor dragging by laser tweezers: fence versus tether," J Cell Biol, vol. 129, no. 6, pp. 1559–74, 1995.

[9] E. D. Sheets, G. M. Lee, R. Simson, and K. Jacobson, "Transient confinement of a glycosylphosphatidylinositol-anchored protein in the plasma membrane," Biochemistry, vol. 36, no. 41, pp. 12449–58, 1997.

[10] J. Gelles, B. J. Schnapp, and M. P. Sheetz, "Tracking kinesin-driven movements with nanometre-scale precision," Nature, vol. 331, no. 6155, pp. 450–3, 1988.

[11] T. Fujiwara, K. Ritchie, H. Murakoshi, K. Jacobson, and A. Kusumi, "Phospholipids undergo hop diffusion in compartmentalized cell membrane," The Journal of Cell Biology, vol. 157, no. 6, pp. 1071–1082, 2002.

[12] G. Mie, "Beiträge zur optik trüber medien, speziell kolloidaler metallösungen," Annalen der Physik, vol. 330, no. 3, pp. 377–445, 1908.

[13] T. Schmidt, G. Schütz, W. Baumgartner, H. Gruber, and H. Schindler, "Characterization of photophysics and mobility of single molecules in a fluid lipid membrane," The Journal of Physical Chemistry, vol. 99, no. 49, pp. 17662–17668, 1995.

[14] T. Schmidt, G. Schütz, W. Baumgartner, H. Gruber, and H. Schindler, "Imaging of single molecule diffusion," Proceedings of the National Academy of Sciences, vol. 93, no. 7, pp. 2926–2929, 1996.

[15] S. Manley, J. M. Gillette, G. H. Patterson, H. Shroff, H. F. Hess, E. Betzig, and J. Lippincott-Schwartz, "High-density mapping of single-molecule trajectories with photoactivated localization microscopy," Nat Methods, vol. 5, no. 2, pp. 155–7, 2008.

[16] J. Wiedenmann, S. Ivanchenko, F. Oswald, F. Schmitt, C. Röcker, A. Salih, K.-D. Spindler, and G. U. Nienhaus, "Eosfp, a fluorescent marker protein with uv-inducible green-to-red fluorescence conversion," Proceedings of the National Academy of Sciences, vol. 101, no. 45, pp. 15905–15910, 2004.

[17] A. Sanamrad, F. Persson, E. G. Lundius, D. Fange, A. H. Gynnå, and J. Elf, "Single-particle tracking reveals that free ribosomal subunits are not excluded from the escherichia coli nucleoid," Proceedings of the National Academy of Sciences, vol. 111, no. 31, pp. 11413–11418, 2014.

[18] M. Stracy, C. Lesterlin, F. Garza de Leon, S. Uphoff, P. Zawadzki, and A. N. Kapanidis, "Live-cell superresolution microscopy reveals the organization of rna polymerase in the bacterial nucleoid," Proceedings of the National Academy of Sciences, vol. 112, no. 32, pp. E4390–E4399, 2015.

[19] T. R. Beattie, N. Kapadia, E. Nicolas, S. Uphoff, A. J. Wollman, M. C. Leake, and R. Reyes-Lamothe, "Frequent exchange of the dna polymerase during bacterial chromosome replication," Elife, vol. 6, 2017.

[20] S. Uphoff, R. Reyes-Lamothe, F. Garza de Leon, D. J. Sherratt, and A. N. Kapanidis, "Single-molecule dna repair in live bacteria," Proceedings of the National Academy of Sciences, vol. 110, no. 20, pp. 8063–8068, 2013.

[21] M. Stracy, M. Jaciuk, S. Uphoff, A. N. Kapanidis, M. Nowotny, D. J. Sherratt, and P. Zawadzki, "Single-molecule imaging of uvra and uvrb recruitment to dna lesions in living escherichia coli," Nat Commun, vol. 7, p. 12568, 2016.

[22] Y. Liao, Y. Li, J. W. Schroeder, L. A. Simmons, and J. S. Biteen, "Single-molecule dna polymerase dynamics at a bacterial replisome in live cells," Biophysical Journal, vol. 111, no. 12, pp. 2562 – 2569, 2016.

[23] B. Turkowyd, H. Müller-Esparza, V. Climenti, N. Steube, U. Endesfelder, and L. Randau, "Chapter seven - live-cell single-particle tracking photoactivated localization microscopy of cascade-mediated dna surveillance," in CRISPR-Cas Enzymes (S. Bailey, ed.), vol. 616 of Methods in Enzymology, pp. 133 – 171, Academic Press, 2019.

[24] J. Elf, G.-W. Li, and X. S. Xie, "Probing transcription factor dynamics at the single-molecule level in a living cell," Science, vol. 316, no. 5828, pp. 1191–1194, 2007.

[25] X. S. Xie, P. J. Choi, G.-W. Li, N. K. Lee, and G. Lia, "Single-molecule approach to molecular biology in living bacterial cells," Annual Review of Biophysics, vol. 37, no. 1, pp. 417–444, 2008. PMID: 18573089.

[26] Z. Liu, L. Lavis, and E. Betzig, "Imaging live-cell dynamics and structure at the single-molecule level," Molecular Cell, vol. 58, no. 4, pp. 644 – 659, 2015.

[27] J. C. Gebhardt, D. M. Suter, R. Roy, Z. W. Zhao, A. R. Chapman, S. Basu, T. Maniatis, and X. S. Xie, "Single-molecule imaging of transcription factor binding to DNA in live mammalian cells," Nat. Methods, vol. 10, pp. 421–426, May 2013.

[28] A. P. Popp, J. Hettich, K. Clauß, L. Schulze, M. Reisser, J. Gebhardt, L. Escoter Torres, and N. H. Uhlenhaut, "DNA residence time is a regulatory factor of transcription repression," Nucleic Acids Research, vol. 45, pp. 11121–11130, 08 2017.

[29] R. Barrangou, C. Fremaux, H. Deveau, M. Richards, P. Boyaval, S. Moineau, D. A. Romero, and P. Horvath, "Crispr provides acquired resistance against viruses in prokaryotes," Science, vol. 315, no. 5819, pp. 1709–1712, 2007.

[30] L. A. Marraffini and E. J. Sontheimer, "Crispr interference limits horizontal gene transfer in staphylococci by targeting dna," Science, vol. 322, no. 5909, pp. 1843–1845, 2008.

[31] R. Edgar and U. Qimron, "The escherichia coli crispr system protects from λ lysogenization, lysogens, and prophage induction," Journal of Bacteriology, vol. 192, no. 23, pp. 6291–6294, 2010.

[32] J. E. Garneau, M. E. Dupuis, M. Villion, D. A. Romero, R. Barrangou, P. Boyaval, C. Fremaux, P. Horvath, A. H. Magadan, and S. Moineau, "The crispr/cas bacterial immune system cleaves bacteriophage and plasmid dna," Nature, vol. 468, no. 7320, pp. 67–71, 2010.

[33] Y. Ishino, H. Shinagawa, K. Makino, M. Amemura, and A. Nakata, "Nucleotide sequence of the iap gene, responsible for alkaline phosphatase isozyme conversion in escherichia coli, and identification of the gene product.," Journal of Bacteriology, vol. 169, no. 12, pp. 5429–5433, 1987.

[34] D. van Soolingen, P. E. de Haas, P. W. Hermans, P. M. Groenen, and J. D. van Embden, "Comparison of various repetitive dna elements as genetic markers for strain differentiation and epidemiology of mycobacterium tuberculosis," J Clin Microbiol, vol. 31, no. 8, pp. 1987–95, 1993.

[35] P. M. A. Groenen, A. E. Bunschoten, D. v. Soolingen, and J. D. A. v. Errtbden, "Nature of dna polymorphism in the direct repeat cluster of mycobacterium tuberculosis; application

for strain differentiation by a novel typing method," Molecular Microbiology, vol. 10, no. 5, pp. 1057–1065, 1993.

[36] F. J. M. Mojica, C. Díez-Villaseñor, E. Soria, and G. Juez, "Biological significance of a family of regularly spaced repeats in the genomes of archaea, bacteria and mitochondria," Molecular Microbiology, vol. 36, no. 1, pp. 244–246, 2000.

[37] R. Jansen, J. D. A. v. Embden, W. Gaastra, and L. M. Schouls, "Identification of genes that are associated with dna repeats in prokaryotes," Molecular Microbiology, vol. 43, no. 6, pp. 1565–1575, 2002.

[38] A. Bolotin, B. Quinquis, A. Sorokin, and S. D. Ehrlich, "Clustered regularly interspaced short palindrome repeats (crisprs) have spacers of extrachromosomal origin," Microbiology, vol. 151, no. 8, pp. 2551–2561, 2005.

[39] F. J. Mojica, C. Díez-Villaseñor, J. García-Martínez, and E. Soria, "Intervening sequences of regularly spaced prokaryotic repeats derive from foreign genetic elements," Journal of Molecular Evolution, vol. 60, pp. 174–182, Feb 2005.

[40] C. Pourcel, G. Salvignol, and G. Vergnaud, "Crispr elements in yersinia pestis acquire new repeats by preferential uptake of bacteriophage dna, and provide additional tools for evolutionary studies," Microbiology, vol. 151, no. 3, pp. 653–663, 2005.

[41] R. Sorek, V. Kunin, and P. Hugenholtz, "Crispr–a widespread system that provides acquired resistance against phages in bacteria and archaea," Nat Rev Microbiol, vol. 6, no. 3, pp. 181–6, 2008.

[42] J. van der Oost, M. M. Jore, E. R. Westra, M. Lundgren, and S. J. Brouns, "Crispr-based adaptive and heritable immunity in prokaryotes," Trends in Biochemical Sciences, vol. 34, no. 8, pp. 401 – 407, 2009.

[43] P. Horvath and R. Barrangou, "Crispr/cas, the immune system of bacteria and archaea," Science, vol. 327, no. 5962, pp. 167–170, 2010.

[44] E. V. Koonin, K. S. Makarova, and F. Zhang, "Diversity, classification and evolution of crispr-cas systems," Current Opinion in Microbiology, vol. 37, pp. 67 – 78, 2017. Environmental microbiology * CRISPRcas9.

[45] K. S. Makarova, Y. I. Wolf, and E. V. Koonin, "Classification and nomenclature of crispr-cas systems: Where from here?," The CRISPR Journal, vol. 1, no. 5, pp. 325–336, 2018.

[46] K. S. Makarova, D. H. Haft, R. Barrangou, S. J. Brouns, E. Charpentier, P. Horvath, S. Moineau, F. J. Mojica, Y. I. Wolf, A. F. Yakunin, J. van der Oost, and E. V. Koonin, "Evolution and classification of the crispr-cas systems," Nat Rev Microbiol, vol. 9, no. 6, pp. 467–77, 2011.

[47] K. Chylinski, E. Charpentier, K. S. Makarova, and E. V. Koonin, "Classification and evolution of type II CRISPR-Cas systems," Nucleic Acids Research, vol. 42, pp. 6091–6105, 04 2014.

[48] J. K. Nunez, P. J. Kranzusch, J. Noeske, A. V. Wright, C. W. Davies, and J. A. Doudna, "Cas1-cas2 complex formation mediates spacer acquisition during crispr-cas adaptive immunity," Nat Struct Mol Biol, vol. 21, no. 6, pp. 528–34, 2014.

[49] J. Wang, J. Li, H. Zhao, G. Sheng, M. Wang, M. Yin, and Y. Wang, "Structural and mechanistic basis of pam-dependent spacer acquisition in crispr-cas systems," Cell, vol. 163, no. 4, pp. 840–53, 2015.

[50] L. A. Marraffini and E. J. Sontheimer, "Self versus non-self discrimination during CRISPR RNA-directed immunity," Nature, vol. 463, pp. 568–571, Jan 2010.

[51] J. Carte, R. Wang, H. Li, R. M. Terns, and M. P. Terns, "Cas6 is an endoribonuclease that generates guide rnas for invader defense in prokaryotes," Genes Dev, vol. 22, no. 24, pp. 3489–96, 2008.

[52] R. E. Haurwitz, M. Jinek, B. Wiedenheft, K. Zhou, and J. A. Doudna, "Sequence- and structure-specific rna processing by a crispr endonuclease," Science, vol. 329, no. 5997, pp. 1355–1358, 2010.

[53] L. Cong, F. A. Ran, D. Cox, S. Lin, R. Barretto, N. Habib, P. D. Hsu, X. Wu, W. Jiang, L. A. Marraffini, and F. Zhang, "Multiplex genome engineering using crispr/cas systems," Science, vol. 339, no. 6121, pp. 819–823, 2013.

[54] M. Chen, A. Mao, M. Xu, Q. Weng, J. Mao, and J. Ji, "Crispr-cas9 for cancer therapy: Opportunities and challenges," Cancer Letters, vol. 447, pp. 48 – 55, 2019.

[55] K. Chen, Y. Wang, R. Zhang, H. Zhang, and C. Gao, "Crispr/cas genome editing and precision plant breeding in agriculture," Annual Review of Plant Biology, vol. 70, no. 1, p. null, 2019. PMID: 30835493.

[56] A. Bao, D. J. Burritt, H. Chen, X. Zhou, D. Cao, and L.-S. P. Tran, "The crispr/cas9 system and its applications in crop genome editing," Critical Reviews in Biotechnology, vol. 39, no. 3, pp. 321–336, 2019. PMID: 30646772.

[57] P. Gao, H. Yang, K. R. Rajashankar, Z. Huang, and D. J. Patel, "Type V CRISPR-Cas Cpf1 endonuclease employs a unique mechanism for crRNA-mediated target DNA recognition," Cell Res., vol. 26, pp. 901–913, 08 2016.

[58] K. M. Lewis and A. Ke, "Building the Class 2 CRISPR-Cas Arsenal," Mol. Cell, vol. 65, pp. 377–379, Feb 2017.

[59] S. Shmakov, O. O. Abudayyeh, K. S. Makarova, Y. I. Wolf, J. S. Gootenberg, E. Semenova, L. Minakhin, J. Joung, S. Konermann, K. Severinov, F. Zhang, and E. V. Koonin, "Discovery and Functional Characterization of Diverse Class 2 CRISPR-Cas Systems," Mol. Cell, vol. 60, pp. 385–397, Nov 2015.

[60] T. Sinkunas, G. Gasiunas, C. Fremaux, R. Barrangou, P. Horvath, and V. Siksnys, "Cas3 is a single-stranded dna nuclease and atp-dependent helicase in the crispr/cas immune system," The EMBO Journal, vol. 30, no. 7, pp. 1335–1342, 2011.

[61] B. Gong, M. Shin, J. Sun, C.-H. Jung, E. L. Bolt, J. van der Oost, and J.-S. Kim, "Molecular insights into dna interference by crispr-associated nuclease-helicase cas3," Proceedings of the National Academy of Sciences, vol. 111, no. 46, pp. 16359–16364, 2014.

[62] Y. Huo, K. H. Nam, F. Ding, H. Lee, L. Wu, Y. Xiao, M. D. Farchione, S. Zhou, K. Rajashankar, I. Kurinov, R. Zhang, and A. Ke, "Structures of CRISPR Cas3 offer mechanistic insights into Cascade-activated DNA unwinding and degradation," Nat. Struct. Mol. Biol., vol. 21, pp. 771–777, Sep 2014.

[63] K. S. Makarova, Y. I. Wolf, O. S. Alkhnbashi, F. Costa, S. A. Shah, S. J. Saunders, R. Barrangou, S. J. Brouns, E. Charpentier, D. H. Haft, P. Horvath, S. Moineau, F. J. Mojica, R. M. Terns, M. P. Terns, M. F. White, A. F. Yakunin, R. A. Garrett, J. van der Oost, R. Backofen, and E. V. Koonin, "An updated evolutionary classification of CRISPR-Cas systems," Nat. Rev. Microbiol., vol. 13, pp. 722–736, 11 2015.

[64] S. J. J. Brouns, M. M. Jore, M. Lundgren, E. R. Westra, R. J. H. Slijkhuis, A. P. L. Snijders, M. J. Dickman, K. S. Makarova, E. V. Koonin, and J. van der Oost, "Small crispr rnas guide antiviral defense in prokaryotes," Science, vol. 321, no. 5891, pp. 960–964, 2008.

[65] R. N. Jackson, S. M. Golden, P. B. G. van Erp, J. Carter, E. R. Westra, S. J. J. Brouns, J. van der Oost, T. C. Terwilliger, R. J. Read, and B. Wiedenheft, "Crystal structure of the crispr rna–guided surveillance complex from escherichia coli," Science, vol. 345, no. 6203, pp. 1473–1479, 2014.

[66] E. R. Westra, P. B. van Erp, T. Kunne, S. P. Wong, R. H. Staals, C. L. Seegers, S. Bollen, M. M. Jore, E. Semenova, K. Severinov, W. M. de Vos, R. T. Dame, R. de Vries, S. J. Brouns, and J. van der Oost, "CRISPR immunity relies on the consecutive binding and degradation of negatively supercoiled invader DNA by Cascade and Cas3," Mol. Cell, vol. 46, pp. 595–605, Jun 2012.

[67] R. Przybilski, C. Richter, T. Gristwood, J. S. Clulow, R. B. Vercoe, and P. C. Fineran, "Csy4 is responsible for crispr rna processing in pectobacterium atrosepticum," RNA Biology, vol. 8, no. 3, pp. 517–528, 2011.

[68] S. Dwarakanath, S. Brenzinger, D. Gleditzsch, A. Plagens, A. Klingl, K. Thormann, and L. Randau, "Interference activity of a minimal Type I CRISPR-Cas system from Shewanella putrefaciens," Nucleic Acids Res., vol. 43, pp. 8913–8923, Oct 2015.

[69] C. Richter, T. Gristwood, J. S. Clulow, and P. C. Fineran, "In vivo protein interactions and complex formation in the pectobacterium atrosepticum subtype i-f crispr/cas system," PLOS ONE, vol. 7, pp. 1–11, 12 2012.

[70] C. R. Hale, P. Zhao, S. Olson, M. O. Duff, B. R. Graveley, L. Wells, R. M. Terns, and M. P. Terns, "RNA-guided RNA cleavage by a CRISPR RNA-Cas protein complex," Cell, vol. 139, pp. 945–956, Nov 2009.

[71] L. Deng, R. A. Garrett, S. A. Shah, X. Peng, and Q. She, "A novel interference mechanism by a type iiib crispr-cmr module in sulfolobus," Molecular Microbiology, vol. 87, no. 5, pp. 1088–1099, 2013.

[72] R. Staals, Y. Zhu, D. Taylor, J. Kornfeld, K. Sharma, A. Barendregt, J. Koehorst, M. Vlot, N. Neupane, K. Varossieau, K. Sakamoto, T. Suzuki, N. Dohmae, S. Yokoyama, P. Schaap, H. Urlaub, A. Heck, E. Nogales, J. Doudna, A. Shinkai, and J. vanÂ derÂ Oost, "Rna targeting by the type iii-a crispr-cas csm complex of thermus thermophilus," Molecular Cell, vol. 56, no. 4, pp. 518 – 530, 2014.

[73] M. A. Estrella, F. T. Kuo, and S. Bailey, "RNA-activated DNA cleavage by the Type III-B CRISPR-Cas effector complex," Genes Dev., vol. 30, pp. 460–470, Feb 2016.

[74] D. Gleditzsch, H. Müller-Esparza, P. Pausch, K. Sharma, S. Dwarakanath, H. Urlaub, G. Bange, and L. Randau, "Modulating the Cascade architecture of a minimal Type I-F CRISPR-Cas system," Nucleic Acids Res., vol. 44, pp. 5872–5882, 07 2016.

[75] P. Pausch, H. Müller-Esparza, D. Gleditzsch, F. Altegoer, L. Randau, and G. Bange, "Structural Variation of Type I-F CRISPR RNA Guided DNA Surveillance," Mol. Cell, vol. 67, pp. 622–632, Aug 2017.

[76] S. H. Sternberg, S. Redding, M. Jinek, E. C. Greene, and J. A. Doudna, "Dna interrogation by the crispr rna-guided endonuclease cas9," Nature, vol. 507, no. 7490, pp. 62–7, 2014.

[77] S. Redding, S. Sternberg, M. Marshall, B. Gibb, P. Bhat, C. Guegler, B. Wiedenheft, J. Doudna, and E. Greene, "Surveillance and processing of foreign dna by the escherichia coli crispr-cas system," Cell, vol. 163, no. 4, pp. 854 – 865, 2015.

[78] D. Singh, J. Mallon, A. Poddar, Y. Wang, R. Tippana, O. Yang, S. Bailey, and T. Ha, "Real-time observation of dna target interrogation and product release by the rna-guided endonuclease crispr cpf1 (cas12a)," Proceedings of the National Academy of Sciences, vol. 115, no. 21, pp. 5444–5449, 2018.

[79] T. Ha, T. Enderle, D. F. Ogletree, D. S. Chemla, P. R. Selvin, and S. Weiss, "Probing the interaction between two single molecules: fluorescence resonance energy transfer between a single donor and a single acceptor," Proc Natl Acad Sci U S A, vol. 93, no. 13, pp. 6264–8, 1996.

[80] V. Globyte, S. H. Lee, T. Bae, J.-S. Kim, and C. Joo, "Crispr/cas9 searches for a protospacer adjacent motif by lateral diffusion," The EMBO Journal, vol. 38, no. 4, 2019.

[81] K. E. Dillard, M. W. Brown, N. V. Johnson, Y. Xiao, A. Dolan, E. Hernandez, S. D. Dahlhauser, Y. Kim, L. R. Myler, E. V. Anslyn, A. Ke, and I. J. Finkelstein, "Assembly and translocation of a crispr-cas primed acquisition complex," Cell, vol. 175, no. 4, pp. 934–946 e15, 2018.

[82] T. Blosser, L. Loeff, E. Westra, M. Vlot, T. Künne, M. Sobota, C. Dekker, S. Brouns, and C. Joo, "Two distinct dna binding modes guide dual roles of a crispr-cas protein complex," Molecular Cell, vol. 58, no. 1, pp. 60 – 70, 2015.

[83] D. Singh, S. H. Sternberg, J. Fei, J. A. Doudna, and T. Ha, "Real-time observation of dna recognition and rejection by the rna-guided endonuclease cas9," Nat Commun, vol. 7, p. 12778, 2016.

[84] D. Singh, Y. Wang, J. Mallon, O. Yang, J. Fei, A. Poddar, D. Ceylan, S. Bailey, and T. Ha, "Mechanisms of improved specificity of engineered cas9s revealed by single-molecule fret analysis," Nat Struct Mol Biol, vol. 25, no. 4, pp. 347–354, 2018.

[85] M. D. Szczelkun, M. S. Tikhomirova, T. Sinkunas, G. Gasiunas, T. Karvelis, P. Pschera, V. Siksnys, and R. Seidel, "Direct observation of r-loop formation by single rna-guided cas9 and cascade effector complexes," Proceedings of the National Academy of Sciences, vol. 111, no. 27, pp. 9798–9803, 2014.

[86] M. Rutkauskas, T. Sinkunas, I. Songailiene, M. S. Tikhomirova, V. Siksnys, and R. Seidel, "Directional R-Loop Formation by the CRISPR-Cas Surveillance Complex Cascade Provides Efficient Off-Target Site Rejection," Cell Rep, vol. 10, pp. 1534–1543, Mar 2015.

[87] C. Gosse and V. Croquette, "Magnetic tweezers: Micromanipulation and force measurement at the molecular level," Biophysical Journal, vol. 82, no. 6, pp. 3314 – 3329, 2002.

[88] Y. Lim, S. Y. Bak, K. Sung, E. Jeong, S. H. Lee, J. S. Kim, S. Bae, and S. K. Kim, "Structural roles of guide RNAs in the nuclease activity of Cas9 endonuclease," Nat Commun, vol. 7, p. 13350, 11 2016.

[89] C. J. Fitzgibbon, E. A. Josephs, P. E. Marszalek, D. D. Kocak, J. McMenemy, and C. A. Gersbach, "Structure and specificity of the RNA-guided endonuclease Cas9 during DNA interrogation, target binding and cleavage," Nucleic Acids Research, vol. 43, pp. 8924–8941, 10 2015.

[90] S. C. Knight, L. Xie, W. Deng, B. Guglielmi, L. B. Witkowsky, L. Bosanac, E. T. Zhang, M. El Beheiry, J.-B. Masson, M. Dahan, Z. Liu, J. A. Doudna, and R. Tjian, "Dynamics of crispr-cas9 genome interrogation in living cells," Science, vol. 350, no. 6262, pp. 823–826, 2015.

[91] D. L. Jones, P. Leroy, C. Unoson, D. Fange, V. Ćurić, M. J. Lawson, and J. Elf, "Kinetics of dcas9 target search in escherichia coli," Science, vol. 357, no. 6358, pp. 1420–1424, 2017.

[92] K. J. Martens, S. van Beljouw, S. van der Els, S. Baas, J. N. Vink, S. J. Brouns, P. van Baarlen, M. Kleerebezem, and J. Hohlbein, "An open microscopy framework suited for tracking dcas9 in live bacteria," bioRxiv, 2018.

[93] J. N. Vink, K. J. Martens, M. Vlot, R. E. McKenzie, C. Almendros, B. E. Bonilla, D. J. Brocken, J. Hohlbein, and S. J. Brouns, "Direct visualization of native crispr target search in live bacteria reveals cascade dna surveillance mechanism," bioRxiv, 2019.

[94] B. Turkowyd, A. Balinovic, D. Virant, H. G. G. Carnero, F. Caldana, M. Endesfelder, D. Bourgeois, and U. Endesfelder, "A general mechanism of photoconversion of green-to-red fluorescent proteins based on blue and infrared light reduces phototoxicity in live-cell single-molecule imaging," Angewandte Chemie International Edition, vol. 56, no. 38, pp. 11634–11639, 2017.

[95] D. Virant, B. Turkowyd, A. Balinovic, and U. Endesfelder, "Combining primed photoconversion and uv-photoactivation for aberration-free, live-cell compliant multi-color single-molecule localization microscopy imaging," International Journal of Molecular Sciences, vol. 18, no. 7, 2017.

[96] A. D. Edelstein, M. A. Tsuchida, N. Amodaj, H. Pinkard, R. D. Vale, and N. Stuurman, "Advanced methods of microscope control using Micro-Mananager software," J Biol Methods, vol. 1, no. 2, 2014.

[97] M. Tokunaga, N. Imamoto, and K. Sakata-Sogawa, "Highly inclined thin illumination enables clear single-molecule imaging in cells," Nat. Methods, vol. 5, pp. 159–161, Feb 2008.

[98] J. Schindelin, I. Arganda-Carreras, E. Frise, V. Kaynig, M. Longair, T. Pietzsch, S. Preibisch, C. Rueden, S. Saalfeld, B. Schmid, J. Y. Tinevez, D. J. White, V. Hartenstein, K. Eliceiri, P. Tomancak, and A. Cardona, "Fiji: an open-source platform for biological-image analysis," Nat. Methods, vol. 9, pp. 676–682, Jun 2012.

[99] S. Wolter, A. Loschberger, T. Holm, S. Aufmkolk, M. C. Dabauvalle, S. van de Linde, and M. Sauer, "rapidSTORM: accurate, fast open-source software for localization microscopy," Nat. Methods, vol. 9, pp. 1040–1041, Nov 2012.

[100] M. Ovesný, P. Křížek, J. Borkovec, Z. Svindrych, and G. M. Hagen, "ThunderSTORM: a comprehensive ImageJ plug-in for PALM and STORM data analysis and super-resolution imaging," Bioinformatics, vol. 30, pp. 2389–2390, Aug 2014.

[101] A. Gahlmann and W. E. Moerner, "Exploring bacterial cell biology with single-molecule tracking and super-resolution imaging," Nat. Rev. Microbiol., vol. 12, pp. 9–22, Jan 2014.

[102] R. Berardozzi, V. Adam, A. Martins, and D. Bourgeois, "Arginine 66 controls dark-state formation in green-to-red photoconvertible fluorescent proteins," Journal of the American Chemical Society, vol. 138, no. 2, pp. 558–565, 2016. PMID: 26675944.

[103] R. Tobes and J.-L. Ramos, "Rep code: defining bacterial identity in extragenic space," Environmental Microbiology, vol. 7, no. 2, pp. 225–228, 2005.

[104] M. Stracy, S. Uphoff, F. Garza de Leon, and A. N. Kapanidis, "In vivo single-molecule imaging of bacterial dna replication, transcription, and repair," FEBS Letters, vol. 588, no. 19, pp. 3585–3594, 2014.

[105] P. J. Lopez, I. Marchand, O. Yarchuk, and M. Dreyfus, "Translation inhibitors stabilize Escherichia coli mRNAs independently of ribosome protection," Proc. Natl. Acad. Sci. U.S.A., vol. 95, pp. 6067–6072, May 1998.

[106] M. Scott, C. W. Gunderson, E. M. Mateescu, Z. Zhang, and T. Hwa, "Interdependence of cell growth and gene expression: Origins and consequences," Science, vol. 330, no. 6007, pp. 1099–1102, 2010.

[107] D. R. Zusman, A. Carbonell, and J. Y. Haga, "Nucleoid condensation and cell division in escherichia coli mx74t2 ts52 after inhibition of protein synthesis," Journal of Bacteriology, vol. 115, no. 3, pp. 1167–1178, 1973.

[108] E. A. Campbell, N. Korzheva, A. Mustaev, K. Murakami, S. Nair, A. Goldfarb, and S. A. Darst, "Structural mechanism for rifampicin inhibition of bacterial rna polymerase," Cell, vol. 104, no. 6, pp. 901 – 912, 2001.

[109] A. Sippel and G. Hartmann, "Mode of action of rifamycin on the rna polymerase reaction," Biochimica et Biophysica Acta (BBA) - Nucleic Acids and Protein Synthesis, vol. 157, no. 1, pp. 218 – 219, 1968.

[110] H. Chen, K. Shiroguchi, H. Ge, and X. S. Xie, "Genome-wide study of mrna degradation and transcript elongation in escherichia coli," Molecular Systems Biology, vol. 11, no. 1, 2015.

[111] S.-T. Liang, M. Ehrenberg, P. Dennis, and H. Bremer, "Decay of rpln and lacz mrna in escherichia coli11edited by d. e. draper," Journal of Molecular Biology, vol. 288, no. 4, pp. 521 – 538, 1999.

[112] L. H. So, A. Ghosh, C. Zong, L. A. Sepulveda, R. Segev, and I. Golding, "General properties of transcriptional time series in Escherichia coli," Nat. Genet., vol. 43, pp. 554–560, Jun 2011.

[113] B. A. Hesselbach and D. Nakada, ""Host shutoff" function of bacteriophage T7: involvement of T7 gene 2 and gene 0.7 in the inactivation of Escherichia coli RNA polymerase," J. Virol., vol. 24, pp. 736–745, Dec 1977.

[114] A. Kuderová, E. Nanak, M. Truksa, and B. Brzobohatý, "Use of rifampicin in t7 rna polymerase-driven expression of a plant enzyme: Rifampicin improves yield and assembly," Protein Expression and Purification, vol. 16, no. 3, pp. 405 – 409, 1999.

[115] S. Bakshi, A. Siryaporn, M. Goulian, and J. C. Weisshaar, "Superresolution imaging of ribosomes and rna polymerase in live escherichia coli cells," Molecular Microbiology, vol. 85, no. 1, pp. 21–38, 2012.

[116] S. Mulepati, A. Héroux, and S. Bailey, "Crystal structure of a crispr rna–guided surveillance complex bound to a ssdna target," Science, vol. 345, no. 6203, pp. 1479–1484, 2014.

[117] W. P. Dempsey, L. Georgieva, P. M. Helbling, A. Y. Sonay, T. V. Truong, M. Haffner, and P. Pantazis, "In vivo single-cell labeling by confined primed conversion," Nat. Methods, vol. 12, pp. 645–648, Jul 2015.

[118] G. H. Patterson and J. Lippincott-Schwartz, "A photoactivatable gfp for selective photolabeling of proteins and cells," Science, vol. 297, no. 5588, pp. 1873–1877, 2002.

[119] D. M. Chudakov, V. V. Verkhusha, D. B. Staroverov, E. A. Souslova, S. Lukyanov, and K. A. Lukyanov, "Photoswitchable cyan fluorescent protein for protein tracking," Nat. Biotechnol., vol. 22, pp. 1435–1439, Nov 2004.

[120] R. Ando, H. Mizuno, and A. Miyawaki, "Regulated fast nucleocytoplasmic shuttling observed by reversible protein highlighting," Science, vol. 306, no. 5700, pp. 1370–1373, 2004.

[121] H. Shroff, C. G. Galbraith, J. A. Galbraith, H. White, J. Gillette, S. Olenych, M. W. Davidson, and E. Betzig, "Dual-color superresolution imaging of genetically expressed probes within individual adhesion complexes," Proceedings of the National Academy of Sciences, vol. 104, no. 51, pp. 20308–20313, 2007.

[122] M. A. Mohr, A. Y. Kobitski, L. R. Sabater, K. Nienhaus, C. J. Obara, J. Lippincott-Schwartz, G. U. Nienhaus, and P. Pantazis, "Rational engineering of photoconvertible fluorescent proteins for dual-color fluorescence nanoscopy enabled by a triplet-state mechanism of primed conversion," Angewandte Chemie International Edition, vol. 56, no. 38, pp. 11628–11633, 2017.

[123] B. P. Cormack, R. H. Valdivia, and S. Falkow, "Facs-optimized mutants of the green fluorescent protein (gfp)," Gene, vol. 173, no. 1, pp. 33 – 38, 1996. Flourescent Proteins and Applications.

[124] V. Adam, M. Lelimousin, S. Boehme, G. Desfonds, K. Nienhaus, M. J. Field, J. Wiedenmann, S. McSweeney, G. U. Nienhaus, and D. Bourgeois, "Structural characterization of irisfp, an optical highlighter undergoing multiple photo-induced transformations," Proceedings of the National Academy of Sciences, vol. 105, no. 47, pp. 18343–18348, 2008.

[125] M. Byrdin, C. Duan, D. Bourgeois, and K. Brettel, "A long-lived triplet state is the entrance gateway to oxidative photochemistry in green fluorescent proteins," Journal of the American Chemical Society, vol. 140, no. 8, pp. 2897–2905, 2018. PMID: 29394055.

[126] B. Moeyaert, N. Nguyen Bich, E. De Zitter, S. Rocha, K. Clays, H. Mizuno, L. van Meervelt, J. Hofkens, and P. Dedecker, "Green-to-red photoconvertible dronpa mutant for multimodal super-resolution fluorescence microscopy," ACS Nano, vol. 8, no. 2, pp. 1664–1673, 2014. PMID: 24410188.

[127] O. M. Subach, G. H. Patterson, L. M. Ting, Y. Wang, J. S. Condeelis, and V. V. Verkhusha, "A photoswitchable orange-to-far-red fluorescent protein, PSmOrange," Nat. Methods, vol. 8, pp. 771–777, Jul 2011.

[128] O. M. Subach, D. Entenberg, J. S. Condeelis, and V. V. Verkhusha, "A fret-facilitated photoswitching using an orange fluorescent protein with the fast photoconversion kinetics," Journal of the American Chemical Society, vol. 134, no. 36, pp. 14789–14799, 2012. PMID: 22900938.

[129] H. N. Ho, D. Zalami, J. Köhler, A. M. van Oijen, and H. Ghodke, "Identifying multiple kinetic populations of dna binding proteins in live cells using single-molecule fluorescence imaging," bioRxiv, 2019.

[130] M. D. Newton, B. J. Taylor, R. P. C. Driessen, L. Roos, N. Cvetesic, S. Allyjaun, B. Lenhard, M. E. Cuomo, and D. S. Rueda, "DNA stretching induces Cas9 off-target activity," Nat. Struct. Mol. Biol., vol. 26, pp. 185–192, Mar 2019.

7 List of Figures

8 List of Tables

9 | Acknowledgements

First, I would like to thank Dr. Ulrike Endesfelder for giving me the great opportunity to perform my Ph.D. work under her supervision and for the amazing support throughout these four years. I wanted to especially thank her for passionate discussions, ideas, support and motivation which encouraged me to expand my knowledge and scientific skills.

Also, I would like to thank the members of my Thesis Advisory Committee: Prof. Dr. Victor Sourjik, Prof. Dr. Knut Drescher and Dr. Hannes Link for helpful discussions and critical opinions on my work.

I would like to thank Dr. Lennart Randau and Hanna Müller-Esparza for giving me an opportunity to work with them together on CRISPR-Cas interference being the main biological application of my PhD work. I am very grateful for this opportunity to explore the novel research field of CRISPR-Cas interference and defence and I am grateful for tehir trust and support.

Likewise, I would like to thank Prof. Dr. Dominique Bourgeois (Institute de Biologie Structurale, Grenoble, France), who together with Dr. Ulrike Endesfelder showed me that studying photophysics can be fascinating for me, molecular biologist.

I am grateful for having an opportunity to work with Dr. Simon Ringgaard and Dr. Alejandra Alvarado and being involved in their fascinating project focused on protein gradient formation of ParC in *Vibrio parahaemolyticus* cells. I hope I will be able to continue this fruitful collaboration.

I would like to also thank my collegues from the RG Endesfelder for your help support and providing a lot of fun during our work. Separately, I want to thank David Virant, who started his Ph.D. work together with me and we spent plenty of time on valuable discussions and supporting each other on many levels. It was a great pleasure to have such a great company.

I want to thank our office mate, María Esteban López, for her positive attitude, patience, and understanding for our discussions within the group. Also, I would like to thank members of AG Sourjik, especially their technical staff and assistants for their amazing work, which made my work much easier.

Finally, I want to thank my family and two amazing friends: Antonina Kirkało-Kowerczyk and Krzysztof Jakub Kowerczyk for their love, friendship, support, and faith.

Bartosz Turkowyd, M.Sc.

MPI for Terrestrial Microbiology and SYNMIKRO
Karl-von-Frisch-Str.16
35043 Marburg, Germany

+49 6421 28 21483

bartosz.turkowyd@synmikro.mpi-marburg.mpg.de
www.endesfelder-lab.org

Scientific interests: Single-molecule localization microscopy, fluorescence microscopy and spectroscopy, molecular biology, Python and Java programming, data analysis and machine learning

University education

From Feb 15 — **PhD project,** Department of Systems and Synthetic Microbiology, MPI for Terrestrial Microbiology and SYNMIKRO, Marburg, Germany

Thesis (on-going) "*Protein dynamic in microorganism research with single-molecule localization microscopy techniques*"

Research Group Dr. Ulrike Endesfelder

Oct 12 – Jul 14 — **Master studies of Biotechnology,** Faculty of Biotechnology, University of Wroclaw, Wroclaw, Poland

M.Sc. thesis (4.5/5.0) "*Construction and characterization transgenic lines of Arabidopsis thaliana with different variants of mitochondrial protease AtFtsH4*"

Research Group Prof. Dr. Hanna Janska

Oct 09 – Sep 12 — **Bachelor studies of Biotechnology,** Faculty of Biotechnology, University of Wroclaw, Wroclaw, Poland

B.Sc. thesis (4.0/5.0) "*Cloning strategies with using of Gateway-type vectors*"

Research Group Prof. Dr. Hanna Janska

Professional experience

Jul – Oct 13 — **Student assistant,** Faculty of biotechnology, University of Wroclaw, Wroclaw, Poland Research project: NR 2011/03/N/NZ2/00221 "*Identification of natural substrate and physiological partners of mitochondrial AtFtsH4 protease from Arabidopsis thaliana. A role of AtFtsH4 in protection of mitochondrial proteome against oxidative stress*", from National Science Center, Poland

Research Group Prof. Dr. Hanna Janska

Scholarships and honors

Jun 18 — DAAD conference grant, CRISPR 2018, Vilnius, Lithuania

Mar 17 — Anal Bioanal Chem Paper Award 2016 (*Anal Bioanal Chem, 408:6885-6911*)